Multifunctional Materials for Energy Harvesting and Sensing

Prashant Kumar

Dissertation submitted to the faculty of the Virginia Polytechnic Institute and State University in partial fulfillment of the requirements for the degree of

Doctor of Philosophy
In
Mechanical Engineering

Shashank Priya
Muhammad R. Hajj
Rui Qiao
Brian Vick

February 22nd, 2019
Blacksburg, VA

Keywords: Shape Memory Alloy, Carbon Nanotubes, Piezoelectric Materials, Nanotube yarns

Multifunctional Materials for Energy Harvesting and Sensing

Prashant Kumar

ABSTRACT

This dissertation investigates the fundamental behavior of multifunctional materials for energy conversion. Multifunctional materials exhibit two or more functional properties, such as electrical, thermal, magnetic etc. In this dissertation, the emphasis is on understanding the principles for energy conversion from one domain to another (e.g. thermal to electrical; or mechanical to electrical) by utilizing nanomaterials and nanostructured materials such as carbon nanotubes, shape memory alloy (SMA), and flexible piezoelectric materials.

Carbon nanotubes (CNTs) are known for their unique electrical and thermal properties. Development of solid-state suspended CNT sheets having extremely low heat capacity per unit area opens an opportunity for utilizing thermoacoustic phenomenon (electrical to thermal to acoustic energy conversion) that results in sound generation over a wide range of frequencies. Detailed theoretical modeling and experiments were conducted for understanding the acoustics generation from multi-wall carbon nanotubes (MWNTs) sheets. The sound pressure level (SPL) of CNT-based thermoacoustic projector (TAPs) is proportional to the frequency and hence the performance reduces in low frequency (LF) region which could be used for noise cancellation, SONAR and oceanography applications. Extensive analytical modeling in conjunction with experiments were conducted involving structure-fluid-acoustic interaction to determine the operational physical behavior of TAPs. Numerical model combines all the controlling steps from power input to acoustic wave generation to the propagation in outer fluid media. Power input to the computational domain is used to determine the frequency dependent thermal diffusive length which governs the generation of TA wave. MWNT yarns/fibers/threads were also designed to harvest ocean wave energy (mechanical to electrical energy conversion). These yarn-based harvesters electrochemically convert tensile or torsional mechanical energy into electrical energy without requiring an external

bias voltage. Harvesters were developed by spinning sheets of forest-drawn MWNTs into high-strength yarns.

SMA wires exhibit two unique properties: thermally induced martensite to austenite phase transformation and super-elasticity (stress-induced martensitic transformation). These properties were implemented for developing the low-grade thermal energy harvesters (thermal to electrical energy conversion). More than half of the energy generated worldwide is lost as unused thermal energy because of the lack of efficient methodology for harnessing the low-grade heat. A systematic study is presented here that takes into account all the key steps in thermal to electrical conversion such as material optimization, thermal analysis and electrical conditioning to deliver the efficient harvester.

Next using thin sheets of piezoelectric materials, strain energy harvesting from automobile tires is studied (strain to electrical conversion. Flexible organic piezoelectric material was utilized for transduction in the harvester for continuous power generation and simultaneous sensing of the variable strain experienced by tire under different driving conditions. Using sensors mounted on a real tire of a mobile test rig, measurements were conducted on different terrains with varying normal loads and speeds to quantify the sensitivity and self-powered sensing operation.

Multifunctional Materials for Energy Harvesting and Sensing

Prashant Kumar

GENERAL AUDIENCE ABSTRACT

This dissertation studies the potential of carbon nanotubes yarns and sheets, piezoelectric sheets and shape memory alloy wires for energy conversion applications. Multiwalled carbon nanotubes (MWNTs) are known for their unique electrical and thermal properties. Large surface area, solid state self-suspended carbon nanotube sheets having extremely low heat capacity per unit area were utilized for design of thermoacoustic projectors operating over a wide range of frequencies. Detailed numerical modeling and experiments were conducted for understanding the acoustics generation from MWNT sheets. Another potential application for MWNT yarns is in ocean wave energy harvesting, where these yarn based harvesters convert tensile mechanical energy into electrical energy. Harvesters were developed by spinning sheets of MWNTs into high-strength yarns.

SMA exhibits unique phase change behavior on mechanical and thermal loading, which were utilized for converting low-grade thermal energy into electrical energy. At low temperature gradients, where there is lack of methodologies for converting thermal energy into electrical energy, SMA wire-based energy harvesters are shown to provide ultra-high power density. Extensive experimentation in conjunction with multi-physics modeling is conducted to provide understanding of energy losses occurring during the thermal to electrical conversion.

Lastly, this dissertation investigates the mechanical to electrical conversion using organic piezoelectric materials. Self-powered strain sensing mechanism for autonomous vehicle will provide new capabilities in monitoring the dynamics and allow developing additional automated controls to assist the driver performance.

Dedicated

To my parents

Acknowledgement

I would like to thank Dr. Shashank Priya (doctoral advisor) for supporting my research and giving me the freedom of exploring novel ideas. My discussions with him led to the development of several new concepts in energy harvesting and sensing. I am thankful to him for always finding time for discussions, advising on research and much more. I couldn't have found a better doctoral advisor! Thank you so much Sir, for all of your support. I would not be where I am today without his efforts in supporting me.

I wish to thank my committee, Dr. Hajj, Dr. Qiao, and Dr. Vick for providing their suggestions and valuable time to improve this research.

I wish to express my gratitude to the CEHMS and BMDL laboratories for their valued support, insight, and collaboration on various research efforts. It has been a great experience working with a group of very dedicated and intelligent colleagues.

I would also like to thank all my friends who have helped me throughout my academic career.

It is beyond my words to thank my dear parents Mr. Dinesh Kumar and Mrs. Manju Devi for the everything they have provided me and for the love and unconditional support bestowed on me. I would like to express my profound gratitude to my wife Anamika Raj for her patience, encouragement and unconditional support. At this point, I can't forget the support provided by my elder brother Mr. Nishant Kumar in pursuing this journey. I would like to thank my in-laws and family members Mr. Anil Sharma, Mrs. Seema Sharma, Mrs. Sangeeta, Mr. Akash Bhushan and Navika for their constant support and love. Last but not the least, I would like to cheers my lovey daughter Praanjali, whose presence and smiles always motivated me to excel in this journey.

Table of Content

List of figures

Chapter 1

Chapter 2

Chapter 3

Chapter 4

Chapter 5

Chapter 6

Chapter 1

Background and Objective

Background

Multifunctional materials (MFMs) combine two or more functional properties such as electrical, thermal, magnetic etc. MFMs can be found in nature or artificially tailored to meet the needs of a particular requirement. Depending upon the system requirements, a structurally robust MFM can be developed by utilizing the advances made in the bottom up approaches (e.g. nanotubes to macroscale sheets). Altering the nanoscale properties of a structurally robust material could provide additional capabilities in sound generation, sensing, thermal energy conversion, mechanical energy conversion and energy storage. The application of such MFMs can be in many industries such as oil and gas, chemical, energy, medicine, electronics etc. [1, 2]

Nature demonstrates variety of examples for the multifunctional behavior, for example, bone, human skin etc. Bones are composites made of different chemicals such as collagen and calcium phosphate, that contribute towards various body functions such as muscle activity, body structure and support. Similar to bone, our skin also contains many components such as receptors, hair follicles, and blood vessels which provides capability for many functions [3]. These natural MFMs have evolved through gradual and slow biological processes. However, man-made MFMs could be engineered faster to exhibit desired combination of properties that meet the specific platform requirements.

In smart world, in order to obtain enhanced system level efficiency while adding new features, MFMs are becoming the choice for product design. The capability of a material to respond according to the changes occurring in the nearby surrounding in a relevant manner will have direct impact on the system performance. Many systems based on these MFMs are being developed to provide dynamic capability in response to changes in external stimuli. This provides advantages in reducing size, weight and complexity while

improving the efficiency and safety [3]. The other advantages of MFMs are that they can be programmed to exhibit specific properties in response to changes occurring in the environment, thereby, providing certain level of predictability in the dynamic conditions. Inspired by the advances made in understanding and implementing MFMs, this dissertation investigates three class of materials that provide unique properties for developing new applications.

Ferreira et al. [1] have discussed the overall cost analysis of the multifunctional material systems (MFMS) comprising of all the categories such as MFM, multifunctional composites (MFC) and multifunctional structures (MFS). The cost analysis is divided into five categories: raw materials, fabrication, assembly, maintenance and non-recurring. In terms of raw material, assembly and maintenance, MFMS have advantage with respect to their counterpart, since the material components can be combined in a calculated manner to achieve particular set of properties that results in reduction of the overall number of parts and thereby improve assembly and maintenance. It is obvious that lesser number of parts in the system will simplify assembly and reduce maintenance [1]. The major challenge in deploying MFMS is cost due to the complex manufacturing process and combination of multiple intellectual resources. Till date manufacturing and material fabrication techniques used to design MFMS are expensive and have limited scope in achieving the scalability. Recent advancements in 3D printing techniques could provide pathway towards manufacturing these complex systems. MFMS involves the core competencies from diverse scientific field and therefore requires collaborations and expertise from various industry [1]. 3D printing enables that collaboration naturally by providing avenue to combine the materials into programmable morphologies.

We can categorize the MFMs into various groups depending upon their response to external input (or stimuli) and functions. For example, piezoelectric material converts electrical signal into mechanical output or vice-versa. Shape memory alloy/polymer have unique properties of stress generation in response to thermal inputs. Materials such as thermoelectric (thermal to electricity conversion and vice a versa), dielectric elastomer (electricity to strain), magnetostrictive (magnetic field to mechanical deformation), smart

gels (thermal, pH responsive) and photochemical (light responsive) etc. are other classes of MFMs or MFMS. Emerging materials such as carbon nanotubes, graphene and other carbonaceous nanomaterials are also considered as MFMs because of their high mechanical strength and electrical/ thermal conductivity. These materials are already exhibiting promising results in energy harvesting and sensing applications.

Another interesting development in the community has been on integration of MFMs into a composite MFM that provides additional capabilities. These materials are being developed for actuation, sensing, energy harvesting and storage. For example, researchers have combined the power producing features of the fiber composites [3, 4]. Each fiber was converted into individual battery by coating the cathode and anode layers along with electrolyte. This concept of making the fiber a multifunctional material and utilizing its surface area as compared to that of foil of a thin film battery helped in generating greater energy output. Piezoelectric material, mentioned earlier, is utilized for all the purposes such as actuation [5], sensing [6] and energy harvesting [7]. The inverse piezoelectric effect (converting electricity into mechanical response) is the primary basis of using it as actuation device. Conventional PZT ceramics (used as actuator) are often bulky and heavy and cause the high stress generation on integrating with the MFMS. Therefore, efforts have been made towards fabricating the nanofiber, and nanorod/wire based piezoelectric materials [8]. By using the direct piezoelectric effect, piezoelectric materials are heavily used for sensing purposes such as structural health monitoring, tire-road interaction sensing, fluid flow sensing etc. In addition, their use in scavenging stray energy from nearby surrounding (or changing one form of energy into other) is gaining momentum. The development of the Internet of Things has accelerated the design and development of low-power sensor systems. Self-powered sensors that can collect and transmit data without any need for external power supply are highly desirable. Piezoelectric MFMs are widely used to harvest mechanical energy. Several piezoelectric materials, such as PVDF, ZnO, and other lead-free piezoelectric materials have been used to develop the nanogenerators for energy harvesting. Apart from piezoelectric materials, various bioinspired MFMs or MFCs are being developed for the above mentioned sensing, actuation and energy harvesting applications.

Shape memory alloy (SMA) and polymers are the another type of functional materials that have wide range of application for actuation [9], sensing [10] and energy harvesting [11]. SMA generates stress due to phase transition on applying the thermal gradient. Design of SMA-based MFMs has evolved significantly over the past few decades. Several industries such as medical, aerospace, and robotics etc. utilize SMA-based MFMs for various electrical, thermal or stress activated actuation. Carbon nanomaterials are another important category of MFMs that are gaining importance across the globe. This is because of their extraordinary mechanical, thermal and electrical properties. Carbon nanotubes (CNTs), graphene, carbon nanofibers are different forms of carbon-materials with significantly different properties. CNT-based twisted yarns are utilized for converting mechanical energy into electrical energy [12] through electrochemical process. Similarly, graphene sheets are also used for many purposes such as sensing and energy harvesting [13]. In addition, these nanomaterials are utilized dopants to the exiting material in order to add new capability. For example, in aircrafts we need a higher electrical conductivity polymer arts to transfer the electricity from thunder. Researchers have studied the polymer matrix nanocomposite filled with carbon based materials for a possible replacement of existing polymer matrix [1, 14].

Various other MFMS are also very important in terms of delivering the different functions for addressing the important needs. For example, thermoelectric, magnetosctrictive, dielectric elastomers materials are also used for different purposes such as thermal energy harvesting [15], magnetic energy harvesting [16] and mechanical actuations respectively [17]. This brief outline to the MFMs/MFMS only scratch the surface of the various ideas, concepts, demonstrations and scientific understanding developed so far. This is indeed a very growing field and has impact in almost all the field of research where materials play the primary role in systems functionality.

In the light of importance of MFMs, this dissertation demonstrates the utilization of few key multifunctional materials such as nanotube materials, shape memory alloy and piezoelectric material to understand the physics of various type of energy conversion and achieve some of the important applications such as energy harvesting, sensing and

actuation in various domains. Figure 1, shows the schematic diagram which describes the broader fields such as sensing, actuation and energy harvesting. As we have seen from above discussion that to give the solutions for mentioned fields, we require a lot of efforts (or may be not possible in many cases) if unifunctional materials are utilized. Therefore, in this work, the study based on different MFMs were developed and addressed the sensing, energy harvesting, and actuation problems. Along developing the study, various analysis and discussions are included to demonstrate importance of this work and its standing with respect to current state of the art technologies.

Carbon nanotubes based sheets and yarns were used for actuation (acoustic generation by actuating plates) and energy harvesting, respectively. CNT thin self-suspended dry sheets (a type of MFM) were utilized to convert electrical energy to thermal to acoustic pressure wave (thermoacoustic). These pressure waves then used to actuate the isotropic plates surrounding it, and produce the vibration. The vibrating plate then produced the vibro-acoustic sound. Further, CNT sheets are twisted to produce yarns and used to convert the ocean wave mechanical energy directly into electrical energy.

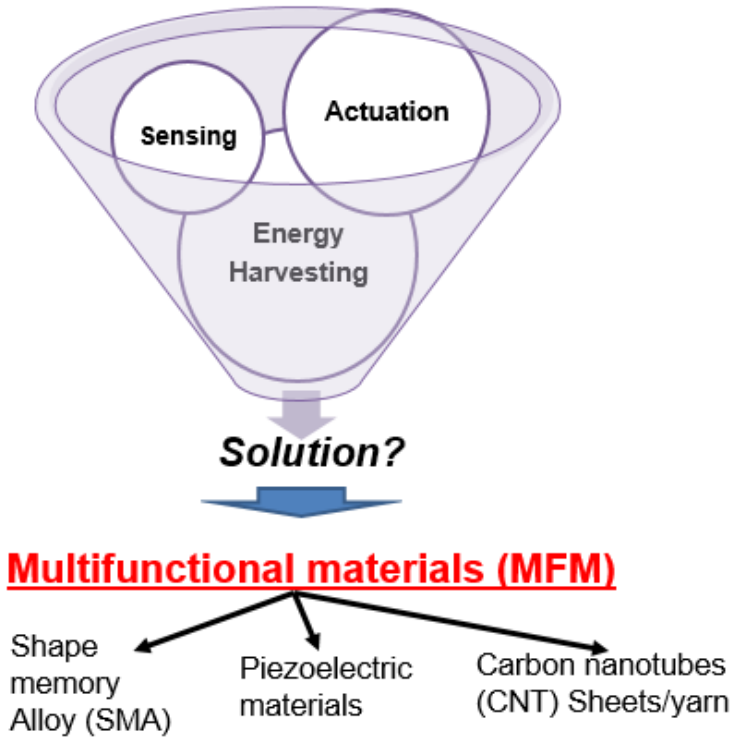

Figure 1: Schematic showing the potential of MFMs for achieving the goals of sensing, actuation and energy harvesting. Three main multifunctional materials: SMA, piezoelectric materials and CNTs are chosen to achieve the above mentioned goals.

SMA materials, as described above, are very effective in converting mechanical response on thermal loading. SMA based wires are utilized to develop systematic study for efficient thermal to electrical energy conversion. An ultrahigh electrical power density has been demonstrated which is enough to power various sensors. Moving forward, another MFM, PVDF material has been utilized to develop the self-powered sensing solution for the tires. This is an attempt to make the tire intelligent and prepare it for the next generation autonomous vehicle. This is the study which demonstrate the real field application of used MFMs.

This work, hence, uniquely position the different MFMs to solve the existing challenges of acoustic generation (by actuation), ocean energy harvesting (mechanical to electrical energy conversion), thermal energy harvesting (thermal to electrical energy conversion), and sensing of vehicle parameters.

Dissertation Objectives

The primary objective of this dissertation is to understand the basic physics of energy conversion mechanisms for a selected group of MFMs with fiber or sheet like morphology (carbon nanotube yarns and sheets, shape memory alloy wires, and piezoelectric polymer thick films). Based upon this understanding, the secondary objective is to demonstrate the application of these selected MFMs in sound generation, energy harvesting and sensing.

MFMs based devices and systems have emerged as a prominent research field and growing at rapid pace. A diverse range of applications (as described in background section) utilize these materials as energy harvester and sensors for structural health monitoring in automotive industries, medical field etc. This rapid progress in the establishment and deployment of MFMs requires investigations across a wide spectrum

of topical areas. There is need to develop fundamental understanding and new ideas which could help in translation of these materials. In addition to material uniqueness, MFM based systems also require various strategies such as system modeling, design and fabrication for the final product to be used for different energy conversion. This dissertation addresses these needs and provides physics of energy conversions utilizing the selected MFMs with special form factor. Key aspects of this dissertation are:

- Investigate the fundamentals and challenges from materials to experimental prototype for energy conversion.
- Demonstrate functional devices and determine their performance parameters under realistic boundary conditions
- Conduct thorough material investigations, mathematical or numerical modeling, and design new experimental techniques to quantify the behavior of MFMs for energy harvesting and sensing purposes.

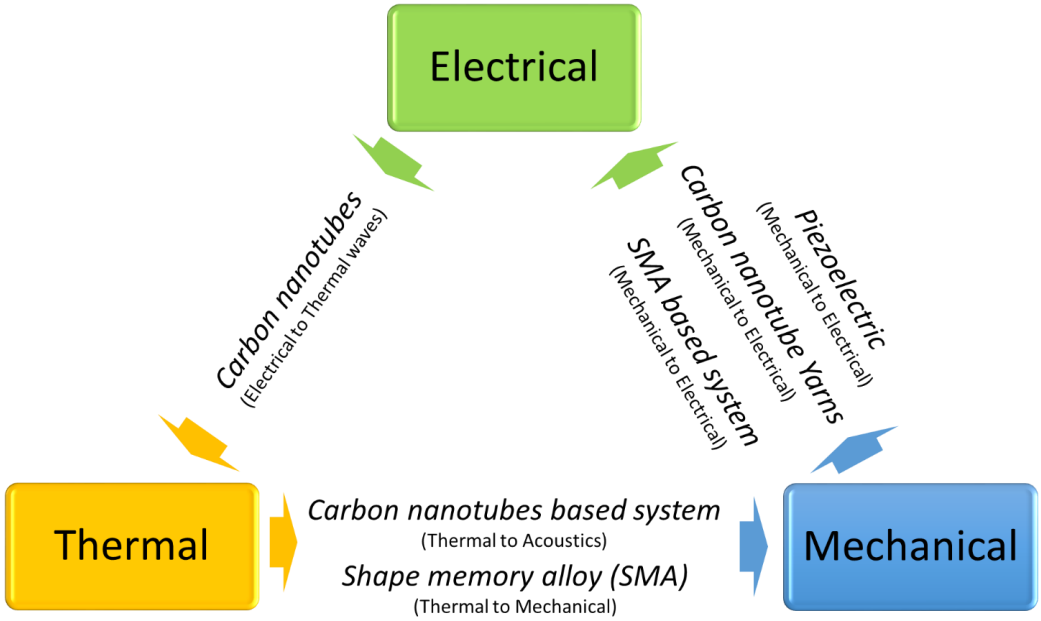

Figure 2: Energy conversion methods by using different MFMs

This dissertation addresses variety of energy transformation techniques using CNT, SMA and piezoelectric materials. Figure 2 shows the schematics of energy conversion. Carbon nanotubes based solid thin sheets were used to convert electrical energy to thermal wave and then acoustics (mechanical energy). CNT based yarns and piezoelectric materials were investigated to convert mechanical energy (from ocean wave or vehicle road interactions) to electrical energy. Memory materials were discussed to develop the low grade thermal waste recovery device to produce electrical energy.

In the following sections, scope and impact of different chapters based on MFMs will be discussed briefly.

Chapter 2 and Chapter 3

Carbon nanotube (CNT) sheets provide the opportunity to develop ultralight, miniature, and flexible sound sources operating over wide frequency domain using thermoacoutic (TA) phenomenon. Based on sheets the TA transducers were developed. Figure 3 shows the important parameters and operational steps which could be optimized for better efficiency.

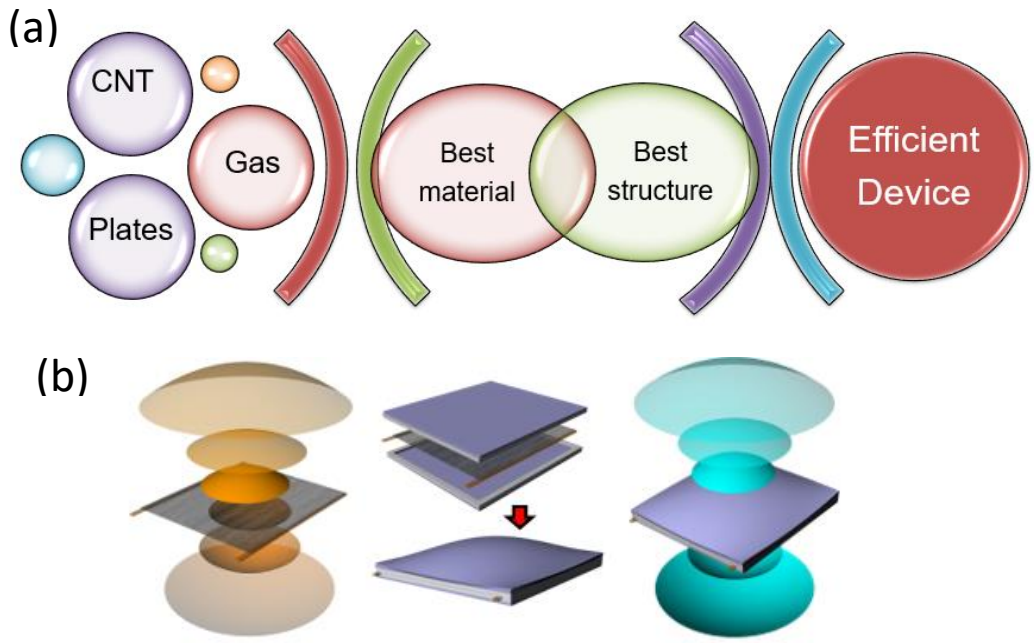

Figure 3: (a) Different parameters important for designing the better thermoacoustic projectors, (b) various steps of thermoacoustic projector (open sheet TA generation, vibration and vibro-acoustic).

A unique feature of TA transducers is the synchronization of various physical effects (vibration dynamics, thermal transport, and molecular dynamics) for achieving high acoustic pressure. The sinusoidal heating of the adjacent gas by the CNT sheet generates the thermoacoustic pressure wave which drives the end plates resulting in sound pressure wave generation in the surrounding fluid domain. Since the input electrical power is converted into acoustic pressure through multiple intermediate steps, a multilayer model was developed in order to include all physical effects, namely: (i) an electrical AC input drives the CNT sheet resulting in a pressure pulse within the closed system, (ii) this internal pressure acts as the driving force for the vibrating plate of the encapsulated TA

projector, and (iii) the vibrating plate generates an acoustic pressure wave in the outer fluid medium. This comprehensive thermo-vibro-acoustic model provides the fundamental foundation needed for a parametric study of the TA performance. After modeling, devices are fabricated and tested systematically tested for vibration and acoustics in air and water medium.

Chapter 4

In renewable resources domain, water wave or ocean (blue energy) is a big source of kinetic energy which is getting attention since few decades. Our globe has two third of its surface covered with ocean and other water bodies. These oceans have a large potential of energy in the form of tidal energy, ocean waves, ocean currents and ocean thermal and salinity gradients [18, 19]. A research predicts the theoretical energy of around 7.4×10^{21} J available per year from the ocean in different forms, which should be enough to fulfill present and future needs of the energy [18]. Water wave available in Deep Ocean is very attractive aspect for energy scavenging, since it is available all day and night, predictable and mostly independent of weather condition unlike solar or wind. Thus, ocean wave harvesting indeed is a good opportunity to meet the global need of energy.

To provide the solution for ocean energy harvesting another MFM- CNT yarn was utilized. This chapter provides the first systematic study of wave energy harvesting based on multiwall nanotubes (MWNT) twisted and coiled yarns. This technology of converting mechanical energy directly to electrical energy is discovered recently by our group [12]. Since it generates energy from twists, thus was called “Twistron”. This is the electrochemical method which because of change in its capacitance can convert mechanical to electrical energy. In this study different yarns were fabricated and a wave generator was designed to run the experiments similar to the ocean wave environment. In all the experiments real ocean water (or 0.6 M NaCl for tank tests) was used to demonstrate the feasibility of the device in real ocean condition. A theoretical framework was developed and empirical relationship was deduced to predict the voltage and compared with the experimental outcomes.

Chapter 5

Lawrence Livermore National Laboratory's recent study (2015) shows that, about 59.1 quadrillion BTU of energy is rejected to the surroundings in the form of waste heat energy [20]. Most of the rejected thermal energy is classified as low-grade waste heat (hot-side temperature less than 230°C). SMA based thermal engine provides transformative pathway to harness the abundant low grade heat currently discarded in ambient as waste, thereby not only providing cost-effective electricity generation but also reducing environmental impact. Practically, SMA engine can be deployed at any location where only moderately high temperature (>60°C) fluid is available (e.g., exhaust and water pipes).

SMAs, explained as unique MFMs, exhibit thermally induced martensite to austenite phase transformation and super-elasticity (stress-induced martensitic transformation). Employing these two characteristics, a thermal engine demonstrated for harnessing waste energy through all modes of heat transfer: convection, conduction, and radiation. Figure 4(a) shows the different phase changes of SMA material on applying mechanical loading and then thermal loading. Initial SMA phase, martensite, goes into de-twinned martensite and on giving the heat energy above the forward transition temperature, it converts into austenite. The initial phase regained my cooling this MFM below the reverse transition temperature. Figure 4(b), (c) and (d) show the two pulley design and steps of converting thermal energy into electricity. Due to phase transition of SMA wire on thermal input, strain develops inside the wire (contracts), and produces the torques in pulley (due to contact friction between wire and pulley). This torque then turns the pulley and attached generator and produces the electricity. A detailed analysis on SMA wires were conducted before utilizing in the two pulley system.

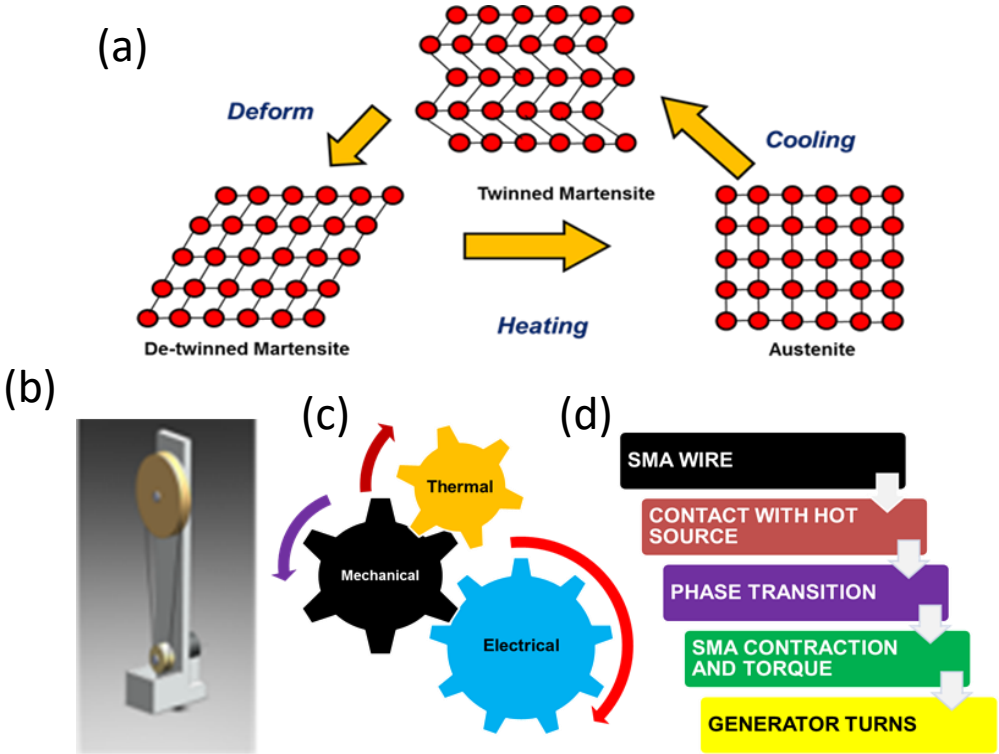

Figure 4: (a) Different phase changes of SMA material on applying mechanical loading and then thermal loading, (b) the two pulley design with SMA wire, (c) &(d) steps of converting thermal energy into electricity

Chapter 6

For the safe and reliable driving these days, vehicles require a large number of sensors and high rate of wireless data transfer to update the information about the surrounding to the driver. These sensors and data transfer requirements are increasing the power requirements rapidly. There is a tremendous amount of study taking place in both academia and industry to provide devices, systems, and techniques that lead to energy efficient self-governing automobile environment. For any vehicle, tire is the most important part and it connects the inner vehicle environment to the outside environment (such as road etc.). In order to develop the autonomous vehicle, it is very important to tap the tire's potential and attempts should be made to make an intelligent tire.

In present work, attempts have been made to provide a cost-effective solution to above mentioned issues and demonstrate a self-powered sensor based upon an organic piezoelectric material (an MFM). A low value of elastic modulus ensures the high strain development in this piezoelectric patch, which is one of the important parameters for strain sensors. The high-power density and high temperature (up to 90°C) stability of organic piezoelectric based harvester is realized for this purpose. Further, energy produced under normal tire condition are used to demonstrate to power various LEDs and wireless systems. This provides an estimate for the power needed to develop efficient wireless data transfer and power management. In order to understand the dynamics of the tire during rotation under load, a mathematical model was developed and used to evaluate various key parameters such as radial and tangential displacement of the tire, and voltage from a flexible piezoelectric sensor. After mathematical analysis, piezo patch was integrated in a tire mounted in a mobile test rig. The tests were performed on different types of roads (under variable wheel loading) to demonstrate the sensing capabilities. These experimental results were also validated qualitatively (voltage trend with velocities) through analytical modeling [7].

References

[1] Ferreira ADB, Novoa PR, Marques AT. Multifunctional material systems: a state-of-the-art review. Composite Structures. 2016;151:3-35.

[2] Gibson RF. A review of recent research on mechanics of multifunctional composite materials and structures. Composite structures. 2010;92:2793-810.

[3] Bar-Cohen Y. Biomimetics: biologically inspired technologies: CRC Press; 2005.

[4] Christodoulou L, Venables JD. Multifunctional material systems: The first generation. JOM. 2003;55:39-45.

[5] Chaudhry ZA, Joseph T, Sun FP, Rogers CA. Local-area health monitoring of aircraft via piezoelectric actuator/sensor patches. Smart Structures and Materials 1995: Smart Structures and Integrated Systems: International Society for Optics and Photonics; 1995. p. 268-77.

[6] Cui H, Hensleigh R, Yao D, Maurya D, Kumar P, Kang MG, et al. Three-dimensional printing of piezoelectric materials with designed anisotropy and directional response. Nature materials. 2019:1.

[7] Maurya D, Kumar P, Khaleghian S, Sriramdas R, Kang MG, Kishore RA, et al. Energy harvesting and strain sensing in smart tire for next generation autonomous vehicles. Applied Energy. 2018;232:312-22.

[8] Wang ZL, Song J. Piezoelectric nanogenerators based on zinc oxide nanowire arrays. Science. 2006;312:242-6.

[9] Garner L, Wilson L, Lagoudas D, Rediniotis O. Development of a shape memory alloy actuated biomimetic vehicle. Smart Materials and Structures. 2000;9:673.

[10] Shahinpoor M. Shape memory alloy temperature sensor. Google Patents; 2005.

[11] Avirovik D, Kishore RA, Vuckovic D, Priya S. Miniature Shape Memory Alloy Heat Engine for Powering Wireless Sensor Nodes. Energy Harvesting and Systems. 2014;1:13-8.

[12] Kim SH, Haines CS, Li N, Kim KJ, Mun TJ, Choi C, et al. Harvesting electrical energy from carbon nanotube yarn twist. Science. 2017;357:773-8.

[13] Bo Z, Shuai X, Mao S, Yang H, Qian J, Chen J, et al. Green preparation of reduced graphene oxide for sensing and energy storage applications. Scientific reports. 2014;4:4684.

[14] Gibson T, Putthanarat S, Fielding JC, Drain A, Will K, Stoffel M. Conductive nanocomposites: focus on lightning strike protection. SAMPE Fall Technical Conference and Exhibition2007. p. 789-95.

[15] Lee H, Sharp J, Stokes D, Pearson M, Priya S. Modeling and analysis of the effect of thermal losses on thermoelectric generator performance using effective properties. Applied Energy. 2018;211:987-96.

[16] Kang MG, Sriramdas R, Lee H, Chun J, Maurya D, Hwang GT, et al. High Power Magnetic Field Energy Harvesting through Amplified Magneto-Mechanical Vibration. Advanced Energy Materials. 2018:1703313.

[17] O'Halloran A, O'malley F, McHugh P. A review on dielectric elastomer actuators, technology, applications, and challenges. Journal of Applied Physics. 2008;104:9.

[18] Ellabban O, Abu-Rub H, Blaabjerg F. Renewable energy resources: Current status, future prospects and their enabling technology. Renewable and Sustainable Energy Reviews. 2014;39:748-64.

[19] Wang ZL, Jiang T, Xu L. Toward the blue energy dream by triboelectric nanogenerator networks. Nano Energy. 2017;39:9-23.

[20] https://www.llnl.gov/news/americans-used-less-energy-2015

Chapter 2

Understanding the Low Frequency Carbon Nanotube Thermo-Acoustic Sonar Projector by Numerical Modeling

Abstract

Carbon nanotube (CNT) sheets exhibiting extremely low heat capacity have provided the opportunity for development of thermoacoustic projectors (TAPs) for a wide range of frequencies (1- 10^5 Hz). The sound pressure level (SPL) of CNT-based TAPs is proportional to the frequency and hence the performance reduces in the low-frequency region. Comprehensive validated model is presented involving structure-fluid-acoustic interaction that shed light on the physical behavior of CNT-based TAPs. The numerical model incorporates all the controlling steps from input electrical power to vibro-acoustic wave generation in outer fluid media. Further, using model, the impact of different parameters on TAP performance has been studied.

Keywords: Thermoacoustic; SONAR; Thermal diffusive length; Carbon nanotubes.

Introduction

Carbon nanotube (CNT) sheets provide the opportunity to develop an ultralight, miniature, and flexible sound sources operating over wide frequency domain using thermoacoustic (TA) phenomenon. There are inherent advantages in using TA phenomenon as compared to electrical loudspeakers and piezo transducers [2, 3]. In CNT-based TA projectors, applied AC current creates a thermal wave in the surrounding-fluid due to the low or negligible thermal mass of the CNTs. This thermal wave causes the expansion and contraction of the surrounding gas and results in the generation of an acoustic wave. Arnold et al.[4] provided an early model describing the TA phenomenon and underlying physics by using a very thin strip of platinum. Recent discovery and development of CNT sheets exhibiting extremely low capacity [5] provide practical thermoacoustic material. Xiao et al. [6] demonstrated a CNT speaker in an air environment and quantified the sound spectra emitted by multi-walled carbon nanotube (MWNT) sheets at different frequencies. Aliev et al. [7] extended the analysis to the water medium and revealed underlying physics governing the frequency dependent behavior. Aside from CNT sheets, other nanostructures such as graphene, indium tin oxide (ITO), aluminum film and suspended metal wire have also been demonstrated as acoustic sources [8-16]. Aliev et al. have presented several alternative materials (MWNT sponge, graphene sponge, gold/ poly(acrylonitrile) (PAN) sheet and ITO/PAN sheet) that can be synthesized using environmentally-friendly process and exhibit reasonable energy conversion efficiency [16]. Building on these prior research, here we present comprehensive numerical modeling along with experimental validations of MWNT sheets based low frequency (LF) TA projectors. This analysis provides the deterministic role of material and structural parameters on efficiency and acoustic power generation and guides towards the development of efficient transducer.

The transducer structure used in our model and experiment is based on a prior study [7]. In this design, a MWNT sheet is suspended between two flexural plates and sealed from the edges by a silicone rubber gasket, as shown in Figure 1(a). The compartment formed between the two plates is filled with a gas such as Xe, Ar, air etc. This transducer design resolved two major problems: (i) enhanced the output of the CNT-based device at

lower frequencies by using a resonant condition, and (ii) provided protection for the CNT sheet under the high power operation in underwater conditions (avoid collapsing of the CNT sheet) [1, 17]. Our detailed validated model results presented here extend to encapsulated devices incorporating more realistic conditions, such as fluid loading (or added mass), elastic edges boundary conditions, revealing the effects on the acoustic and vibration performance of the device which has not been covered in prior efforts [18-21].

A unique feature of TA transducers is the synchronization of various physical effects (vibration dynamics, thermal transport, and molecular dynamics) for achieving high acoustic pressure. The sinusoidal heating of the adjacent gas by the CNT sheet generates the thermoacoustic pressure wave which drives the end plates resulting in sound pressure wave generation in the surrounding fluid domain. Since the input electrical power is converted into acoustic pressure through multiple intermediate steps, we developed a multilayer model in order to include all physical effects, namely: (i) an electrical AC input drives the CNT sheet resulting in a pressure pulse within the closed system, (ii) this internal pressure acts as the driving force for the vibrating plate of the encapsulated TA projector, and (iii) the vibrating plate generates an acoustic pressure wave in the outer fluid medium. This comprehensive thermo-vibro-acoustic model provides the fundamental foundation needed for a parametric study of the TA performance. Through this model, we computed the realistic behavior of a device in both air and water loading.

General description, problem statement and numerical approach

Figure 1(a) shows the schematic of the working principal of encapsulated TA projector based on MWNT. An electrical signal is given to the MWNT through electrodes, which produce TA modulated pressure in the chamber between the isotopic plates (marked with red arrows in Figure 1(a)). This conversion is facilitated due to the extremely low or negligible thermal mass of the CNT. Further, TA pressure (at variable frequency) is used as a forcing function for plate vibration, and this vibration then produces the sound pressure wave, having maximum pressure at the resonance of the system. As we could see from the process of electrical to vibro-acoustic conversion, each physical step is

extremely sensitive and a small variation in any of the steps could result in a significant change in the final output. This generates a need for investigation of each physics and its impact on the final outcome. To solve the above-mentioned multiphysics problem we proposed a numerical modeling concept which divides the problem into three layers:

Layout of complete modeling of TA device through different layers of physics

Figure 1(b) provides a schematic of the multilayer model that incorporates the physics of the device as follows:

- 1st Layer
  - This is the first physics of TA projector, which involves TA generation from electricity. We investigated this phenomenon separately as an open system (no plates are introduced), as shown in schematics of layer 1 in Figure 1(b). The goal is to make sure that TA generation through this physics is accurate since this is one of the most important inputs for further physical phenomenon.
  - The primary purpose is to quantify energy dissipation from the MWNT sheet and evaluate its impact on the generation of the pressure wave.
  - Develop an understanding of TA wave generation in different gaseous media and verify and validate with theoretical and experimental results.
  - Analyze the spatial distribution of pressure and input for the 2nd and 3rd layers
- 2nd Layer:
  - Verified and validated TA pressure in the above step is now used as force function for the plate vibration in the encapsulated device (closed system), as shown in schematics of layer 2 in Figure 1(b).
  - Develop an understanding of vibrational characteristics of a device in the air for more realistic boundary condition i.e. elastic foundation at the edges.

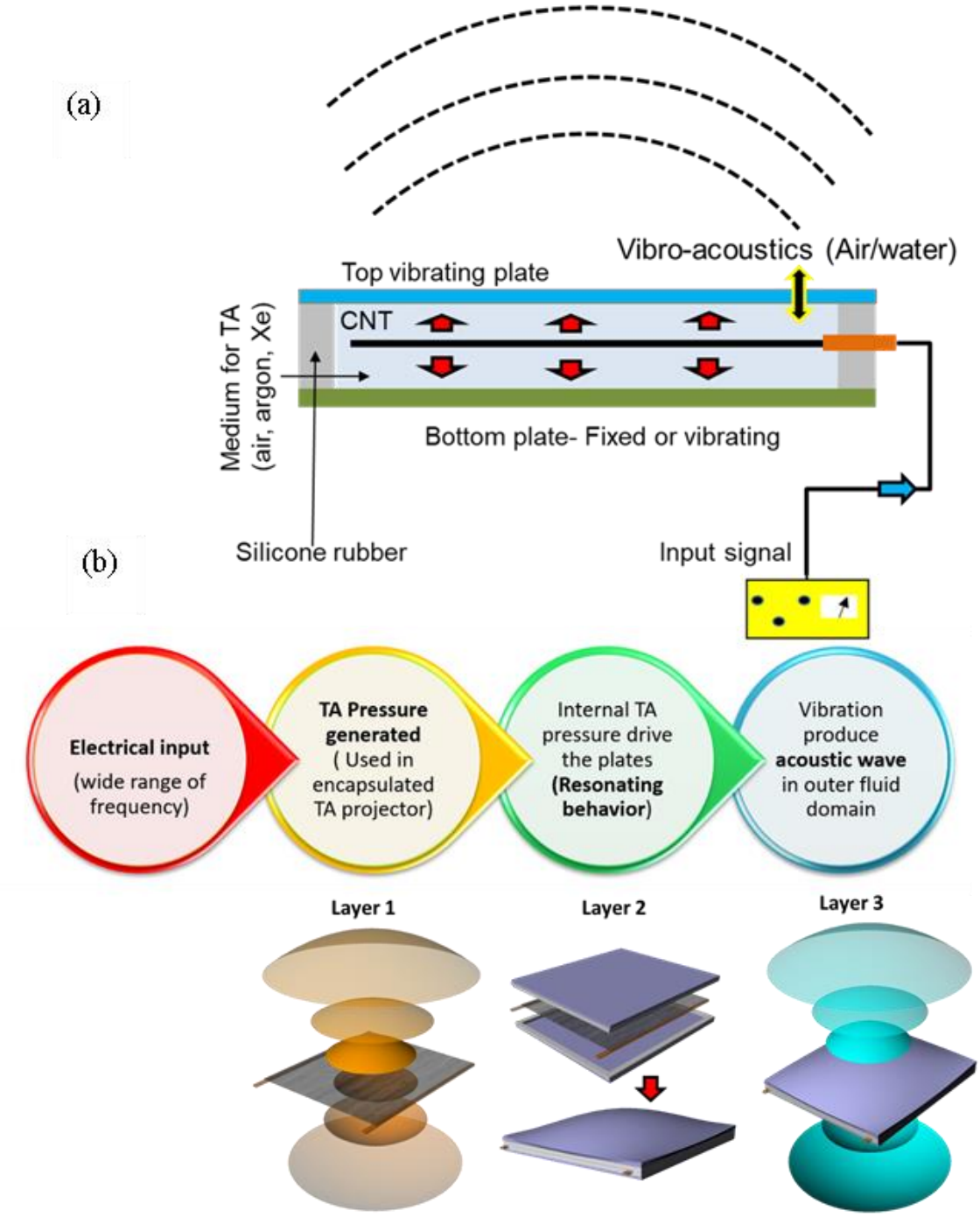

Figure 1: (a) Schematic of the complete encapsulated device showing the electrical input to the vibro-acoustic (b) Multilayer modeling layout for TAP and corresponding schematics for each layer.

- 3rd Layer:
    - Based on the inputs of the above layers, we investigated the vibro-acoustic generation in the surrounding environment (air and water) of the encapsulated device (schematic of layer 2, Figure 1(b). This layer shows the integrated device model which includes the physics from the above model

Theoretical description for computational analysis

Layer 1: Thermoacoustic modeling (open system)

The goal of this layer is to investigate the TA wave generation and heat transfer analysis from CNT sheets in an open system. This step is foundational for the next layers of modeling for an encapsulated device. According to literature [22, 23] and considering the fact that MWNTs retain negligible heat, all the input sinusoidal current I for a given CNT resistance R at a frequency $\omega/2$ (heating twice each periodic cycle) (Eq.1) is

$$\left(I \sin\frac{1}{2}\omega t\right)^2 R = P_H - P_H e^{i\omega t} \tag{1}$$

converted into thermal power output (P_H) by Joule heating of the nearby surrounding.

This periodic electric power will result in heating of the surrounding gas on a temporal basis and thereby generate a pressure variation in the form of TA waves. Considering the near field TA pressure as a planar wave, the general form of time-dependent equations [22, 23] showing thermo-acoustic coupling are given by Eq. 2 and 3 as:

$$\frac{\partial^2 P}{\partial t^2} - \frac{P_a}{\rho_a}\frac{\partial^2 P}{\partial x^2} = \frac{P_a}{T_a}\frac{\partial^2 T}{\partial t^2} \tag{2}$$

$$\frac{\partial T}{\partial t} - \alpha\frac{\partial^2 T}{\partial x^2} = \frac{\gamma - 1}{\gamma}\frac{T_a}{P_a}\frac{\partial P}{\partial t} \tag{3}$$

where ρ_a = gas density, α =thermal diffusivity, $\gamma = C_p / C_v$ (heat capacity ratio of gas), T_a and P_a are ambient temperature and pressure. The overall heat balance including the heat production and heat loss through the thin film of CNT can be written as:

$$P_H - P_H e^{i\omega t} = \rho_a V C_h \frac{dT}{dt} - 2Sk\frac{dT}{dx} \tag{4}$$

where ρ_a = gas density, V =volume of CNT film, C_h = heat capacity (in this case=0), S = flat area of CNT film, and k = thermal conductivity of the surrounding fluid. In a prior study [24] it was shown that the contribution of convective heat transfer and radiative heat transfer is comparatively less than the heat conduction from thin film to the surrounding fluid. Therefore, only conductive heat loss is considered in our analysis.

Layer 2: Structural vibration

This layer includes the basic equation of structure which was solved in a computational framework. The equation of the structure separating the inner domain and outer domain is written as [25, 26]:

$$-\rho\omega^2 u_l - \nabla.\sigma_{lm,n} = F_v \tag{5}$$

Where ρ is density, ω is vibrating frequency, u_l is structural displacement, $\sigma_{lm,n}$ is stress tensor within the structure and F_v is body force. The above equation derived from Newton's 2nd law of motion. Strain (ε) and stress at respective boundaries can be represented as below

$$\varepsilon_{no}(u) = \frac{1}{2}(u_{n,o} + u_{o.n}) \tag{6}$$

$$\sigma_{lm}(u)n_m = F_s - p_e|_{s_1} n_l \tag{7}$$

$$\sigma_{lm}(u)n_m = F_s + Pn_l^{'} \tag{8}$$

Where P is internal pressure (TA), F surface force, n is a normal vector and p_e is pressure in the external domain (outside the structure).

Layer 3: Acoustics in outer medium

Sound pressure in the external medium can be solved through Neumann problem using Helmholtz equation below:

$$\nabla^2 p_e + k^2 p_e = S \quad and \quad k^2 = \frac{\omega^2}{c^2} \tag{9}$$

$$\frac{\partial p_e}{\partial n} = \omega^2 p_e u.n \tag{10}$$

Where c is the sound velocity and S is the external sound source.

Experimental

Samples fabrication for validating the open system modeling (layer 1)

MWNT forest was synthesized by chemical vapor deposition (CVD). Highly oriented, non-densified MWNT sheets having thicknesses of about 18-20 μm were pulled from these forests using dry-state technology [27]. The optical transparency of one sheet is around 85-89%. For the open system experiments, we fabricated two single sheet samples: a small sample with dimensions of 1.65×2 cm^2 and resistance around 511 Ω; and a larger sample with dimensions 18×3.2 cm^2 and resistance of 3600 Ω, where the first dimension is the CNT orientation direction and the indicated resistance is for this direction for all described results, unless otherwise indicated. Copper electrodes were used for suspending the sheets and providing electrical voltage input.

Experimental setups for model validation

For the open sheet acoustic measurement, we used a microphone (B&K 4138) having a sensitivity of 52.4 mV/Pa.

Numerical results and discussion

A comprehensive finite element method (FEM) model (using the above governing equations) and results for our TAP which describes the phenomenon proposed in all the modeling layers is presented. Starting with thermal power input (equation 1), a detailed study was conducted using COMSOL v5.3 for the thermoacoustic to vibro-acoustic generation.

Layer 1: Thermoacoustic in open system

In this section, results of thermoacoustic generation by CNT sheet is discussed. Since the heat capacitance of the porous CNT sheet is negligible, it is modeled as a very thin layer of surrounding fluid (such as Air, Ar, and Xe), approximately 18 μm thick, with the different area that serves as the volumetric heat source for thermal wave generation. Mesh sensitivity is shown in Figure 2(a). The cross-section of the fluid domain length for

this first layer of modeling is shown in Figure 2(b). A spherical fluid domain surrounding the MWNT sheets is truncated with a 0.1m perfectly matched layer (PML) for acoustic propagation. Figure 2(c) shows a qualitative depiction of the thermal wavelength during TA generation. It is evident from the images that an increase in frequency results in a decrease in the thermal diffusion length ($l = \sqrt{\alpha / \pi f}$, α - thermal diffusivity, and f - frequency). The thermal diffusion length represents the heat distribution from the heat source at a particular frequency in nearby space and determines the propagation characteristic of the TA wave. Material properties are shown in Table 1.

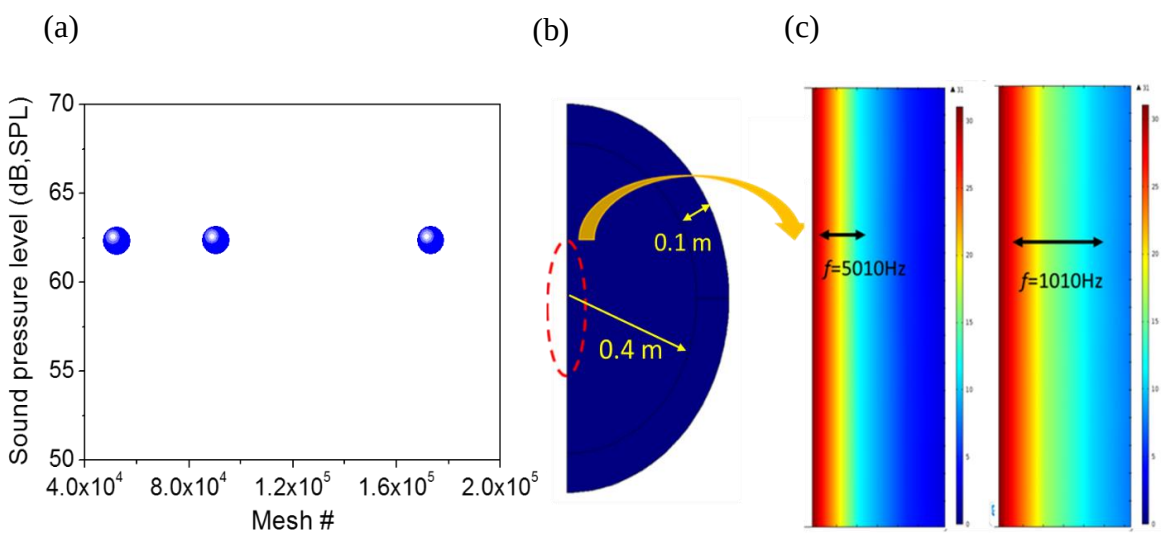

Figure 2: (a) Mesh sensitivity test results, (b) Modeling domain for thermoacoustic (TA) evaluation, (c) thermal diffusive length generation at different frequencies

Material properties [1]: Table 1

	Air	**Argon**	**Xenon**
Molar mass – M (g/mol)	28.9	39.95	131.3
Heat capacity- Cp (J/kg/K)	1006.3	521.5	158.3
Density - ρ (kg/m^3)	1.184	1.634	5.369
Sound speed- v (m/s)	343	320	169

Using the numerical model, a series of parametric studies (different surrounding gases, CNT sheet length, and width) were conducted to evaluate the qualitative and quantitative characteristics of the TA wave. We started the numerical analysis with a smaller sample of 1.65 x 2 cm^2 and conducted frequency sweeps (100-10,000 Hz) at a fixed input power of 1 W in air domain to obtain the frequency response as shown in Figure 3(a). With the increase of frequency, we obtained a linear trend of sound pressure level (SPL). For verification of the numerical model, results are compared with the analytical model [1] and found to be in a close match. Further, the results from our model are compared with the experimental results for similar sample and condition and a close agreement is obtained. The maximum error was less than 5%. The deviation of experimental results at a few frequencies can be explained by the fact that in a real situation there is non-uniform heating between MWNT and electrodes, while in our model the heat capacity of the CNT sheet was taken to be zero. The sample size considered here has a Rayleigh Distance (RD) of ~1 cm (surface area/wavelength) at the maximum frequency used in the analysis. Therefore, measurement, numerical evaluation, and analytical values at a distance of 3 cm may be considered in the acoustic far field, where pressure waves start spreading as a spherical wave. Our modeling results capture the trend where on increasing frequency, SPL also increases when the input power is fixed (as we observed in measured values).

After analysis of smaller sample, we investigated the acoustic behavior of large surface area sample (18 cm x 3.2 cm). Figure 3(b) shows the comparative results. We measured the pressure vs frequency trend for two distances (3 cm and 30 cm) to understand the structural contribution (surface area) of MWNT sheet towards sound generation. With reference to RD, we can safely consider 3 cm as near field and 30 cm as far-field zones across the frequency range considered here. In near field, we observed that the numerical and experimental values are in close agreement above 200 Hz. Below this frequency range, our model is over predicting sound pressure level. Since at low frequency the wavelength of the system is large, there is more contribution of dimensions in near field zone. It can also be observed that our modeling results and experimental results are below the theoretical line, this is because theory is valid for the domain where acoustic wave from the source starts spreading as a spherical wave. This theoretical result matched

qualitatively and quantitatively in above mentioned case because sample dimension was small and it behaved like a point source as the distance increased. After evaluation of sound pressure in near field, we conducted the comparative study at 30 cm (potentially a far field) and found that theoretical, experimental and numerical results are in close agreement. This shows that at long distance the contribution of sound source dimension is less and source starts acting as a spherical acoustic source. Inset image of Figure 3(b) shows the long MWNT sheet and experimental setup.

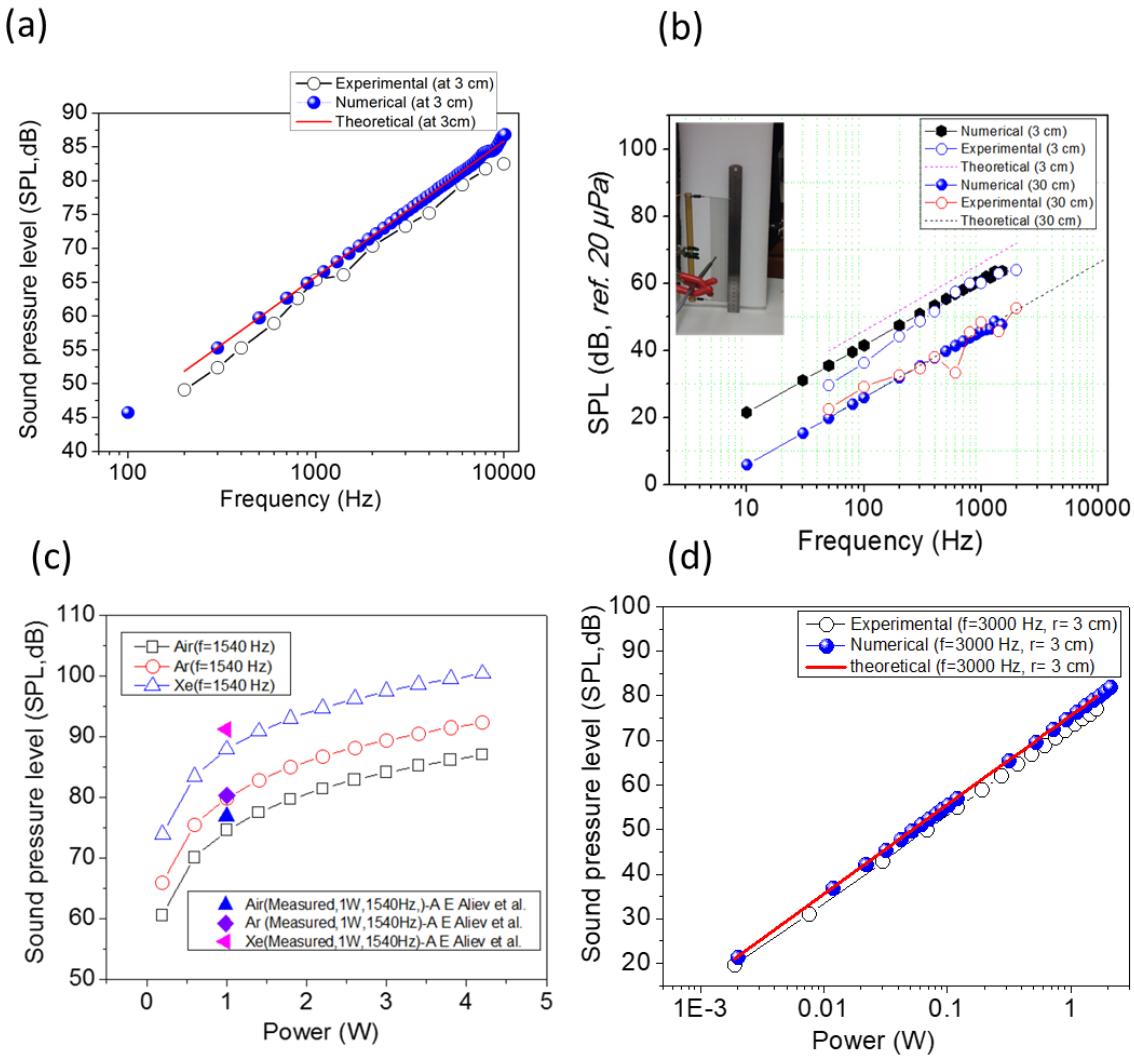

Figure 3: (a) Sound pressure level (SPL) in air with increase of frequency. Inset images show the experimental setup. CNT sheet used for experiment and modeling has dimension: 1.65×2 cm^2.All the results are shown for power: 1W and at distance: 3 cm, (b)

SPL in air with increase of frequency for the large MWNT sample. Inset images show the experimental setup. CNT sheet used for experiment and modeling has dimension: 18×3.2 cm^2. All the results are shown for power: 1W and at distance: 3 cm and 30 cm, (c) Sound pressure level (SPL) comparison of modeling with literature values [1], (d) SPL in air with increase of power.

Next, we compared the pressure generated by power sweep in open system at a fixed frequency boundary condition. As a first step, SPL was calculated at 1540 Hz for different input power and compared with experimental results published by Aliev et al. [1] (Figure 3(c)). As can be seen from Figure 3(c), experimental results are in close agreement with modeling trend for a fixed power in the different fluid environment. Figure 3(d) shows the detailed comparison of numerical, experimental and theoretical results of small sample for power sweep. The figure confirms the validity of our model and illustrates the perfect linear trend with 6 dB/octave increase. All the numerically solved pressure value were recorded at 3 cm above the MWNT sheet for validation.

Once the 1st layer model was validated using experimental and theoretical results, a detailed thermoacoustic analysis for open system was conducted as a function of frequency with different parameters such as various MWNT surface area, variable distance, and different surrounding mediums. Figure 4(a) shows the comparison of SPL in different gas medium such as air, Ar and Xe for 5 cm x 5cm MWNT. We obtained trends similar to the experimental results shown elsewhere [1]. These results reinforced that Xenon is the better medium for TA wave propagation. Figure 4(b) shows the frequency response results at variable distance and different surrounding medium for the MWNT of dimension 15 cm x 15 cm. The detailed spatial pressure distribution is shown in Figure 4(c). Also, it can be seen from the inset image (Figure 4(c)) that the PML is completely absorbing the incoming acoustic wave and there is no reflection to the acoustic domain.

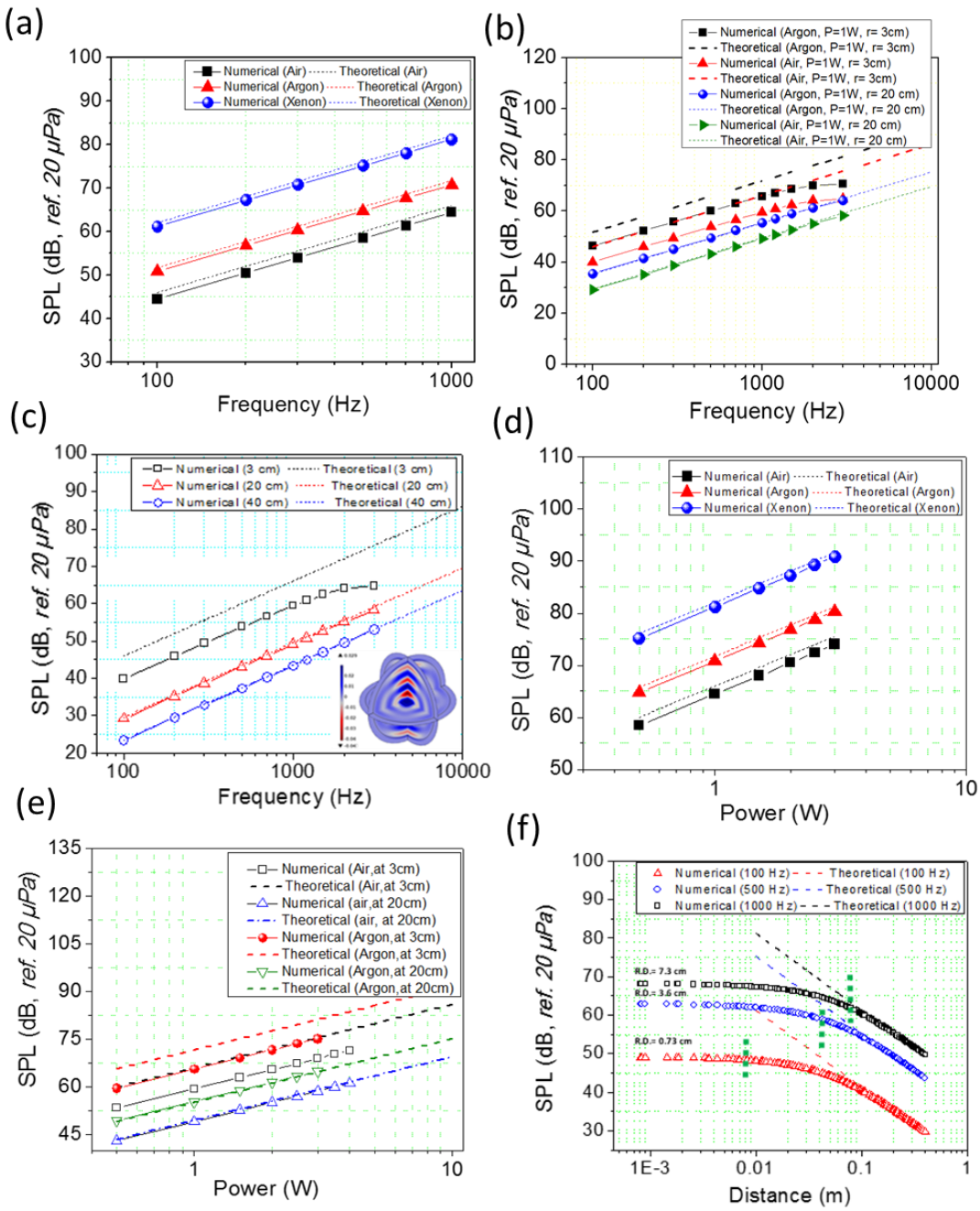

Figure 4: (a) Numerical and theoretical SPL in air, argon and xenon with increase of frequency for 5×5 cm^2 sheet, (b) comparison of SPL in air and argon gas for 15×15 cm2, (c) Numerical and theoretical SPL for 15×15 cm2 in air at different distance of 3 cm,20 cm and 40 cm. Inset image shows the spatial pressure variation, (d) Numerical and theoretical SPL in air, argon and xenon with increase of power for 5×5 cm^2 sheet, (e)

numerical and theoretical SPL for 15×15 cm^2 in air and argon at different distance of 3 cm and 20 cm, (f) SPL with increase of distance at different frequencies. Raleigh distance (R.D.) is shown by a green vertical dashed line.

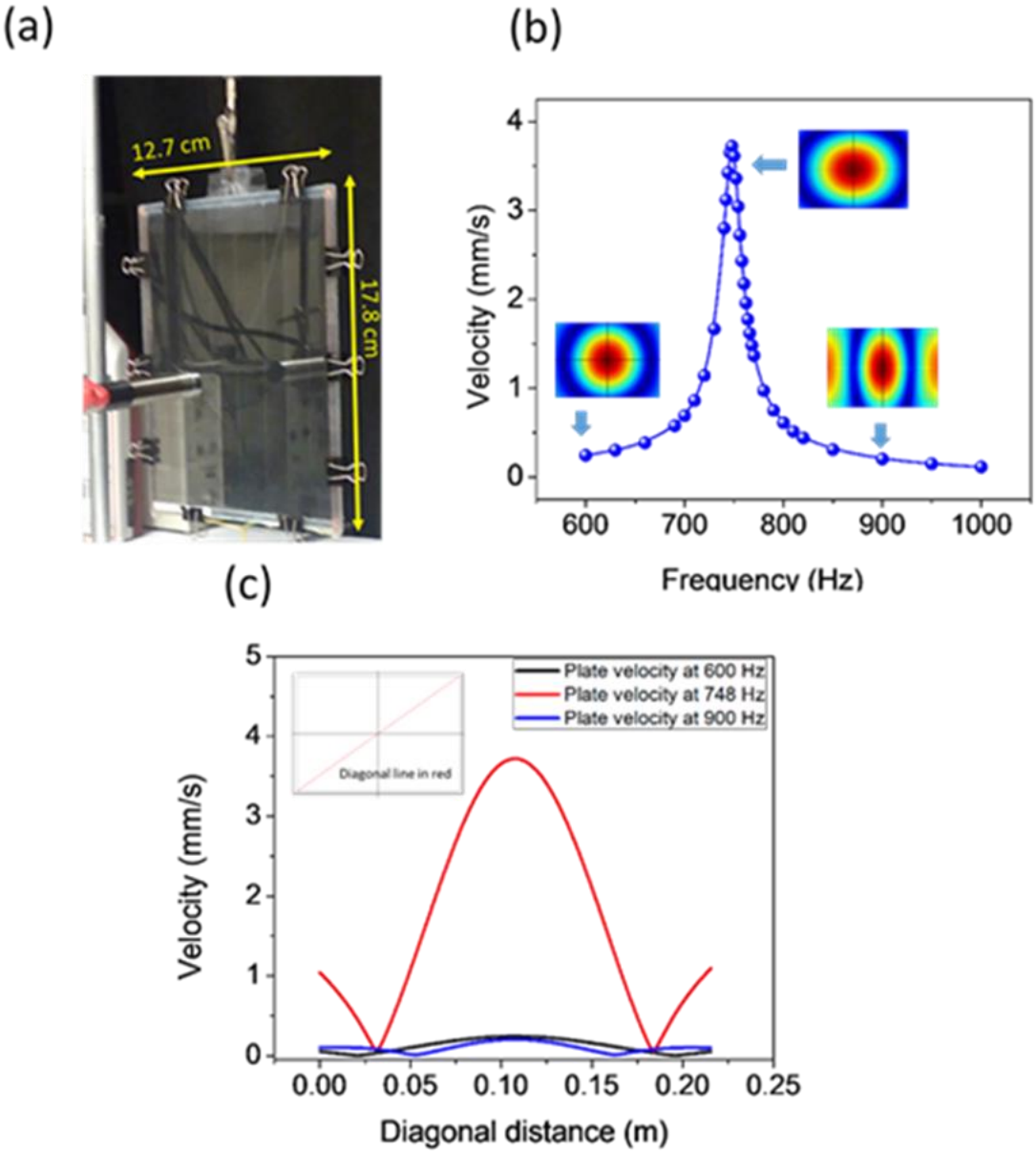

Figure 5: (a) TAP used for layer 2 and 3 results and other parametric analysis, (b) Simulated frequency response of the vibrating plate in 2nd layer modeling, (c) Simulated velocity profile across the diagonal of the TAP shown in Figure 2(a).

Material properties of elastic materials: Table 2

	Al	**Glass**	**Carbon fiber**
Density - ρ (kg/m^3)	2700	2230	1650
Young modulus (Pa)	70e9	64e9	90e9
Poisson's ratio	0.33	0.2	0.3

Figure 4(d) shows the numerical calculated SPL vs theoretical line in different gas surroundings for 5cm x 5cm sheet. Figure 4(e) shows modeling results for argon and air medium for a sheet of dimension 15cm x 15cm. In Figure 4(f) we show the SPL variation of MWNT sheet (15 cm x 15 cm) for different distance and frequencies. It is being observed that for relatively higher frequency (1000 Hz) the RD is showing a true representation of transition of near to far field since results are following the 6 dB decay in SPL on doubling the distance after that point. Similar trends were not observed for lower frequencies because structural effects (source dimensions) play an important role in the sound generation in near field. This could be explained by the similar example of rigid circular piston having radius 'a', radiating into near space. For low frequencies (ka <1), the far field distance along the axis is highly dependent on the radius of radiating piston and starts beyond '2a'.[28]

The above investigation, which involves the evaluation of TA pressure near the large surface area MWNT, was extremely important. As discussed in our Figure 1(a), in next layers of modeling, the open sheet will be encapsulated by isotropic plates which will be separated by a small distance (in the near field) from the MWNT sheet. Therefore, we need the correct near field pressure as the driving force at the surface of encapsulating plates for further accurate modeling outcomes. Numerical analysis has a clear advantage over basic analytical solutions in evaluating the near field TA pressure for different MWNT sheets.

Layer 2: Isotropic plates encapsulation and vibration analysis

In the first layer of the model, we characterized the thermoacoustic wave motion in open fluid domain. However, dynamics will change if the TA wave generating heat source becomes confined inside a resonating structure where the gas volume of the chamber also changes with vibrating plates. In the 2nd layer of modeling, we evaluated the vibration characteristics of the plates (driven by TA wave) of an encapsulated glass device shown in Figure 5(a). The experimental acoustic performances of the device are already demonstrated in previous work [24]. Since we already explained that the encapsulated device contains the silicone rubber gasket as the boundary sealing, we have also introduced the similar elastic edges (instead of clamped-clamped or simply supported) boundary condition having spring effect to mimic the real experimental conditions. We kept the other simulation inputs similar to the experimental analysis as described in the literature [24]. Figure 5(b) shows the frequency response of the device's plate velocity at a power input of 1W. We observed only one peak (at around 748 Hz) in the frequency range considered here. The normalized velocity profiles have also been shown at different frequencies in Figure 5(b) to illustrate the dynamic behavior of the plate. We can observe a significant change in surface velocity profile across the frequency spectrum. Figure 5(c) shows the quantitative velocity comparison of the points along the diagonal of the device (inset image) at three frequencies. At resonance frequency, we observed the maximum velocity amplitude ~ 3.7 mm/s. Figure 5(c) also illustrates the visible effect of the elastic edges boundary condition, and we observe the velocity of ~1 mm/s at the resonance frequency. This is worthwhile to mention that, the soft edges (silicone rubber) are important for our device design, since, it helps in better vibration of the plates (compare to simply supported condition) at lower frequencies. Table 2 shows some of the material properties used (or will be used late) for simulations.

Layer 3: Isotropic plates encapsulation and vibration analysis

Before starting the discussion for layer 3, it is important to mention that layer 2 and 3 of the model are fully coupled, and through our FEM model we computed the coupled behavior of the TA, vibrating structure and outer fluid acoustic wave and considered the impact of each physics on each other for final results evaluation. For clarity, we have described the results separately.

In this layer, we discuss the sound pressure wave generated by encapsulated device discussed in layer 2. The structural dynamics and the TA interact with each other to produce acoustic waves outside the encapsulated device, i.e. a vibro-acoustic wave driven by TA wave. Figure 6 shows the schematic of vibro-acoustic modeling which represents the normal incident of TA wave on plate and spherical sound wave generation in the outer medium. We assumed no acoustic transmission through the isotropic plate at its resonance, since there is a large impedance mismatch between chamber filled gas and the plate [29].

The results from this layer of the model were validated through systematic experimental results published by Aliev et al.[24]. Figure 7(a) shows the frequency sweep of the device for sound pressure calculation at power input of 1W. Similar to the vibration results we observed one peak (at around 748 Hz) in the frequency range considered here. We ran simulations for different damping ratios and found that for ζ=0.03, the simulation results match closely with the experimental results. The inset image shows the frequency response of projector for different damping. Figure 7(b) shows the comparison of results when the device was made more rigid by constraining the soft edge boundary conditions through clips (shown in Figure 5(a)). Due to this constraint, the spring constant of the device increased and hence frequency was increased. We simulated this condition by increasing the spring stiffness of the silicone edges. Results show close agreement of experimental and modeling results at ζ=0.03. Inset image of Figure 7(b) shows the zoomed frequency range. Further, we calculated the pressure vs distance relationship for three different frequencies from our model. Figure 7(c) shows that the pressure decreases linearly (in log scale) after the Raleigh distance (i.e. ~5 cm), and hence confirms the *1/r* decay of far-field pressure with respect to distance away from the device. Figure 7(d) shows the experimental results that validated the model prediction of normalized pressure. In this case, the normalization is done by dividing the pressure with input power. Due to the limitation of our FEM model we could not get the well-matched results for the higher power input to the device. At higher power input, due to excessive heat accumulation with the encapsulated chamber, the device no longer behaves linearly. Adding more physics to our

FEM model could make it more complex and we considered it beyond the scope of this work. However, we demonstrated good agreement of results up to 40W of power input.

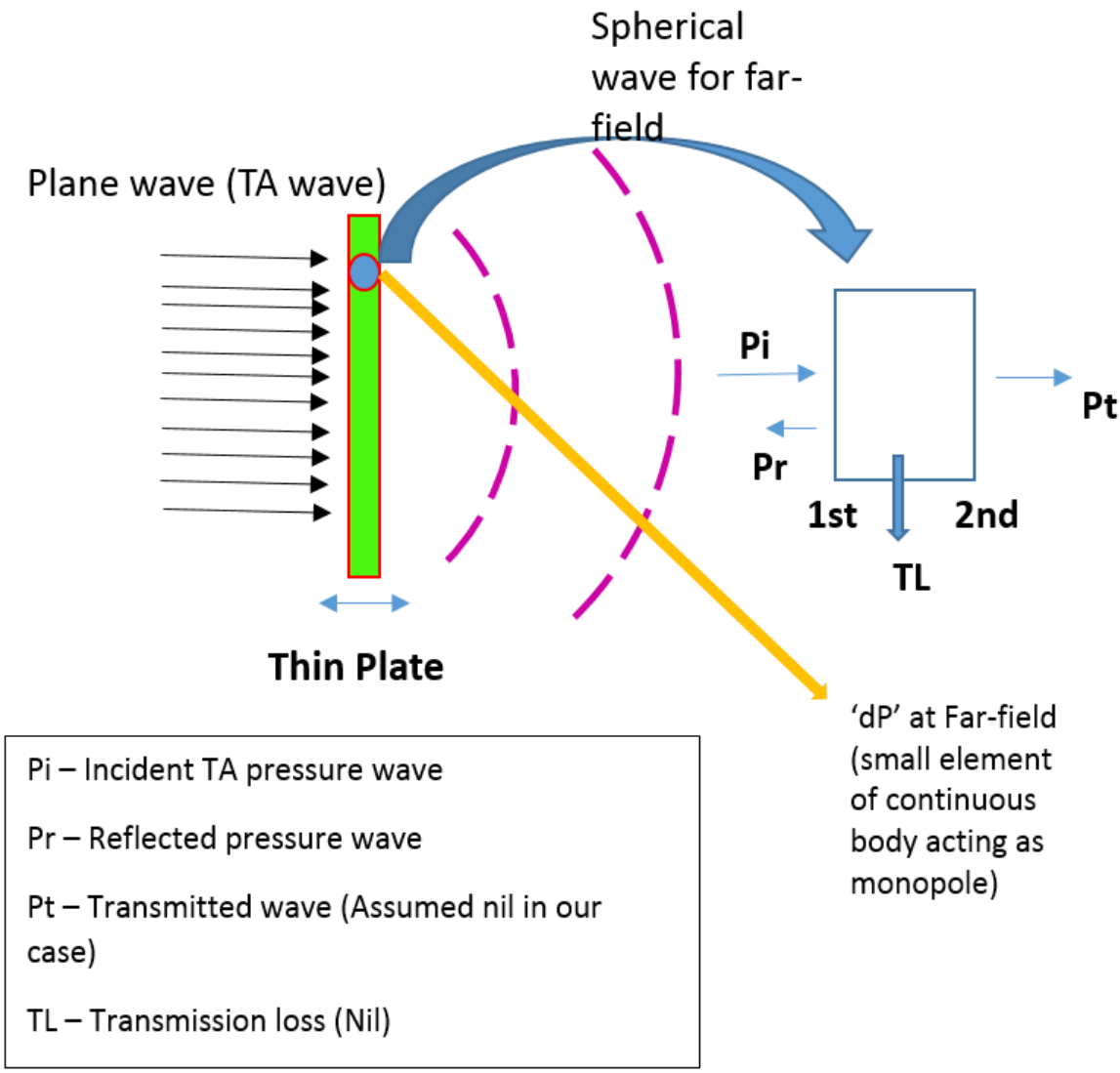

Figure 6: Schematic showing vibro-acoustic layer of modeling.

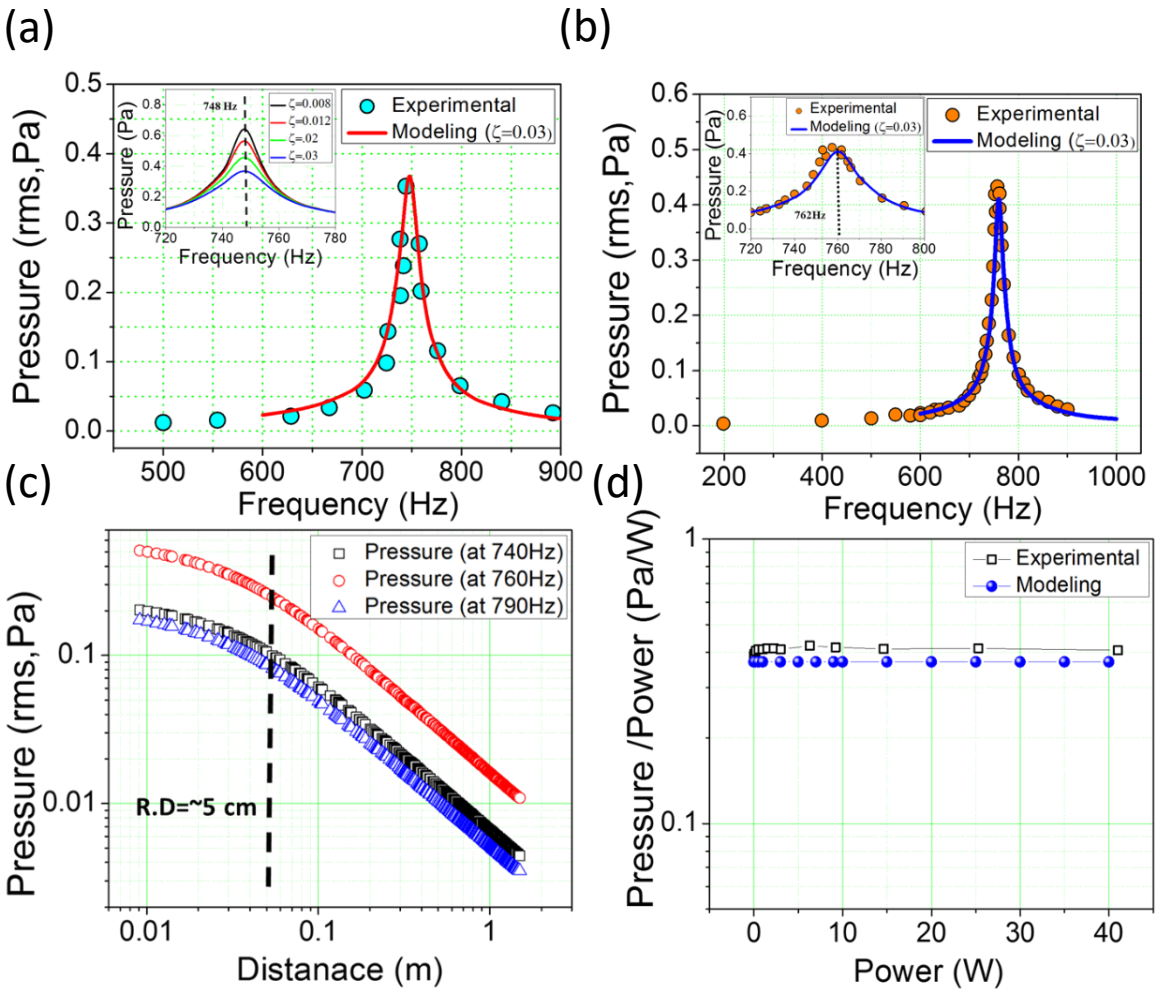

Figure 7:(a) comparison of experimental and modeling frequency response of the glass projector, (b) Experimental and modeling results comparison on increasing the device's stiffness, (c) Pressure vs distance calculation for three different frequencies, (d) pressure/ power vs power plots for experimental and modeling results.

Analysis of parameter space from integrated model

In this section, using our validated model, we investigated the important parameters such as chamber fluid loading, external water loading, internal static pressures, chamber volume variation, different plate materials etc. which could be important for the efficient device design. We created the numerical experiments on the same glass device and filled the encapsulating chamber with different gases or fluid such as Xe, Ar, and water. Figure

8(a) illustrates the effect of different gas on device performance. We can observe that Xe filled device operates at a higher resonance frequency, around 16% higher than argon and air-filled device. In all the cases the outer fluid medium is air. Also, through results, we can observe a marginal increase of frequency in the argon filled device compare to the air filling. The reason for this effect could be attributed to the change in density of the filling gases, which eventually cause the additional aerodynamic spring effect (or add more stiffness) to the system during vibration. Higher density gases could produce higher additional spring effect, which increases the overall frequency. Similar trends of increasing frequency with cavity density were also observed by Dowell et al. in their work [30]. Interestingly, with an increase in the density of filled gases, fluid loading (or added mass) effect also increases. However, Xe, Ar, and air will be considered as weak fluid loading, though the effect cannot be neglected completely. Figure 8(a) shows the frequency response of the device filled with water as well. Here we could see the significant decrease in resonance frequency in comparison to the gas-filled device. This can be explained by the fact that, since the density of water is extremely high than the other gases, the impact of fluid loading will be more pronounced than the additional stiffness provides by the camber fluid. We also compared the pressure response of different filled devices qualitatively. It can be observed further, although there is negligible difference in the pressure output for the gas-filled device at their respective resonance frequency (similar to Aliev et al.[1]), a significant decrease in pressure of water filled device is observed (around 4 times). The actual sound generation of liquid filled devices could be worse because MWNT sheets get collapsed in the liquid surroundings. This is the limitation of our FEM model, that we do not include structural damage of the CNT sheet.

Further, to investigate more about the filled devices, we simulated the air-filled device and the liquid filled device under the water loading. In this case, the outer medium of air is replaced with water (with added mass effects). As expected, Figure 8(b) shows the lower resonance frequency of liquid filled devices comparing to air-filled device. However, this is interesting to note that the difference in pressure output between the two devices has decreased compared to the case when the outer medium was air. The

reduction of sound pressure is ~ 2 times. This could happen because of a better impedance match of water filled devices in the water surrounding than air. For simplicity, we kept the glass device dimensions same for current and future analysis until mentioned separately. However, the conclusion of the analysis would remain the same for other device dimensions if containing isotropic plates.

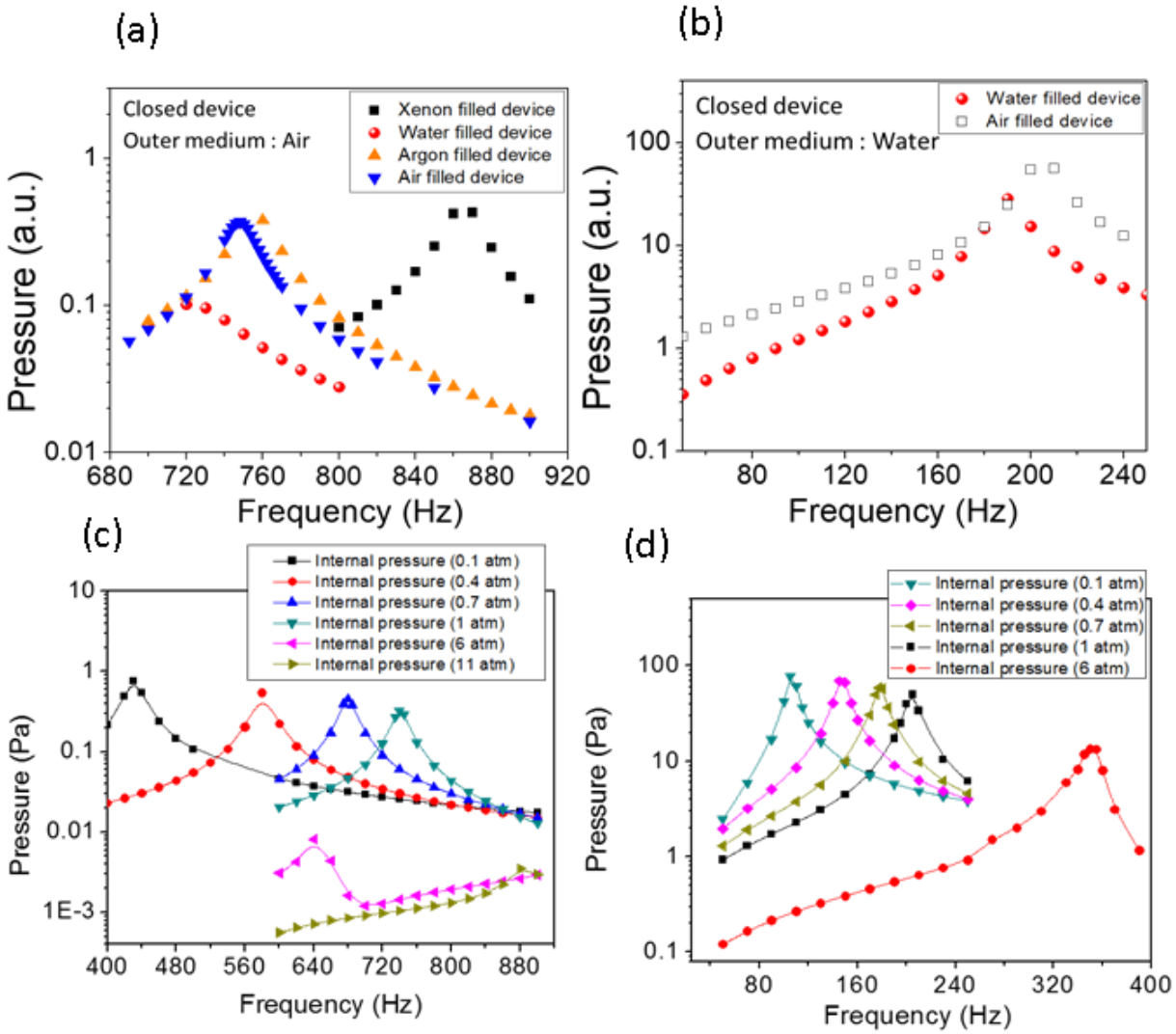

Figure 8:(a) Frequency response of TAP having different internal fluid loading in air medium, (b) comparison of air-filled and water filled device in water medium, (c) frequency response of TAP with different internal pressure in air surrounding, (d) frequency response of TAP with different internal pressure in water surrounding.

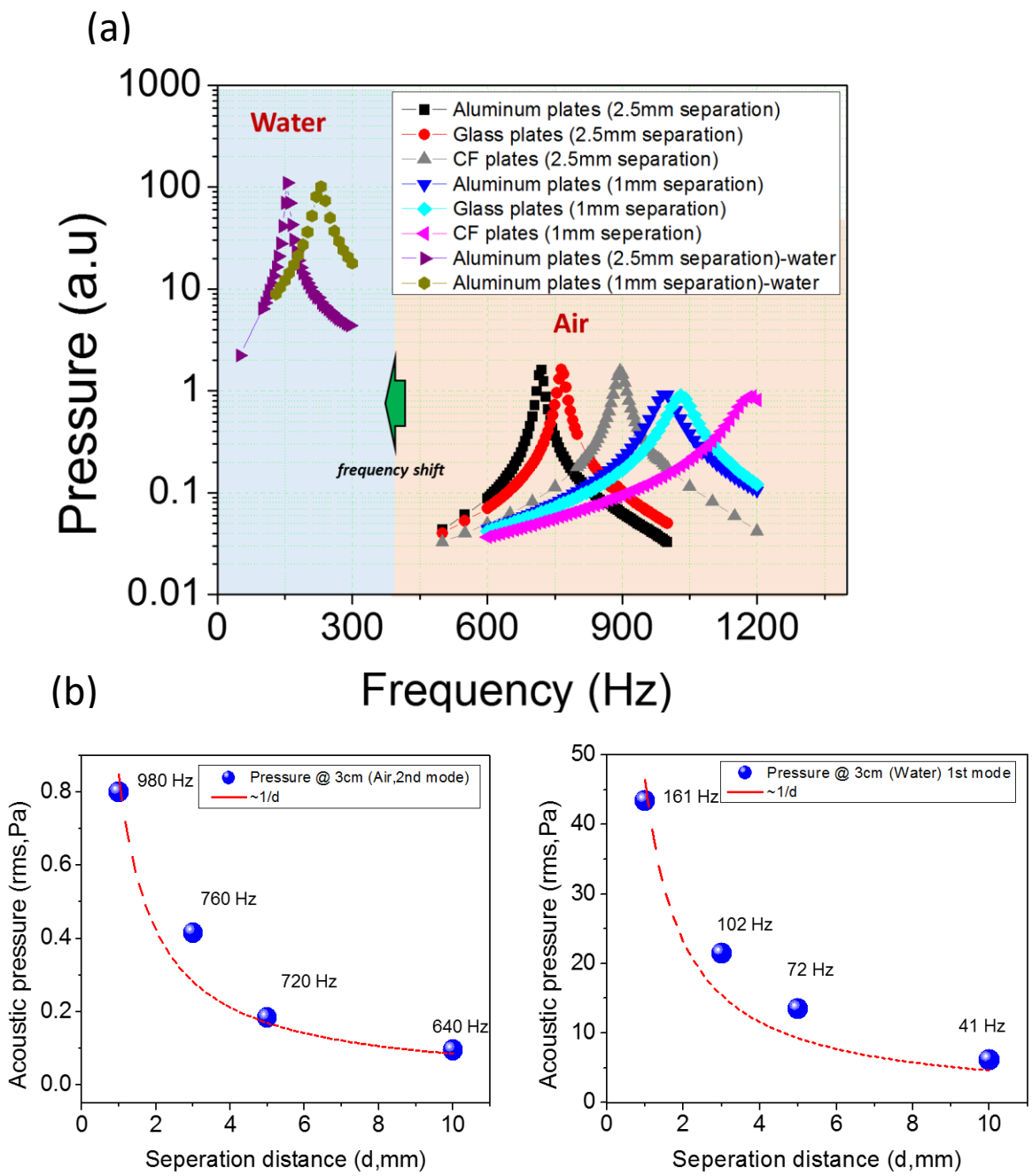

Figure 9: (a) frequency response of several devices made of Aluminum, glass, and carbon fiber (CF) plates under two category of plates separation: 1 mm and 2.5 mm. The effects of air and water loading are calculated through numerical analysis, (b) Acoustic pressure decrease in air and water with the increase of separation (frequency also decrease with the increase of separation)

Next, we investigated the impact of the different internal static pressure of air-filled glass device (same device used in layer 2-3) in sound generation and structural behavior in air/water surroundings. Due to the limitation of our FEM model, which could not capture molecular physics, we confined our study to the pressure range belongs to the fluidic regime. Aliev et al.,[1] discuss the impact of static pressure increase in a rigidly closed chamber and found no major change in TA pressure. However, in our simulation results for the vibrating device in Figure 8(c) and Figure 8(d), we observed the significant change in device resonance frequency and pressure wave generation in both air and water medium. With the increase in internal pressure (0.1 atm to 11 atm), our resonant system becomes stiffer which causes the shift in resonance frequency of the device. Moreover, an increase in internal pressure increases the in-plane tension within the vibrating plate which could reduce the vibrating amplitude of the plates and hence a reduction in pressure output is observed. At high internal pressure (6 or 11 atm), our simulations results (Figure 8(c)) show the negligible sound pressure generation in air surrounding. However, under the water loading (Figure 8(d)), we observe a significant sound pressure in water medium even at higher internal pressure such as 6 atm.

Now we utilized the model to predict the behavior of different dimension TA projectors. We developed the numerical model for various devices based on aluminum (Al), carbon fiber (C.F.), and glass plates. In all the devices, we kept the plates dimension as 15 cm ×15 cm × 0.08 cm, and used the Ar gas in the encapsulated volume. In the first set of devices, the separation between Al, C.F., and glass was kept at 1 mm, while in the 2nd category the separation was extended to 2.5 mm. The separation between the plates was provided by silicone rubber. Figure 9(a) shows the calculated results for different devices. It can be observed from the results that the devices having less separation (1 mm) between the plates have higher resonance frequencies. The lower thickness of silicone strip used here made the system relatively rigid (highly stiff) and increased the resonance frequency in comparison to 2.5 mm separation. Further, results illustrate that Al-plate based device has a lower frequency compared to other considered materials. Numerical experiments provided the quantitative effect of separation on the device's resonance frequency. It was also found that Al is a good choice for device fabrication (for

low frequency). In the case of water, we observed the frequency shift compared to that of air because of added mass on the plate structure. In water, peak frequencies corresponding to 151Hz and 230 Hz were calculated for 2.5 mm and 1 mm separation Al-devices respectively. All the pressure values are shown in arbitrary units since the damping coefficient is not used in any of the simulations. Further, with one such device (Al-plate and argon filled), we investigated the effect of plate separation on sound pressure generation and frequency shift. Figure 9(b), illustrates the decrease in sound pressure and frequency in air and water, on increasing the separation of encapsulating plates. By increasing the separation, we introduce the more flexible boundary condition of silicone rubber because of which the frequency decreased in both air and water medium. Also, due to the increase in separation between MWNT sheet and plate, the TA pressure will exert relatively less force on the plates which results into a decrease in vibro-acoustic output.

In summary, we developed the first comprehensive model for the MWNT-based TA projector that takes electrical power as an input and provides the acoustic pressure output in outer fluid media. This model provides a deeper understanding of the various layer of physics involved in the operation of low-frequency thermoacoustic SONAR projector.

Conclusion

This study provides a first comprehensive numerical model of MWNT sheet based acoustic transducer, targeting low-frequency response in water. An integrated multilayer model was developed to predict the performance of the TA transducer under different fluidic environments. All modeling results were verified and validated through analytical solutions, results reported in the literature and systematic experiments. The study for an open system, having different sheet dimensions and surrounding mediums, was used to calculate the TA SPL distribution. Further, the effects of different sample dimensions on SPL (in the near and far field) were studied through modeling along with experimental validations. Following the open system modeling, we developed the vibro-acoustic model, and investigated the key parameters such as chamber filling, internal pressure, chamber volume etc. and their effects on LF TA projector device functioning.

References

[1] Aliev AE, Gartstein YN, Baughman RH. Increasing the efficiency of thermoacoustic carbon nanotube sound projectors. Nanotechnology. 2013;24:235501.

[2] Preumont A, Francois A. Piezoelectric array sensing for real-time, broad-band sound radiation measurement. International Conference on Adaptive Structures and Technologies, 10 th, Paris, France2000. p. 37-44.

[3] Bédard M, Berry A. Development of a directivity-controlled piezoelectric transducer for sound reproduction. Journal of Sound and Vibration. 2008;311:1271-85.

[4] Arnold H, Crandall I. The thermophone as a precision source of sound. Physical review. 1917;10:22.

[5] Zhang X, Jiang K, Feng C, Liu P, Zhang L, Kong J, et al. Spinning and processing continuous yarns from 4-inch wafer scale super-aligned carbon nanotube arrays. Advanced Materials. 2006;18:1505-10.

[6] Xiao L, Chen Z, Feng C, Liu L, Bai Z-Q, Wang Y, et al. Flexible, stretchable, transparent carbon nanotube thin film loudspeakers. Nano letters. 2008;8:4539-45.

[7] Aliev AE, Lima MD, Fang S, Baughman RH. Underwater sound generation using carbon nanotube projectors. Nano letters. 2010;10:2374-80.

[8] Suk JW, Kirk K, Hao Y, Hall NA, Ruoff RS. Thermoacoustic sound generation from monolayer graphene for transparent and flexible sound sources. Advanced Materials. 2012;24:6342-7.

[9] Tian H, Ren T-L, Xie D, Wang Y-F, Zhou C-J, Feng T-T, et al. Graphene-on-paper sound source devices. ACS nano. 2011;5:4878-85.

[10] Shinoda H, Nakajima T, Ueno K, Koshida N. Thermally induced ultrasonic emission from porous silicon. Nature. 1999;400:853.

[11] Niskanen AO, Hassel J, Tikander M, Maijala P, Grönberg L, Helistö P. Suspended metal wire array as a thermoacoustic sound source. Applied Physics Letters. 2009;95:163102.

[12] Nakajima Y, Sugimoto T. Flexible sound generator based on thermoacoustic effect. Sensors, 2012 IEEE: IEEE; 2012. p. 1-4.

[13] Chitnis G, Kim A, Song SH, Jessop A, Bolton J, Ziaie B. A thermophone on porous polymeric substrate. Applied Physics Letters. 2012;101:021911.

[14] Tian H, Xie D, Yang Y, Ren T-L, Wang Y-F, Zhou C-J, et al. Transparent, flexible, ultrathin sound source devices using indium tin oxide films. Applied Physics Letters. 2011;99:043503.

[15] Tian H, Xie D, Yang Y, Ren T-L, Feng T-T, Wang Y-F, et al. Poly (3, 4-ethylenedioxythiophene): poly (styrenesulfonate)-based organic, ultrathin, and transparent sound-emitting device. Applied Physics Letters. 2011;99:233503.

[16] Aliev AE, Mayo NK, Jung de Andrade M, Robles RO, Fang S, Baughman RH, et al. Alternative nanostructures for thermophones. ACS nano. 2015;9:4743-56.

[17] Aliev AE, Mayo NK, Baughman RH, Avirovik D, Priya S, Zarnetske MR, et al. Thermoacoustic excitation of sonar projector plates by free-standing carbon nanotube sheets. Journal of Physics D: Applied Physics. 2014;47:355302.

[18] Tong L, Lim C, Li Y. Gas-filled encapsulated thermal-acoustic transducer. Journal of Vibration and Acoustics. 2013;135:051033.

[19] Vesterinen V, Niskanen A, Hassel J, Helisto P. Fundamental efficiency of nanothermophones: Modeling and experiments. Nano letters. 2010;10:5020-4.

[20] Asgarisabet M, Barnard A. Multi-Physics Simulation of Ultra-Lightweight Carbon Nanotube Speakers. SAE International Journal of Materials and Manufacturing. 2017;10:395-401.

[21] Asadzadeh S, Moosavi A, Huynh C, Saleki O. Thermo acoustic study of carbon nanotubes in near and far field: Theory, simulation, and experiment. Journal of Applied Physics. 2015;117:095101.

[22] McDonald FA, Wetsel Jr GC. Generalized theory of the photoacoustic effect. Journal of Applied Physics. 1978;49:2313-22.

[23] Lim CW, Tong L, Li Y. Theory of suspended carbon nanotube thinfilm as a thermal-acoustic source. Journal of Sound and Vibration. 2013;332:5451-61.

[24] Aliev AE, Codoluto D, Baughman RH, Ovalle-Robles R, Inoue K, Romanov SA, et al. Thermoacoustic sound projector: exceeding the fundamental efficiency of carbon nanotubes. Nanotechnology. 2018;29:325704.

[25] Multiphysics C. v. 5.2. COMSOL AB, Stockholm, Sweden. 2015.

[26] Ohayon R, Soize C. Computational vibroacoustics in low-and medium-frequency bands: damping, ROM, and UQ modeling. Applied Sciences. 2017;7:586.

[27] Zhang M, Fang S, Zakhidov AA, Lee SB, Aliev AE, Williams CD, et al. Strong, transparent, multifunctional, carbon nanotube sheets. Science. 2005;309:1215-9.

[28] Keele Jr DB. Low-frequency loudspeaker assessment by nearfield sound-pressure measurement. Journal of the audio engineering society. 1974;22:154-62.

[29] Pierce AD. Acoustics: an introduction to its physical principles and applications: McGraw-Hill New York; 1981.

[30] Dowell E, Voss H. The effect of a cavity on panel vibration. AIAA journal. 1963;1:476-7.

Chapter 3

Understanding the Low Frequency Carbon Nanotube Thermo-Acoustic Sonar Projector by Experimental Analysis

Abstract

The ability of continuous sound generation across the wide range of frequency spectrum by an acoustic source, which is ultra-light and flexible and has no vibrating parts, provokes a lot of interest of the acoustic community. In this method of acoustic generation, electrical input is converted into thermal wave through micron thick carbon nanotubes (CNT) and produce thermoacoustic. However, at the lower frequency, open sheet CNTs have very low sound pressure levels and acoustic efficiency. In addition, operating at high electrical power input, the nanoscale thick CNTs are very sensitive to the environment and need some protective covering in an inert environment. In this work, two thermoacoustic high-power low-frequency (LF) devices (<180 Hz) are demonstrated that provide a systematic understanding of efficiency and power variation in both air and water medium at lower frequency regime.

Keywords: Nanotubes, Low-frequency, Acoustics

Introduction

Thermoacoustic (TA) sound generation shows the potential of addressing the low-frequency domain for ultra-thin, light weight and flexible speakers and sonar devices [1]. Recent studies on TA sound generation using carbon nanotubes (CNTs) sheets and alternative nanostructures have shown that the sound pressure is proportional to the applied frequency [2]. The extremely small heat capacity per unit area of a thin sheet CNT gives a wide frequency response and produce a higher sound pressure at high frequency. However, in the low-frequency region, where the utility of SONAR projectors is more, sound pressure level is extremely low (shown in the previous chapter). For the open CNT sheet operation, the other drawbacks such as mechanical strength and environmental sensitivity at higher temperatures also prevail. Keeping these limitations in mind, in this study we demonstrate the encapsulated device for low-frequency sound generation.

Decarpigny et al. [3] have discussed the need for low-frequency acoustic devices (100-3000 Hz) in the field of SONAR and oceanography while explaining the challenges with piezoelectric and magnetostrictive low-frequency devices. Dubus et al. [4] have discussed the limits of hydroacoustic, variable reluctance and piezoelectric projectors illustrating how the lowering of frequencies increases the dimensions/volume or weight of the device. Aliev et al. [5] provided a breakthrough in demonstrating low-frequency MWNT sheet based projectors that exceeded the weight/dimension limits of alternative materials. In their design, a MWNT sheet was suspended between two flexural plates and sealed from the edges by a silicone gasket. The compartment formed between the two plate was filled with different gases such as Xe, Ar, air etc. This transducer design was extremely effective and solved two major problems: (i) it enhanced the output of the CNT-based device at lower frequencies by using a resonant condition, and (ii) provided protection for the CNT sheet for the high input power operation in underwater harsh conditions (to avoid collapsing the CNT sheet) [6, 7]. We build on these studies, and utilize them to improve the robustness of the lightweight, high power and low frequency (LF) sound projector (<180 Hz underwater).

In this work, two low frequency encapsulated devices were fabricated based on CNT sheets. Then, we performed extensive experimental analysis for closed systems in different thermodynamic regimes. A series of measurement techniques were developed for laboratory-scale characterization of the acoustic performance of LF TA devices over a wide range of frequency under varying power and loading conditions in both air and water medium. Vibrational characterization of TA device in both air and water media was conducted and a relationship between the generated acoustic pressure and vibration modes was established. A unique feature of TA transducers is the synchronization of various physical effects (vibration dynamics, thermal transport, and molecular dynamics) for achieving high acoustic pressure. The sinusoidal heating of the adjacent gas by the CNT sheet generates the thermoacoustic pressure wave which drives the end plates resulting in sound pressure wave generation in the surrounding fluid domain.

Experimental

Fabrication

Two resonant encapsulated devices based on free standing highly aligned MWNT sheets were fabricated to demonstrate the low-frequency applications.

Device #1 consists of three layers of MWNT sheets attached to the interdigitated electrodes and suspended between two equally thick (.81mm) square aluminum plates having dimensions 6”x6”. The enclosure between two plates was sealed by soft 3 mm wide silicone strips with a thickness of 1.38 mm. This helped in providing an effective free boundary condition for plate vibrations. The measured overall impedance for this device was 60 Ω. Schematic is shown in Figure 1(a).

Device #2 is composed of three layers of MWNT sheet (attached to the interdigitated electrodes) suspended between two square aluminum plates having dimensions of 6”x6”. The top, radiating plate and bottom base- plate thicknesses were 1.8 mm and 3.4 mm respectively. A soft seal was used between the two plates. The enclosure between two plates was sealed by soft 3 mm wide silicone strips with thickness of 2.8 mm. The input impedance of the overall system was 50 Ω. For the better heat dissipation, a fin structure was introduced which helped in heat removal from inside at higher power of operations (shown in Figure 1(b)).

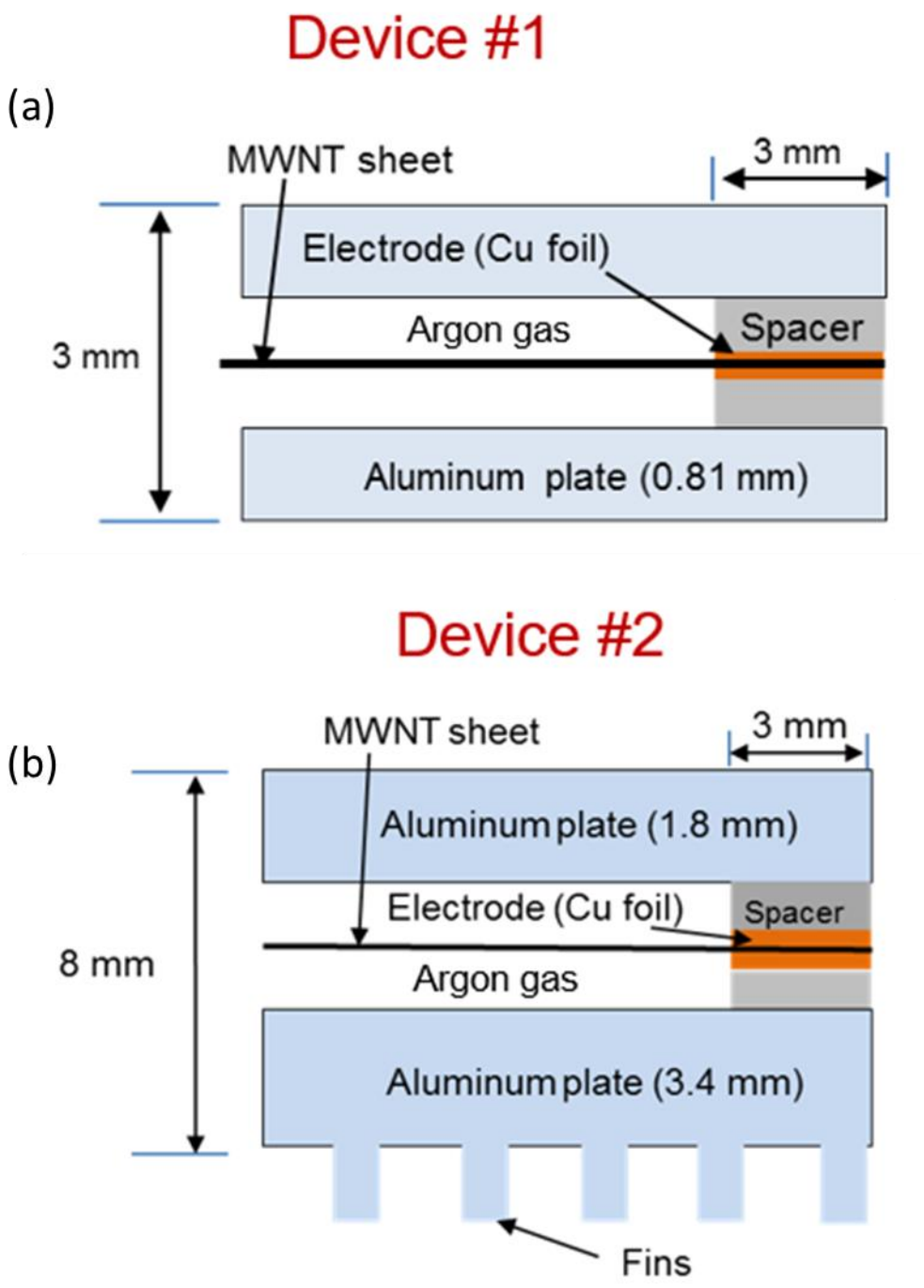

Figure 1 :(a) and (b) schematics of two different encapsulated device .

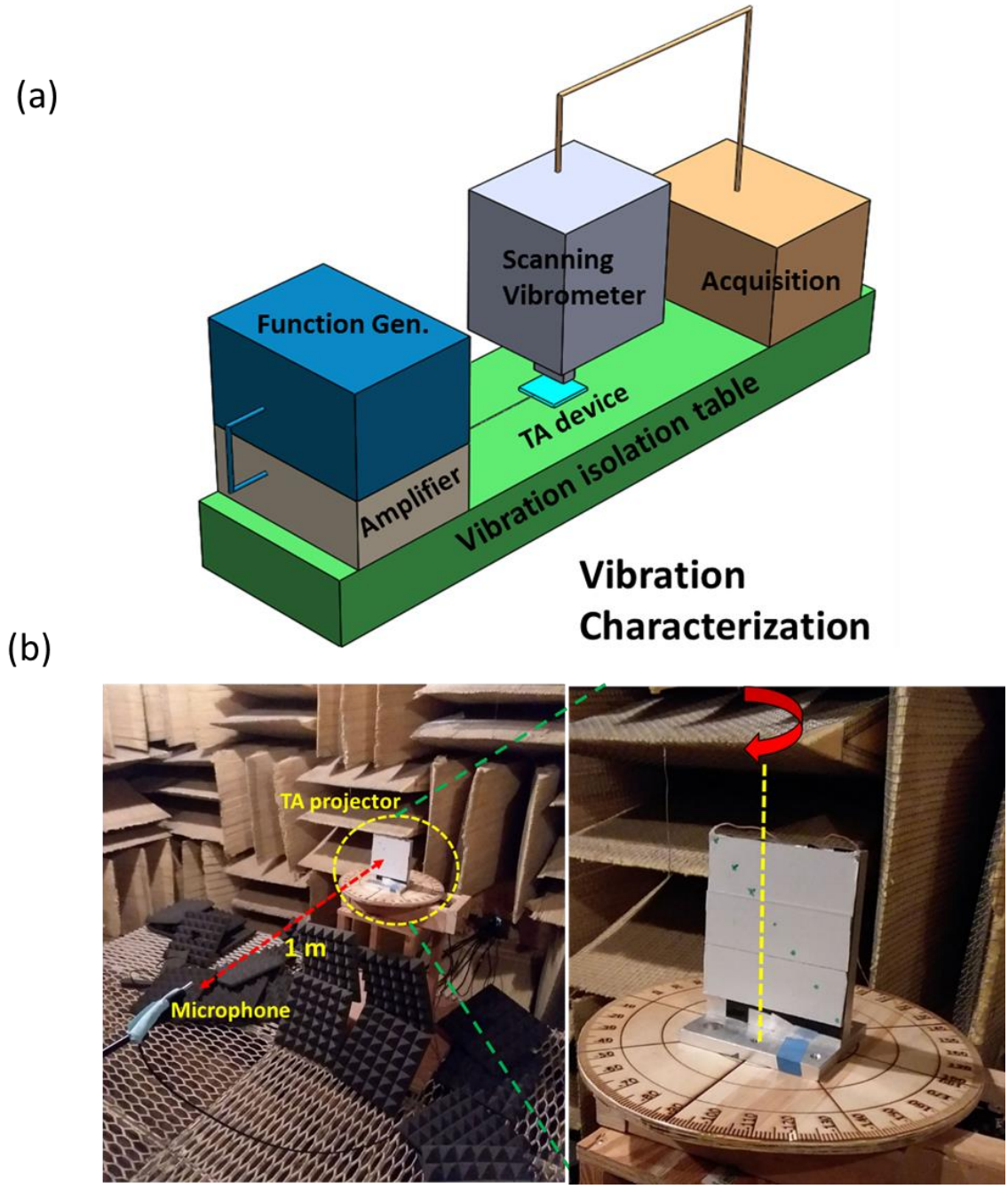

Figure 2: (a) Schematic of vibrational characterization experimental setup, (b) Anechoic chamber experimental setups for sound pressure measurement in air.

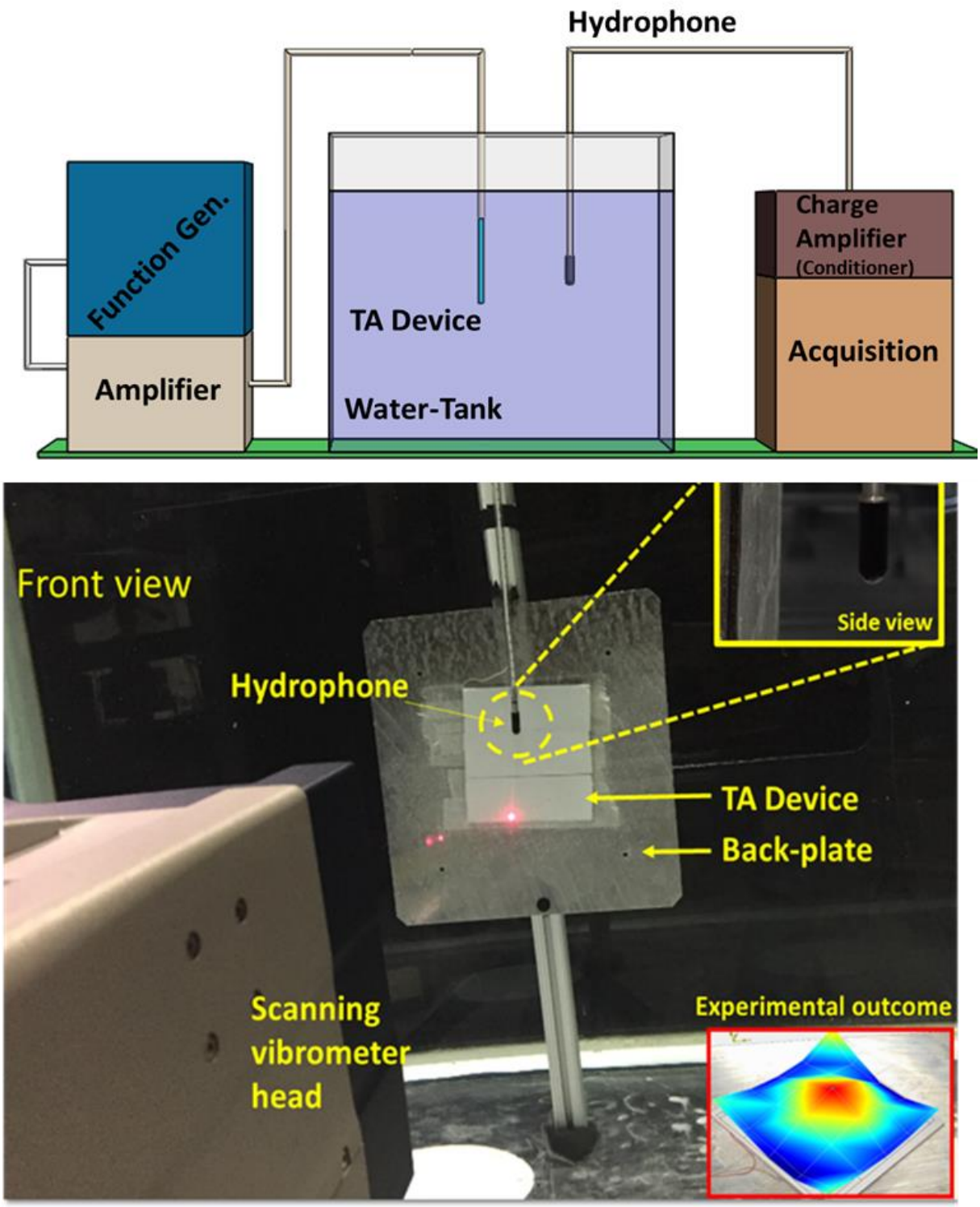

Figure 3: Underwater vibration and acoustic measurement setups

Experimental characterization

For the encapsulated device, Figure 2 shows the schematic diagram and actual images of the experimental setup used for vibration and acoustics characterization in the air medium. A PSV-500 2D laser scanning vibrometer was used for measuring the vibration characteristics of the encapsulated device (Figure 2(a)). An inbuilt function generator and acquisition system was used for sending the input and receiving the signals respectively. We used the high-speed bipolar amplifier (HSA 4052) for amplifying the input signals to the device.

For the acoustic measurement in the air we placed our device in full anechoic chamber. The purpose of the chamber was to avoid any reflection from the walls even at high power input to the device. Figure 2(b) shows the experimental setup for the TA projector. The chamber used here has cut off frequency of 100 Hz. The device was installed on a rotary platform which was allowed to rotate at every 5° through a controlling unit. The sound pressure was recorded through the microphone at 1 m of the distance.

For the underwater measurements, an experimental setup was developed in a tank (dimensions: 72” × 36” ×62”), to understand the acoustic behavior of the device and the impact of water loading on vibration. Scanning head and single point vibrometers (Polytec PDV-100) were simultaneously used to measure the plate velocity. A hydrophone (Brüel & Kjær 8103) was placed above the device surface to capture the underwater acoustic pressure. A Kistler type 5010 signal conditioner was used to condition the signal coming out of the hydrophone. Figure 3 shows the water tank setup.

Results and discussion

In the previous chapter, through the model, it has been indicated that Xenon is better gas than Argon and air for achieving better transduction of TA wave in an open system. For the closed system (encapsulated devices), sound pressure is independent of gas properties other than γ. Argon is a more cost-effective choice and thus utilized in developing practical devices. The efficiency of the encapsulated device is given by Eq. (1) [4] which indicates that the efficiency is inversely proportional to f^2. The efficiency of

the device when driven near resonance can be enhanced by improving the resonance quality factor of encapsulating plates.

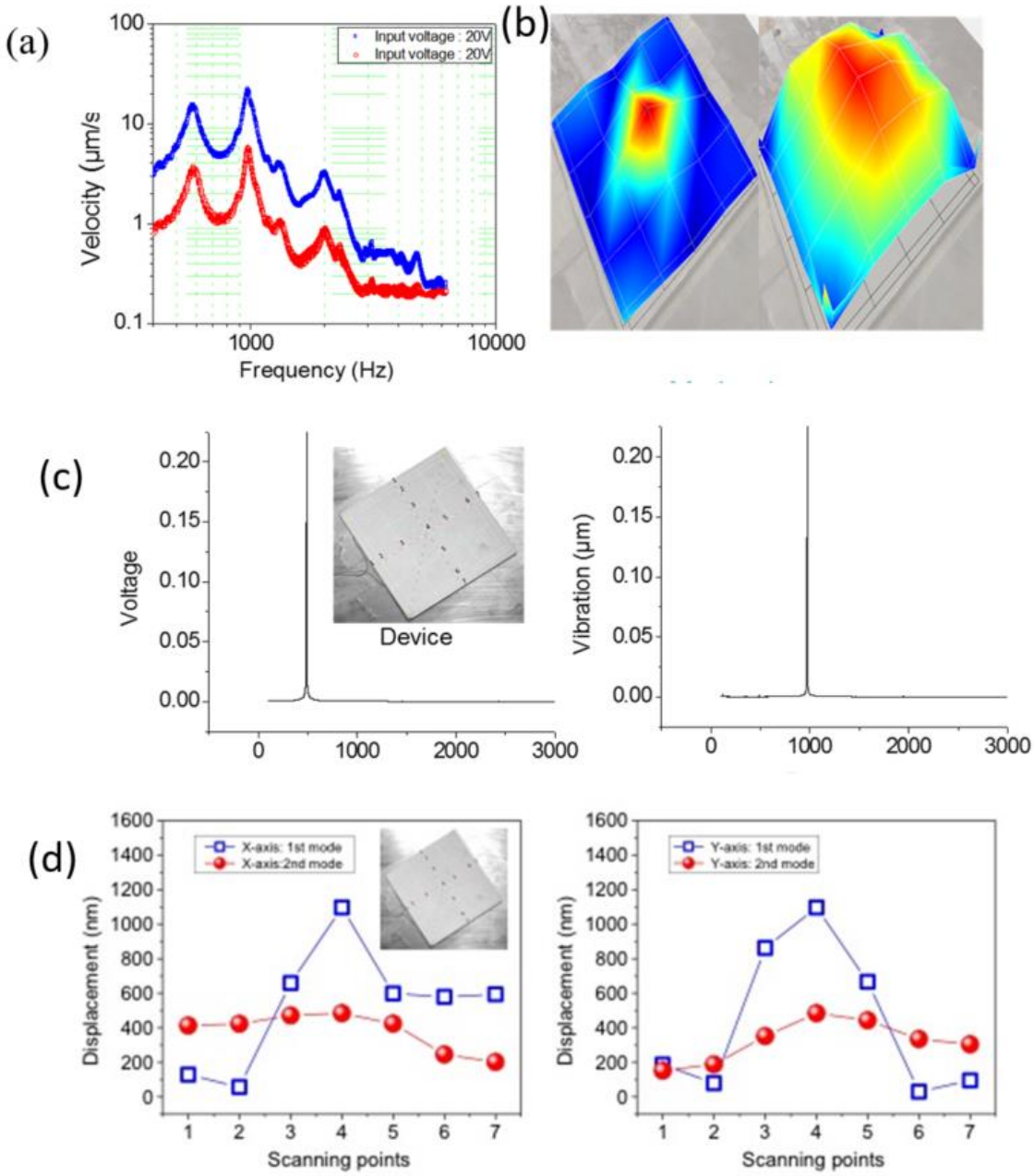

Figure 4: (a) Frequency response of device 1, (b) mode shapes in air, (c) Input at half of the output frequency, (d) displacement profile across x and y-axis.

$$\eta = \frac{(\gamma - 1)^2 \rho_f Q^2}{2\pi^3 \rho_p^2 h_p^2 h_g^2 f^2 \upsilon_f} P_h \tag{1}$$

where γ is the heat capacity ratio, Q is the quality factor of vibrating plates, v_g is the speed of sound , V is the encapsulated volume, ρ_{air} is density of air, P_h is power input, and f is operating frequency.

We fabricated two devices having different edge boundary conditions. A complete experimental study of vibration and acoustic experiments was performed on both the devices. To avoid any confusion, firstly, we discussed all the vibration and acoustics results of device #1 then we analyzed the device #2. In our previous chapter, 1st layer of model helped in deciding the plate separation distance on the basis of the thermal diffusion length calculation. The second and third layer of model gave us the understanding of plate separation impact on peak frequency change in different surrounding medium. The separation is based on three prominent features: (i) the plate should be far away from thermal diffusion length, (ii) the peak vibration amplitude should not be large enough to touch the suspended CNT sheet (at resonance frequency), and (iii) the separation should be close enough such that the acoustic pressure effectively drives the encapsulating plates.

Vibration tests were performed under the boundary conditions: bottom plate fixed. This boundary condition was investigated to demonstrate the sound radiation when only one plate is vibrating. Experiments were run on the device mounted on a heavy plate. The reasons for mounting the device were to suppress the bottom plate vibration, and to allow the upper plate to radiate the sound wave in outer fluid media. We used a burst chirp signal (10V and 20V) with 70% length. The upper plate was discretized into 49 scanning points and each point was scanned by a 2D laser vibrometer to examine the vibrational response.

Figure 4(a) shows the velocity results of the top plate, while the bottom plate is fixed, with frequency sweep (up to 6000 Hz by burst chirp). Two dominant peaks at 580Hz and

972Hz were identified. Figure 4(b) shows the mode shapes obtained by activating the device with sinusoidal input at half of the peak frequency. Due to the double heating frequency with each cycle of sine input (Figure 4(c)), half of the frequency was used to obtain the desired response. Figure 4(d), shows the x-axis and y-axis top plate vibration displacement amplitude. The maximum displacement of around 1.2 micrometers has been obtained on providing the 3W of power input. On visualizing the mode shapes, it can be observed that the average velocity/displacement in the 2nd mode shape is more than that in the 1st mode. In the 2nd mode, the whole plate is vibrating in the same phase, while in the 1st mode the central part and the edges are relatively out of phase. This explains that in air medium the maximum output of the device is at 2nd peak frequency.

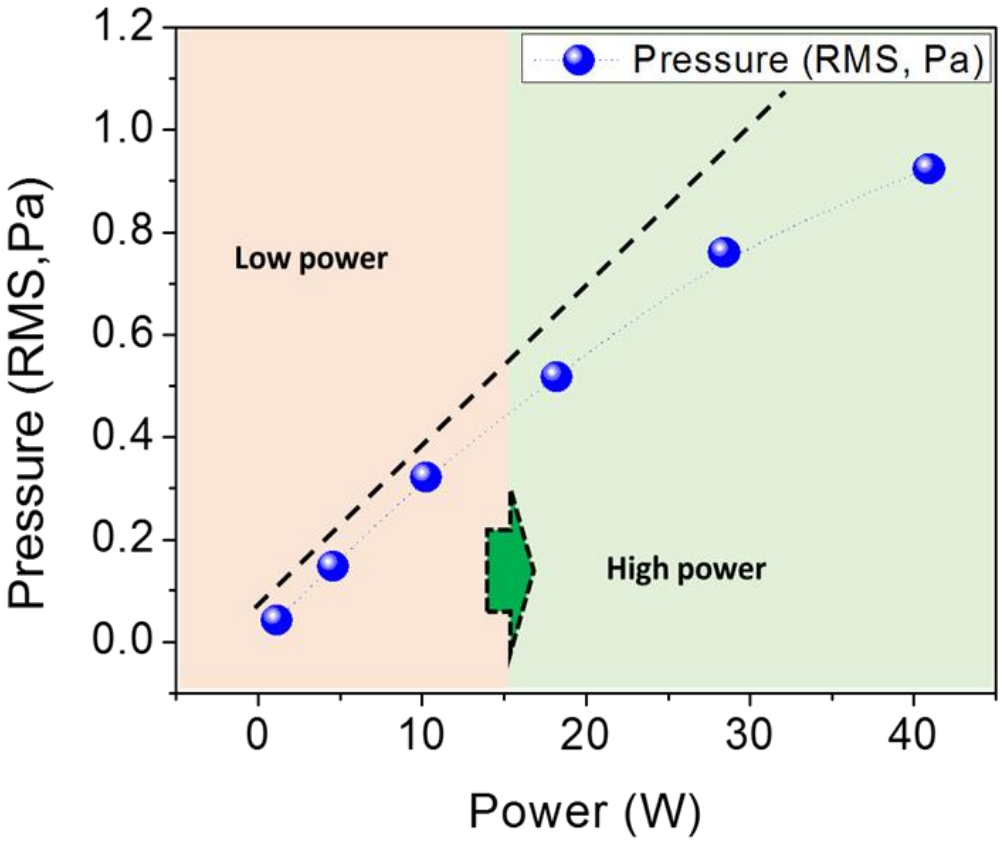

Figure 5: Pressure vs power for device 1 in air medium.

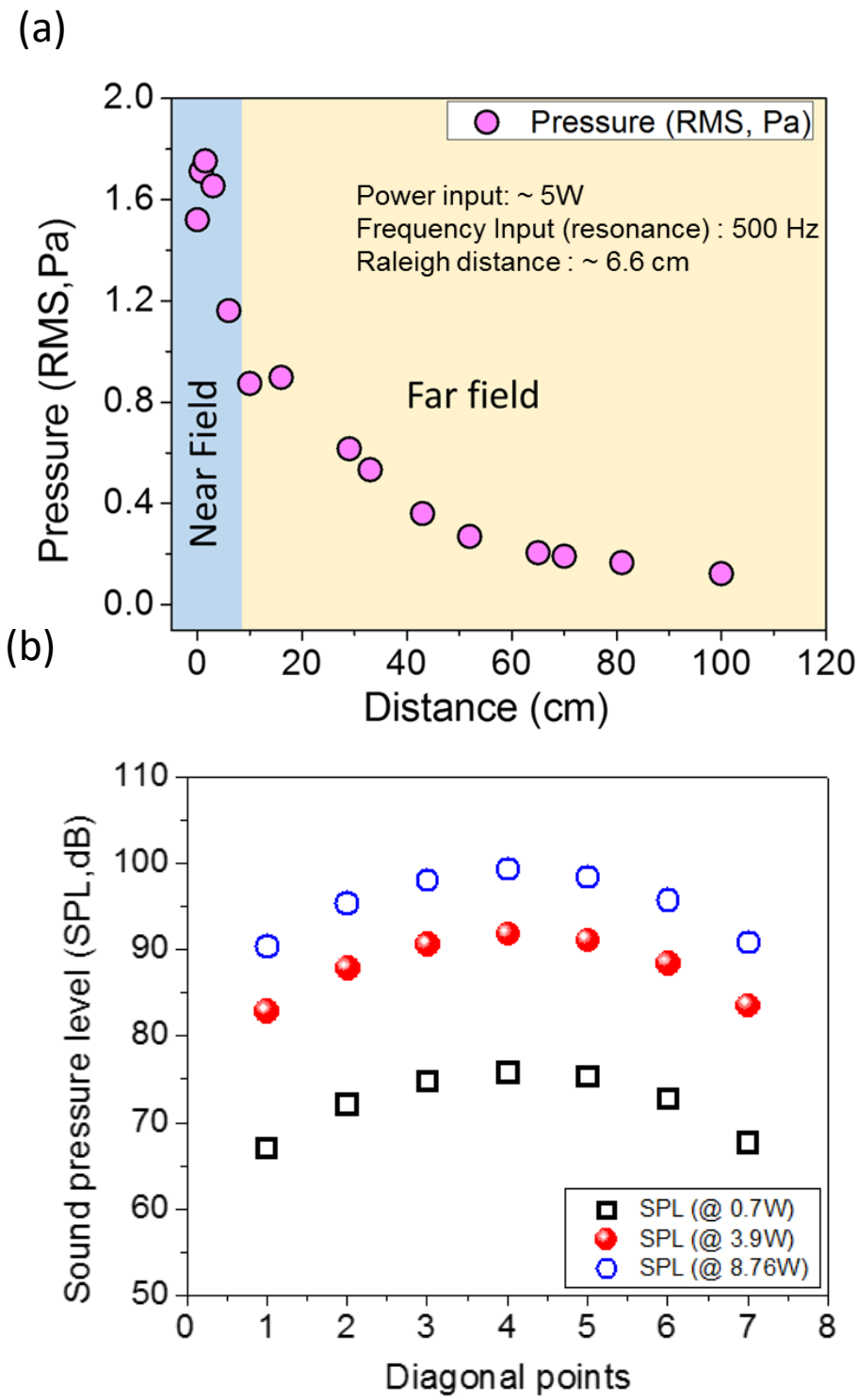

Figure 6: (a) Pressure vs distance for device 1, (b) Pressure across the diagonal points of device 1 at different power

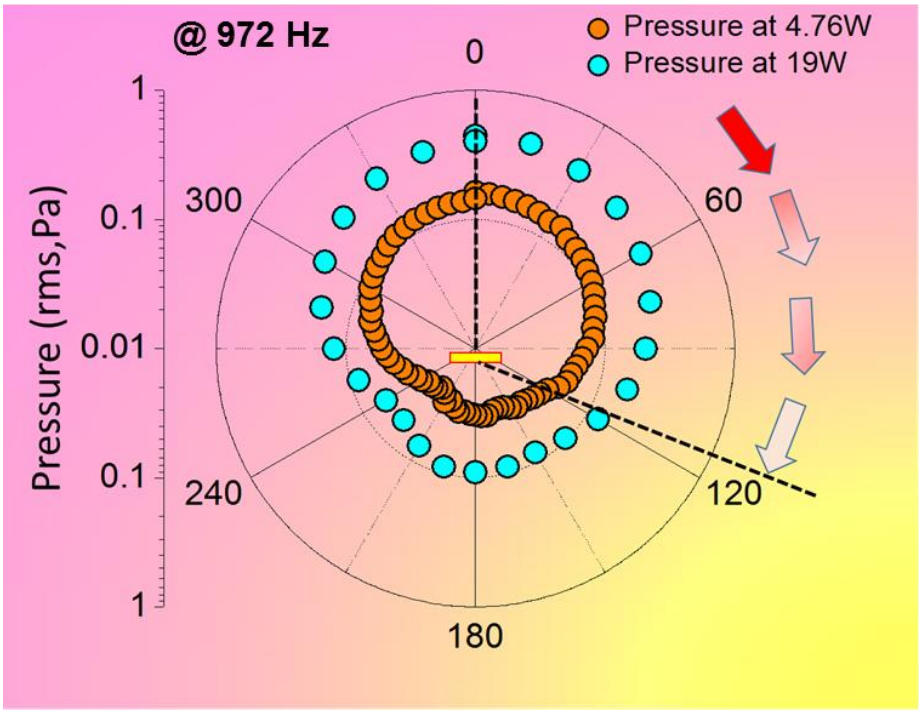

Figure 7: Directivity of device 1 at two different power input.

Next, acoustic measurements were conducted at the 2nd peak frequency for a range of parameters. Figure 5 shows the acoustic pressure at 3 cm standoff from the device at different average power input. The device shows a linear trend with increasing input power. However, to the higher power, a non-linearity is observed because of excessive heat generation in the small encapsulated chamber. To avoid excessive heating of the device we used a large aluminum plate as the bottom plate (for heat dissipation) but still, this was effective up to lower power only. Figure 6(a) shows the acoustic pressure with variable distance. Pressure in the near field (approximately up to Raleigh Distance (RD)-surface area/wavelength of the sound wave, 6.6 cm) was random, but on increasing the distance it followed a trend of approximately -6 dB per doubling in distance. It is also observed from the experiment that while scanning different points across the diagonal (Figure 6(b)), the pressure first increased and then decreased. This shows the symmetry with respect to the central line which is similar to the mode shape obtained. All experiments in air successfully demonstrate the low-frequency operation (580 and 972 Hz) of the fabricated device. Clearly, here we show the acoustic generation by resonant

behavior at low frequency. A large gain in acoustic pressure due to a mechanical quality factor (Q), shows the merits of an encapsulation resonance over an open device for low-frequency applications. Further, we measured the directivity of device#1. At ~486 Hz (half of the 2nd peak frequency) we gave the sinusoidal voltage to the device and measured the sound pressure (which was at 972 Hz) by rotating 360 ^{o}. In this experiment, the bottom plate was fixed, and only the top plate was allowed to radiate the sound. Figure 7 shows the directivity of the device. It can be observed that mostly the device showed the uni-directional sound pattern. This figure could also be used to calculate the efficiency of the device.

After characterizing the device in air, experiments were set up for underwater testing. Figure 8(a) shows the results for water tank when hydrophone was placed at 3 cm above the device. As observed from the pressure-frequency response, the peak frequency for the setup was ~167 Hz. Similar behavior of frequency response observed for lowering the device inside the water for deferent depth (0,1 and 2 feet). The significant drop in resonance frequency in comparison to air can be best explained as the impact of water loading. Figure 8(b) shows the resonance mode shapes at 167 and 330 Hz. In contrast to the air medium, the first mode shape in water has a higher averaged velocity than the second mode. Figure 8(c) shows a comparison of the velocities along the x-axis for the 1st mode and 2nd mode of the device operating in air and in water. It is observed that in the first mode the velocity in water is slightly more than that in the air, but the opposite trend is observed in the second mode. This velocity behavior could be explained by the damping effect of the entrained gas in the device and the elastomer support at the edges of the device. In the next set of experiments, the relationship between input power and output pressure was developed under the water tank acoustic boundary conditions. Similar to the previous experiments, power input at half of the peak frequency was increased and pressure data was captured by the hydrophone. Figure 8(d) shows the results for output pressure as a function of input power. Under this acoustic boundary condition, generated pressure followed the linear path with lower input power and became non-linear at higher power. The saturation limit occurs because of increase in background temperature in the encapsulated chamber of the device at higher power input.

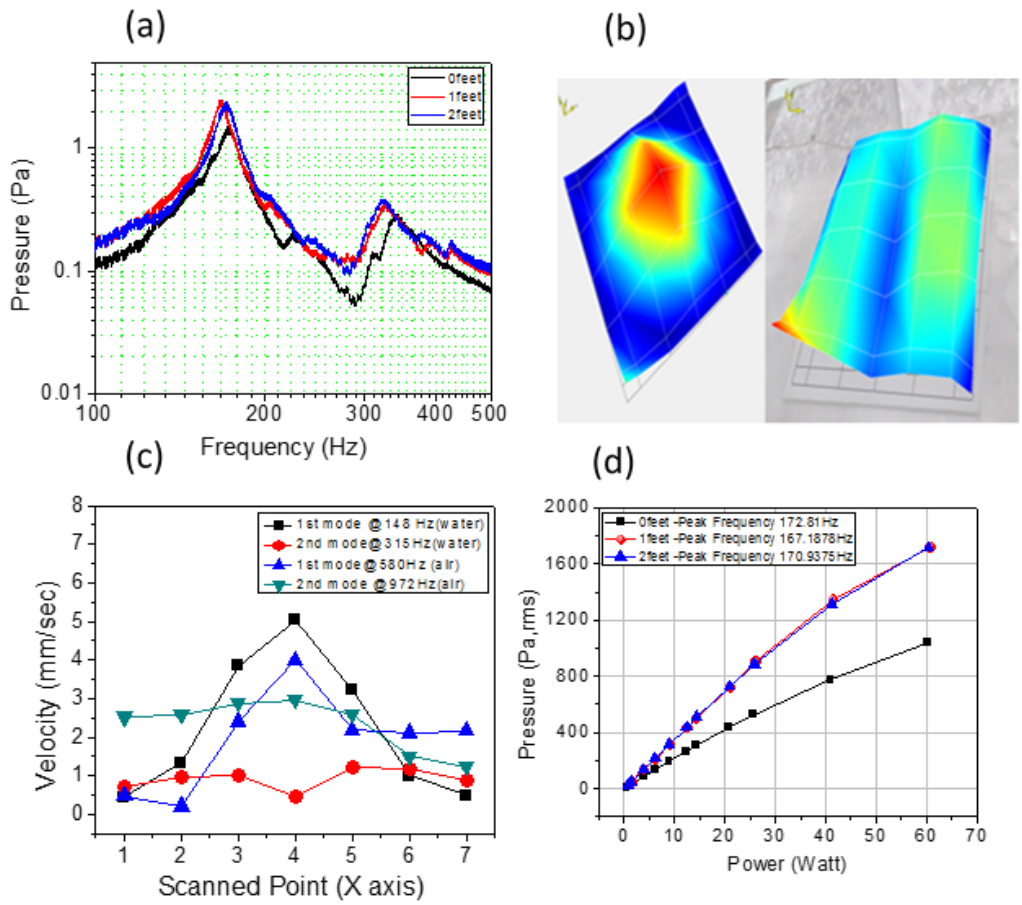

Figure 8: (a) Vibrational frequency response for device 1 in water, (b) mode shapes in water medium, (c) Velocity comparison of radiating plate in air and water, (d) measured sound pressure in water medium.

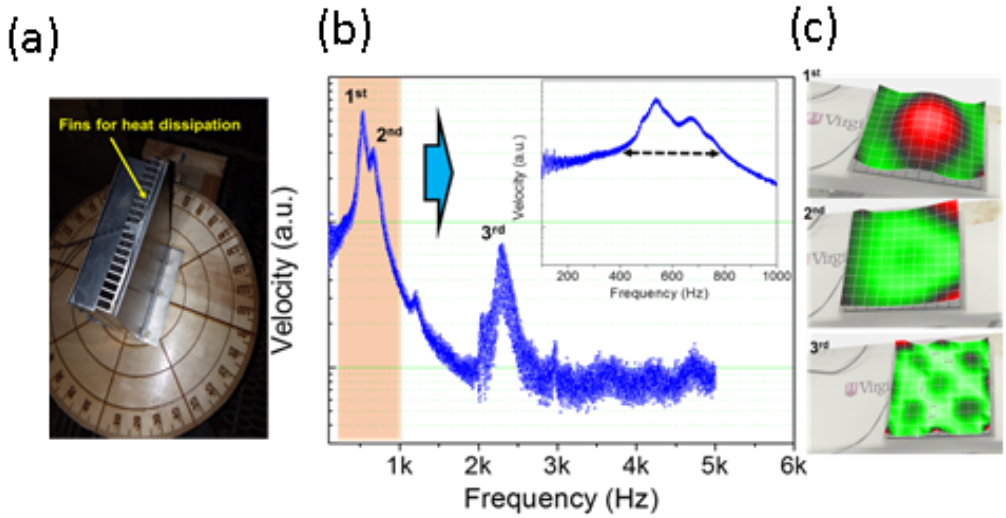

Figure 9: (a) Device 2, (b) Vibrational frequency response, (c) Mode shapes of device 2.

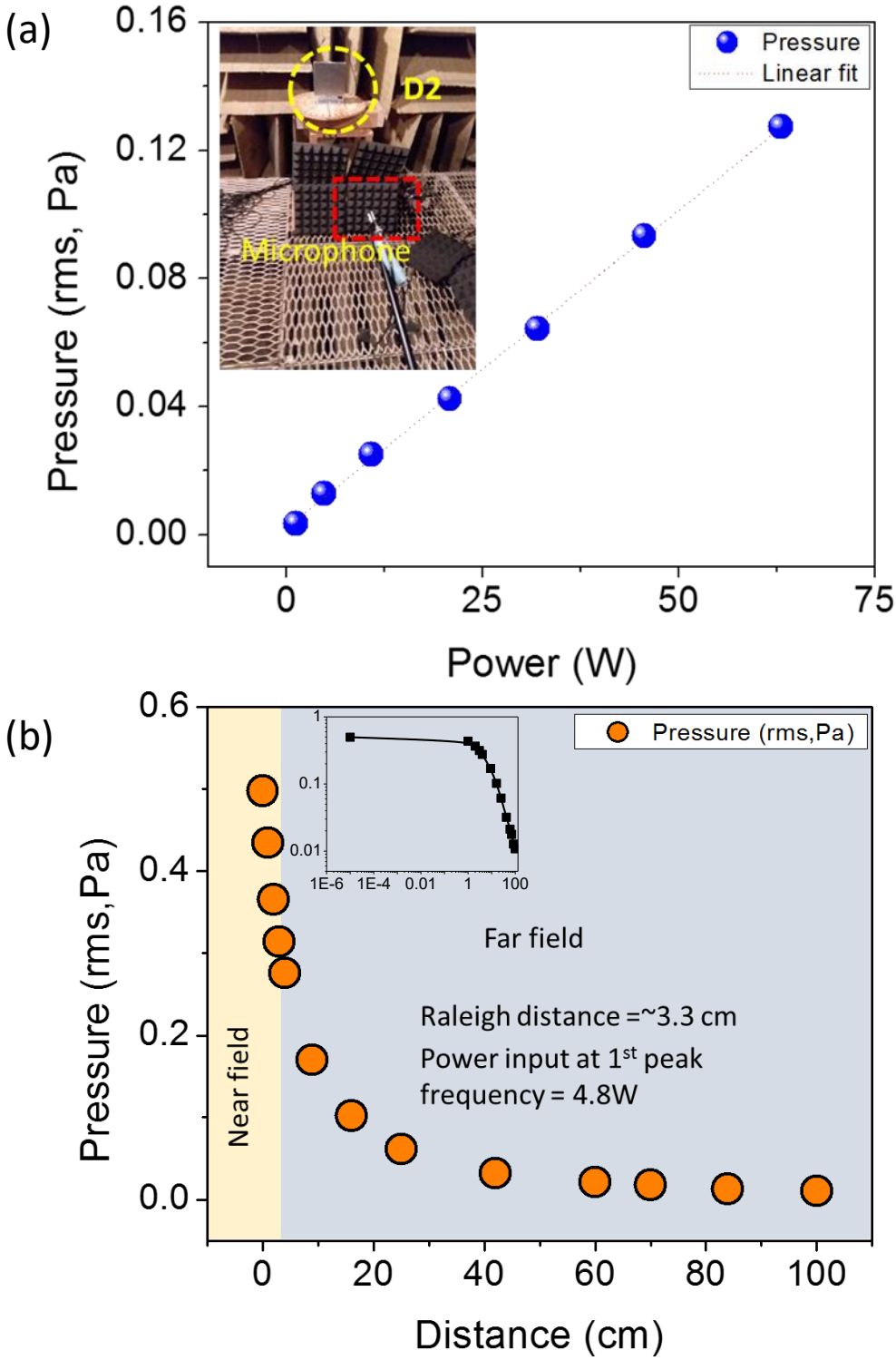

Figure 10: (a) Pressure vs power for device 2 in air medium, (b) Pressure vs distance for device 2 in air medium.

After characterizing the first device, here we provide some of the important results for the 2nd device which demonstrates the lower frequency of operation as well.

The experimental boundary conditions are similar to the conditions used for device#1 characterization. Figure 9(a) shows the device. As mentioned earlier, this device has fin structures. Below the fin, a heavy plate is used to suppress the vibration from the bottom plate. Figure 9(b) shows the frequency response of the device on giving the burst chirp input up to frequency 6000 Hz. From the frequency response of device#2, we observed that the 1st peak frequency has a higher response in the air than the 2nd peak frequency. This was reverse in device#1. The main reason for this reversal could be attributed to the use of heavy top plate for this device. First peak frequency is around 500 Hz. Although, other peak frequencies were also observed, however they were not very important for us in terms of acoustic generation. Figure 9(c) shows the first three mode shapes correspond to three peak frequencies. From these normalized mode shapes, we can clearly observe that 1st mode is pushing more volume of air with respect to other mode shapes, which help in the acoustic generation.

After the vibration analysis, acoustics experiments for this device under anechoic environment were performed. Figure 10(a) shows the power sweep and acoustic pressure (at 500 Hz). Interestingly, opposite to the previous device, we did not observe any non-linearity in device performance. This is because of the introduction of the fin structure at the bottom plate of the device. Fin structures helped in heat dissipation which kept the background temperature lower within the encapsulated chamber. We ran the experiments up to ~ 65 Watts average power, and sound pressure measured at 3 cm. Although, this device behaves linearly at higher power and performs at relatively lower frequency, the acoustic pressure output is less than that of the device #1. Inset image shows the experimental setups. Figure 10(b) shows the pressure variation of the device with respect to distance (up to 1m). Inset image shows the pressure vs distance in log scales. As this device operates at a lower frequency the near field for this system shrink to 3.3 cm (matching with Raleigh distance). After 3.3 cm, 1/r pressure decay has been observed. Since this device though demonstrate the lower frequency of operation (due to heavy

plates and thicker silicone boundary sealing), the acoustic performance was less compared to the device#1.

Conclusion

This study provides a comprehensive experimental characteristic of MWNT sheet based acoustic transducer targeting low-frequency response (< 1 kHz in air and < 180 Hz).. The key findings and demonstration of the experimental outcomes are listed below:

- Two LF transducers were fabricated and complete vibrational and acoustical characterizations were conducted to identify the operating frequency range. An operating frequency range of less than 180 Hz was obtained for transducer of dimension 6”x6’ and weight 160-190 gm. Tailoring the plate thickness and sealing could lower the working frequency to around 125 Hz in water.
- Our device shows a maximum output at its second resonance frequency (972 Hz) in air and at first resonance frequency in water (~170 Hz). In air, the maximum performance of device was 0.23 Pa/W and in water the performance was 28.7 Pa/W. It has been demonstrated that, with respect to open system transducer, encapsulation can provide a 10-12-fold acoustic pressure at resonance.
- Out transducer was found to exhibit stable operation over a long interval while operating at high power (~60W).

References

[1] Xiao L, Chen Z, Feng C, Liu L, Bai Z-Q, Wang Y, et al. Flexible, stretchable, transparent carbon nanotube thin film loudspeakers. Nano letters. 2008;8:4539-45.

[2] Aliev AE, Mayo NK, Jung de Andrade M, Robles RO, Fang S, Baughman RH, et al. Alternative nanostructures for thermophones. ACS nano. 2015;9:4743-56.

[3] Decarpigny J-N, Hamonic B, Wilson OB. The design of low frequency underwater acoustic projectors: present status and future trends. IEEE Journal of Oceanic Engineering. 1991;16:107-22.

[4] Dubus B, Mosbah P, Hartmann J-R, Garcin J. Ultra-low frequency underwater acoustic projectors: Present status and future trends. Proceedings of Meetings on Acoustics ICA2013: ASA; 2013. p. 030020.

[5] Aliev AE, Lima MD, Fang S, Baughman RH. Underwater sound generation using carbon nanotube projectors. Nano letters. 2010;10:2374-80.

[6] Aliev AE, Gartstein YN, Baughman RH. Increasing the efficiency of thermoacoustic carbon nanotube sound projectors. Nanotechnology. 2013;24:235501.

[7] Aliev AE, Mayo NK, Baughman RH, Avirovik D, Priya S, Zarnetske MR, et al. Thermoacoustic excitation of sonar projector plates by free-standing carbon nanotube sheets. Journal of Physics D: Applied Physics. 2014;47:355302.

Chapter 4

Carbon Nanotube Yarn Based Ocean Wave Energy Harvester

Abstract

Ocean waves are one of the most abundant renewable energy sources. In a recent discovery, carbon nanotube yarn (CNTY) harvesters have shown to be a promising pathway for converting kinetic energy directly into electrical energy. CNTY harvesters can electrochemically convert tensile energy to electricity. Here the implementation of CNTY harvesters in the ocean environment and quantify the performance under different wave characteristics such as amplitude and frequency has been demonstrated. In all the experiments either ocean water directly or a similar concentration of 0.6M NaCl have been used. Using only 0.5 mg of active material (42 times lighter than the average weight of house fly), the CNTY harvester produces power of .88 W/kg specific power when oscillated by water column at 0.5 Hz. The presented harvester is ultra-lightweight, non-corrosive, and a non-resonant system that can perform over a broad range of frequencies. The long stroke length and flexibility of the CNTY harvester allows integration with a mechanical frequency amplifier to translate the low frequency mechanical wave energy into high frequency electrical energy.

Keywords: Ocean waves, Carbon nanotube yarn, Energy harvesting

Introduction

In order to reduce dependence on fossil fuels and the carbon footprint in the environment, renewable energy sources such as solar, wind and hydro power are being developed [1-4]. However, there remains some limitations in scaling the deployment of renewables in terms of geography, cost and lifetime. For example, solar energy is available only during limited hours in a day and is dependent upon seasonal variations and altitudes. Similarly, there are operational constraints on wind energy and hydro power plants as they require considerable infrastructural development [5-8]. On the other hand, ocean wave (blue energy) has emerged as a promising source of renewable energy [9]. Almost two third of earth's surface is covered with ocean or other bodies of water, where, energy is available in the form of tides, waves, currents, thermal and salinity gradients [10, 11]. Approximately 7.4 x 10^{21} J of energy is available each year from the ocean in these different forms [10]. The low frequency water waves available in the deep ocean are attractive for energy scavenging, because of their continuous availability. However, there are challenges in converting low frequency mechanical energy to electrical energy due to technological limitations in the deep ocean [12]. Here, we provide a novel approach for wave energy harvesting using multiwall carbon nanotubes (MWNT) based yarns.

Ocean wave energy harvesting was envisioned long time ago [13], but not much progress has been made in its practical deployment. Ocean harvesters are generally divided into two broad categories: the more mature electromagnetic generator (EMG) based converters and emerging functional materials based technologies. A large number of attempts have been made in developing electromagnetic based wave energy converters (WEC) at small (generally prototype) and large scale [14-25]. Though electromagnetic WEC technology is widely used, it has many limitations. Wave oscillation in the ocean is random in nature and exists at low frequencies (< 0.1-5 Hz), where EMG doesn't work efficiently [12, 26]. Also, a large scale deployment of these technologies requires a supportive infrastructure development and huge maintenance costs [12, 20]. Alternatives to EMG based WECs are functional material based technologies. Dielectric elastomers harness electricity by converting a change in capacitance into electrical charge [27-30]. Triboelectric nanogenerators (TENG) convert mechanical energy directly in to electrical

energy [31]. Several architectures based on TENG have been proposed to provide suitable solutions to blue energy harvesting [11, 26, 32-37]. Recently, carbon nanotube yarn (CNTY) harvester was successfully used to demonstrate direct conversion of kinetic energy into electrical energy [38]. Inspired by this study, here we provide a systematic investigation on wave energy harvesting using MWNT based twisted and coiled yarns. This electrochemical conversion method relies on a change in capacitance to convert mechanical to electrical energy without any external biasing.

We fabricated several different types of MWNT yarns to understand the wave energy harvesting performance. An experimental setup was designed for harvester evaluation in either ocean water or 0.6 M sodium chloride (NaCl) solution. From the experiments conducted in this study, we demonstrate ~ 0.88 W/kg of specific power at the wave oscillations of 0.5 Hz. A novel mechanism is utilized for producing high frequency (20 to 40 Hz) electricity generation from relatively low frequency input wave oscillations. Interestingly, yarns were found to exhibit higher efficiency between 12 to 40 Hz input excitation [38]. The advantages of nanotube yarn are flexibility, simpler fabrication process, corrosion resistance, long stroke length, and wide bandwidth.

Experimental Method

1. Twisted and coiled yarn preparation and characterization

We fabricated twisted and coiled yarn from MWNT sheets drawn from CNT forests and layered on each other. The forests were grown through a chemical vapor deposition (CVD) method and the nanotube yarn was prepared using a cone spinning method. For evaluating various energy harvesting parameters, several yarns with different lengths and varying MWNT sheets were prepared. In the cone spinning method, layers of 5 cm wide MWNT sheets were placed on each other. To make the layered sheets stable, we used double sided carbon tape on the top and bottom for attaching both ends of the MWNT sheets. The total length of the stack was ~20 cm. After making the stack, we curved both ends of carbon tape simultaneously to achieve a cylindrical shape, which was then twisted to produce the yarn. Figure 1 shows the process of the yarn fabrication. Figure 1

(a) shows the cone spinning and symmetrical twisting across the central line during yarn fabrication. For this procedure, we used a tensile load of 30 g to generate sufficient spring stiffness in the coiled yarn. A total number of 655 turns were made to complete the coiling. Samples with 2 layer, 5 layer and 10 layers were fabricated for different experimental setups. We also prepared one sample of a Dual-Archimedean coil (Figure 1 (b)), in which the flat ends are twisted instead of a cylinder, to generate the yarn. The yarn morphology was observed using field-emission scanning electron microscopy (LEO 1550) and atomic force microscopy (Bruker nanoscope IV).

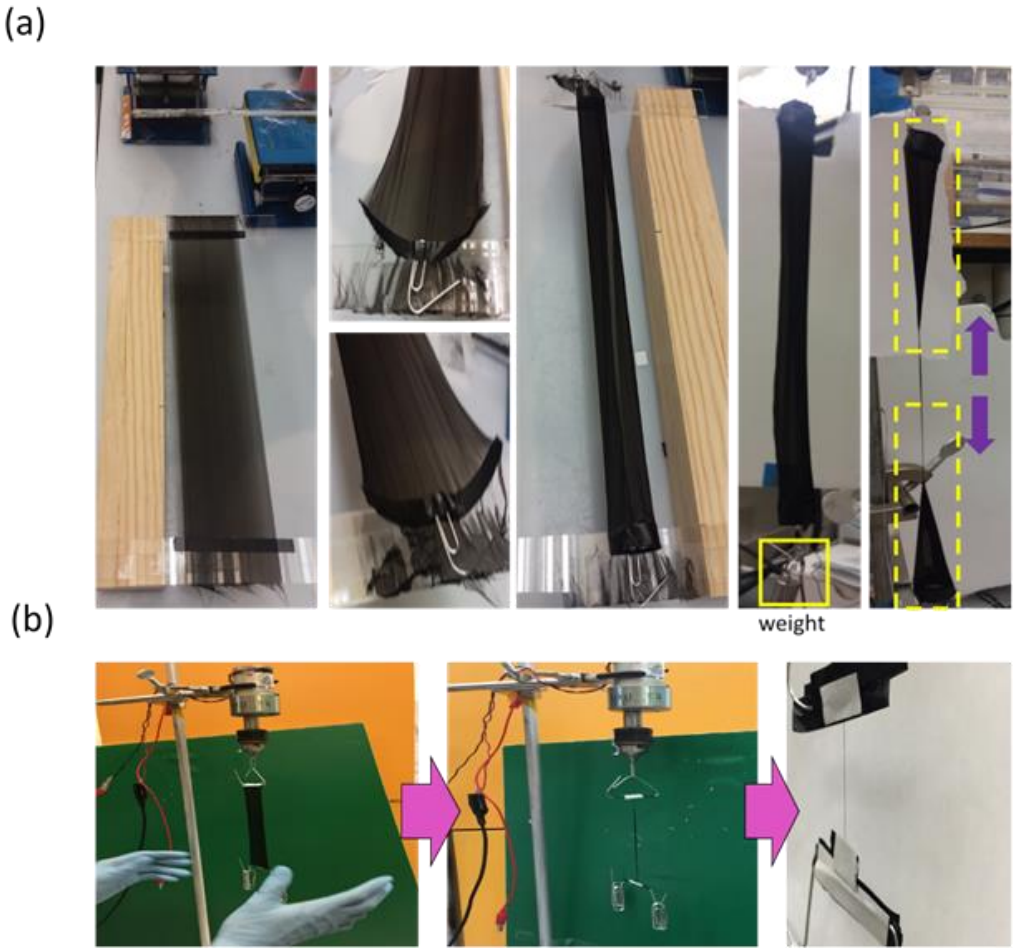

Figure 1: Yarn fabrication:(a) Cone spinning yarn fabrication, (b) dual-Archimedean yarn fabrication.

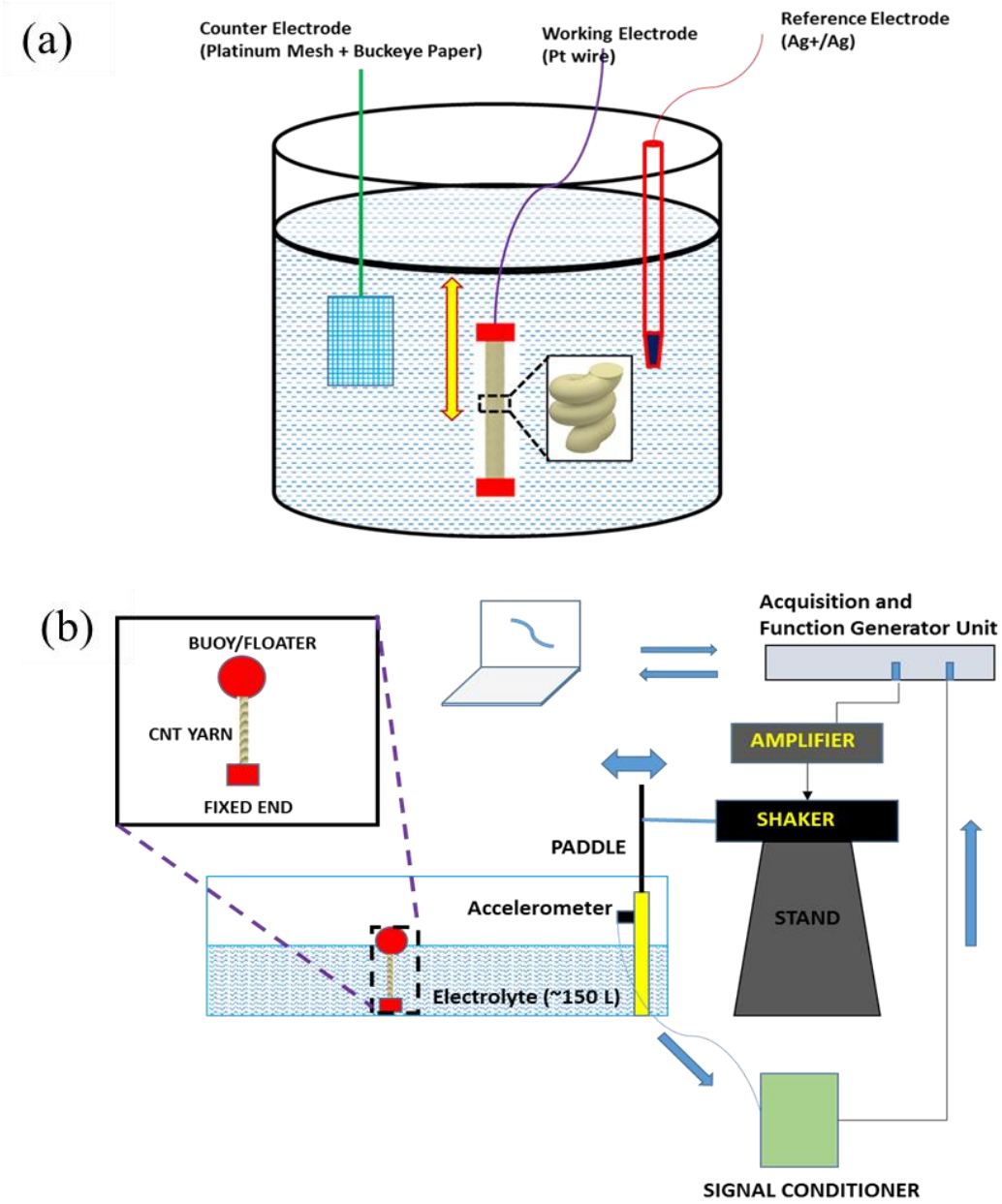

Figure 2: (a) Schematics showing the three-way electrode system for the experimental measurements. Yarn is designated as working electrodes, platinum mesh with buckypaper as counter electrodes and Ag/AgCl as a reference electrode. OCV was measured between working electrode and Ag/AgCl in all the experiments, (b) detailed schematics of experimental setup used for wave generation. Stable standing waves are generated for different amplitudes to characterize the MWNT harvester.

2. Experimental setups

Several different experimental setups were designed to characterize the performance of yarns in the ocean-like environmental conditions within the laboratory.

Tank and wave generator setup: A tank of dimension 48” x 18” x 20” was selected to generate standing waves for the systematic analysis. Figure 2 (b) shows the schematics of the experimental apparatus. For creating an artificial ocean environment, we prepared ~150 liters of electrolyte of 0.6M NaCl. The volume was optimized to obtain effective wave oscillations at low frequencies. A flat acrylic paddle was rigidly attached with shaker to push the water for developing the waves. A series of tests were performed to determine the amplitude and frequency of the shaker that generated wave without turbulence. A function generator (AFG3022C) was coupled with shaker (APS Electro-Seis) through an APS dual mode power amplifier (Model#114) for generating sinusoidal output. A PCB Piezotronics accelerometer (SN#30480) was mounted on the paddle to capture the dynamics. A PCB Piezotronics signal conditioner (Model#482A16) was used for conditioning the output signal from the accelerometer, and a digital oscilloscope (KEYSIGHT DSO1014A) was used to record the output voltage from the yarns. For this experiment, we used 10 layered thick yarn to withstand the wave force. The harvesting device was composed of a spherical float, the yarn and a rigid fixture attached to the bottom of the tank.

Small scale setup: A small scale box setup consisting of an 11cm column filled with electrolyte was designed to characterize the systematic response of MWNT yarns under heave motion. In this setup, we pushed a heavy plunger block down to oscillate the water vertically at different frequencies. A rectangular box shaped float attached to the yarn allowed free movement under the heave motion. The other end of the yarn was attached to a magnetic slider, which was controlled by a permanent magnet mounted outside of the apparatus. For the electrolyte, 0.6M of NaCl, TOPFIN Seawater and 0.1M HCL solution were evaluated.

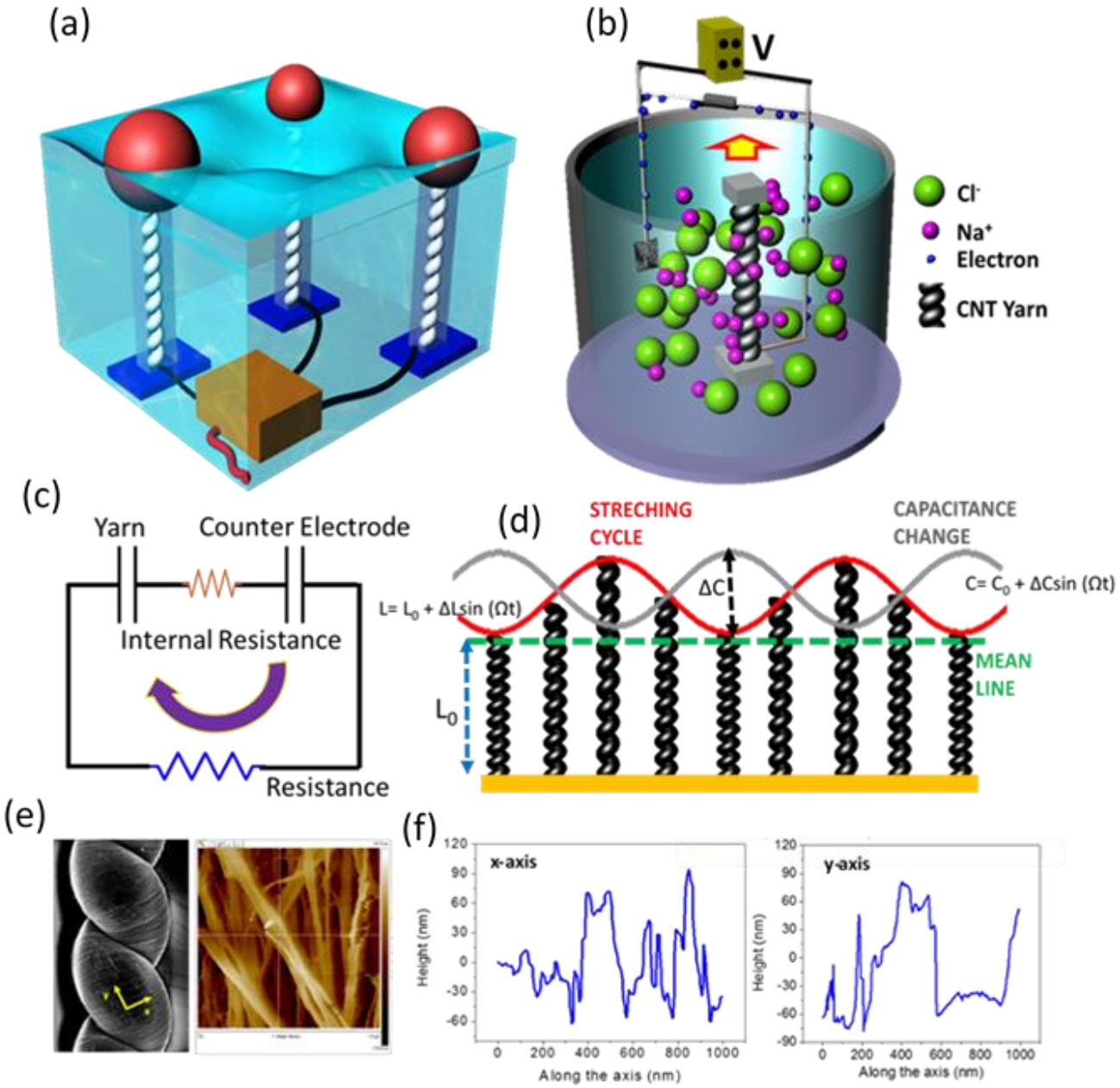

Figure 3: (a) Schematic showing the yarn-buoy configuration in ocean wave, (b) schematic showing the CNT yarn harvester in NaCl electrolyte, (c) equivalent electrical circuit diagram for CNT yarn energy harvester, (d) schematic showing the correlation of yarn stretching under wave and the capacitance change, (e) SEM and AFM images showing the surface morphology of yarn, (f) the height profiles across and along the thread of the CNT yarn (x-axis and y-axis shown in Fig. 1(e)).

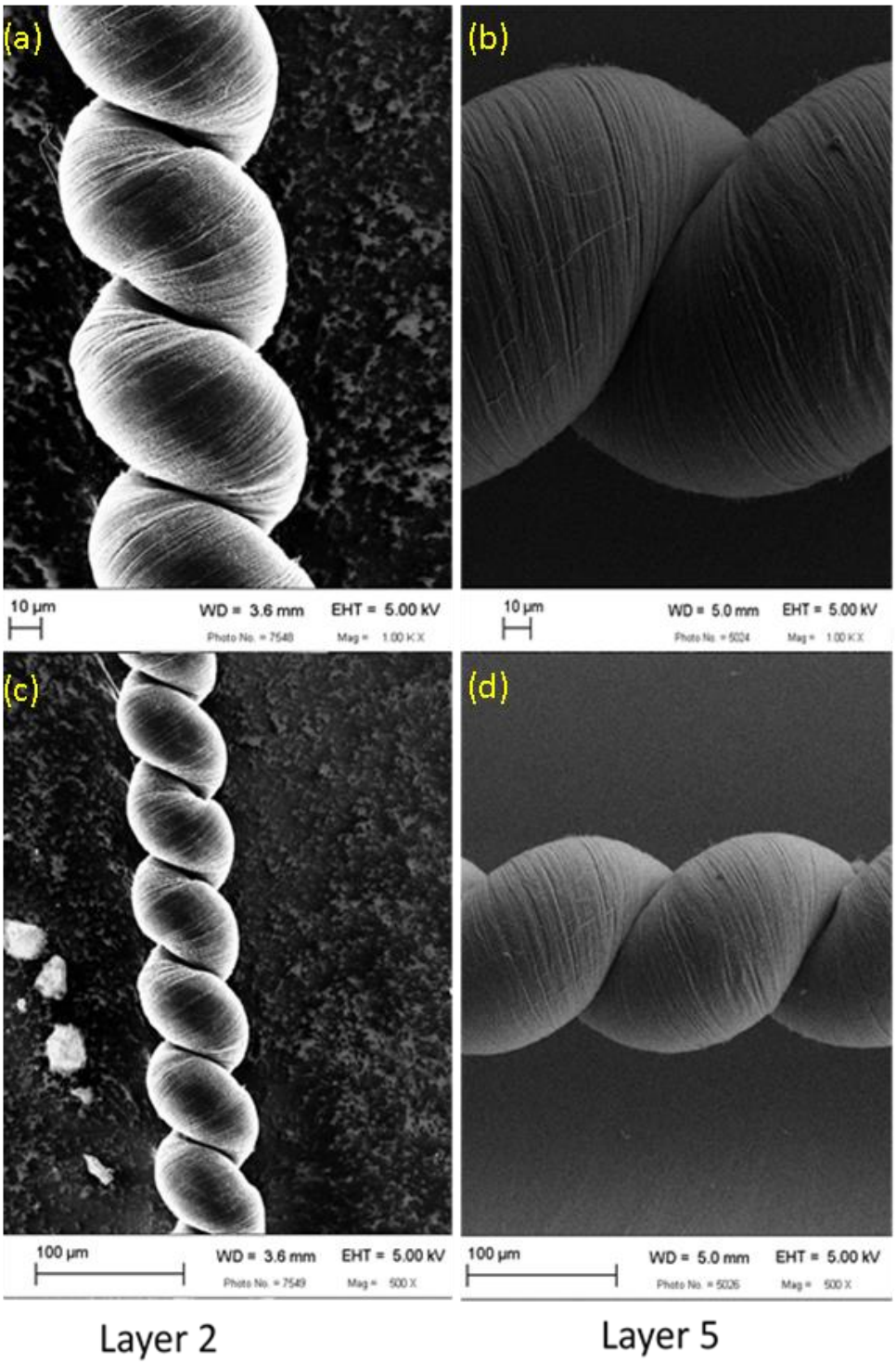

Figure 4: SEM images of 2 layer and 5-layer yarn: (a) and (c) 2-layer yarn, (b) and (d) 5-layer yarn.

Acoustic measurements: To demonstrate the potential for a direct-energy source, the load of a small 3300 Hz PZT transducer was used. A PSV-500 scanning vibrometer was then used for characterizing the vibration dynamics of the acoustic source.

Results and discussion

Figure 3(a) shows the schematic of CNTY based energy harvester with three long coiled yarns attached with buoy. Figure 3(b) represents the electrochemical aspects of our energy harvester, where a yarn (working electrode) is dipped in NaCl aqueous solution having Na^+ and Cl^- ions along with meshed platinum containing buckypaper (counter electrode). Under varying mechanical input, the changing length of the yarn in the electrolyte results in the potential difference. For simplicity, the yarn and counter electrode are represented as a capacitor in the circuit diagram (Figure 3(c)). These two electrochemical double layer electrodes were connected through internal resistance (provided by electrolyte) and external resistance. Figure 3(d) briefly shows different stages of yarn's pulling and releasing during operation. The maximum stretching of the coiled yarn resulted in minimum capacitance. The dynamic behavior of yarn's length (L) and capacitance (C) can be illustrated by eq (1) and eq (2) as:

$$L = L_o + \Delta L \,\mathrm{Sin}(\Omega t) \tag{1}$$

$$C = C_o - \Delta C \,\mathrm{Sin}(\Omega t) \tag{2}$$

where L_o gives initial yarn length, ΔL is change in yarn length, Ω is the stretching frequency, C_o is initial yarn capacitance and ΔC is change in capacitance. A mechanical input to the yarn in the form of sinusoidal pulling and releasing results the sinusoidal capacitance changes in yarn. This change in capacitance causes the voltage oscillation between two electrodes and generates current through an external resistance. It is worthwhile to mention that energy output may significantly depend on quality and morphology of the yarn. Therefore, in order to investigate the quality of our fabricated yarn we conducted the scanning electron microscopy (SEM) and atomic force microscopy (AFM) experiments. Figure 3(e) shows the SEM and AFM images of one of the cone spun 5-layer yarn. The SEM micrographs (Figure 3(e) and Figure 4) clearly show nice coiling of the yarn without any visible defect. Surface morphology of the CNT yarn was further analyzed by AFM with tapping mode scan. The scanning was performed

in 1 µm × 1 µm area, and the height profiles were collected across and along the thread of the CNT yarn.

In AFM topography, we can observe the individual thin fibers of the CNT yarn, which was also elucidated in SEM image in Figure 5. Figure 3(f) shows the height variation across two directions (x- axis and y-axis) as indicated in SEM image of Fig. 1(e). From the height variation and AFM topographic image we observed that the height variation along the x- axis is more than that along the y-axis.

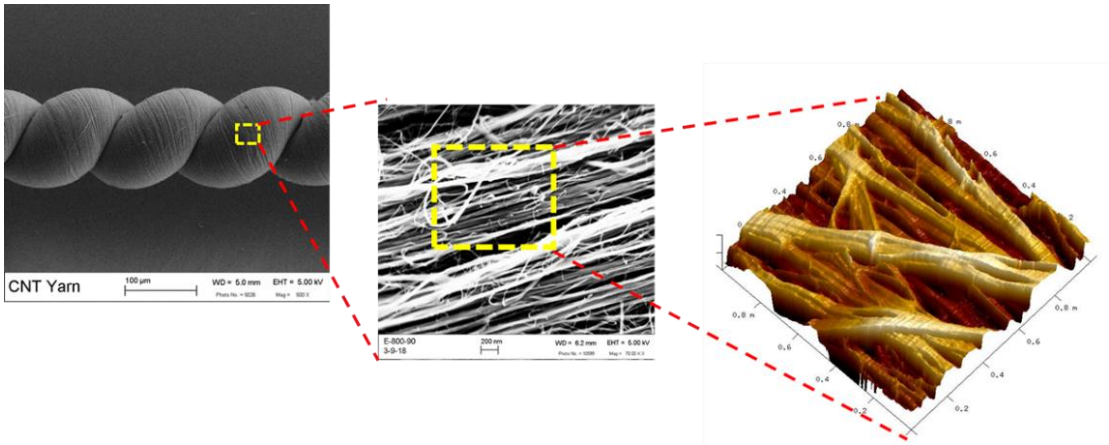

Figure 5: SEM and AFM image of 5-layer CNT yarn.

Low frequency oscillatory motion available in the ocean environment can be efficiently harvested using MWNT yarns to generate electricity. Before starting the wave motion test, we characterized a 5-layer yarn in the small scale setup, under controlled movement. In this study, we pulled the yarn with a certain stroke length input to provide a predefined strain. Previously, we have demonstrated that the voltage output could be highly dependent on the developed strain [38]. The controlled experiments performed in present work, helped us to evaluate the maximum output performance from the yarn based harvester. We further used controlled yarn stretching to evaluate the open circuit voltage (OCV) under wave oscillation induced strain.

Figure 6(a) shows results of a cyclic voltammetry test at 0% strain, between 0.3 to 0.6V for a 5-layer yarn working electrode and Ag/AgCl reference electrode. This test was used to understand the electrode capacitance. We started the electrical characterization by

measuring the OCV voltage with respect to the Ag/AgCl of a 2.14 cm long yarn under 10% of strain. We further applied the same strain at various frequencies in the range of 0.10 - 1.0 Hz. Here, we focused our study only on the low frequency regime to demonstrate the feasibility of the ocean wave energy harvesting. At 10% strain, the CNT yarn was found to result 14 mV of OCV, as shown in Figure 6(b). It can be observed from these results that the voltage output remains constant with increasing frequency in the range of 0.10 – 1.0 Hz, indicating its frequency independent behavior. Next, we stretched the yarn with different strain values over the range of 15-35%, and measured a systematic linear increase up to a maximum OCV of 48 mV, as shown in Figure 6(d). Based on these experimental results, an empirical expression was developed to demonstrate yarn's strain vs OCV, as shown by (eq 3):

$$V = (1.3314)S(\%) + 0.8 \tag{3}$$

The strain value was limited to 35% in order to avoid any damage to the yarn. We also measured the short circuit current (SCC) generated using the yarn, which was found to increase with increasing frequency at a fixed strain input, as shown in Figure 6(c). The specific peak to peak SCC was found to increase from ~208 A/kg to 675 A/kg with increasing frequency over the range of 0.1-1 Hz at 35% strain. The weight of the yarn used in this experiment was 0.5 mg.

Building upon the empirical relationship of OCV (independent of yarn's weight), a systematic modeling and experiments were performed to reveal the theoretical and experimental correlation between the amplitude of the wave (generated in lab environment) and OCV from the yarn in 0.6M NaCl electrolyte solution. Firstly, we provide the dynamic modeling of buoy under the influence of incident standing wave [15]. Figure 7(a) shows the schematic of harvesting system and the associated forcing functions. Due to small wave amplitude to wavelength ratio the disturbance/radiation from the buoy was neglected. Modeling was performed in two steps. In the first step, fluid forces on the surface of the buoy were investigated to understand the dynamic behavior of spherical buoy, and in the second step, base excitation induced vibration approach was used. The condition of the unattached (to the twisted yarn) buoy was

initially studied to understand the effect of damping, added mass and other hydrodynamic forces. Figure 7(b) shows the dynamic motion of the buoy without yarn attached to it. This graph is used to validate the experimental data obtained separately for spherical buoy movement under wave, and to investigate the broader damping effects (including hydrodynamic non linearity, added mass and skin friction effects etc. of the sphere in the oscillation mode). This step can reduce one variable ('c', damping) in modeling equations. Thus, the yarn will have spring constant as only variable under stretching. Mathematical modeling for ocean harvesting is shown in next section.

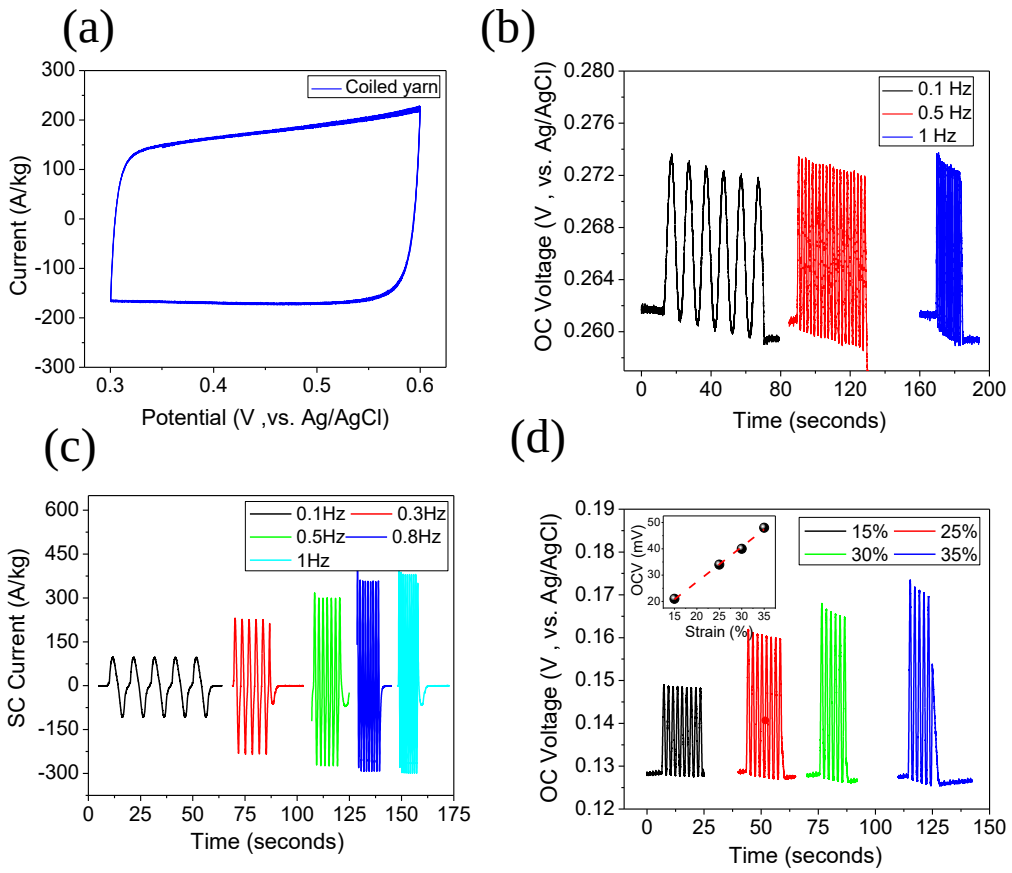

Figure 6: 5 layered MWNT yarn harvester characterization by stretching: (a) Cyclic voltammetry curve for the un-stretched yarn, (b) peak-peak OCV for different frequencies at fixed stretching of 10% strain, (c) frequency dependent SCC at fixed stretching of 35% strain, (d) OCV at different strain at fixed frequency of 0.5 Hz. Inset image shows the strain vs OCV generated. A perfect linear trend observed.

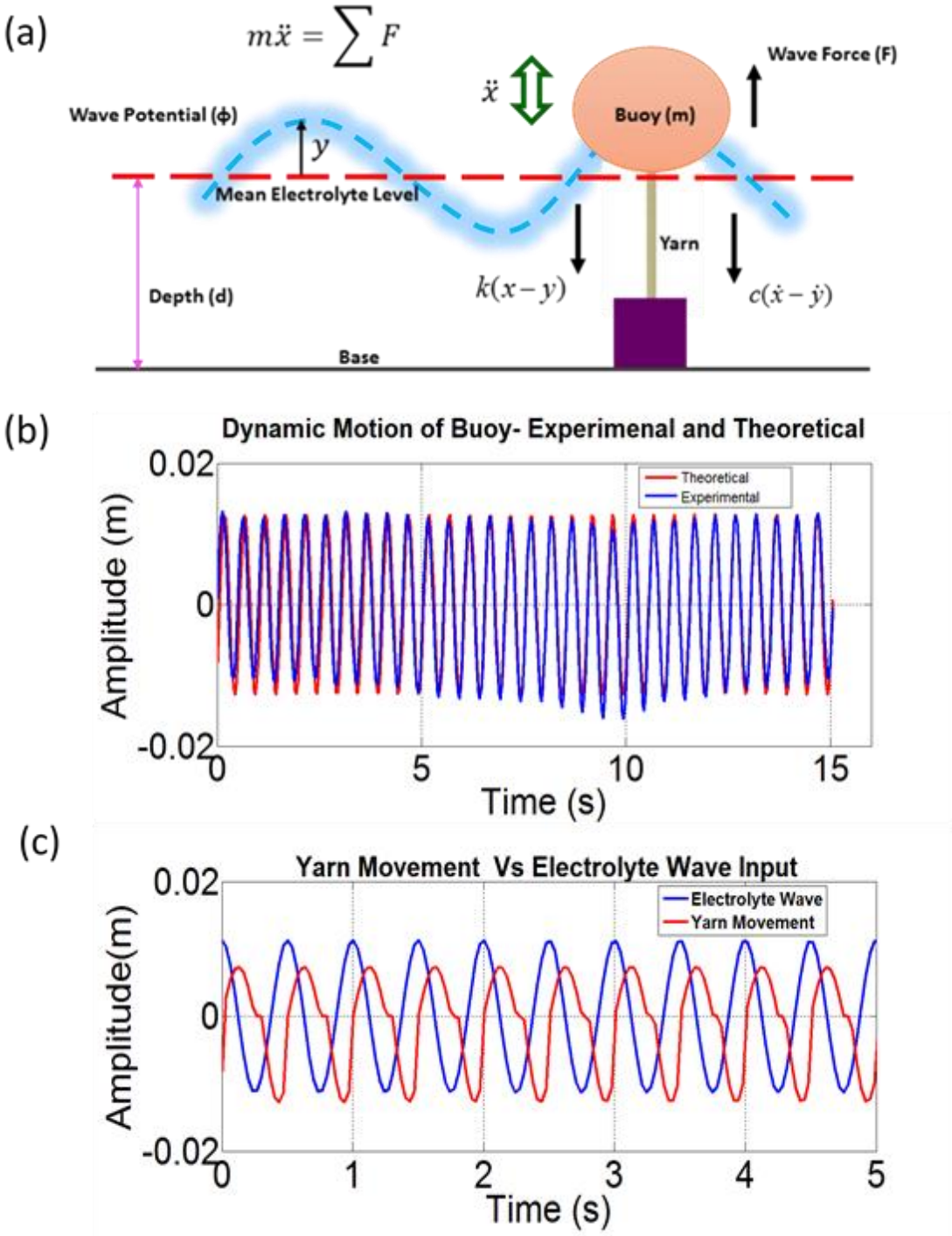

Figure 7: Modeling results :(a) Schematic showing forces acting during wave motion, (b) Experimental and modeling of float and evaluation of broader damping coefficient (c= 5), (c) Electrolyte wave and yarn dynamics comparison.

Modeling and empirical development

Wave potential for standing wave is given as:

$$\phi_I = \frac{gY}{\omega}[\frac{\cosh k(d+z)}{\cosh kd}]\cos kx \cos \omega t \tag{4}$$

Vertical force by this incident wave is represented as:

$$F = -\rho \iint \frac{\partial \phi_I}{\partial t} dS \tag{5}$$

$$F = \frac{2\pi\rho g Y R^2}{\cosh(kd)} \int_0^{\theta} (\cosh k(d - t + R - R\cos\theta) \sin\theta \cos\theta d\theta \tag{6}$$

On evaluating Eqn. (6) in MATHEMATICA, we can find the incident wave force acting on the buoy.

Using the value of force in the vibration equation below results in Eqn. (7):

$$\ddot{x} + \frac{c}{m}\dot{x} + (\frac{k1 + \rho Ag}{m})x = (\frac{F + \rho AgY}{m})\cos\omega t + \frac{cY\omega}{m}\sin\omega t \tag{7}$$

Yarn stretching equation (buoy movement):

$$X = ((\frac{F + \rho AgY}{m})/T)\cos(\omega t - \theta_1) + (\frac{cY\omega}{m}/T)\sin(\omega t - \theta_1) \tag{8}$$

In the final form of the equation it has been considered that when X <0 then $k1$=0 for snarling condition. Parameters A and B are defined as:

$$A = (\frac{F + \rho AgY}{m})/T \quad \text{And} \quad B = \frac{cY\omega}{m}/T \tag{9}$$

Some other constants used in evaluating final form of equation are defined as:

$$k_{eq} = (\frac{k1 + \rho AgY}{m}), \quad \xi = \frac{c}{2\sqrt{mk_{eq}}} \quad \text{and} \quad \omega_n = \sqrt{\frac{k_{eq}}{m}} \tag{10}$$

$$\text{T} = \sqrt{(\omega^2{}_n - \omega^2)^2 + (2\xi\omega\omega_n)^2} \tag{11}$$

where d is the depth of the tank, z is the distance of the points from the surface, R is the radius of the sphere buoy, t is the depth of buoy submerged in fluid, Y is the input wave amplitude, g is the acceleration due to gravity, ω is the driving frequency in radians, ω_n is the natural frequency, F is the incident force by wave potential, ρ is the density of fluid,

A is the cross-section areas submerged in fluid, m is mass of buoy, c is damping and other hydrodynamic coefficient, and θ_1 is the phase angle.

Mechanical to electrical conversion

After completing the force analysis in fluid environment, a simple time variable steady state equation is proposed for the float movement or yarn stretching. Equation (12) shows the superposition of two linear waves:

$$X_p = A\cos(\omega t - \theta_1) + B\sin(\omega t - \theta_1) \tag{12}$$

Coefficients A and B are described above in the analysis, ω is wave frequency driving the CNT yarn harvester, θ_1 is the respective phase lag compared to the incident water standing wave. Maximum strain can be calculated from the above expression for any ω as:

$$S_{\max}(\%) = \frac{\sqrt{A^2 + B^2}}{l} \times 100 \tag{13}$$

S is strain developed and l is the original length of CNT yarn. The final goal of all the force and vibration analysis is to estimate the desired theoretical OCV values on giving strain as input. In order to understand the mechanical to electrical conversion, experimental data was analyzed and the empirical relationship between OCV as a function of strain at fixed frequency is developed by curve fitting as shown below:

$$V = (1.3314)S(\%) + 0.8 \tag{14}$$

where V is the *Open Circuit Voltage,* $S(\%)$ is the percentage *strain and* f is the *frequency of excitation*. Standing waves produced the strain in the yarn which resulted in change of its capacitance in electrolyte solution thereby providing the voltage output.

This illustrates that the wave input of different amplitude produced strains in CNT yarn (during stretching) which in turn produced overall peak to peak output voltages in 0.6M NaCl solution. The assumptions in the modeling included: no effect of diffraction and

radiation while sphere oscillation, steady state of the system, approximation of the CNT yarn mechanical properties, lumping all the damping, hydro elasticity and other factors into one constant 'c' which was estimated from the experimental data (equal to 5) **, l**inear wave theory was utilized, hydrodynamic non linearity was neglected during calculations**,** hydrostatic component in pressure is neglected, and lastly linear behavior of CNT yarn was assumed.

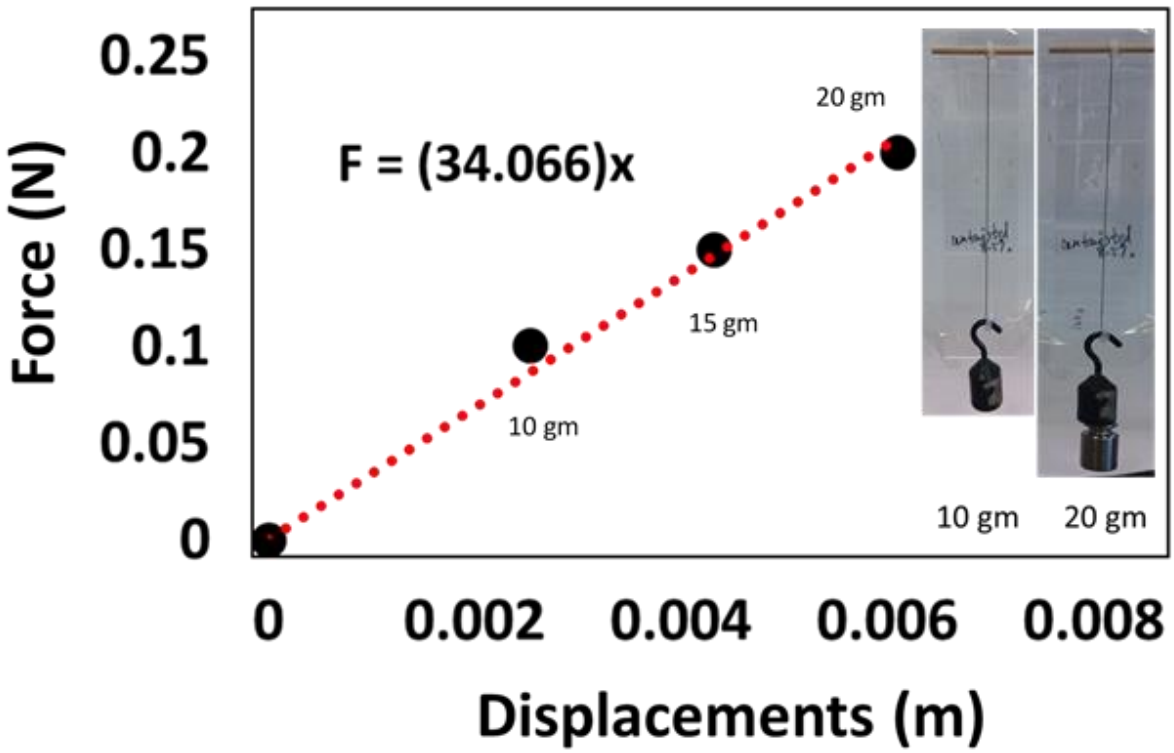

Figure 8 : Linear relation for calculating spring constant of 10 layer yarn.

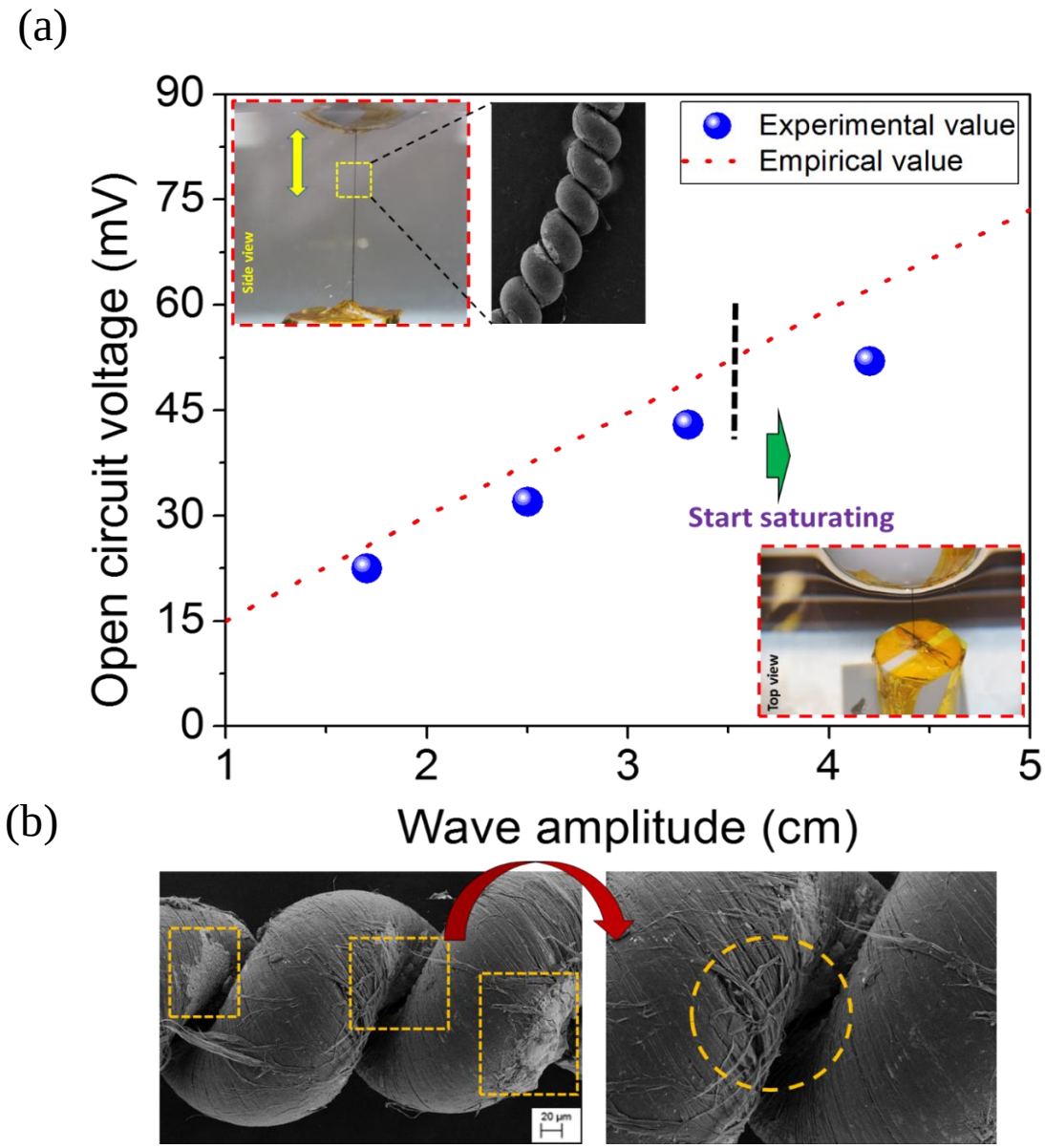

Figure 9: OCV generation in standing wave environment: (a) Wave modeling and empirical OCV comparison with experimental results at different wave input amplitude. In all the experiments frequency remain constant = 2 Hz. A dashed vertical line shown in the graph beyond which experimental OCV starts saturating. Inset images show the front/top views of the harvester and SEM image of yarn used, (b) SEM image taken after the yarn is utilized for harvesting. Dashed boxes shows the presence of NaCl particles at the junctions of coils. Another SEM image is the zoomed section, showing the wear and tear of the yarn after long use in wave environment (~ 6 hours).

Wave experiments

Solving the equations in MATLAB environment, Figure 7(c) shows the results of wave input to the harvesting system, and yarn stretching with stiffness ($k1$) ~ 35 N/m. Figure 8 shows the measured results for evaluating the stiffness constant for wave energy harvesting. The snarling effect of CNT yarn was taken into consideration by assuming the stiffness zero (no force), while, buoy was going down from mean electrolyte level. It can be observed from the results (Figure 7(c)) that there is a phase lag, and sinusoidal distortion between the input (standing wave) and output (float or yarn movement), resulting in possible phase lag between wave input and Open Circuit Voltage (OCV). Therefore, in our modeling approach, we used the wave amplitudes as an input (at fixed frequency of 2 Hz), and evaluated the strain developed in the yarn (for the given buoy). This strain was further used in the empirical formula to evaluate the final OCV voltage. Experiments were also performed under the same set of conditions, as used in modeling. The yarn length for the experiments was kept at ~7.5 cm. To withstand the fluid forces due to the wave oscillations, 10 layers of MWNT were used in yarn preparation.

Figure 9(a) shows a comparison of experimental measurements and the empirical expression for OCV. Inset shows the front/top views of the buoy attached with the yarn, and the SEM image of the yarn. We experimentally measured 52 mV OCV at a wave amplitude of 4.3 cm, and 22.5 mV at 1.7 cm. As can be seen from the Figure 9(a), the calculated OCV values overestimate the measured results. However, the results were in close agreement at lower amplitude of wave input. The model presented here considers only heave motion of the buoy, which was dominant factor even in experimental values at low wave heights. At higher wave amplitudes, obtained by pushing more water through paddle, turbulence was found to occur. The turbulence and enhanced hydrodynamic forces increased the rolling and pitching of the spherical buoy, thereby deviating from the expected linear trend in heave motion, consequently, the electrical output started to saturate. The other factors, which could cause deviation from the theoretical analysis, could be wall-effects, bending and torsional effects in the yarn, and electrolyte concentration (used in large volume here). Additionally, we performed an

experiment on a “dual-Archimedean” yarn for the ~2.5 cm of wave input, which resulted in OCV of 17.5 mV (Figure 10). With the same condition, cone spun yarn resulted in almost double output in comparison to the “dual-Archimedean” yarn. At 2.5 cm of wave input, the cone spun yarn yielded ~32 mV of OCV. The excellent performance of the cone spun yarn can be attributed to the uniform stress distribution [38]. During all the experiments, we tethered the top point of spherical buoy to avoid any untwisting of the yarn under wave influence. Figure 9(b) shows the SEM micrographs indicating the subtle changes in the local morphology of the yarn after ~6 hours of operation under strong wave forces. The NaCl particles were found to be accumulated at the junction of the coils, as seen in the SEM micrographs (Figure 9(b)). These results clearly show the robustness of our yarn based ocean energy harvester which is important for extended period of operation. Because the high wave amplitude was causing rolling and pitching motions, for next set of characterization, we used a smaller setup, where, only heave motion of buoy was achieved.

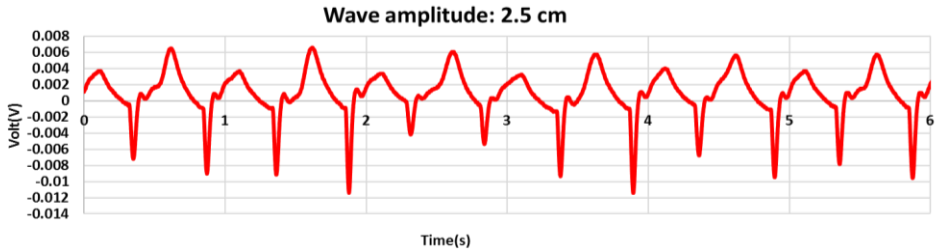

Figure 10: Voltage generation by Dual-Archimedean yarn in wave environment.

Figure 11(a) shows the side and front views of the small scale setup indicating the position of the clamp attaching the yarn and the float. This analysis was performed on the same yarn, which was used in the previous controlled stretching experiments. The 11 cm column of electrolyte was oscillated at different frequencies and amplitudes. Figure 11(b) shows the specific current at each frequency of water column oscillation displays a monotonically increasing value with frequency. At 0.1 Hz, the current was measured to be ~129 A/kg, which then increased to ~498 A/kg at 1 Hz. In this set of experiments, the electrolyte surface wave amplitude was maintained at ~ 1.54 cm for all the considered frequencies.

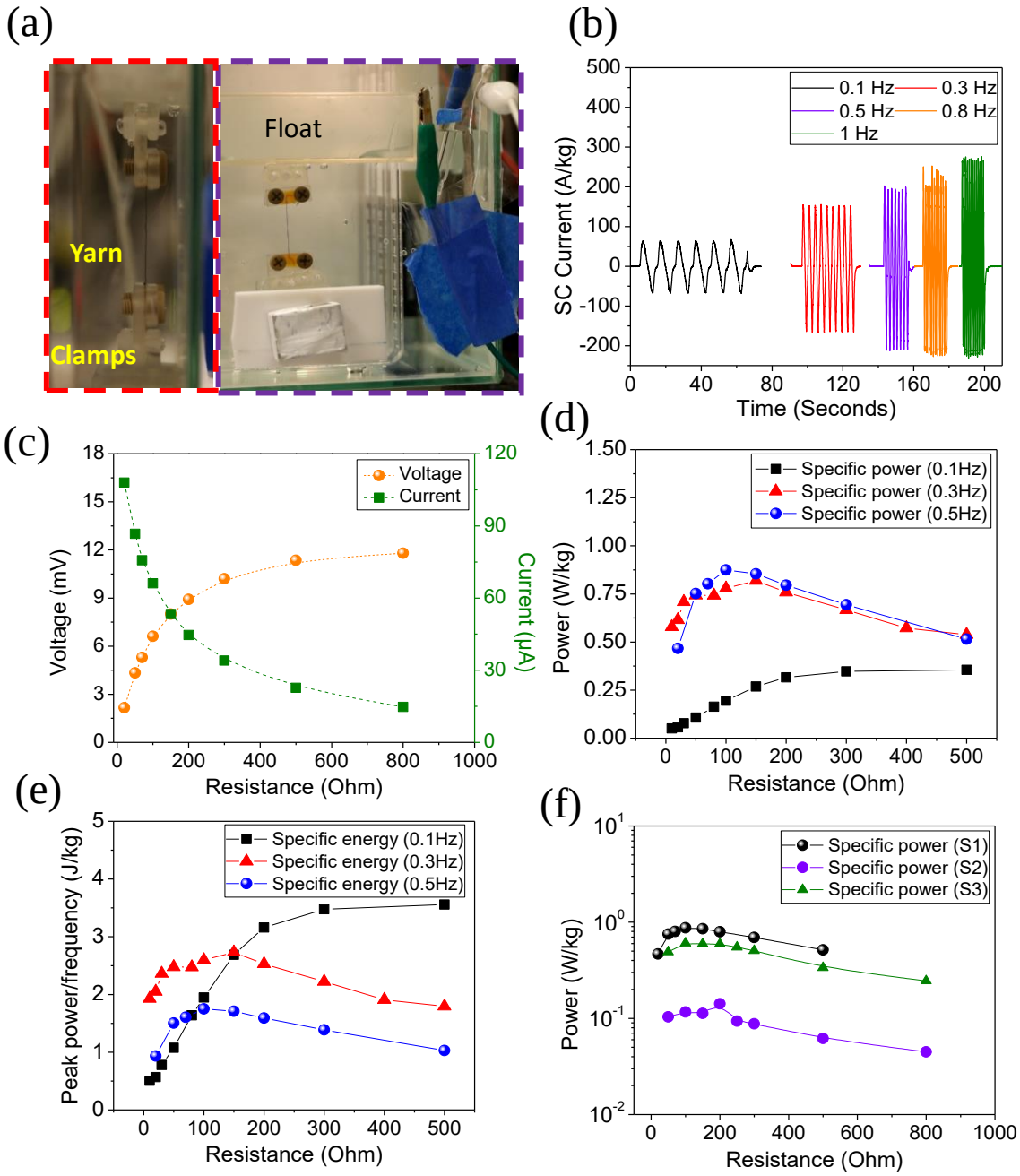

Figure 11: 5 layered MWNT yarn harvester characterization by water column oscillation: (a) Small scale setup for generating the heave motion of float, (b) frequency dependent SCC at fixed amplitude (1.54 cm), (c) voltage and current at variable resistances at 0.5 Hz frequency, (d) power generated from the harvester at different resistances and different frequencies, (e) specific energy (power normalized with frequency) across the variable resistance, (f) specific power at different resistances and wave amplitudes (S1= 1.54 cm, S2= 0.7 cm and S3= 1.23 cm).

Figure 11(c) shows the resistance sweep tests (0-800 Ω) at 0.5 Hz. The voltage was found to increase continuously up to saturation at the higher resistance values. At 800 Ω, the voltage was found to be ~12 mV. One expects a maximum power output at the optimum resistance value, which matches the impedance of the harvester.

We evaluated the power from the resistance sweep. Figure 11(d) shows the detailed results of power produced at frequencies of 0.1 Hz, 0.3 Hz and 0.5 Hz. The output power was found to increase with increasing frequency. From the power vs resistance results, we observed a change in optimal resistance. The optimal value of the resistance decreased to 100 Ω from 300 Ω with an increase in frequency from 0.1 Hz to 0.5 Hz. The maximum measured power at 0.5 Hz was found to be ~0.88 W/kg. Power values at frequencies 0.1 Hz and 0.3 Hz were found to be ~0.36 W/kg and ~0.82 W/kg, respectively. The specific energy per cycle, or power normalized with frequency, is shown in Figure 11(e). As expected, the maximum value of specific energy per cycle was observed at the lowest frequency of 0.1 Hz. Values of measured specific energy of ~ 3.56 J/kg, 2.73 J/kg and 1.75 J/kg were recorded at frequencies 0.1 Hz, 0.3 Hz and 0.5 Hz, respectively.

In next experimental study, we recorded the quantitative change in the peak power values at different amplitudes of the oscillating electrolyte column at fixed frequency of 0.5 Hz. Figure 11(f) shows the power results for different strains. We obtained maximum specific power (by resistance sweep) of 0.88 W/kg, 0.6061 W/kg and 0.1418 W/kg at amplitudes of 1.54 cm, 1.23 cm and 0.7 cm, respectively. The OCV generated with respect to different wave amplitude is shown in Figure 12.

In addition to the aforementioned experiments on 5-layer yarn devices, we also characterized the 2 layer yarns of length 1.67 cm and weight 0.168 mg in our small scale setup under electrolyte oscillation. Figure 13(a), (c) and (e) show the resulting OCV, SCC, specific power (at 0.5 Hz), and specific energy per cycle performance. At around 15% strain, power obtained was 0.48 W/kg at 400 Ω. Comparing the 2 layer and 5 layer harvesters, for a given frequency, the matching impedance decreased significantly with

the increase in number of layers. The 2-layer yarn experiments were also performed with 0.1M HCl as the electrolyte. In wave motion producing ~8-10 % strain in the yarn, the obtained OCV and SCC at 1 Hz were 54 mV and 2213 A/kg and power was 3.1 W/kg at 0.5 Hz, as shown in Figure 13(b), (d) and (f). These results clearly demonstrate the advantage of HCl electrolyte over ocean water. However, in this work we stress on the ocean wave harvesting for practical applications, and provide fundamental understanding of the harvester's behavior under varying wave conditions.

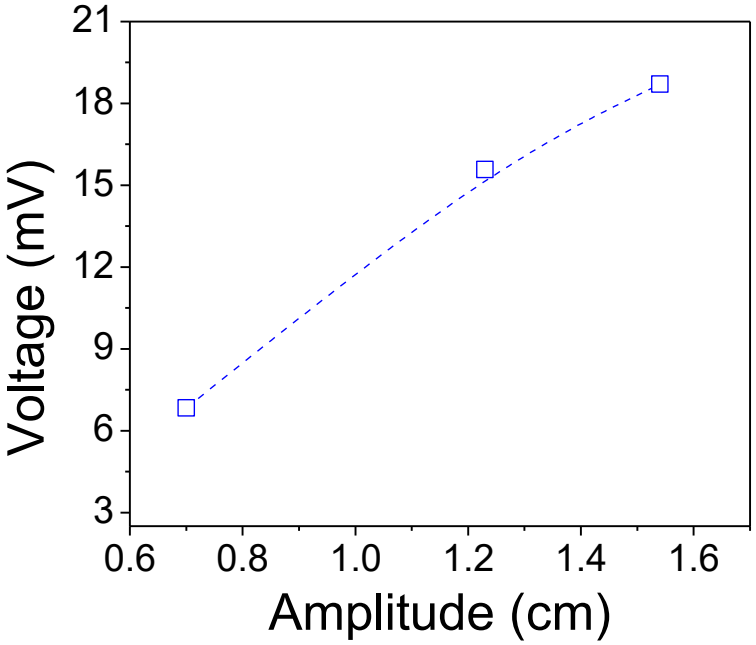

Figure 12: Voltage generation in small setup on different amplitude of water oscillation.

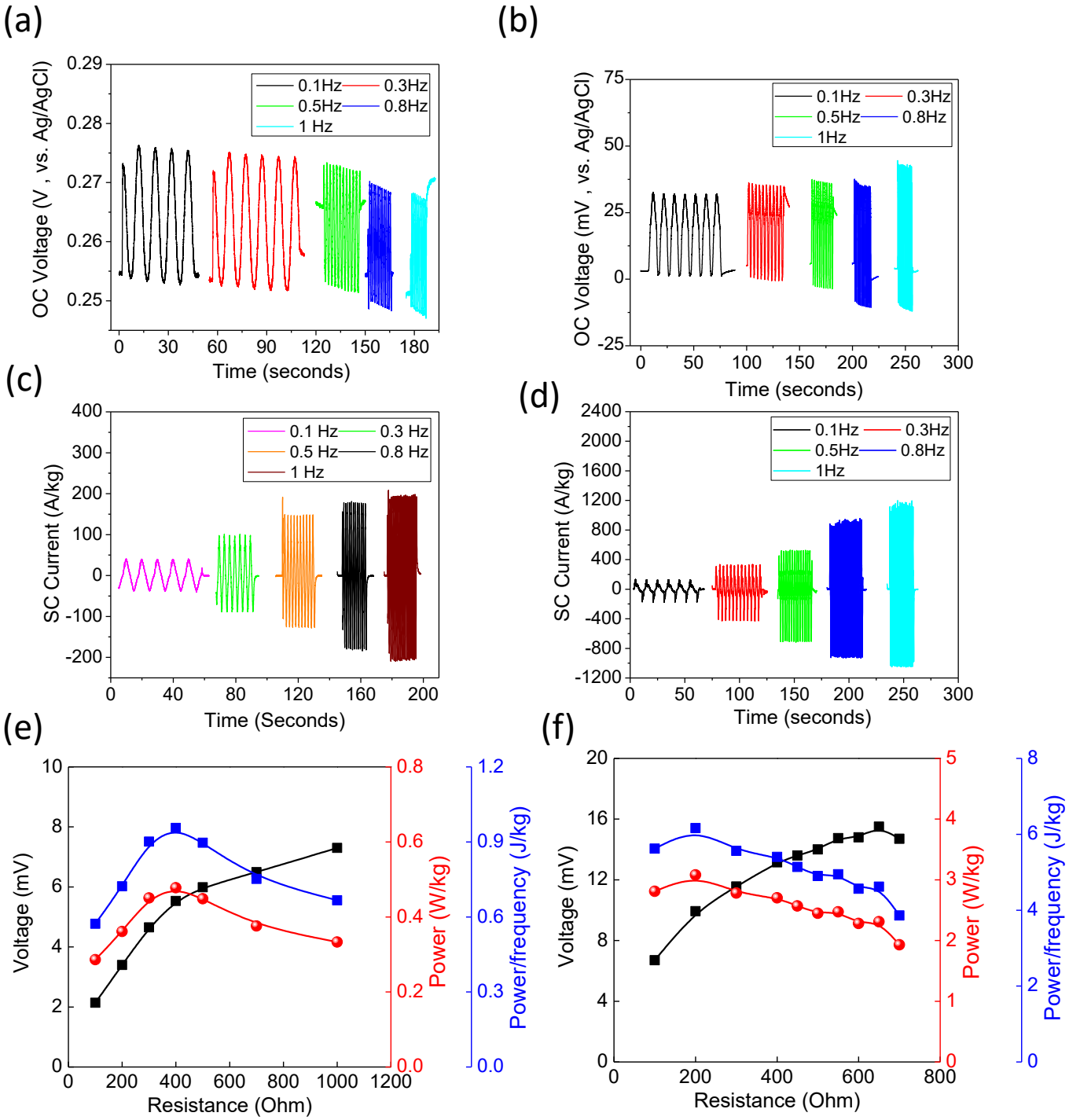

Figure 13: 2-layer yarn characterization in ocean water and 0.1M HCl solution: (a) OCV of yarn in ocean water at different frequencies, (b) OCV of yarn in 0.1M HCl at different frequencies, (c) SCC of yarn in ocean water, (d) SCC of yarn in 0.1M HCl, (e) specific power and energy in ocean water, (f) specific power and energy in 0.1M HCl.

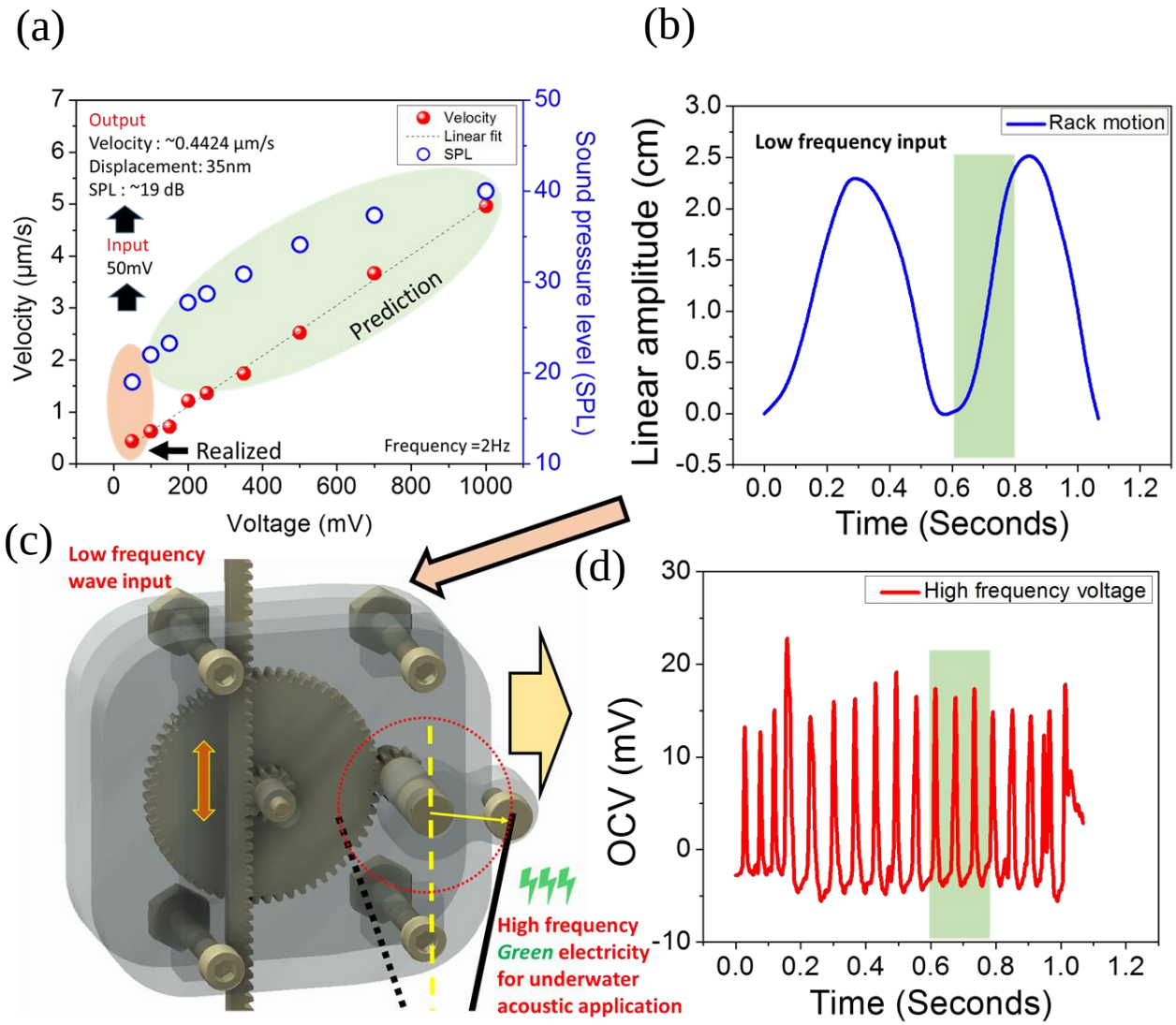

Figure 14: Potential application: Infrasound generation and mechanical amplification of frequency: (a) PZT transducer velocity and sound pressure level (SPL) at different input voltage at 2Hz frequency, (b) low frequency input from shaker (mimicking the water wave motion) to the frequency amplifier, (c) design showing the gear box which amplifies the wave frequency to produce electricity. Black thick line represents the yarn attached to the system, (d) high frequency OCV output on low frequency mechanical input.

Wave energy harvester demonstration

We demonstrated the response of the harvester under load by applying a small PZT piezoelectric transducer. A PSV-500 scanning vibrometer was then used for characterizing the vibration dynamics of the transducer. The equivalent voltage required to drive the transducer was generated from two yarn harvesters connected in series and driven by wave motion at 2Hz. The laser vibrometer measured the surface velocity of the transducer and the sound pressure level was calculated from the specific acoustic impedance of air (sound pressure⁄acoustic impedance = velocity). Figure 14(a) shows the measured and predicted infrasound pressure generation at different voltage input. At this small scale, we generated 19 dB of sound pressure in air with 50 mV of the voltage input.

To make our yarn harvester more efficient, we demonstrate a mechanical frequency amplification mechanism to step-up the low frequency energy from the wave oscillation (Figure 14(c)). In this setup, the rack to input gear is 1 rotation per 2 cm linear motion of the rack, and the input gear is compounded to a 60:12 (5:1) rotational ratio. Thus, the total ratio is 2.5 rotations per cm of travel. For example, a 4cm travel from a 2cm center-to-peak amplitude wave at 1 Hz would give 4cm / 0.5 seconds x 2.5 rotations/cm = 20 Hz rotation. At 2cm amplitude for the wave, the output is 10 Hz rotation from a 0.5 Hz wave input and 40 Hz at a 2 Hz wave input. We can conclude from the above discussion that if this mechanism is used for large scale ocean wave, where, wave amplitude is as high as 2 m at 0.5 Hz, then our harvester can easily produce electricity at higher frequencies (~1000 Hz) Figure 14 (b)-(d) shows procedure at small scale to provide high frequency electrical output, Figure 14(b) is the shaker input to our mechanical amplifier similar to the ocean wave. We pushed and pulled the rack by ~2.2 cm at 2 Hz frequency. On receiving the linear input to the rack the yarn stretched and released periodically (path of yarn showed in Figure 14(c)) at high frequency. Figure 14(d) shows the peak to peak OCV of around 22 mV at frequency of 20 Hz. This amplification can easily be tailored by different input to the mechanical frequency amplifier.

The unique properties such as flexibility, and long stroke length of our yarn harvesters could facilitate us to demonstrate the high frequency electrical output. High frequency

operation not only make our yarn more efficient, but it also could help in efficient energy conversion and its transmission to grid systems in more real scenarios of ocean energy harvesting [12].

Conclusion

We presented the first systematic study of ocean wave energy harvesting using new twisted- and coiled-MWNT yarn based electrochemical transduction that converts mechanical to electrical energy through a change in capacitance. These yarns are highly flexible, non-resonant and non-corrosive. They exhibit a long stroke length, and high power density. Some of the key aspects of this study are below:

- Wave modeling was developed for the harvester to evaluate the strain in the yarn which was used in empirical formula to get the OCV.
- An experimental set up, mimicking the real ocean wave condition, was designed to demonstrate the robustness of the nanotube yarns and its feasibility under fluid loading.
- 0.5 mg of yarn produced 0.88 W/kg at 0.5 Hz under the water oscillation amplitude of 1.54 cm. The output power was found to increase with frequency (but non resonant).
- We proposed a mechanical frequency amplification mechanism to obtain the high frequency electrical output. This mechanism could make the underwater acoustic communication possible from yarn harvesters. We realized around high frequency voltage output of 22 mV at 20 Hz on providing wave input condition of 2 Hz.

References

[1] Jacobson MZ, Delucchi MA. Providing all global energy with wind, water, and solar power, Part I: Technologies, energy resources, quantities and areas of infrastructure, and materials. Energy policy. 2011;39:1154-69.

[2] Delucchi MA, Jacobson MZ. Providing all global energy with wind, water, and solar power, Part II: Reliability, system and transmission costs, and policies. Energy policy. 2011;39:1170-90.

[3] Khaligh A, Onar OC. Energy harvesting: solar, wind, and ocean energy conversion systems: CRC press; 2009.

[4] Painuly JP. Barriers to renewable energy penetration; a framework for analysis. Renewable energy. 2001;24:73-89.

[5] Boyle G. Renewable energy: OXFORD university press Oxford; 2004.

[6] Lund H. Large-scale integration of wind power into different energy systems. Energy. 2005;30:2402-12.

[7] Ackermann T. Wind power in power systems: John Wiley & Sons; 2005.

[8] Ansar A, Flyvbjerg B, Budzier A, Lunn D. Should we build more large dams? The actual costs of hydropower megaproject development. Energy Policy. 2014;69:43-56.

[9] Wang ZL. Catch wave power in floating nets. Nature. 2017;542:159.

[10] Ellabban O, Abu-Rub H, Blaabjerg F. Renewable energy resources: Current status, future prospects and their enabling technology. Renewable and Sustainable Energy Reviews. 2014;39:748-64.

[11] Wang ZL, Jiang T, Xu L. Toward the blue energy dream by triboelectric nanogenerator networks. Nano Energy. 2017;39:9-23.

[12] Scruggs J, Jacob P. Harvesting ocean wave energy. Science. 2009;323:1176-8.

[13] Salter SH. Wave power. Nature. 1974;249:720-4.

[14] Gemme DA, Bastien SP, Sepe RB, Montgomery J, Grilli ST, Grilli A. Experimental testing and model validation for ocean wave energy harvesting buoys. Energy Conversion Congress and Exposition (ECCE), 2013 IEEE: IEEE; 2013. p. 337-43.

[15] Grilli ST, Grilli AR, Spaulding ML, Bastien SP, Sepe Jr RP. Small buoys for energy harvesting: Experimental and numerical modeling studies. The Twenty-first International

Offshore and Polar Engineering Conference: International Society of Offshore and Polar Engineers; 2011.

[16] Boström C, Lejerskog E, Stålberg M, Thorburn K, Leijon M. Experimental results of rectification and filtration from an offshore wave energy system. Renewable Energy. 2009;34:1381-7.

[17] Leijon M, Bernhoff H, Agren O, Isberg J, Sundberg J, Berg M, et al. Multiphysics simulation of wave energy to electric energy conversion by permanent magnet linear generator. IEEE Transactions on energy conversion. 2005;20:219-24.

[18] Wolfbrandt A. Automated design of a linear generator for wave energy Converters-a simplified model. IEEE transactions on magnetics. 2006;42:1812-9.

[19] Prudell J, Stoddard M, Amon E, Brekken TK, Von Jouanne A. A permanent-magnet tubular linear generator for ocean wave energy conversion. IEEE Transactions on Industry Applications. 2010;46:2392-400.

[20] Von Jouanne A. Harvesting the waves: researchers are closing in on how best to harness the power of the ocean. Mechanical Engineering-CIME. 2006;128:24-8.

[21] Waters R, Stålberg M, Danielsson O, Svensson O, Gustafsson S, Strömstedt E, et al. Experimental results from sea trials of an offshore wave energy system. Applied Physics Letters. 2007;90:034105.

[22] Liang C, Ai J, Zuo L. Design, fabrication, simulation and testing of an ocean wave energy converter with mechanical motion rectifier. Ocean Engineering. 2017;136:190-200.

[23] https://oscillapower.com/waveenergy/

[24] http://www.oceanpowertechnologies.com/.

[25] http://www.oceanharvesting.com/start.

[26] Jiang T, Yao Y, Xu L, Zhang L, Xiao T, Wang ZL. Spring-assisted triboelectric nanogenerator for efficiently harvesting water wave energy. Nano Energy. 2017;31:560-7.

[27] Chiba S, Waki M, Wada T, Hirakawa Y, Masuda K, Ikoma T. Consistent ocean wave energy harvesting using electroactive polymer (dielectric elastomer) artificial muscle generators. Applied Energy. 2013;104:497-502.

[28] Vertechy R, Fontana M, Papini GR, Forehand D. In-tank tests of a dielectric elastomer generator for wave energy harvesting. SPIE Smart Structures and Materials+ Nondestructive Evaluation and Health Monitoring: International Society for Optics and Photonics; 2014. p. 90561G-G-11.

[29] Jean P, Wattez A, Ardoise G, Melis C, Van Kessel R, Fourmon A, et al. Standing wave tube electro active polymer wave energy converter. Proc SPIE2012. p. 83400C.

[30] Papini GPR, Vertechy R, Fontana M. Dynamic model of dielectric elastomer diaphragm generators for oscillating water column wave energy converters. Proc ASME 2013 Conf Smart Mater Adapt Struct Intell Syst, Snowbird, UT, USA, OMAE, V001T03A0382013.

[31] Fan F-R, Tian Z-Q, Wang ZL. Flexible triboelectric generator. Nano energy. 2012;1:328-34.

[32] Ahmed A, Saadatnia Z, Hassan I, Zi Y, Xi Y, He X, et al. Self-Powered Wireless Sensor Node Enabled by a Duck-Shaped Triboelectric Nanogenerator for Harvesting Water Wave Energy. Advanced Energy Materials. 2016:1601705.

[33] Xi Y, Guo H, Zi Y, Li X, Wang J, Deng J, et al. Multifunctional TENG for Blue Energy Scavenging and Self-Powered Wind-Speed Sensor. Advanced Energy Materials. 2017:1602397.

[34] Chen J, Yang J, Li Z, Fan X, Zi Y, Jing Q, et al. Networks of triboelectric nanogenerators for harvesting water wave energy: a potential approach toward blue energy. ACS nano. 2015;9:3324-31.

[35] Wang X, Wen Z, Guo H, Wu C, He X, Lin L, et al. Fully Packaged Blue Energy Harvester by Hybridizing a Rolling Triboelectric Nanogenerator and an Electromagnetic Generator. ACS Nano. 2016;10:11369-76.

[36] Wang X, Niu S, Yin Y, Yi F, You Z, Wang ZL. Triboelectric Nanogenerator Based on Fully Enclosed Rolling Spherical Structure for Harvesting Low-Frequency Water Wave Energy. Advanced Energy Materials. 2015;5.

[37] Li X, Tao J, Zhu J, Pan C. A nanowire based triboelectric nanogenerator for harvesting water wave energy and its applications. APL Materials. 2017;5:074104.

[38] Kim SH, Haines CS, Li N, Kim KJ, Mun TJ, Choi C, et al. Harvesting electrical energy from carbon nanotube yarn twist. Science. 2017;357:773-8.

Chapter 5

High Efficiency Low-temperature Gradient Thermal to Electrical Conversion

Prashant Kumar, Ravi Anant Kishore, Deepam Maurya, Colin J Stewart, Reza Mirzaeifar, Eckhard Quandt, and Shashank Priya

(Under review in journal: Applied Energy)

Abstract

More than half of the energy generated worldwide is lost as unused thermal energy because of the lack of efficient methodology for harnessing the low-grade heat. Here we demonstrate that shape-memory alloy (SMA) can be an effective mechanism for recovering low-grade heat. SMAs exhibit thermally induced martensite to austenite phase transformation and super-elasticity (stress-induced martensitic transformation). Employing these two characteristics, we demonstrate a thermal engine for harnessing waste energy through all modes of heat transfer: convection, conduction, and radiation. An optimized SMA engine generated 36 W from 1 kg or 234 kW of electricity from 1 m^3 of active material. A continuous three-day operation of several SMA engines could generate 7.2 kWh of electricity when installed on a 500 m long hot pipe network. This generated power can reduce the carbon footprint by 11.8 pounds of CO_2 illustrating the promise of this technology for addressing climate change.

Keywords: Shape Memory Alloy (SMA); Martensite; Austenite; Pseudo-elasticity; Heat engine; Energy harvesting.

Introduction

Among the various forms of environmental energy available around us, thermal energy is the most abundant and ubiquitous. Thus, there has been considerable efforts towards developing techniques for conversion of thermal energy into electrical energy, using mechanisms such as thermoelectric [1-5], pyroelectric [6-8], thermomagnetic [9-12], thermo-acoustics [13], thermo-electrochemical [14, 15], and tensile muscles [16]. Out of these choices, thermoelectric generators (TEGs) have dominated the scientific interest in capturing locally available thermal energy. A major part of this thermal energy is in the form of low grade (<100°C) waste heat (Figure 1(a)). However, there is significant drop in the performance (efficiency ~1-3%) of TEGs, when hot-side temperature is below 100 ^{o}C [17]. Other techniques mentioned above, in current form, provide small output power density and thus, still remain early-stage laboratory research. On the other hand, thermodynamic cycles based engines such as Rankine cycle engines, are extremely bulky and not efficient (~2.8-5.5%) in these low temperature regimes (hot side temperature <100°C) [18, 19]. In trying to address this decades old grand challenge, we made a breakthrough in demonstration of small-scale heat engine based on shape memory alloy (SMA). SMA based engine was designed to operate at temperatures less than 80°C with the ambient acting as heat sink. The engine relies on two fundamental properties of SMA: (i) super-elasticity, and (ii) thermally induced martensite to austenite phase transformation.

There have been several attempts to develop the SMA system for converting heat energy into output mechanical work[20, 21] [22]. Recently, Sato et al.[23] have presented the large scale working device based on SMA that demonstrated 1.155 W output power for 40.25 cm^3 of active material volume (5 belt, weight of active material ~ 0.262 kg, device dimension: 18.50 cm x 5.50 cm x 5 cm). However, most of these previous designs have remained laboratory experiments and their reliability and durability for a long-term domestic or commercial application remain challenging. Especially for the devices requiring rotation, challenges arise from the fact that heat needs to be captured from the source (hot-side temperature less than 80°C) at a very fast rate (several hundred rotations per minute) through an extremely thin interface (SMA wire diameter less than few

hundred microns). Also, the residual heat in the wire has to be completely discarded to the ambient at an equally fast rate to achieve continuous operation. As the size of SMA engine is reduced, the hot-side and the cold-side come closer to each other, which results in continuous accumulation of heat after each cycle. Eventually, the accumulated heat stops the functioning of the device due to insufficient cooling. This has been the challenge towards realizing small scale SMA engine for past four decades (since 1975).

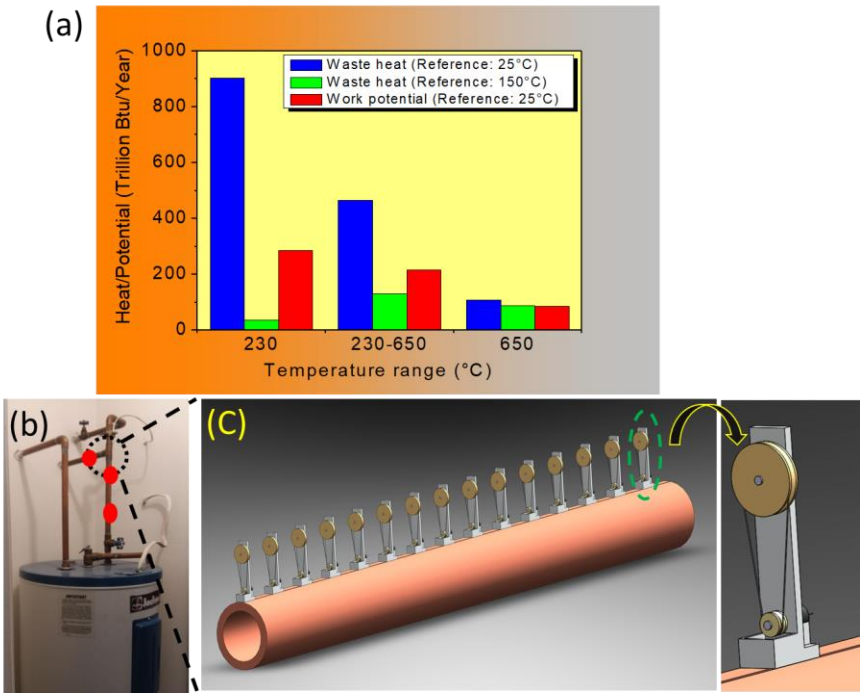

Figure 1: Thermal energy available at various locations (industry, home, and geothermal sites) for potential deployment of SMA based heat engine. (a) A bar chart representing the potential of thermal energy harvesting in various categories (subdivided on the basis of temperature range).[24] The graph is redrawn on the basis of data given in reference 36, (c) Various home and industrial hot pipe locations for effective utilization of SMA engine, (d) An array of SMA engines deployed on pipe (along with single device) for the prospective utilization of hot thermal zone for maximizing the power and reducing the carbon foot print.

Here, we analyzed a small scale SMA engines operating at hot-side temperatures less than 100 °C and overcoming all of the above mentioned challenges. The potential of our SMA engine can be recognized from the data presented in Figure 1(a). This data shows the amount of waste heat available corresponding to different thermal gradients and low grade heat (230 °C) is the major component of total waste heat. There are many geothermal locations (wells and springs)[25] can be observed across the United States, which could provide the opportunity for deployment of SMA engine arrays demonstrated in this study. Figure 1(b) shows various locations of hot pipes (in the industrial and residential settings) with low thermal gradient waste heat.

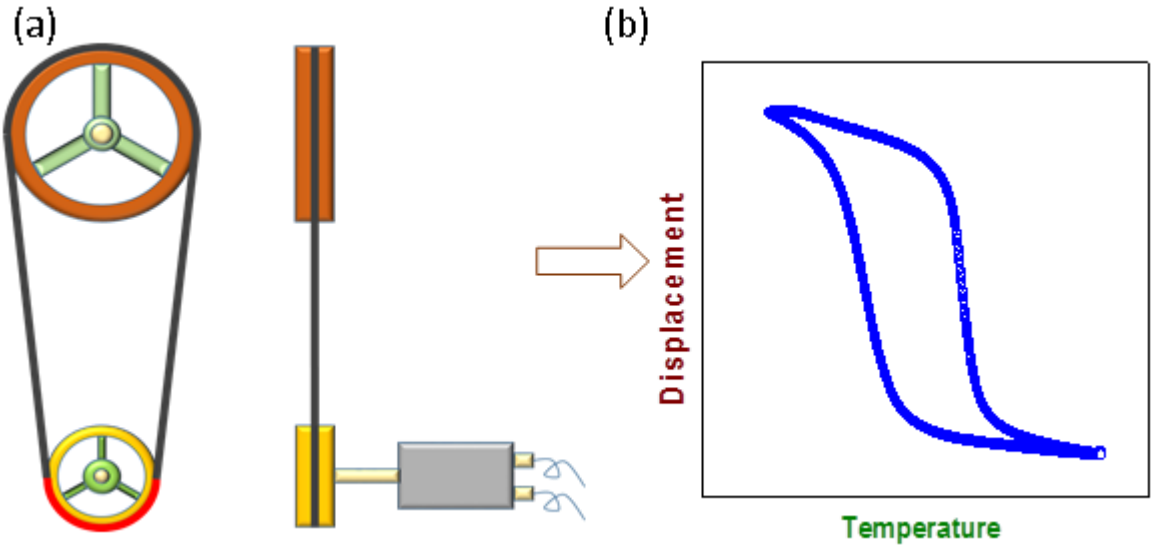

Figure 2: (a) Schematic of shape memory alloy engine, (b) Schematic representation of displacement vs. temperature profile of shape memory alloy. With increase in temperature, displacement decreases and generates the differential tension across the pulley.

For harvesting this abundant amount of low grade thermal energy, the SMA wire needs to possess a low transition temperature, smaller hysteresis, low heat capacity, high thermal conductivity, and a high thermo-elastic efficiency. Therefore, extensive investigations were conducted on phase transition behavior, thermodynamic properties, and thermal hysteresis of SMA wires. Using the measured SMA material characteristics,

we designed engine comprising of two pulleys with different diameters, a thin SMA belt around two pulleys, and a small DC electric generator (Figure 2). Figure 1(c) shows schematics of array of SMA engines deployed on hot pipes (Figure 1(c)). Our SMA engine was found to generate sufficient power needed for powering water health monitoring sensors and acoustic devices with hot-side temperature ranging between 60-80 °C. It is worthwhile to mention that the engine design presented here can be used at much lower hot-side temperatures (10 °C above the ambient) if the transition temperature of SMA can be reduced by modifying its composition [26]. The long–term operational test (continuous three day operation) on the SMA wire indicated no significant change in the thermo-mechanical properties. The analysis presented later, projects that our SMA engine can generate 7.2 kWh over three-day period in an industrial setup comprising of 500 m long hot pipe network. This generated power can reduce the carbon footprint by 11.8 pounds of CO_2.

Results

In the first stage, we performed material investigations to identify the most suitable SMA alloy composition for engine design. Focus in this stage was on understanding the fundamental material behavior under cyclic temperature and stress variations. In the second stage, we performed thermal transport analysis to ensure rapid heat transfer rate across the SMA wire. Lastly, in the third step, we performed systematic experiments on heat engine to fully quantify the device performance.

SMA investigations for design of heat engine

A comprehensive differential scanning calorimetry (DSC) analysis was performed on different SMA wires available commercially in order to understand the thermal deformation cycle and identify the composition which has maximum thermodynamic efficiency at low temperatures under stress free condition. Five samples of NiTi were used in as-received form for the DSC test: Wire 1 (0.25 mm, Muscle wires), Wire 2 (0.38 mm, DYNALLOY, Inc), Wire 3 (0.2 mm, Johnson Matthey), Wire 4 (0.38 mm, DYNALLOY, Inc), and Wire 5 (0.44 mm, Sci-supply)). Figure 3(a)-(e) show the hysteresis across phase change and the transition temperature for each sample. Using this

experimental heat flow diagram, the critical temperatures - M_s (martensite start), M_f (martensite finish), A_s (austenite start), and A_f (austenite finish) - for forward and reverse transformation were quantified. It can be seen from Figure 3 that wire 5 has the lowest forward transition temperature of 48°C, which is most suitable for our heat engine. The difference between thermal energy going-in and coming-out of the wires was found to be very small, which should be the case since the DSC tests were run under no stress condition (no work). Residual heat accumulation may cause thermo-mechanical fatigue in the system. Figure 4 (a), (b) and (c) show detailed results on phase transition of annealed sample. Thermal annealing results in shift of transition temperature from 48 °C to 54 °C. SMA wire was also characterized using dynamic mechanical analyzer (DMA) in order to determine the force dynamics and viscoelasticity properties. Detailed comparative study of damping and storage modulus values for as-received and annealed SMA samples are shown in Figure 5-7. We observed that with increase of frequency the damping coefficient decreases, and with increase of temperature scan rate the transition temperature of the wire increases.

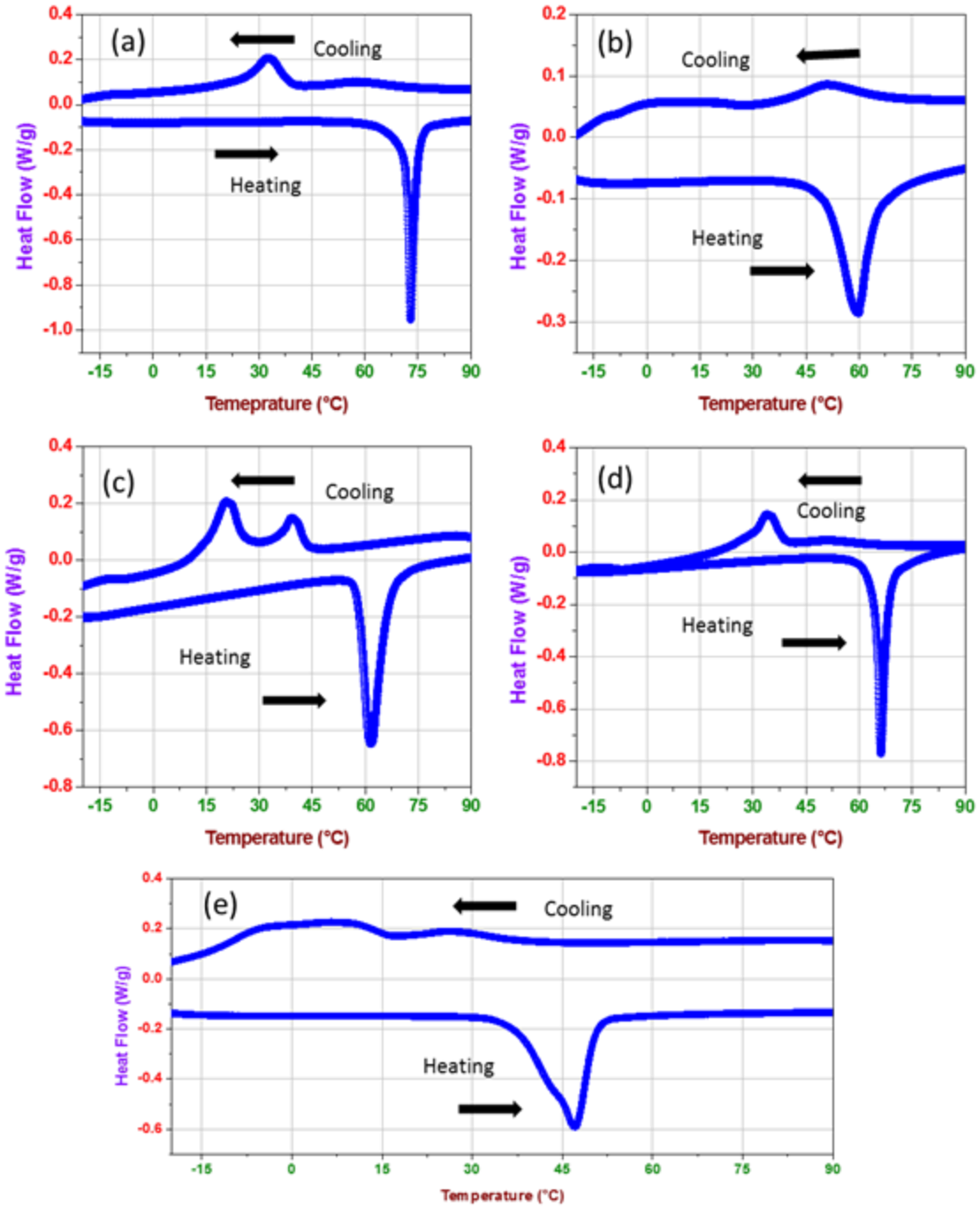

Figure 3: DSC results for five different wires from various companies, (a) Wire 1 (0.25 mm, Muscle wires), (b) Wire 2 (0.38 mm, DYNALLOY, Inc), (c) Wire 3 (0.2 mm, Johnson Matthey), (d) Wire 4 (0.38 mm, DYNALLOY,Inc), and (e) Wire 5 (Sci-supply).

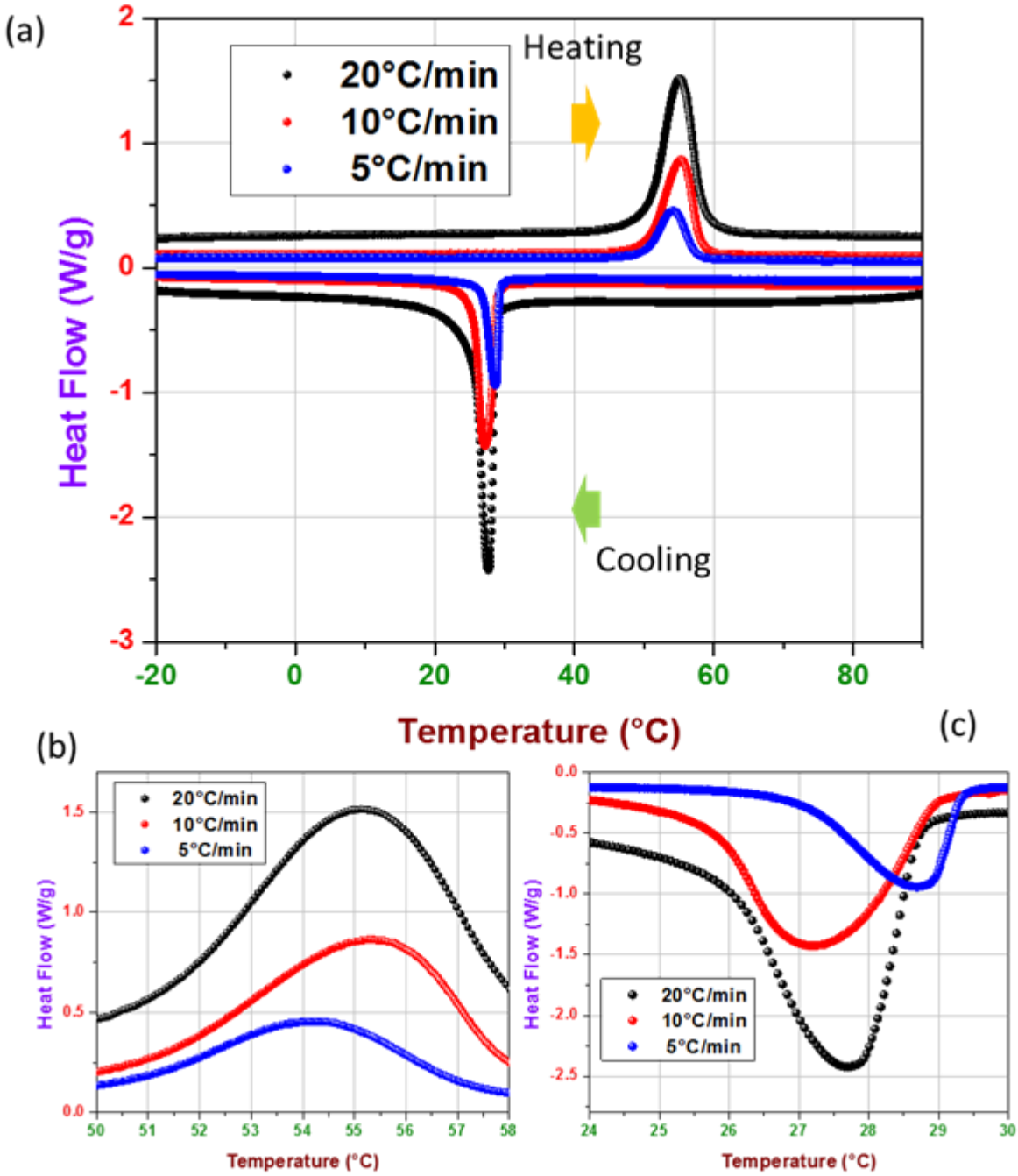

Figure 4: DSC results for annealed SMA wire (selected for SMA engine) at different temperature scanning rate; 5,10 and 20°C/min. Annealing was done at 600 °C for 30 minutes, (a) complete cycle of heating and cooling of sample, (b) and (c) enlarged graphs of heating and cooling profile, and the comparison at different temperature ramping rate.

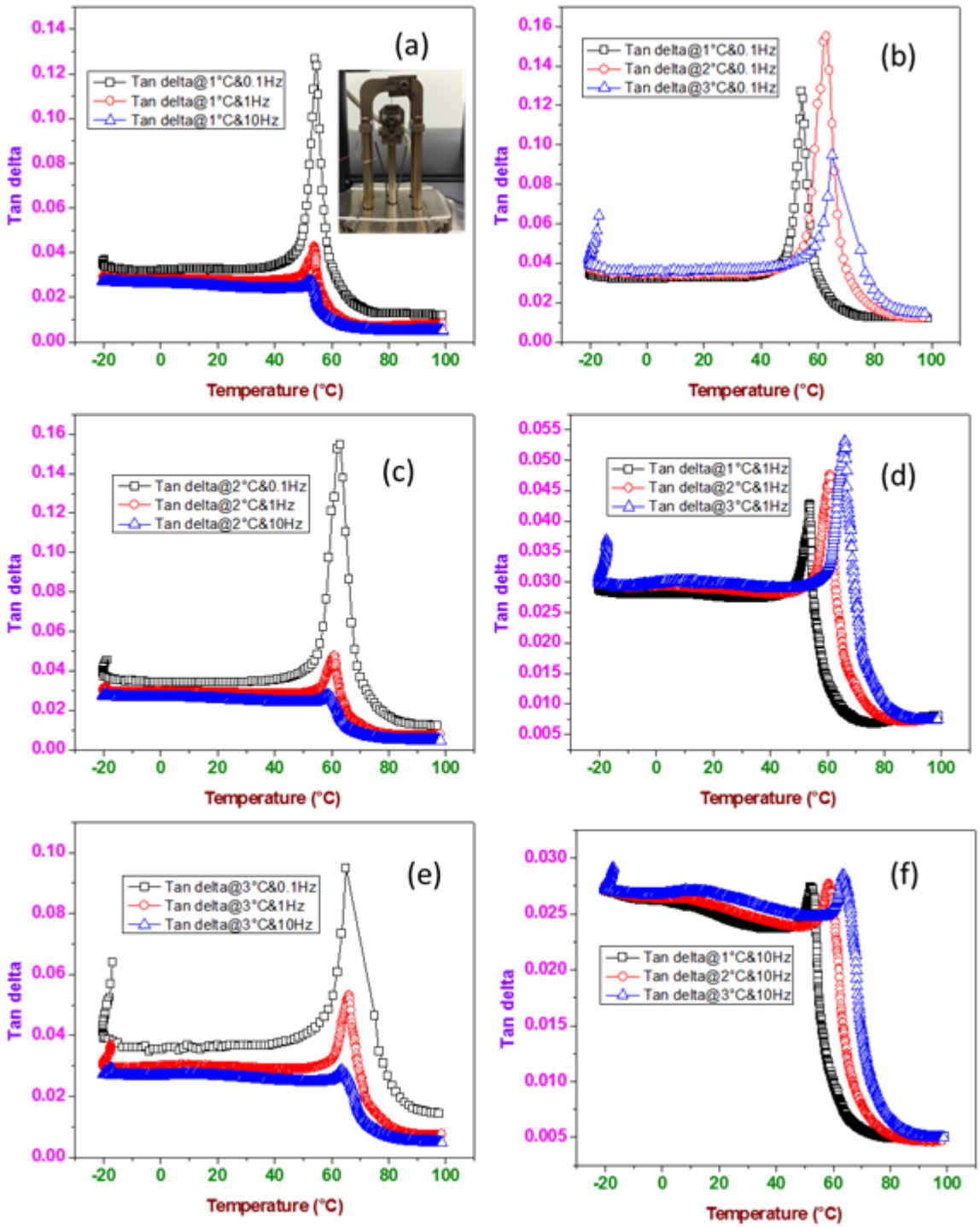

Figure 5: DMA results for un-annealed selected NiTi wire, (a), (b),(c),(d),(e) and (f) shows the comparison of tan delta results of wire for different temperature scan rates and frequencies.

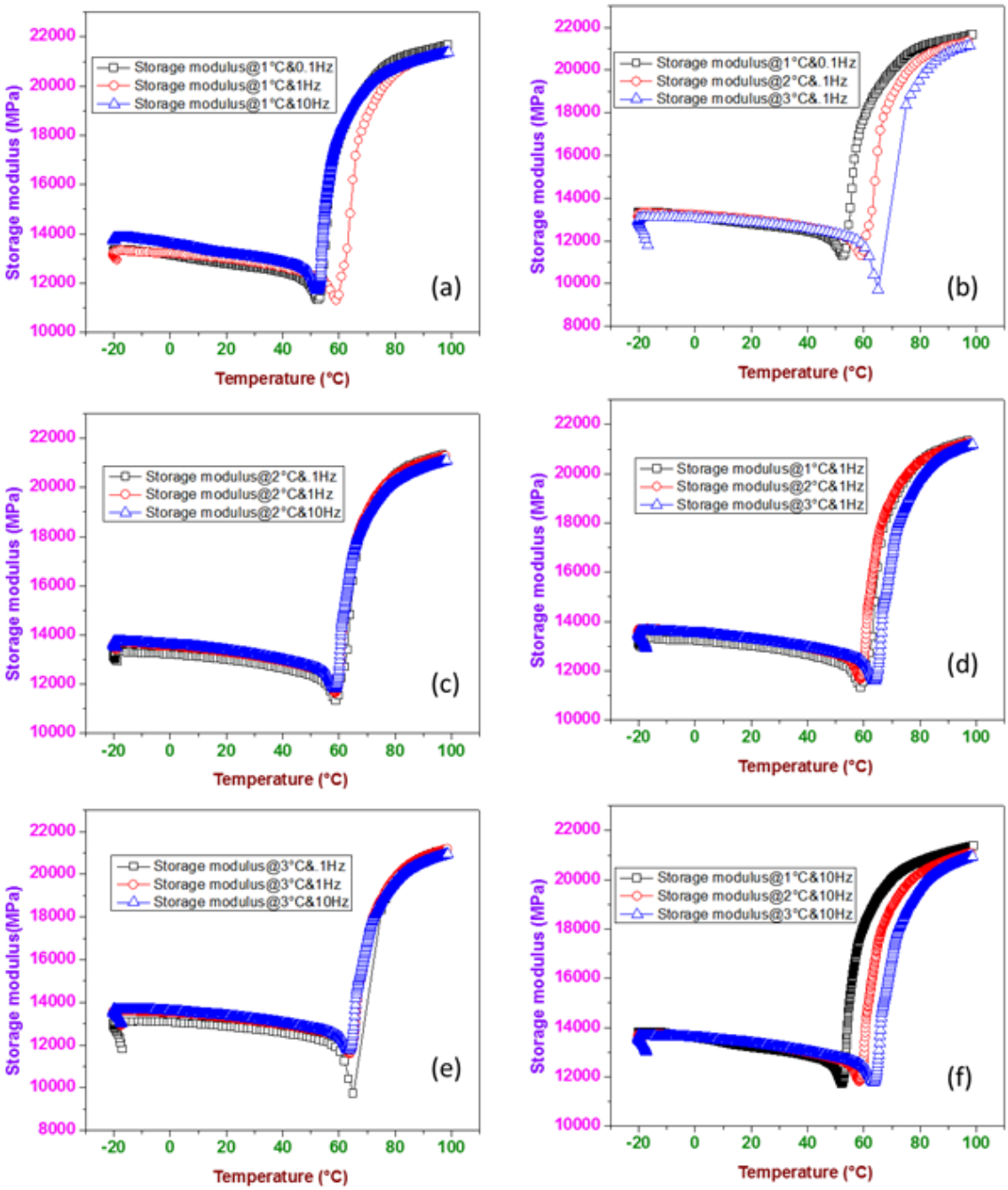

Figure 6: DMA results for un-annealed selected NiTi wire, (a),(b),(c),(d),(e)and (f) shows the comparison of storage modulus results for different temperature scan rates and frequencies.

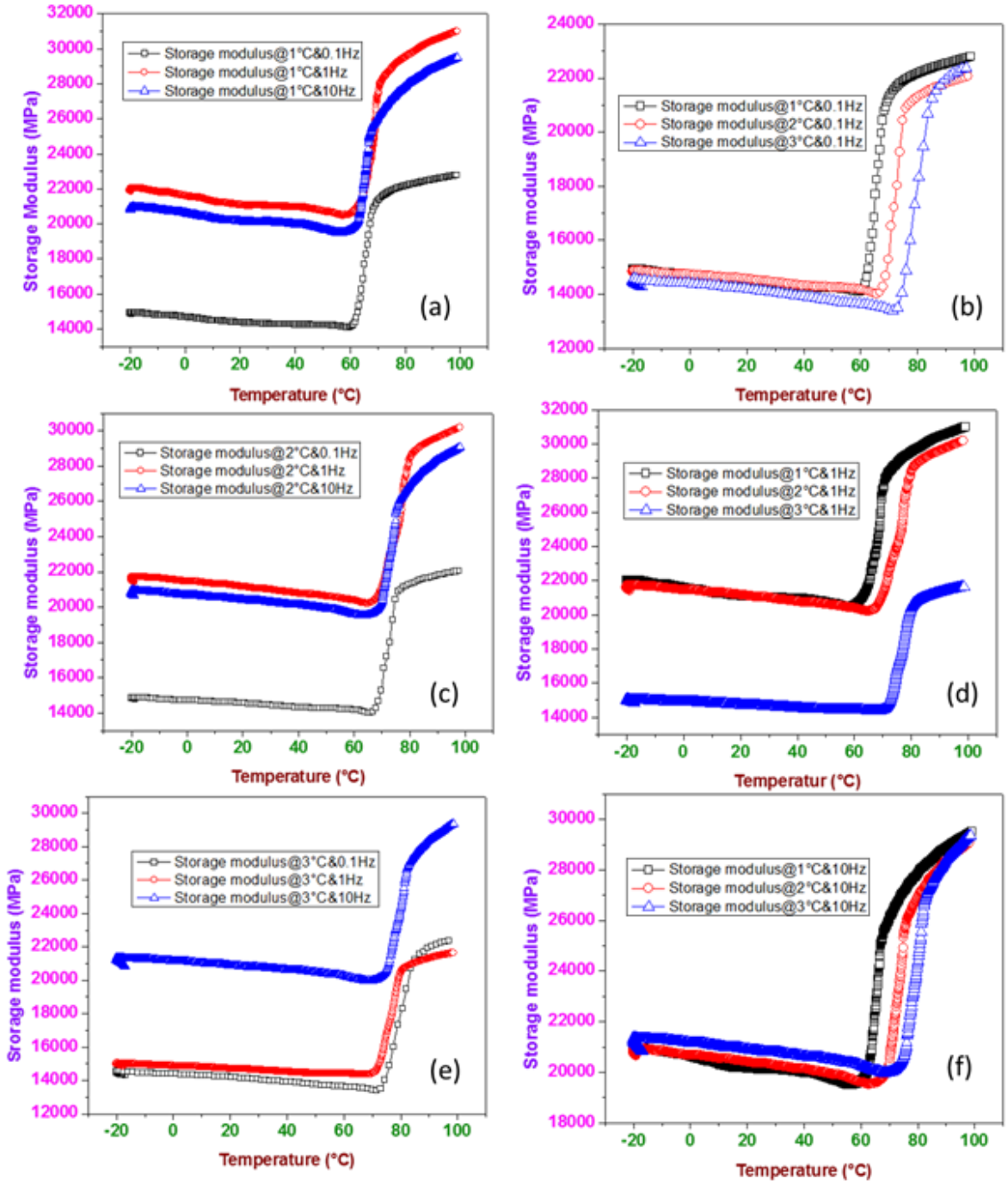

Figure 7: DMA results for annealed selected NiTi wire, (a),(b),(c),(d),(e)and (f) shows the comparison of storage modulus results for different temperature scan rates and frequencies.

Thermal modeling of rotary SMA engine

The exact analytical thermal modeling of rotary SMA engine is complex due to curvature effect in heat transfer, dynamic metal to metal contact heat transfer, non-linear response to thermal input etc. However, a simplified solution can be obtained which provides realistic estimation for SMA engine behavior. For reducing the modeling complexity, we converted the lopped wire into linear profile and allowed it to move through hot source as shown in Figure 8. In our model, a wire is moving from negative direction to positive direction and passing through heat source placed at origin. Heat transfer analysis on an element (dx) of moving wire is shown in equation (1):

$$q = q + \frac{dq}{dx}dx + \dot{m}C_p dT + dq_c + dq_r \tag{1}$$

where q is heat flow, m is weight of wire, C_p is heat capacity of wire

Moving mass can be further given by equation (2)

$$\dot{m} = \rho AV \tag{2}$$

where ρ is SMA density, A is cross section area of wire, V is velocity of wire.

Conductive heat transfers while heat source is at origin can be given by equation (3)

$$q = -kA\frac{dT}{dx} \tag{3}$$

where k is thermal conductivity of SMA wire. The convective heat loss through moving element of wire is given by equation (4)

$$dq_c = h(T - T_\infty)dA \text{ and } dA = Pdx \tag{4}$$

where h is heat transfer coefficient and T_∞ is ambient temperature. Thermal radiation component is given by equation (5) as:

$$dq_r = \varepsilon\sigma(T^4 - T^4{}_\infty)dA \tag{5}$$

where σ is Stefan–Boltzmann constant, ε is emissivity. Since the temperature difference is not that significant, the thermal radiation impact can be safely being ignored.

The heat equation for moving wire through stationary heat source is shown in equation (6)

$$\frac{d^2T}{dx^2} + \frac{\rho C_p V}{k}\frac{dT}{dx} - \frac{hP}{kA}(T - T_\infty) - \frac{\varepsilon\sigma P}{kA}(T^4 - T^4{}_\infty) = 0 \tag{6}$$

On solving the heat equation, an expression of distance dependent temperature is obtained as shown in equation (7)

$$T(x) = T_\infty + C_1 e^{-\frac{1}{2}x\left(\frac{C_p V \rho}{k} - \frac{\sqrt{4hkP + AC_p{}^2 V^2 \rho^2}}{\sqrt{A}k}\right)} + C_2 e^{-\frac{1}{2}x\left(\frac{C_p V \rho}{k} + \frac{\sqrt{4hkP + AC_p{}^2 V^2 \rho^2}}{\sqrt{A}k}\right)} \quad (7)$$

Constants C_1 and C_2 are determined using two boundary conditions, such as the temperature of the wire at two locations (obtained experimentally from IR Thermography).

Thermal analysis parameters[27]:

Table 1

Density (Kg/m^3)	Heat Capacity (J/(kg·K))	Thermal Conductivity (W/m-K)	Ambient Temperature (^oC)
6450	322	18	22

Figure 9 (a) and (b) show the vibration characteristic of the wire for mentioned thermal experiment. As can be seen from the figures, wire has sufficient vibration in horizontal direction which has significant contribution in overall cooling of the active material.

Thermal analysis of the heat engine

The power output of an SMA engine primarily depends on the thermoelastic cycle frequency i.e. the rate at which the phase transition occurs in forward and reverse directions. The efficiency of SMA engine can be enhanced by avoiding excessive heating or cooling during the thermal cycle. In order to analyze the temperature distribution along the wire under operating conditions (experimental configuration is described in Figure 10), thermal videos were recorded for various sections of the wire, as shown in Figure 11, while maintaining the wire speed at 0.25 m/s. The first section was considered 1 cm above the hot pulley to avoid the transient effects of thermal zone generated from hot source which assisted in measuring the correct temperature values on wire surface.

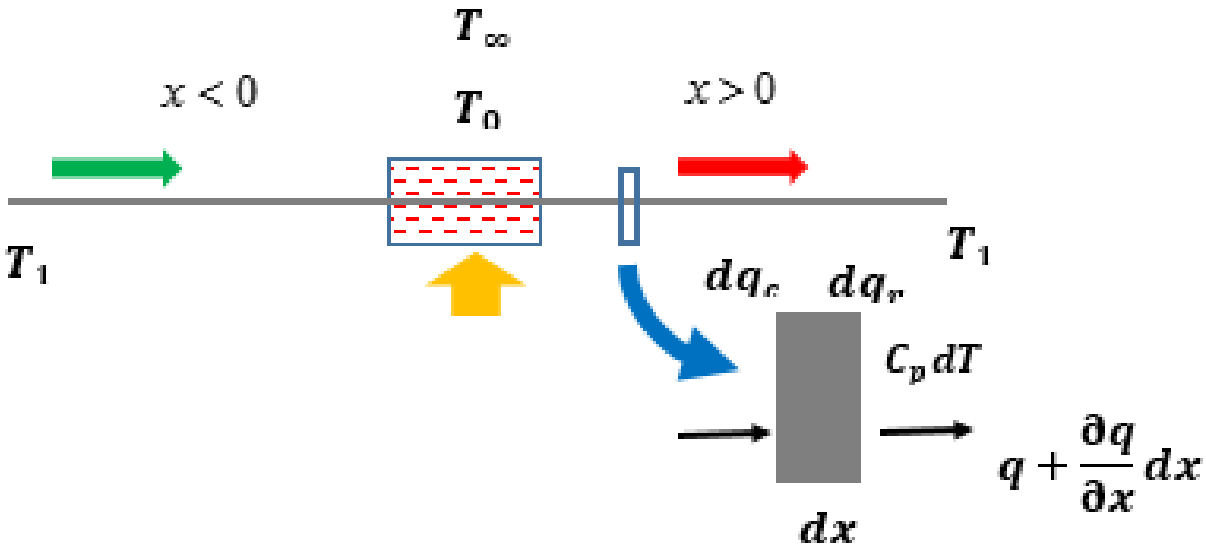

Figure 8: Conceptual diagram for modeling of moving wire. For simplicity of modeling, wrapped wire is converted into linear moving wire.

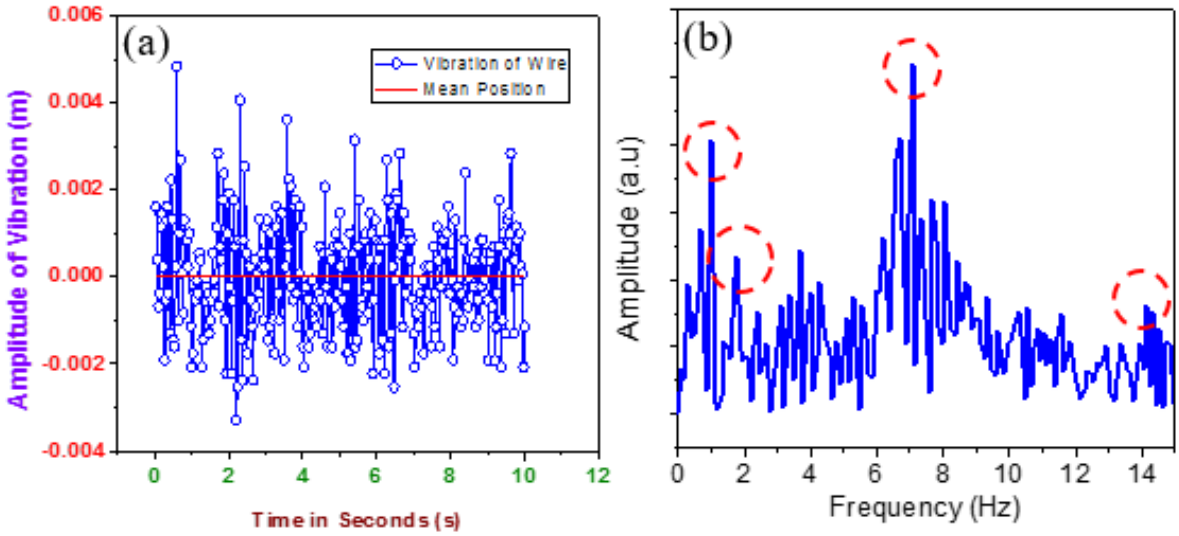

Figure 9: (a) Horizontal vibration profile of wire during system operations, (b) The time domain vibration profile is converted into frequency domain to observe the dominant frequencies.

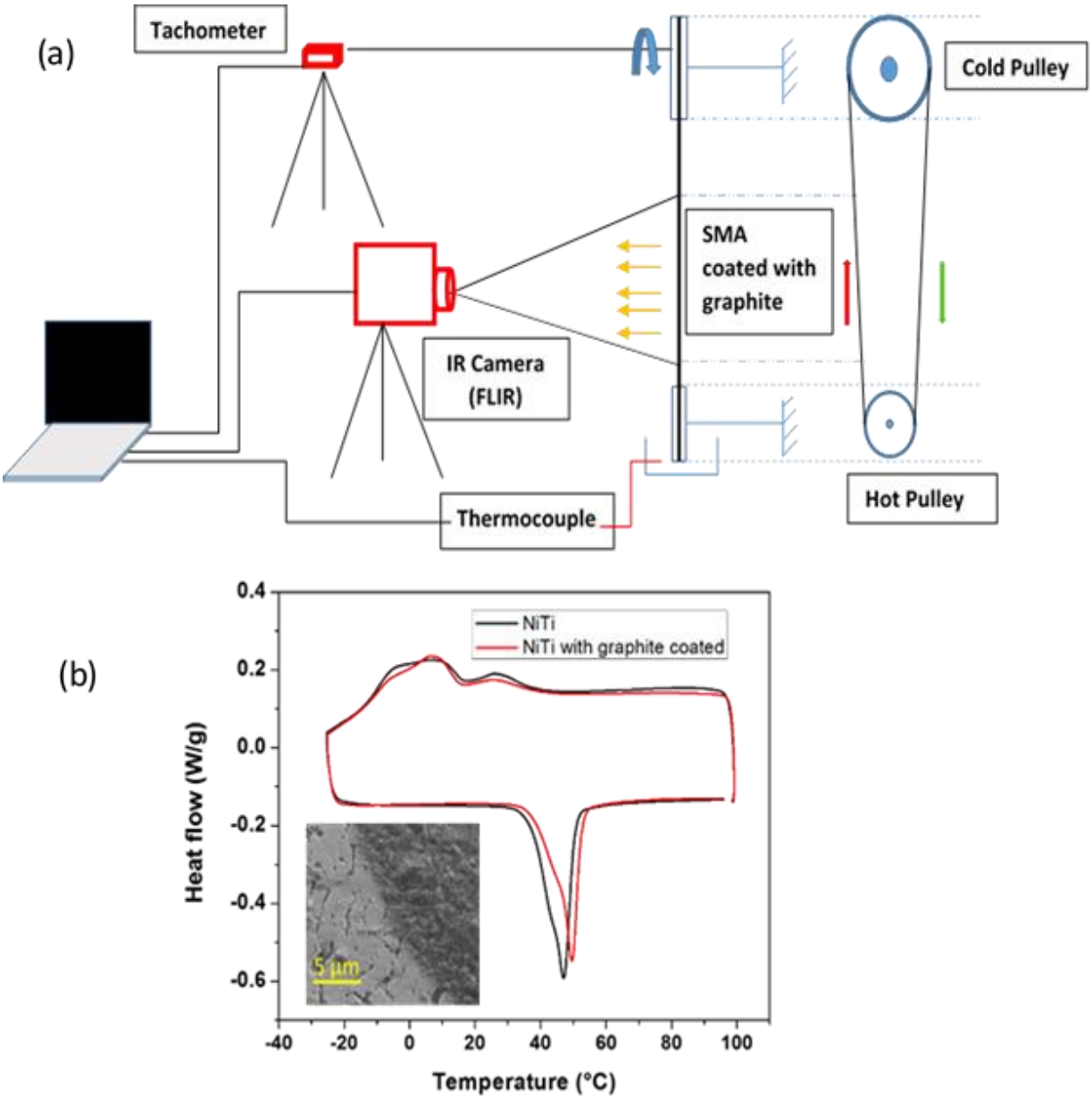

Figure 10: (a) Schematic showing the setup for thermal analysis of thin dynamic shape memory wire (graphite coated) wrapped around pulleys, (b) Differential scanning calorimetry (DSC) results for SMA wire, with and without graphite coating. The differences are small, therefore, any significant effect on wire behavior during thermal analysis has been neglected.

The vibration of SMA wire plays important role in determining the performance of heat engine, as it enhances the convective cooling of the wire. The convective heat transfer coefficient, h, in this case, depends on the velocity of the wire in the direction of rotation as well as vibrational speed in the normal direction.

A high resolution camera was used to capture the vibration of the moving wire along with the thermal videos. The high resolution videos were then processed using MATLAB to obtain vibrational characteristics. Figure 9(a) and (b) show the vibration profile of wire in the time domain and qualitative Fast Fourier Transformation (FFT) response. The wire is vibrating without any fixed pattern and the frequency response splits into many major frequencies between, ~ 0 to ~15 Hz.

Figure 11(b) compares the temperature across a selected section of wire obtained experimentally and empirically using equation (7) for different values of heat transfer coefficient. It can be noted that at h=250 W/m^2-K, analytical results are in close agreement with the experimental results (maximum deviation less than 3%). This predicted heat transfer coefficient includes the simultaneous effect of forced convection due to linear speed (due to rotation of the pulley) and vibration of the wire. Validated analytical model was used to evaluate the temperature profile of the wire for heat transfer coefficients ranging from 200-400 W/m^2-K, using equation (7). As cooling coefficient approaches 320 W/m^2-K (with the wire speed of 1.8 – 2 m/s), the temperature of wire reduces by 3.75 °C more (compare to h=200 W/m^2-K) in the first section of the wire. This overall analysis indicates the location of wire where the reverse phase transition temperature is achieved. We use this information to optimize the length of the wire in order to reduce the size of heat engine. Figure 11(c) shows the temperature profile of wire loop starting from the emerging point near the lower pulley to the upper pulley and from the upper pulley to lower pulley. Figure 11(d) compares the temperature profile obtained using our empirical model (equation (7)), experimental results, and the results obtained from the model proposed by Kase et al.[28] Our results differ from the model prediction of Kase et al. by 6-7%, which can be correlated with the difference in the experimental setup and vibrational dynamics of the wire that includes the wire curvature effect. Figure

11(d) shows the effect of curvature near the upper cold pulley on the temperature profile of wire.

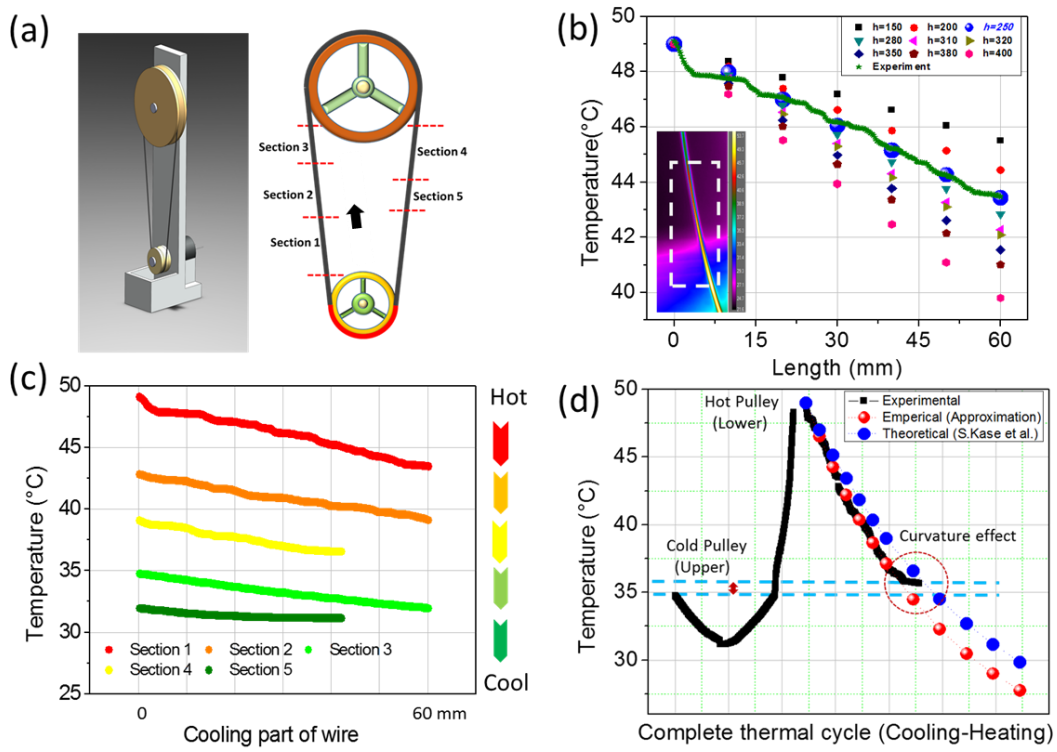

Figure 11: Dynamic thermal investigation of thin SMA wire (active material in the engine) by IR thermography. (a) Basic design of the SMA engine. The active material is divided into many sections for accurate thermal profiling of thin and vibrating wires, (b) Experimentally obtained temperature profile of moving wire (in steady state) for 1st section of active material at particular dynamic condition and its comparison with modeled temperature profile at different predicted heat transfer coefficients (*h*). Temperature profile obtained at *h*=250 W/K-m^2 is matching with experiments, (c) Temperature profile for the all the sections where wire is cooled continuously after emerging from hot source. Section just before hot source acts as transition zone for heating of cooled wire, (d) Complete thermal cycle of engine from heating-cooling-heating, and comparison of cooling profile with predicted h value and theoretical relationship developed by S.Kase et al.[28]

SMA heat engine performance

Next, we quantified the performance of the engine by cycling the heat source (water) temperature from 55-85 °C. The martensite to austenite transition completes at 54 °C, thus, the hot-side temperature was maintained above 55 °C. The heat sink temperature was fixed at ambient temperature. It is important to note that in Figure 12, the angular speed of pulley does not follow the same path during heating and cooling cycle. As shown in Figure 13(a), the angular velocity of pulley varies in proportion with temperature. We conducted the study to know the reversibility of our engine. With very slow rate of increasing temperature the mechanical behavior (RPM) of the engine evaluated experimentally. As shown in Figure 12 one cycle of gradual heating and cooling followed the different path of mechanical behavior. With this experimental results we can conclude that the mention engine is slightly irreversible in nature and doesn't follow the reversible path.

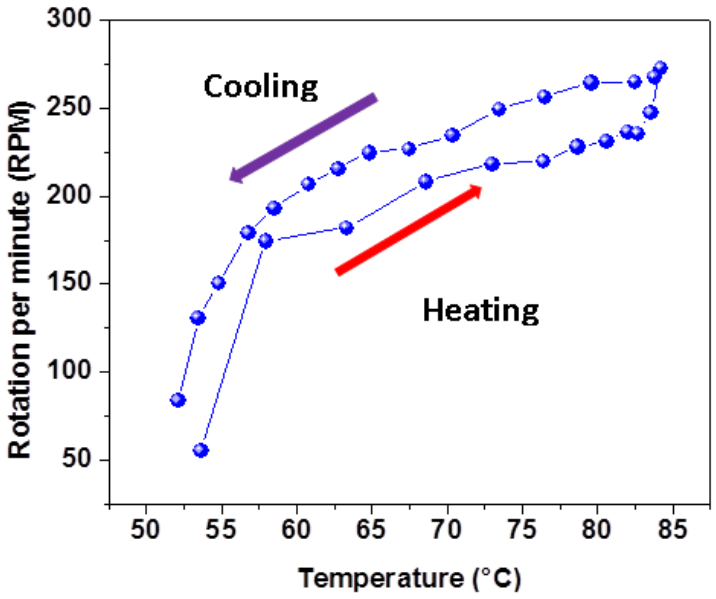

Figure 12: Reversibility test of heat engine. Hysteresis is observed for dynamic system in forward and reverse cooling

Another important parameter that affects the system's efficiency was found to be the dip angle, the angle made at the center by portion of the lower pulley exposed to heat source. Figure 13(b) compares the variation in angular speed with time at three different dip angles when the heat source is fixed at 70°C. It is interesting to note that there exists an optimal dip angle (~ 56°) for maximum angular speed. The angular speed was found to first increase with increase in dip angle due to the increased heat inflow. The angular speed is maximum when the dip angle is approximately equal to contact angle of SMA wire with the pulley. Increasing the dip angle further reduces the angular speed. This could happen because of increase in drag forces with increase in dip angle.

An optimized SMA engine with respect to heat source temperature and dip angle was examined under different heating modes: hot water bath, hot air, and radiative heating from a hot plate. Figure 13 (c) and (d) show the SMA engines speed (rate per minute) operating under different heat sources. The temperature of hot air was maintained at 125 °C. The hot plate temperature was fixed at 250°C and the gap distance between hot plate and wire was 1 cm. In order to enhance the heat transfer, silver paste was applied on inside the groove of lower pulley. It can be noted from Figure 13 (c), that the silver paste improves the angular speed of SMA engine. The maximum angular speed of the lower pulley in the steady state was measured to be 164 rpm and 268 rpm for hot air and hot plate, respectively.

Figure 13 (d) shows the angular speed of the upper pulley at different hot-side temperatures after the system has reached steady state. It can be seen that the SMA engine achieves a maximum angular speed when hot-side temperature is 80 °C and the corresponding angular speed is 420 rpm. It should be noted that the speed shown on y-axis of Figure 13 (c) is the rpm of the lower pulley; whereas, the rpm shown in Figure 13 (d) is the rpm of the upper pulley, which is three times lower than that of the lower pulley. From these results it can be concluded that the SMA engine performs best when the heat source is hot water. This is expected as the heat transfer coefficient in case of water is much higher than that of air. Therefore, in the remainder of this study, hot water is used as the heat source.

In rotational dynamics, mechanical power is given as the product of torque and angular speed, and it can be expressed as[29]:

$$P_{mech} = I \times \frac{d\omega}{dt} \times \omega \tag{8}$$

where I is the moment of inertia of pulleys, dω/dt is angular acceleration of pulleys, and ω is angular speed (rad/s). In order to determine the mechanical power, we first decoupled the electrical generator from SMA engine. The angular speed of pulley was then recorded from the instant rotation starts to the time rotation reaches the steady state. Variation of angular speed as a function of time for upper and lower pulleys is shown in Figure 14(a). A sixth order polynomial function was used to obtain a functional relationship that describes the angular speed of the pulley with respect to time. The angular acceleration of the upper and lower pulleys can be determined by taking the time derivative of the polynomial expression. Angular acceleration multiplied with the total moment of inertia of the rotating body provides the torque. Moment of inertia (*I*) of the pulleys was obtained using a CAD software, SOLIDWORKS and then the mechanical power was determined using equation (8).

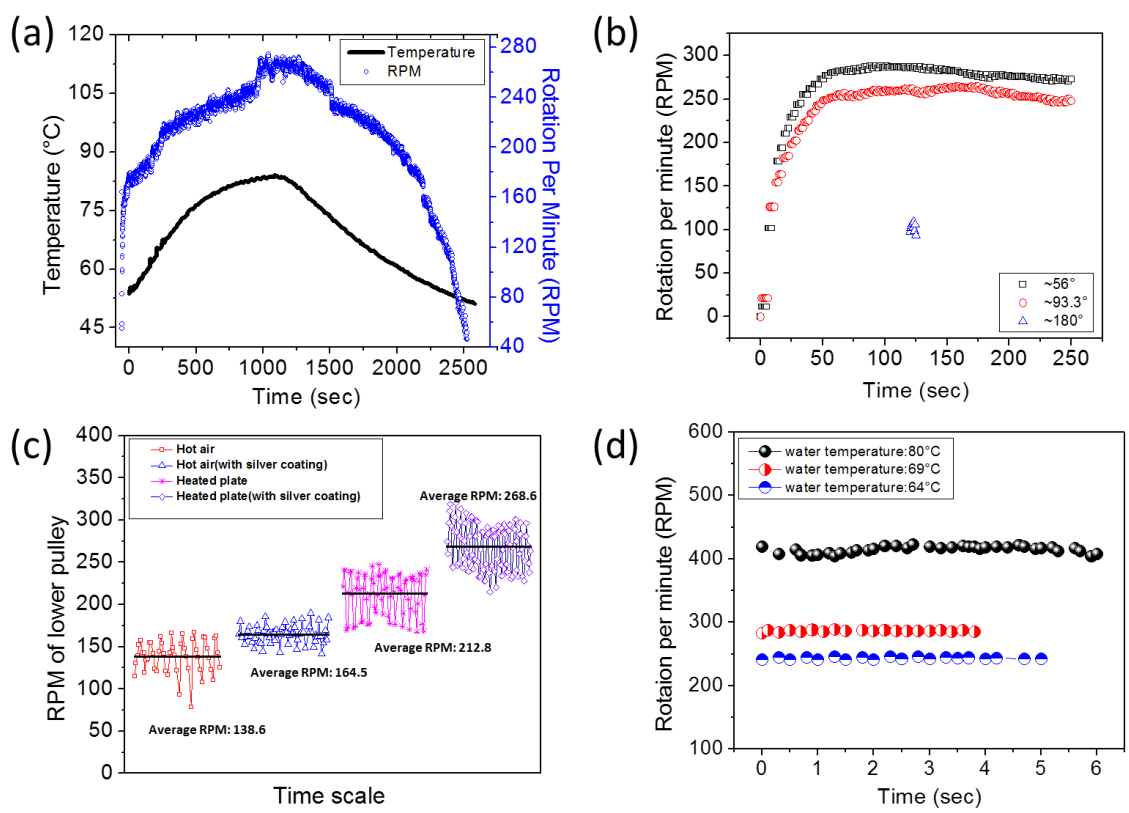

Figure 13: Performance characterization of optimized SMA engine for energy harvesting purposes. (a) SMA engine performance under load for increasing and decreasing the temperature continuously, (b) performance optimization of SMA engine at different dip angle (length of wire exposed to hot bath), (c) engine performance (in terms of lower pulley rotation) with different form of non-contact heat sources such as hot air and hot plates, (d) SMA engine performance (in terms of upper pulley rotation) at different temperature of hot bath.

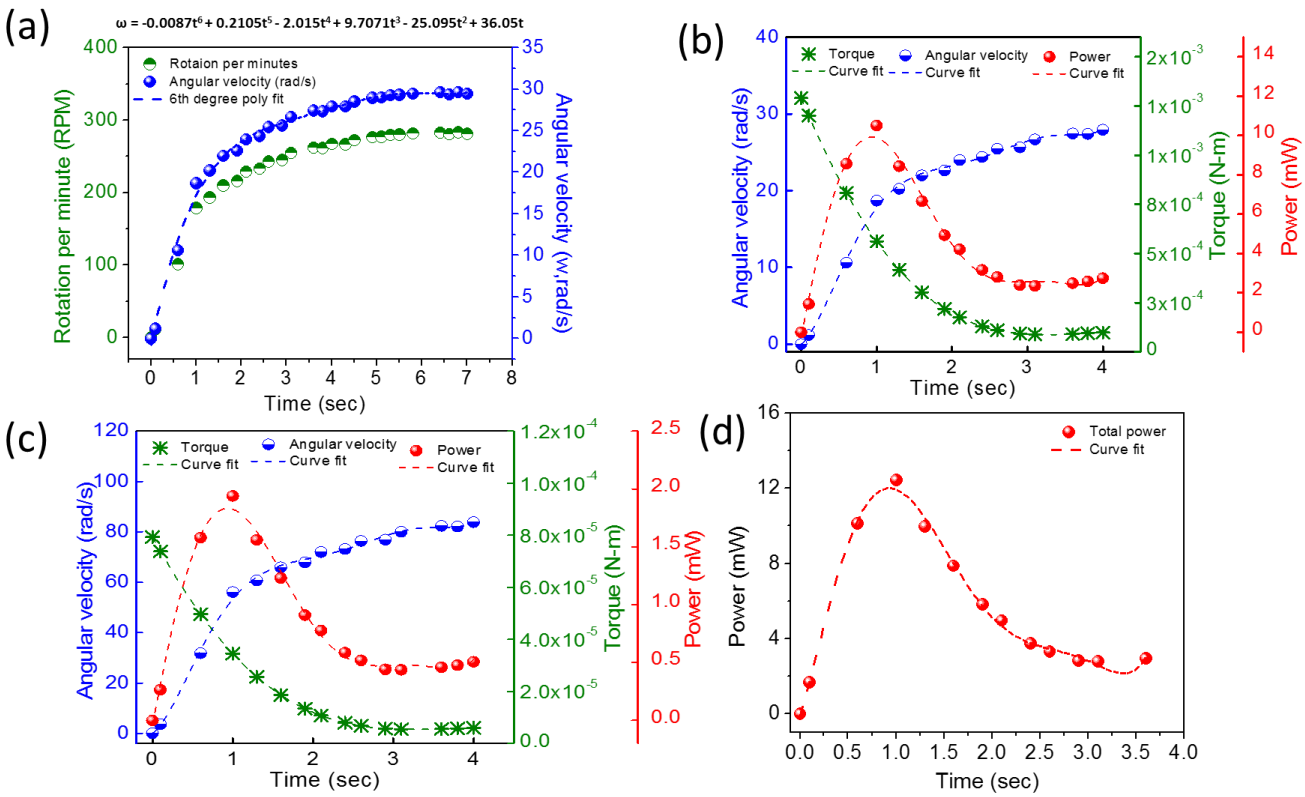

Figure 14: Mechanical power calculation for SMA engine. (a) Angular velocity of upper pulley along with 6th order polynomial curve fit when hot water is maintained at 69°C, (b) Angular velocity, derived torque and mechanical power (considering the upper pulley) in time domain, (c) Angular velocity, derived torque and mechanical power (considering the lower pulley) in time domain, (d) final evaluated mechanical power of whole SMA enegine when hot water bath is at 69°C.

Figure 14(b) and (c) show the angular speed, torque, and mechanical power of the upper and lower pulleys, respectively, at hot water temperature (T_w) of 69 °C. These figures depict that the torque is maximum when the pulley is just about to rotate (start-up torque), it decreases as the angular speed increases, and it diminishes to zero after the steady state is achieved. The mechanical power is zero at the beginning (since the system is at rest), it increases with the increase in angular speed until it gains a maximum value (when product of torque and angular speed is highest), and then it slowly decreases. Figure 14(d) depicts the total mechanical power of the SMA engine at $T_w = 69$ °C. The maximum mechanical power can be found to be 12.5 mW. Figure 16(a) shows the comparison of mechanical power at two different hot water temperatures: $T_w = 69$ °C and 80 °C. The maximum mechanical power obtained by the engine is 26mW at $T_w = 80$ °C, which is more than twice the mechanical power obtained at $T_w = 69$ °C. The specific mechanical power, calculated by dividing the mechanical power over the mass of the active component (SMA wire in this case), was found to be 52 W/kg at $T_w = 80$ °C.

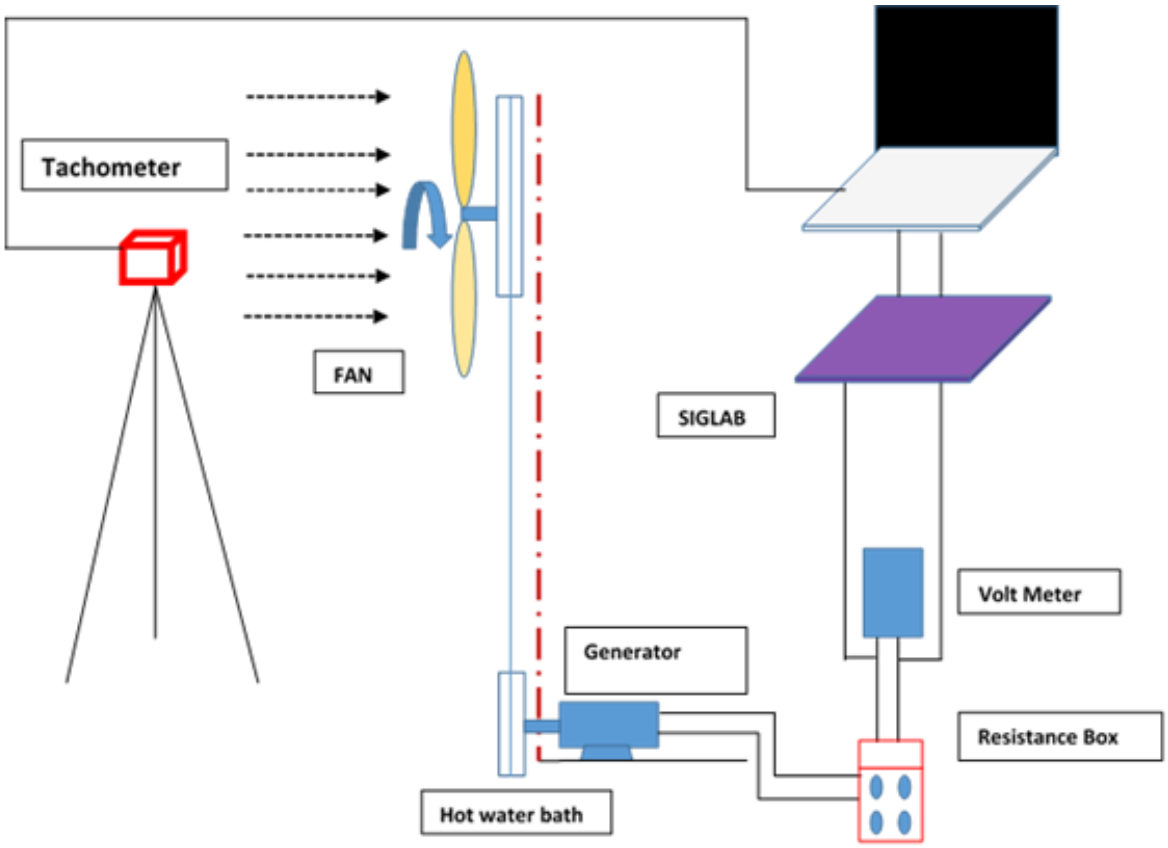

Figure 15: Schematic showing the experimental setup for quantifying the conversion of thermal energy into electrical energy

In order to quantify the electrical power output, we connected a small permanent magnet DC motor (rated at 6 V) with the shaft of the lower pulley. Detailed experimental setup is shown in Figure 15. Figure 16(b) shows the variation of generator's shaft rpm and external load resistance at different heat source temperatures (hot water). It can be seen that at a fixed load the shaft rpm increases with increase in the hot water temperature. At fixed temperature, the rpm first increases with increase in the load resistance and then saturates. Figure 16(c) shows the output DC voltage (V) and the output current (I) obtained for different load resistances at a fixed hot water temperature of 80°C. V-I plots at other hot water temperatures are not shown for the purpose of graphical clarity. The voltage follows similar trend as the rpm of the generator's shaft, and the maximum output voltage of 1.7 V was obtained at 80ºC when the generator has virtually no load (at 500Ω). Figure 16(d) depicts the electrical power output as a function of external resistance at different values of heat source temperature. It can be seen that SMA engine generates maximum electrical power output of 18 mW across 70 Ω load resistance when hot water temperature is 80 °C. The electrical power can be scaled up by using multiple uncoupled devices connected to a common heat source. To illustrate scalability of our engine, we designed experiments with three harvesting units (Figure 17(a)) and the corresponding results are shown in Figure 17(b). The maximum output power can be obtained to ~24 mW at hot-side of 69ºC (adding the individual power of each device).

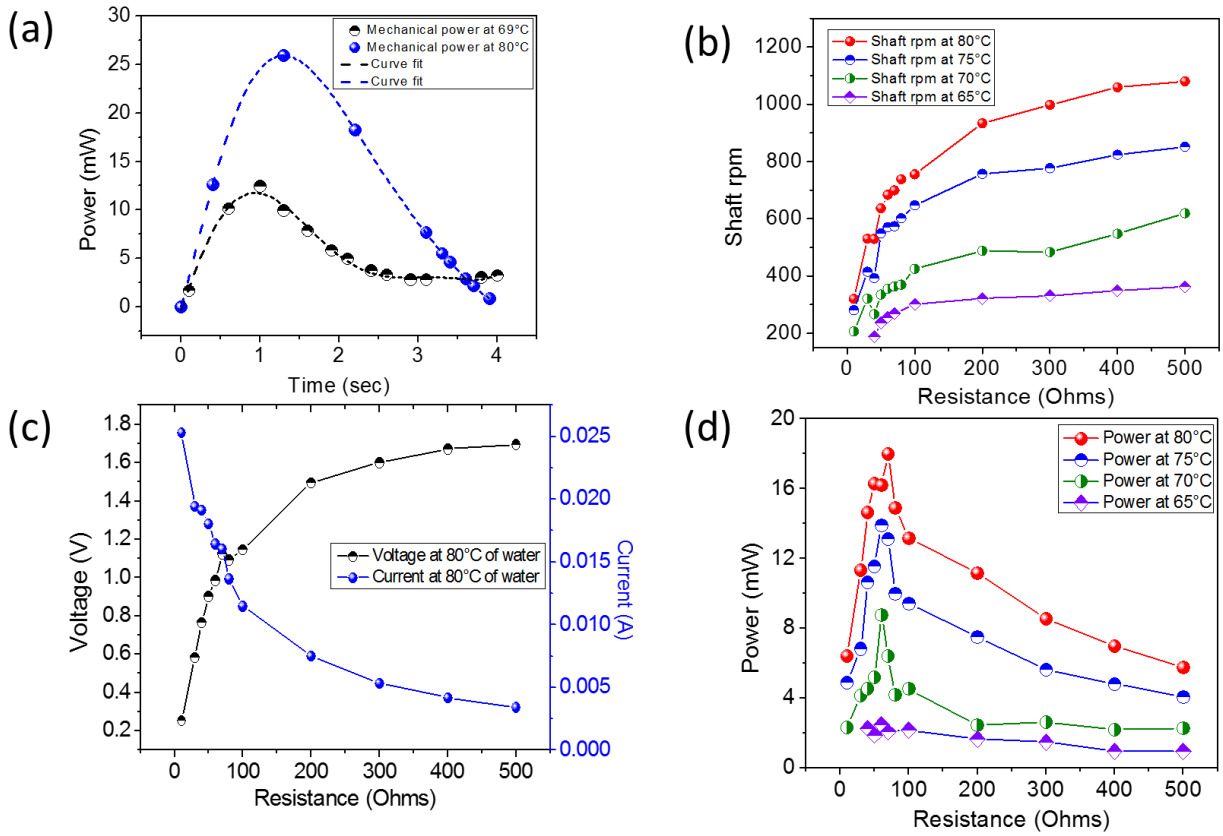

Figure 16: SMA engine performance. (a) Mechanical power for two different thermal input conditions. Maximum mechanical power obtained is 52W/kg (26mW) for operating range considered in this study, (b) Generator (motor operated in reverse) shaft rotation per minute (rpm) at different load with different thermal input temperature from hot water bath, (c) Output current and output voltage as a function of external load resistance for particular thermal input condition, (d) Power obtained as a function of external applied resistance at different thermal input. Maximum electrical power obtained is 36W/kg (18mW) within the operating temperature range at 69% of generator efficiency. The matching external resistance for maximum power output is 70Ω.

(a)

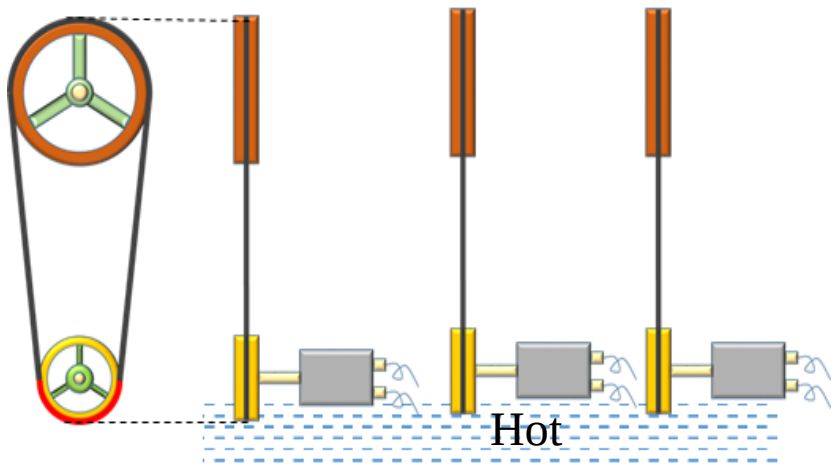

(b)

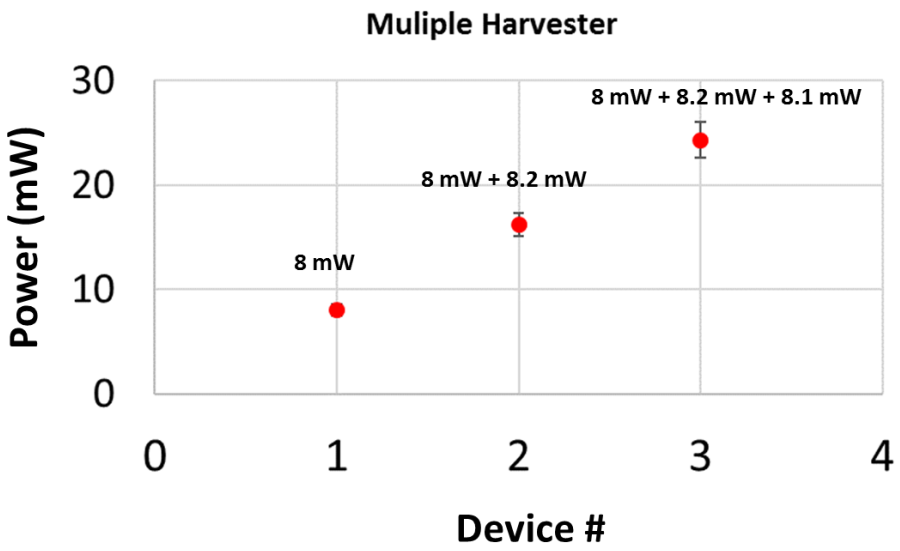

Figure 17: (a) Schematic of multiple shape memory alloy engine in a constant temperature reservoir, (b) Summation of maximum dc power obtained from three different SMA based heat engines

Thermoelastic cycle of SMA engine and efficiency

Traditionally, the thermodynamic efficiency of a heat engine is obtained using certain idealized thermodynamic cycles, such as Carnot cycle for the ideal heat engine, Joule cycle for the jet turbine engine, and Clausius-Rankine cycle for the steam electric power plant. The one fundamental assumption common in all these conceptual cycles is the thermodynamic reversibility of the processes occurring along the thermodynamic paths in these cycles. In reality, none of the actual thermodynamic processes are completely

reversible. In the case of SMA, the forward and reverse phase transformations are not reversible. Figure 18 (a) shows the phase change of SMA material with temperature. We used Maxwell model described by Ziolkowski [30] to formulate the thermodynamic cycle of SMA engine. The thermodynamic cycle of SMA engine is based on the Maxwell model shown in Figure 18. Figure 18 (b) is stress-strain (σ-ε) diagram and Figure 18 (c) is temperature-entropy (T-s) diagram[31].

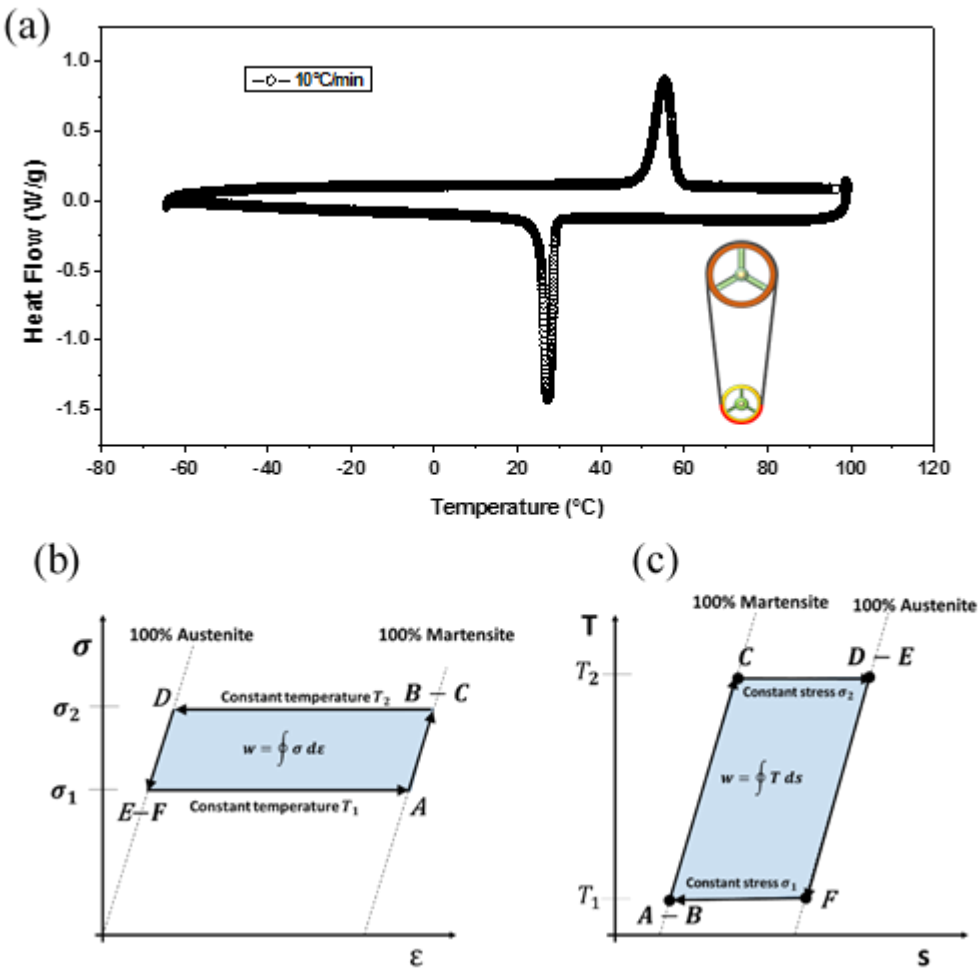

Figure 18: (a) DSC analysis of SMA wire with temperature ramping rate of 10°C/min. (b)-(c) Thermodynamic cycle for shape memory alloys [31].

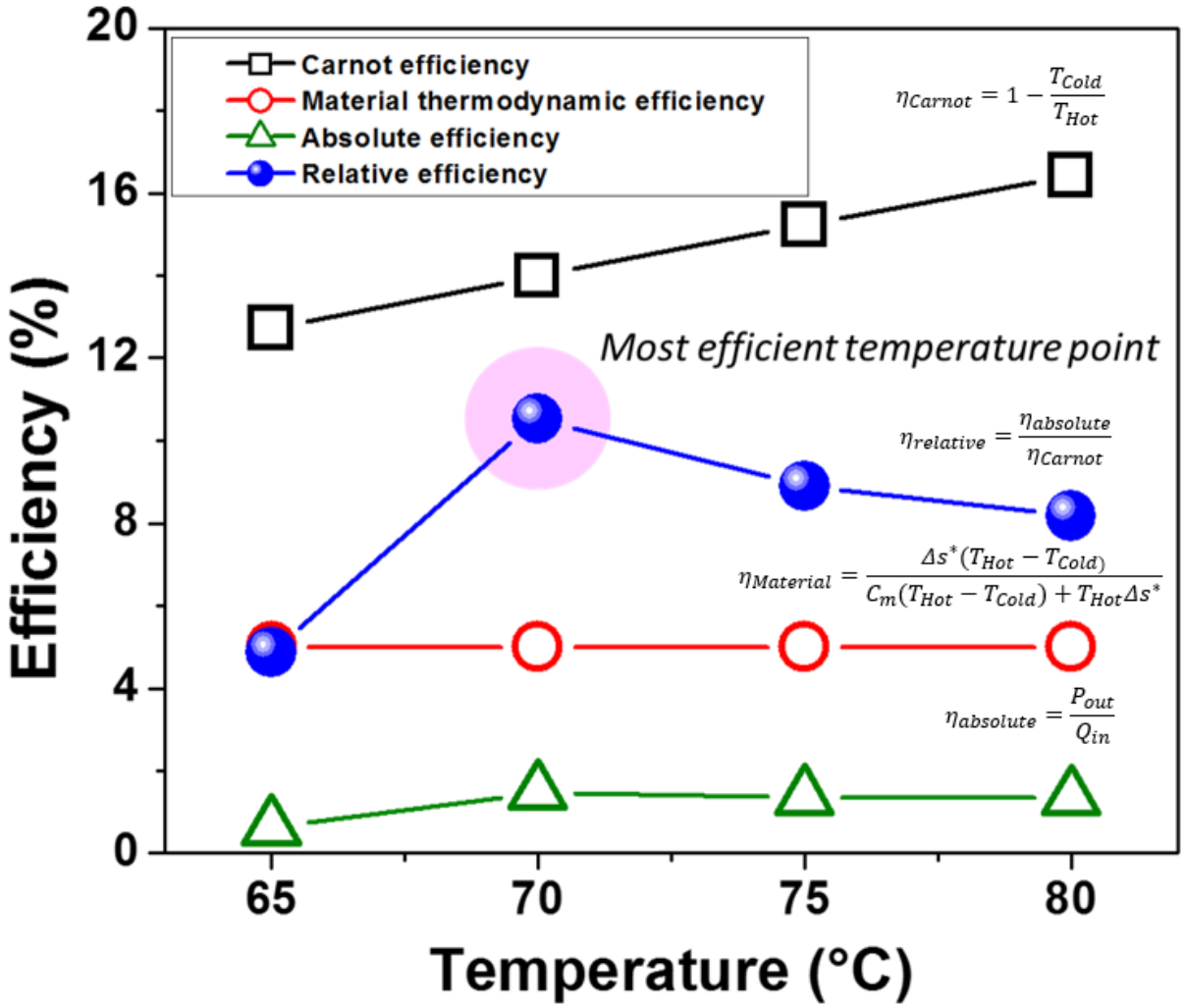

Figure 19: Efficiency of low temperature small-scale SMA engine. Comparison of different type of efficiencies for the SMA engine. Carnot efficiency is calculated from heat source and sink temperatures. Absolute efficiency is system's actual efficiency and evaluated as electrical power output/ thermal energy input. Material thermodynamic efficiency is deduced from the phase transition curve of SMA wire by using fundamentals of thermodynamics. This gives the maximum material capacity for power scavenging. Relative efficiency is defined as absolute efficiency/Carnot efficiency. SMA engine performs maximum efficiency when hot water bath is at 70°C.

Thermodynamic efficiency of the heat engine can be shown as

$$\eta = \frac{w}{q_{in}} = \frac{\oint \sigma d\varepsilon}{q_{in}} = \frac{(C_m - C_a)\,(T_2 - T_1) + T_2 \Delta s_{MA} - T_1 \Delta s_{AM}}{C_m\,(T_2 - T_1) + T_2 \Delta s_{MA}} \quad (9)$$

In case $C_m \approx C_a$ and $\Delta s_{MA} \approx \Delta s_{AM} = \Delta s^*$, equation (9) reduces to $\eta = \frac{\Delta s^*(T_2 - T_1)}{C_m\,(T_2 - T_1) + T_2 \Delta s^*}$

The SMA element temperature rises from T_1 to T_2.

Tension in the wire causes the stress in the element to increase from σ_1 to σ_2.

Constant specific heat capacity C_m.

Δs_{AM} represents change in entropy due to austenite-martensite phase change and C_a denotes specific heat capacity of the austenite phase.

Figure 19 compares the efficiencies calculated for SMA heat engine. SMA material's thermodynamic efficiency is calculated to be 5.0% using equation (9). The absolute efficiency of SMA engine is 1.5%, which is 10.5% of the Carnot efficiency. It should be noted that although output power increases with increase in hot water temperature, the efficiency is maximum at 70 °C. This is an important observation because the forward phase transformation occurs at 54 °C, which is effectively achieved when hot water temperature is 70 °C. Overheating the SMA wire beyond this temperature decreases the system's efficiency. The optimal heat source temperature is the one where 100% forward phase transformation is completed. This is also true for the heat sink temperature. Over-heating or under-cooling decreases the system's efficiency.

The effectiveness of the SMA heat engine was compared with other existing technologies used for thermal-to-electrical energy conversion. In this domain, a thermoelectric generator (TEG) is the most popular device. Normally, the output power and efficiency of TEGs are not readily available for operation below 100°C. We therefore developed a numerical model using ANSYS workbench v17.0 to determine these quantities and validated our calculations with the experimental results reported by Hao et al. [1] The numerical model was then used to produce the power and efficiency data for TEG operating below 100 °C. Supplementary Figure 20 compares the numerical results with the experimental results, which were found to be in close agreement. The numerical model was then modified to account for ambient as the heat sink. From this analysis, at

temperature above 70 °C, SMA engine is competitive (Figure 21(a)) with TEG. Figure 21(b) compares different power indices in terms of active material power density and active material specific power for TEG and SMA engine. The SMA engine can be seen to be competitive with TEG in all the attributes. Further, we compared the cost of our engine with one of the commercially available TEG and found that SMA engine is much cheaper solution (refer next section).

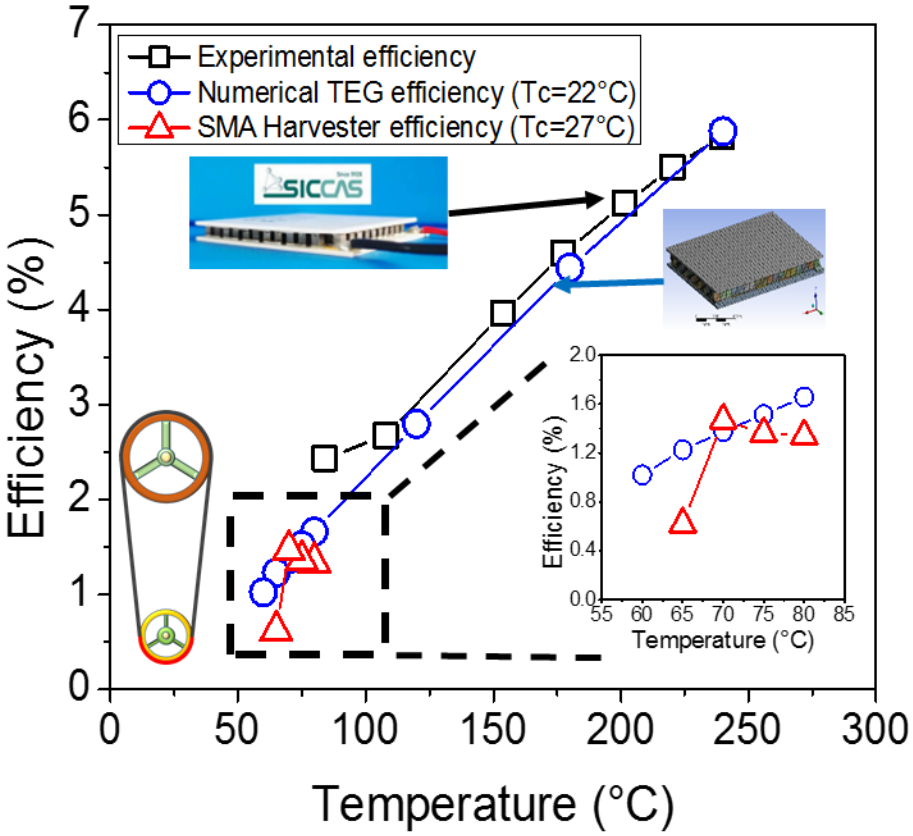

Figure 20: Comparison of efficiencies between experimental results (Hao et al.[1]) and simulation results of the thermoelectric device for higher temperature (>100°C). Extrapolated simulated efficiency results of thermoelectric device for lower temperatures (<100°C) are compared with experimentally obtained SMA-engine.

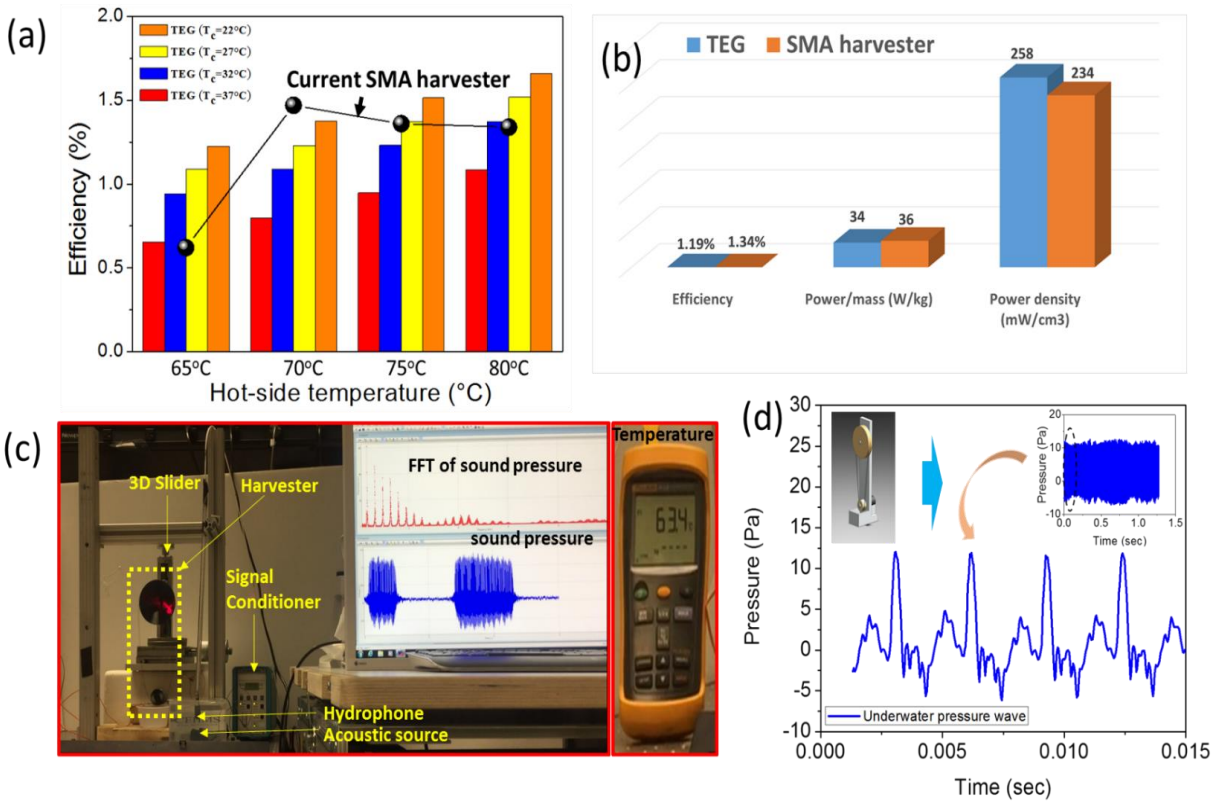

Figure 21: Comparison of SMA engine with existing state of the art thermal energy harvesting technology such as TEG, and experimental setup for powering acoustic projector. (a) Simulation results on TEG under different boundary conditions and comparison with the efficiency of basic version of SMA engine, (b) Various power density indices such as power per unit volume and power per unit mass of active materials along with efficiency are compared for TEG and SMA engine, (c) Experimental setup for demonstration of practical thermal energy harvesting for real-time under water acoustic measurement, (d) Time domain acoustic pressure waveform generated in water from a small SMA engine. The pressure was recorded at 2 cm above the device by hydrophone.

Recently, thermal energy harvesting using tensile muscles has been reported[16], which were shown to exhibit 7.2 W/kg at temperature difference of 70 °C. Comparatively, SMA engine provides the specific power of 36 W/kg at lower temperature difference of 58 °C. In another recent study, a small scale thermo-magnetic harvester has been realized for harvesting thermal gradient by using phase transformations in gadolinium[10]. On the

basis of information available, we evaluated the specific realized power as ~0.6 W/kg for the temperature gradient (ΔT) of 80 °C. This implies that the SMA engine presented in this study exhibits improved performance compared to all current thermal energy harvesting technologies.

Cost comparison with TEG

In this section we compared our harvesting method with TEG module[32] which operates in the same temperature range (< 85°C). The bulk cost of this device is around $21. This device produced around 3 mW when there is no external air flow. In our case, the cost of 1 m of the SMA wire is around $4.75[33]. Currently we are using ~0.5 m of SMA material. Fabrication of metallic and plastic pulley could add $3 per heat engine. Thus, the total cost of laboratory scale heat engine will be ~$6. Our heat engine does not require any additional heat sink or forced cooling mechanism, which ensures its hassle-free operation. With the same temperature range of operation, we could generate around 18 mW of power, as compared 3 mW from TEG. Thus, our heat engine generates 6 times more power at ~1/3rd of the cost compared to TEG.

Demonstrations of SMA heat engine and future impact

We successfully demonstrated several practical applications which could be powered by SMA heat engine. In first demonstration, we continuously operated a sound projector in both air and water medium. Figure 21(c) shows the sound generation in water medium. The sound pressure is recorded by hydrophone (Brüel & Kjær type-8103). Figure 21(d) shows the wave form for generated acoustic pressure. This demonstration paves the pathway for self-sustained air/under-water acoustic communication. We also demonstrate the real time water-health monitoring using the SMA heat engine (Figure 22). This application provides direction for the development of self-sustained health monitoring devices that can be deployed in residential buildings and in natural environments such as hot springs. Next, we evaluated the impact of our heat engine at large scale for long duration of time. Through DMA experiments (Figure 23), we show that the SMA can undergo thermal cycling for three days without any degradation. On the basis of these

outcomes we predict that if our heat engine is operated for 1-3 days it can generate 2.4-7.2 kWh of energy (equivalent to 3.93 – 11.8 pounds of CO_2). Detailed calculations are shown in next section. To further strengthen our arguments for long term operation, we operated heat engine for continuous 10 hours at 65ºC in laboratory environment (Figure 24), and did not observe any change in the performance.

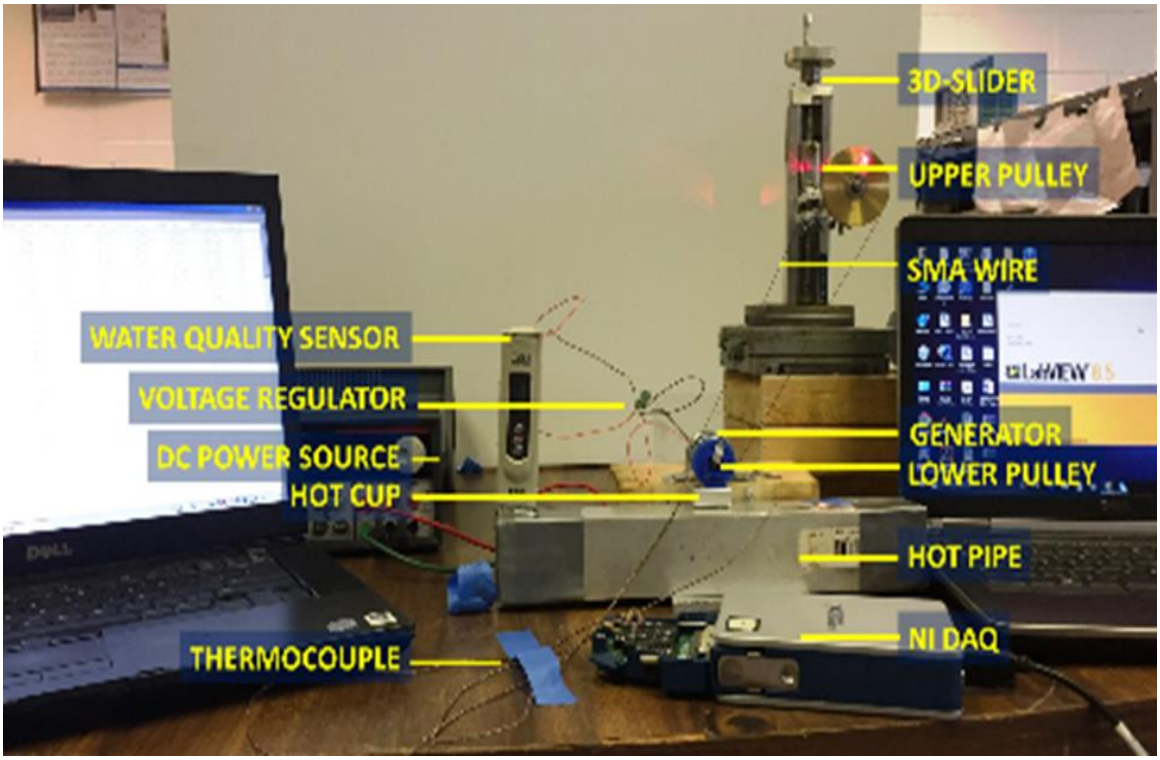

Figure 22: Experimental setup of SMA heat engine for real-time water health monitoring. Low-grade waste thermal energy is converted into mechanical energy and subsequently into electrical energy. For demonstrating the real applications, we coupled the SMA engine with different kind of devices such as water health monitoring sensors. Setup includes SMA wire, hot pipe, Kapton flexible heater (OMEGA Engineering), DC supply (KEITHLEY 2230G-30-1), amplifier, two pulleys, NI-DAQ (M/N: 9171), K-type thermocouple (OMEGA Engineering), step up voltage regulator (POLOLU), water quality sensor-TDS-3(HM DIGITAL) and 3D slider.

The durability of our system is related to the fact that phase transformation happens instantaneously at each point of the material which experiences the required temperature changes. However, in a bulk material, the temperature will not rise and drop uniformly over the whole volume (i.e. the cross-section of wire). If the temperature changes are concentrated at the surface of the wire, the whole material would not be contributing to the phase transformation, and thereby, reduce efficiency. Also a non-uniform distribution of phase transformation triggers the fatigue failure. The observed efficiency and the fatigue resistance of the system further attests the robustness of our engine. The selection of smaller radius wire and enhanced heating time, ensured a uniform phase transformation (forward and reverse) in the wire. More explanation could be found in next section.

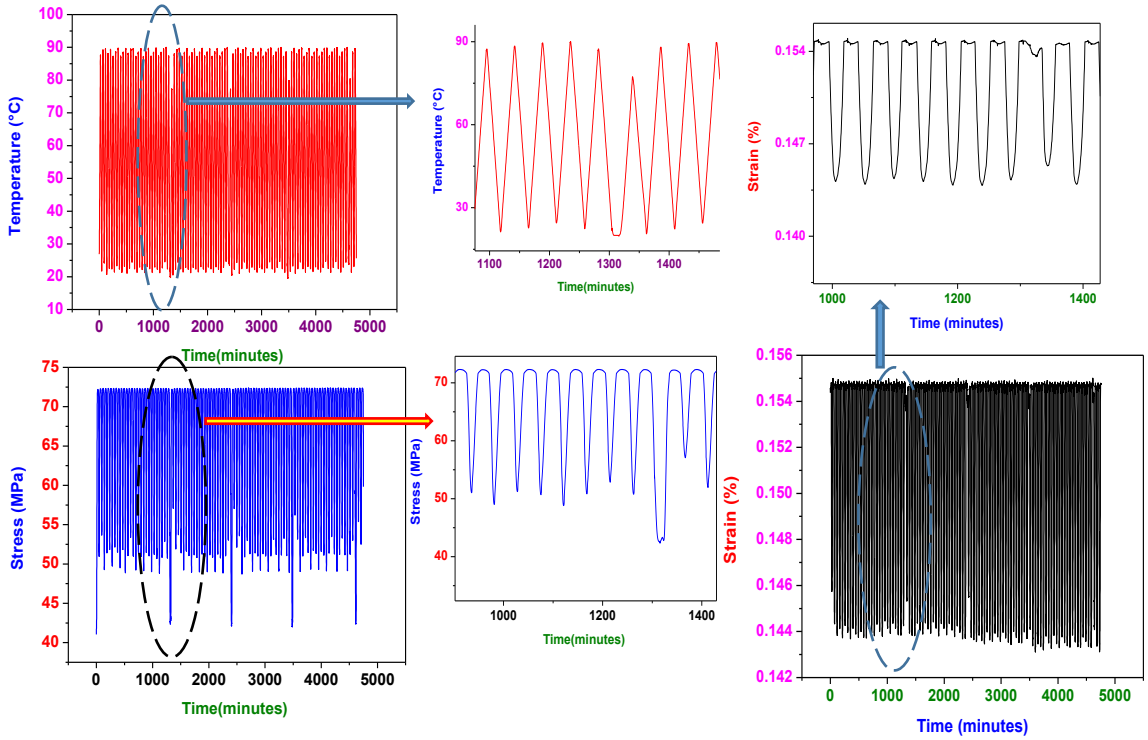

Figure 23: DMA tests for evaluating stress and strain of SMA wire for 3 days.

Brief calculations for carbon foot printing

<u>If device is mounted directly on pipes</u>: one prototype installed around the circumference of a pipe in vertical position. If we consider the per unit length of pipe,

then 1m pipe (if width of device is 2 inches) can easily accommodate 19*1= 19-20 devices. As demonstrated, 18 mW can be produced with equivalent dimensions by using hot water source. Considering the practical operating conditions, it can be safely assumed that 1 device of given dimension can produce = 18*0.55 = ~10 mW.

For 1 m of pipe

No. of device installed ~20

In 1 day, the amount of energy produced by 1m of pipe = .01W*20*24Hrs=4.8WH

In 3 operating days for which we checked the wire stability under DMA test (Figure 23)), the amount of energy produced by 1 m of pipe= 4.8*3 WH=14.4 WH, where WH=Watt Hours

The calculations shown above are for 1m pipe only, but in actual buildings the magnitude of energy generated for 1 day or year will be very high due to availability of long network of pipes.

If we assume the 500 m of pipe network, then amount of energy for 3 days would be =7200 WH =7.2 kWh

Carbon footprints calculations:

As per interface shown on below site

(https://www.epa.gov/energy/greenhouse-gas-equivalencies-calculator)

Our system (in 3 days) in comparison to the energy sources could reduce 11.8 pounds of CO_2

Detailed explanation of long term operation of SMA engine

During the heat engine operation, each material point on the wire experiences a cycle of forward and reverse phase transformation within ~1.5 seconds. With this speed, each material point is exposed to the hot and cold ambient for approximately 0.0033 and 0.3267 seconds, respectively. By considering the small diameter of the wire (0.44 mm) and moderately low temperature difference between the hot and cold sides, a uniform temperature (and consequently phase transformation) distribution in the cross-section can be expected [34, 35]. The observed fatigue resistance of the wires (the wire remains tight and no drop in the efficiency was observed in ~24000 cycles) can be attributed to the

uniform distribution of phase transformation in the cross-section. The non-uniformity in the phase transformation distribution is one of the main reasons behind initiation and propagation of dislocations, particularly from the grain boundaries in polycrystalline bulk materials [36-38]. The multiple experiments indicated the same efficiency and fatigue resistance even for enhanced cycles of operation. Recently, it was reported that by slightly modifying the composition of SMA and modulating phase transition behavior, an extraordinary high fatigue resistance can be obtained [39].

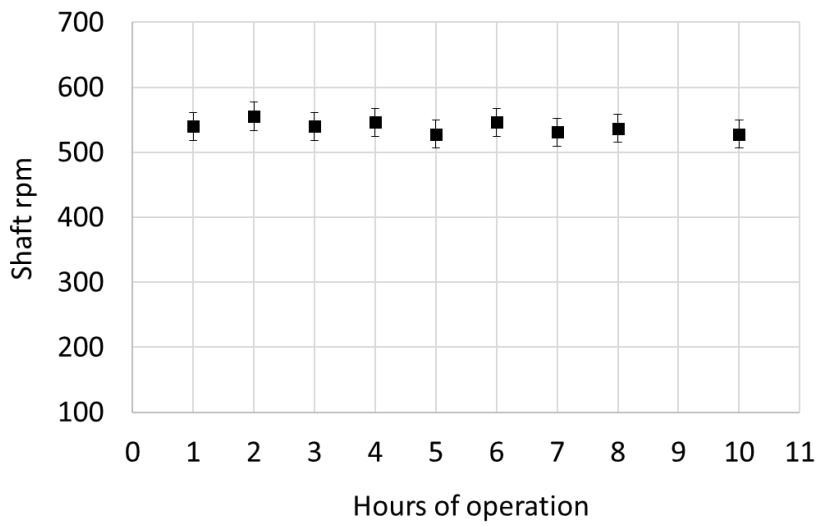

Figure 24: Long hour of operation of SMA heat engine. Lower pulley shaft rpm is shown for 10 hours of operation in lab environment.

Conclusion

In summary, we demonstrate operation of a low grade SMA heat engine that operates below 80°C using ambient as the heat sink. Among the different heat sources examined, the SMA engine performed best with the hot water as the heat source. The maximum mechanical power of the SMA heat engine was found to be 12.5 mW at 69 °C and 26 mW at 80 °C. The mechanical power density of the engine was calculated to be 52 W/kg of the active mass (SMA wire). The maximum electrical power of the SMA heat engine was found to be 8.8 mW at 70 °C and 18 mW at 80 °C. The electrical power density of

the engine was calculated to be 36 W/kg of the active mass (SMA wire). The SMA material's thermodynamic efficiency was found to be 5.0%. The maximum thermal-to-electrical conversion efficiency of the engine was 1.5%, which is 10.5% of the Carnot efficiency. The engine was successfully demonstrated for powering acoustic projector and water health monitoring sensors. Results show that SMA heat engines of the dimensions shown here can reduce 3.93 pounds of CO_2 (carbon footprint) production per day.

Methods and Experiments

The experiments consisted of three main steps. In the first step, differential scanning calorimetry (DSC) and dynamic mechanical analyzer (DMA) studies were performed on five different SMA wires and based upon the results most optimum wire was selected. The SMA wires were cut into small pieces and the test specimens were washed thoroughly with acetone to remove any surface impurities. Before recording the final readings, each test specimens were heated and cooled multiple times in the temperature range of -40 °C to 100 °C in a closed furnace with heating/cooling rate of 10 °C/min. Further, DMA tests were conducted on the selected SMA wire. During these measurements, the sample was scanned from -20 °C to 100 °C at different temperature scan rates (1 °C/min, 2 °C/min and 3 °C/min) and frequencies (0.1 Hz,1.0 Hz, and 10 Hz). In the second step, dynamic thermal analysis was performed on the selected wire. The goal of the experiment was to identify the temperature distribution of the moving wire during operation, right from the point where the wire moves out of the contact with the heat source to the point where it returns back to make contact with the heat source. This experiment is extremely important to understand the thermal response of the SMA wire vis-à-vis thermoelastic cycle efficiency of the SMA material when it is pre-stressed between the pulleys. The detailed schematic of the experimental setup is shown in Figure 10(a). Since the SMA wire was thin (~ 0.44 mm) and moving, the experiment was very sensitive to external factors such as ambient temperature and air speed. Therefore, the entire experimental set-up was thermally isolated during the measurements. Infrared (IR) camera (FLIR SC6700, FLIR Systems, Inc.) was used to capture the radiation coming from the thin moving SMA wire and the temperature gradient was evaluated accordingly.

Before running the experiments, IR camera was calibrated with a thermocouple by matching the surface temperature of the stationary wire under ambient condition (at 22°C). In order to mitigate the experimental error due to the reflections from the surroundings, the entire experimental setup was painted black and covered with black fabrics. In addition, in order to obtain the accurate and high resolution thermal data, the entire engine was divided into small sections and the IR radiation coming from each section was captured separately. Also, a thin graphite layer was deposited on the SMA wire in order to enhance its surface emissivity. Before capturing any data from IR camera, a preliminary thermal analysis (DSC) was conducted to understand the effect of the graphite layer on SMA wire. Figure 10(b) shows the DSC results before and after graphite coating indicating very minor differences. Inset shows the scanning electron microscope (SEM) image having graphite coating. All the thermal videos representing the dynamics of wire were processed using a MATLAB code to obtain the temperature profile. In order to minimize the inconsistency during experiments, temperature data from several videos were averaged and a final temperature gradient was obtained along the length of the wire.

In the third and last step, we measured the power output of SMA engine. Figure 15 shows the schematic diagram of experimental set-up used to measure the mechanical and electrical power output. Two pulleys of different diameters (optimized diameter ratio 1:3) were fixed on two ends of 3-D slider stand through two small ball bearings. The SMA wire was looped around the two pulleys. The optimal distance of 6.50” was maintained between the two pulleys and the length of the wire was determined after running several preliminary experiments. The shaft through the lower pulley was connected to a small permanent magnet DC generator (rated at 6V and Model # RF-500TB). A small portion of the SMA wire maintaining contact with the lower pulley was heated either through hot water bath or a heat gun or radiation from a hot plate. The generator was connected to a resistance box (RS-201, IET LABS Inc.) whose resistance could be varied between 0 to 500 Ω to identify the optimal load. A data acquisition system, SIGLAB-SIGDEMO was used to acquire the voltage waveform. A voltmeter (FLUKE 179) was also connected in parallel to the external resistance to monitor the output voltage. An optical tachometer

(SHIMPO DT-209X) was used to measure the angular speed of the rotating pulleys. The vibration of the moving SMA wire was captured using a high resolution camera and the video was image-processed using a MATLAB code to evaluate the vibrational characteristics such as amplitude and frequency.

References

[1] Hao F, Qiu P, Tang Y, Bai S, Xing T, Chu H-S, et al. High efficiency Bi 2 Te 3-based materials and devices for thermoelectric power generation between 100 and 300° C. Energy & Environmental Science. 2016;9:3120-7.

[2] Zheng X, Liu C, Yan Y, Wang Q. A review of thermoelectrics research–Recent developments and potentials for sustainable and renewable energy applications. Renewable and Sustainable Energy Reviews. 2014;32:486-503.

[3] Elsheikh MH, Shnawah DA, Sabri MFM, Said SBM, Hassan MH, Bashir MBA, et al. A review on thermoelectric renewable energy: Principle parameters that affect their performance. Renewable and Sustainable Energy Reviews. 2014;30:337-55.

[4] Rowe DM. Thermoelectrics, an environmentally-friendly source of electrical power. Renewable energy. 1999;16:1251-6.

[5] Riffat SB, Ma X. Thermoelectrics: a review of present and potential applications. Applied thermal engineering. 2003;23:913-35.

[6] Ravindran S, Huesgen T, Kroener M, Woias P. A self-sustaining micro thermomechanic-pyroelectric generator. Applied Physics Letters. 2011;99:104102.

[7] Sebald G, Guyomar D, Agbossou A. On thermoelectric and pyroelectric energy harvesting. Smart Materials and Structures. 2009;18:125006.

[8] Sebald G, Lefeuvre E, Guyomar D. Pyroelectric energy conversion: optimization principles. IEEE transactions on ultrasonics, ferroelectrics, and frequency control. 2008;55.

[9] Ujihara M, Carman G, Lee D. Thermal energy harvesting device using ferromagnetic materials. Applied Physics Letters. 2007;91:093508.

[10] Chun J, Song H-C, Kang M-G, Kang HB, Kishore RA, Priya S. Thermo-Magneto-Electric Generator Arrays for Active Heat Recovery System. Scientific Reports. 2017;7:41383.

[11] Elliott J. Thermomagnetic generator. Journal of Applied Physics. 1959;30:1774-7.

[12] Stauss H. Efficiency of thermomagnetic generator. Journal of Applied Physics. 1959;30:1622-3.

[13] Smoker J, Nouh M, Aldraihem O, Baz A. Energy harvesting from a standing wave thermoacoustic-piezoelectric resonator. Journal of Applied Physics. 2012;111:104901.

[14] Lee SW, Yang Y, Lee H-W, Ghasemi H, Kraemer D, Chen G, et al. An electrochemical system for efficiently harvesting low-grade heat energy. 2014.

[15] Abraham TJ, MacFarlane DR, Pringle JM. High Seebeck coefficient redox ionic liquid electrolytes for thermal energy harvesting. Energy & Environmental Science. 2013;6:2639-45.

[16] Kim SH, Lima MD, Kozlov ME, Haines CS, Spinks GM, Aziz S, et al. Harvesting temperature fluctuations as electrical energy using torsional and tensile polymer muscles. Energy & Environmental Science. 2015;8:3336-44.

[17] Ismail BI, Ahmed WH. Thermoelectric power generation using waste-heat energy as an alternative green technology. Recent Patents on Electrical & Electronic Engineering (Formerly Recent Patents on Electrical Engineering). 2009;2:27-39.

[18] Hettiarachchi HM, Golubovic M, Worek WM, Ikegami Y. Optimum design criteria for an organic Rankine cycle using low-temperature geothermal heat sources. Energy. 2007;32:1698-706.

[19] Barbier E. Geothermal energy technology and current status: an overview. Renewable and Sustainable Energy Reviews. 2002;6:3-65.

[20] Wakjira JF. The VT1 shape memory alloy heat engine design: Virginia Polytechnic Institute and State University; 2001.

[21] Schiller EH. Heat engine driven by shape memory alloys: prototyping and design: Virginia Tech; 2002.

[22] Avirovik D, Kumar A, Bodnar RJ, Priya S. Remote light energy harvesting and actuation using shape memory alloy—piezoelectric hybrid transducer. Smart Materials and Structures. 2013;22:052001.

[23] Sato Y, Yoshida N, Tanabe Y, Fujita H, Ooiwa N. Characteristics of a new power generation system with application of a shape memory alloy engine. Electrical Engineering in Japan. 2008;165:8-15.

[24] Johnson I, Choate WT, Davidson A. Waste Heat Recovery. Technology and Opportunities in US Industry. BCS, Inc., Laurel, MD (United States); 2008.

[25] https://maps.nrel.gov/geothermal-prospector/.

[26] Villanueva A, Gupta S, Priya S. Lowering the power consumption of Ni-Ti shape memory alloy. SPIE Smart Structures and Materials+ Nondestructive Evaluation and Health Monitoring: International Society for Optics and Photonics; 2012. p. 83421I-I-12.

[27] Tadesse Y, Thayer N, Priya S. Tailoring the response time of shape memory alloy wires through active cooling and pre-stress. Journal of Intelligent Material Systems and Structures. 2010;21:19-40.

[28] Kase S, Matsuo T. Studies on melt spinning. I. Fundamental equations on the dynamics of melt spinning. Journal of Polymer Science Part A: General Papers. 1965;3:2541-54.

[29] Kishore RA, Coudron T, Priya S. Small-scale wind energy portable turbine (SWEPT). Journal of Wind Engineering and Industrial Aerodynamics. 2013;116:21-31.

[30] Ziótkowski A. Theoretical analysis of efficiency of shape memory alloy heat engines (based on constitutive models of pseudoelasticity). Mechanics of materials. 1993;16:365-77.

[31] Qian S, Ling J, Hwang Y, Radermacher R, Takeuchi I. Thermodynamics cycle analysis and numerical modeling of thermoelastic cooling systems. International Journal of Refrigeration. 2015;56:65-80.

[32] https://www.digikey.com/product-detail/en/marlow-industries,-inc/EHA-PA1AN1-R03/1681-1087-ND/7537072?WT.srch=1&gclid=EAIaIQobChMIpNPlk_Xk3QIVCFSGCh2dOQH7EAQYAiABEgLFzfD_BwE.

[33] http://www.dynalloy.com/flexwire_70_90.php.

[34] Mirzaeifar R, DesRoches R, Yavari A. Analysis of the rate-dependent coupled thermo-mechanical response of shape memory alloy bars and wires in tension. Continuum Mech Therm. 2011;23:363-85.

[35] Mirzaeifar R, DesRoches R, Yavari A. Is the Stress Distribution Uniform in the Cross Section of Sma Bars Subjected to Uniaxial Loading? Is It Related to Rate Dependency? Proceedings of the Asme Conference on Smart Materials, Adaptive Structures and Intelligent Systems (Smasis 2011), Vol 1. 2012:281-8.

[36] Mirzaeifar R, DesRoches R, Yavari A, Gall K. A micromechanical analysis of the coupled thermomechanical superelastic response of textured and untextured polycrystalline NiTi shape memory alloys. Acta Mater. 2013;61:4542-58.

[37] Yazdandoost F, Mirzaeifar R. Tilt grain boundaries energy and structure in NiTi alloys. Computational Materials Science. 2017;131:108-19.

[38] Yazdandoost F, Mirzaeifar R. Generalized stacking fault energy and dislocation properties in NiTi shape memory alloys. Journal of Alloys and Compounds. 2017;709:72-81.

[39] Chluba C, Ge W, de Miranda RL, Strobel J, Kienle L, Quandt E, et al. Ultralow-fatigue shape memory alloy films. Science. 2015;348:1004-7.

Chapter 6

Energy Harvesting and Strain Sensing in Smart Tire for Next Generation Autonomous Vehicles

Deepam Maurya,* Prashant Kumar*, Seyedmeysam Khaleghian, Rammohan Sriramdas, Min Gyu Kang, Ravi Anant Kishore, Vireshwar Kumar, Hyun-Cheol Song, Jung-Min Park, Saied Taheri, and Shashank Priya

***These authors contributed equally to this work.**

Published in Applied Energy. 2018; 232:312-22

Abstract

In this paper, we demonstrate the feasibility of the strain energy harvesting from the automobile tires, powering wireless data transfer with enhanced frame rates, and self-powered strain sensing. For this, we used a flexible organic piezoelectric material for continuous power generation and monitoring of the variable strain experienced by a tire under different driving conditions. Here, we report enhanced power output of ~580µW at 16 Hz (~70 mph) using our energy-harvester and tire strain sensor mounted on a section of a tire, which directly powered 78 LEDs. We further demonstrated that the stored energy was sufficient to sense the tire deformation, and transmit the data wirelessly with an enhanced frame rate to control system of a vehicle. Using sensors mounted on a real tire of a mobile test rig, measurements were conducted on different terrains with varying normal loads and speeds to quantify the sensitivity and self-powered sensing operation. These results provide a foundation for self-powered real-time sensing and energy efficient data transfer in autonomous vehicles.

Introduction

In autonomous vehicles, energy requirement has been increasing rapidly with the increased number of power-hungry onboard sensors, and the enhanced requirement for an increased rate of wireless data transfer for safe and reliable driving. There is a tremendous amount of development taking place in both academia and industry to provide devices, systems, and techniques that lead to energy efficient self-governing automobile environment [1, 2]. For automobiles, tires act as an interface between the vehicle control system and the external environment. In order to achieve tire-based self-powered sensing of the external environment, recent focus has been on developing smart tires [3, 4]. The sensor arrays, in smart tires, are used for monitoring and evaluating different physical quantities such as road/terrain characteristics, air pressure, road/tire friction, loadings, wear, and hydroplaning [5]. These quantities are then used by intelligent algorithms for enhancing the consistency, longevity, safety, stability and fuel efficiency of a vehicle [3, 6, 7].

The smart tires are not only beneficial for the autonomous cars (Figure 1(a)), but, also will be helpful in controlling tire-related crashes in traditional vehicles. The tire-related crashes can be extremely deadly, and sometimes highly damaging to the environment also, as shown in Figure 1 (b). According to a report [8], out of the total number of crashes, the tire-related crashes were approximately 6%, 4.6%, 4.3%, and 3.5% for passenger cars, SUVs, pickups, and vans, respectively. Among different kinds of vehicles, the tire-related crashes (as shown in Figure 1(c)) were highest for the light passenger car (66.3%), which was followed by SUVs (17.4%), pickups (11.1%), and vans (4.9%). Therefore, developing an energy efficient smart tire has been one of the important aspects in achieving fully autonomous vehicles. Global initiatives such as European Union project APOLLO (2003) and Bridgestone/Firestone recall helped to fuel the momentum of intelligent tire development in the beginning of 21st century [9, 10]. During initial stages of research, the main focus was to develop the tire pressure monitoring system (TPMS) [11, 12]. However, recent studies have shown that other characteristics such as road friction, tire-road interactions, and wheel loads are equally important to ensure better and safe driving [3, 4, 7, 13, 14].

Different methods such as accelerometers [7, 15], piezo-based [16, 17], magnetic-based [13, 18, 19], capacitive-type [20, 21], and surface acoustic wave (SAW) [22, 23] have been used in previous studies to measure the parameters such as acceleration, strain, temperature, and pressure. All these technologies have their advantages and limitations with respect to tire platform. For example, accelerometers are easy to integrate and can work over a wide range of temperature, however, these types of sensors are rigid, expensive, not compatible with large deformations, and extremely sensitive to the surrounding noise [3]. Capacitive sensors are good candidates for pressure sensing and strain measurements [21, 24], but suffer from the drawback that its sensitivity varies with temperature and hence need additional compensation circuits [3]. Pohl et al. used SAW technique to estimate the tire deformations and frictional characteristics [25], however, this method often needs additional acquisition systems, wireless communication infrastructure, passive external power, and may have difficulty to withstand large deformation of a tire [6, 26]. Most of these embedded sensors require a robust wireless infrastructure along with the power source. For example, TPMS [12, 27], which is integrated in each wheel to monitor the tire pressure, usually, consists of a pressure sensor, a microcontroller for processing, a radio frequency (RF) communication system to wirelessly transmit the data to the vehicle's central receiving unit, and a battery as a power source. This scenario is expected to become more complex with the increasing number of sensors in the next generation of the autonomous vehicles [28]. Enhanced number of sensors require additional power, which further depends on the rate of the data transfer. Although batteries are the easy and inexpensive source for providing constant voltage supply, they have a major drawback of their limited utilization time, and high labor cost for replacement [4, 29]. The limited availability of energy restricts the use of increased frame rate for the wireless data transfer, which renders reduced reaction time for the driver in case of an emergency.

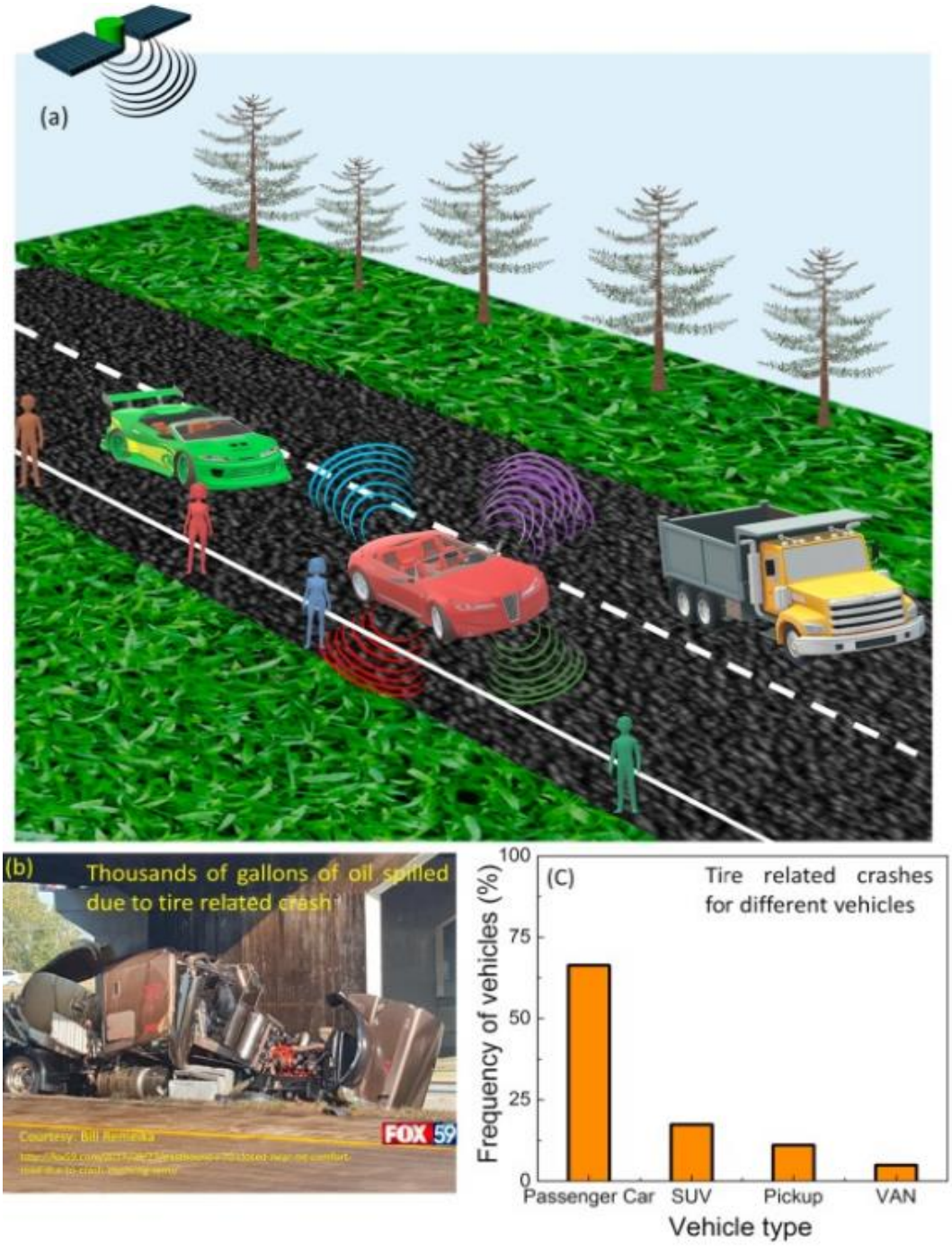

Figure 1: (a) Schematic of an autonomous vehicle on the road. (b) Oil spill due to a flat tire-related accident causing serious environmental threat. (c) The distribution (%) of tire-related crash vehicles including their types. (Source: U.S. Department of Transportation, National Highway Traffic Safety Administration)

To replace these batteries, various energy harvesting technologies have been developed for harnessing the untapped mechanical energy of tire to electricity, which otherwise goes waste. Most of the vehicle-related energy harvesting technologies are focused on harvesting energy from the vehicle vibration and/or exhaust heat with the aim of reducing the dependency on the vehicle's main heavy battery and extra load on the engine [30, 31]. Some of these methods of tire energy harvesting utilized following transduction materials: electromagnetic [32, 33], piezoelectric [12, 29], microfiber/piezoelectric composites [26, 34], and nanogenerators (based on triboelectric and Zinc Oxide (ZnO)) [35, 36]. However, most of these harvesters had certain limitations. For example, electromagnetic harvesters are cost-effective, but difficult to integrate due to their large size. Furthermore, MFCs and nanogenerators are flexible in nature and may have enhanced power density. However, the fabrication process of these materials is complex, and involves multiple steps, which render them expensive. The integration of these sensors would dramatically increase the cost of the tire. Additionally, because these harvesters are very sensitive to the temperature, the increased tire temperature during motion could be an issue [34]. The resonance based PZT harvesters were not able to function beyond the certain frequency ranges and required tip masses making system bulky to integrate in a tire. On the other hand, flexible PVDF based harvester appears to be the perfect match for harvesting tire strain energy considering large deformation of tires and ease in integration. Therefore, to achieve cost-effective and robust intelligent tires, one needs to develop an effective self-powered sensing method, which does not depend on the external power source. Furthermore, the sensing element should be extremely easy to integrate to avoid complexity and possess low stiffness [3, 4]. These flexible sensors should have stable behavior as a function of temperature with low fatigue.

In present work, we have attempted to provide a cost-effective solution to above mentioned issues and demonstrate a self-powered sensor based upon an organic piezoelectric material. A low value of elastic modulus ensures the high strain development in this piezoelectric patch, which is one of the important parameters for strain sensors. We realized the high-power density and high temperature (up to 90°C)

stability of organic piezoelectric based harvester. Further, we demonstrate that the generated energy from this piezoelectric patch in normal tire condition is sufficient to power 78 LEDs and wireless systems. This provides an estimate for the power needed to develop efficient wireless data transfer and power management. In order to understand the dynamics of the tire during rotation under load, we developed a mathematical model and evaluated various key parameters such as radial and tangential displacement of the tire, and voltage from a flexible piezoelectric sensor. After mathematical analysis, we integrated piezo patch in a tire mounted in a mobile test rig. The tests were performed on different types of roads (under variable wheel loading) to demonstrate the sensing capabilities. These experimental results were also validated qualitatively (voltage trend with velocities) through analytical modeling.

Experimental

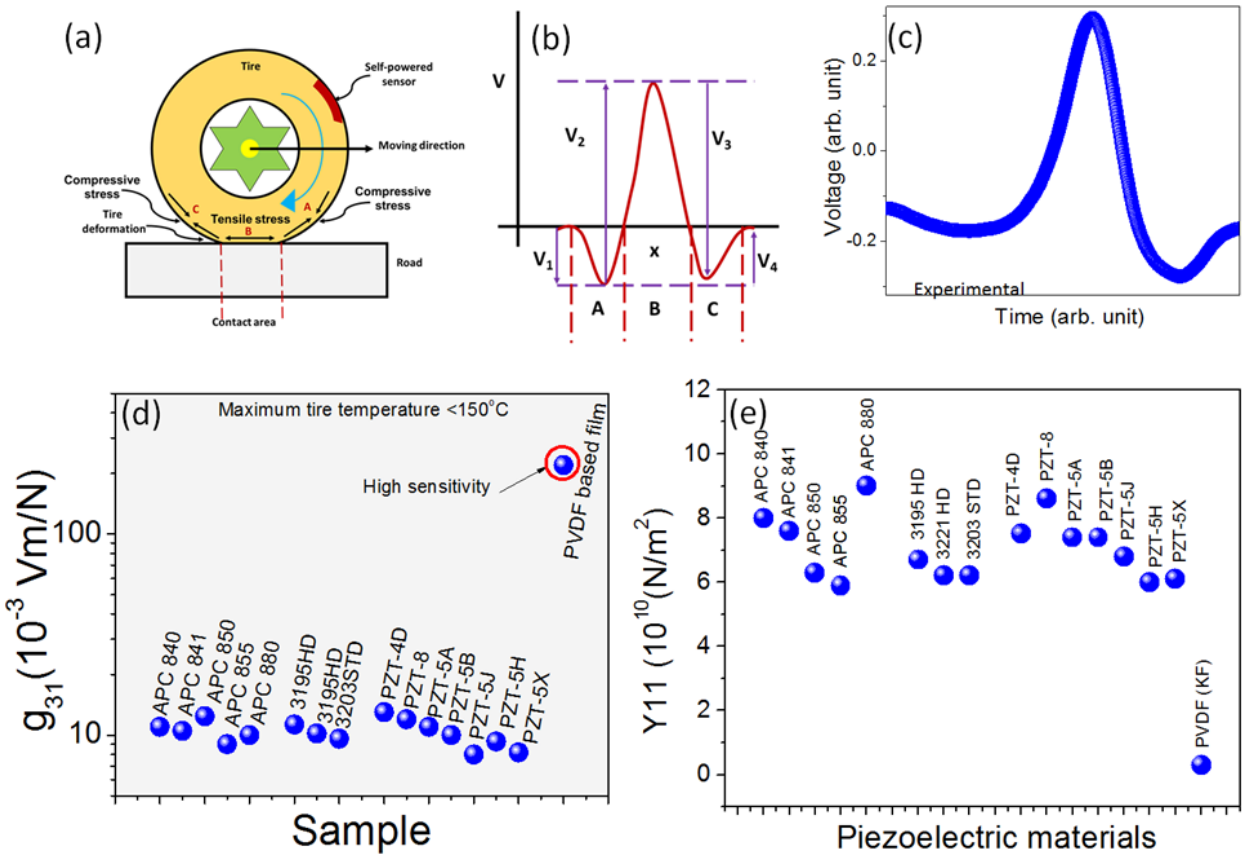

Figure 2: (a) Schematic of the tire deformation with different types of strain. (b) Schematic waveform generated due to the tire deformation. (c) Experimental waveform due to the tire deformation. (d) Voltage coefficient of various piezoelectric materials. (e) Young's modulus of various piezoelectric elements.

In order to measure the strain in the tire and for their health monitoring, the piezoelectric material was used. First, to assess the power requirements, we mounted a PVDF based piezoelectric patch (KF Piezo film, KUREHA) on a section of the tire. The list of properties for this material has been provided in the Table 1. The tire-section was rigidly secured at two ends to provide the cantilever boundary condition on a vibration isolation smart table (Newport ST series). The shaker, which was coupled with a function generator through an amplifier (HP 6826A), was used to excite the tire-section. The output voltage was measured using an oscilloscope (DSO1014A, Keysight). The 2D scanning laser vibrometer (Polytec PSV-500) was used to measure the displacement and the dynamic profile of tire-section in a lab environment. Furthermore, we conducted the experiments to evaluate the thermal stability and reversibility of the functional response of piezoelectric patch. A heat gun was used to heat the system, and the temperature was measured through a *K*-type thermocouple. During tapping on the tire (through a shaker), we tried to emulate the real displacement profile of a moving tire in the lab environment. Furthermore, we demonstrated powering of 78 LEDs, and the capability of the wireless data transfer from a sensor (MIDASCON) using energy stored from the piezoelectric patch integrated on a tire-section. Lastly, we mounted our sensor on the real tire (Goodyear, model # P245/70R17) installed on a mobile tire test rig. These field tests were performed using different normal loads and speeds at Virginia Tech Transport Institute (VTTI).

Results and discussion

Figure 2(a) shows the schematic of the tire deformation during motion of a typical vehicle. Please note three zones of the tire deformation; A and C are compressive zones, and B is the tensile zone. During motion on a given terrain, the deformation of the tire generates a waveform sensed through a self-powered piezoelectric sensor. This waveform

is schematically shown in Figure 2(b) [34]. Using our piezoelectric based self-powered sensor, mounted on the tire, we experimentally observed similar waveform due to tire deformation. The waveform characteristics are a function of varying load depending upon vehicle, speed, and terrain etc. PVDF based organic piezoelectric materials are an excellent choice here because of a wide frequency range of operation, sensitivity (Figure 2(d)), and small Young's modulus (Figure 2(e)). Further, this polymer-based piezoelectric material is stable up to 90°C (Figure 3(a)), which meets the requirement for mounting within a tire.

In order to characterize the voltage output characteristics of the piezoelectric sensor, mechanical excitation from a shaker was utilized. Figure 4(a) shows a photograph of the sensor mounted on a section of a tire, where shaker is behind this tire-section. The dynamics of the piezoelectric sensor, on such excited tire-section, was investigated using a laser vibrometer. Tire section was discretized into many points, which were scanned through a laser. The root mean square (RMS) displacement profile, during one of the measurement, can be seen in Figure 4(b).

Table- 1 Properties of the commercial PVDF based piezoelectric patch*

Property	**Unit**	**Value**
Density	ρ 10^3 kg/m3	1.78
Dielectric constant	ε_r	13
Piezoelectric constant	d_{31} pc/N	25
	e_{31} mc/m2	75
	g_{31} mVm/N	220
Elongation	MD	% (at Break): 20-30
	TD	% (at Yield): 5-7

* http://www.piezofilms.com/products.html

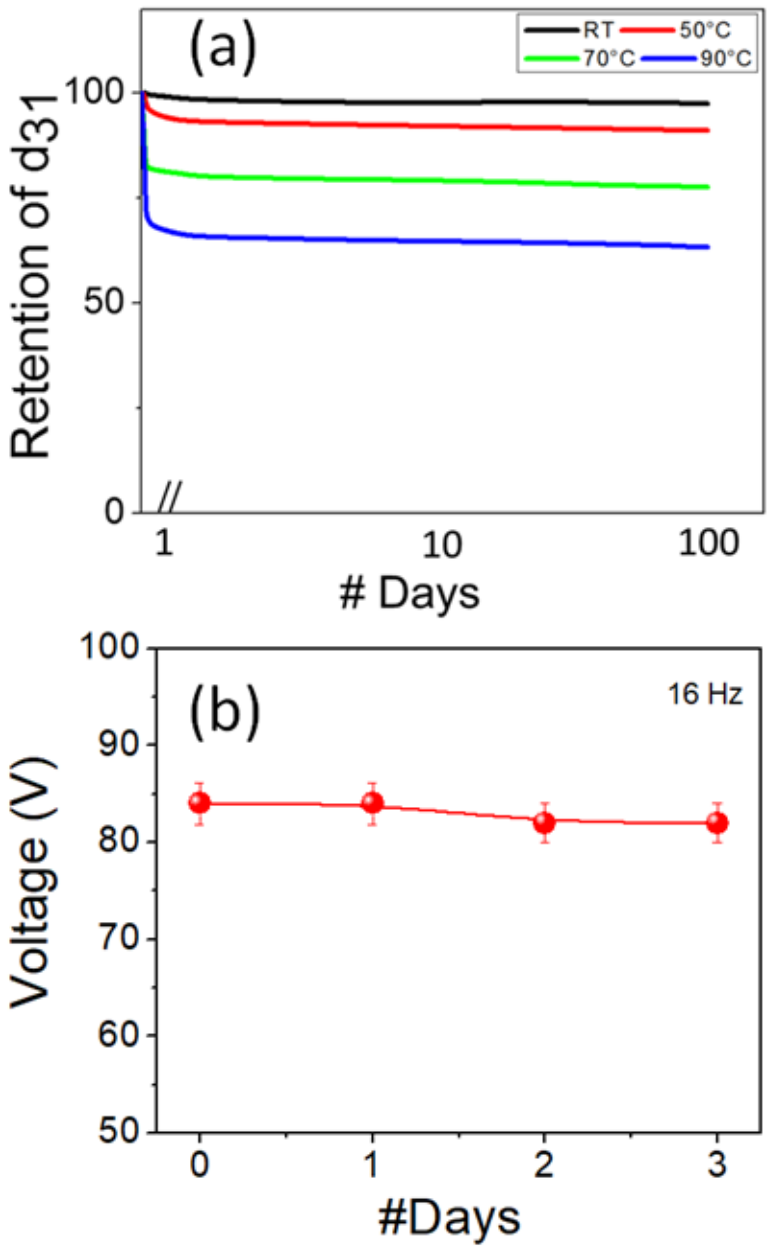

Figure 3: (a) Retention percentage of PDVF property, used in the study, at different temperatures. The material shows the good retention of d_{31} even at a higher temperature for a long duration (100 days) (replotted from datasheet http://www.piezofilms.com/products.html), (b) Patch voltage output versus a number of days under mechanical excitation of 16 Hz.

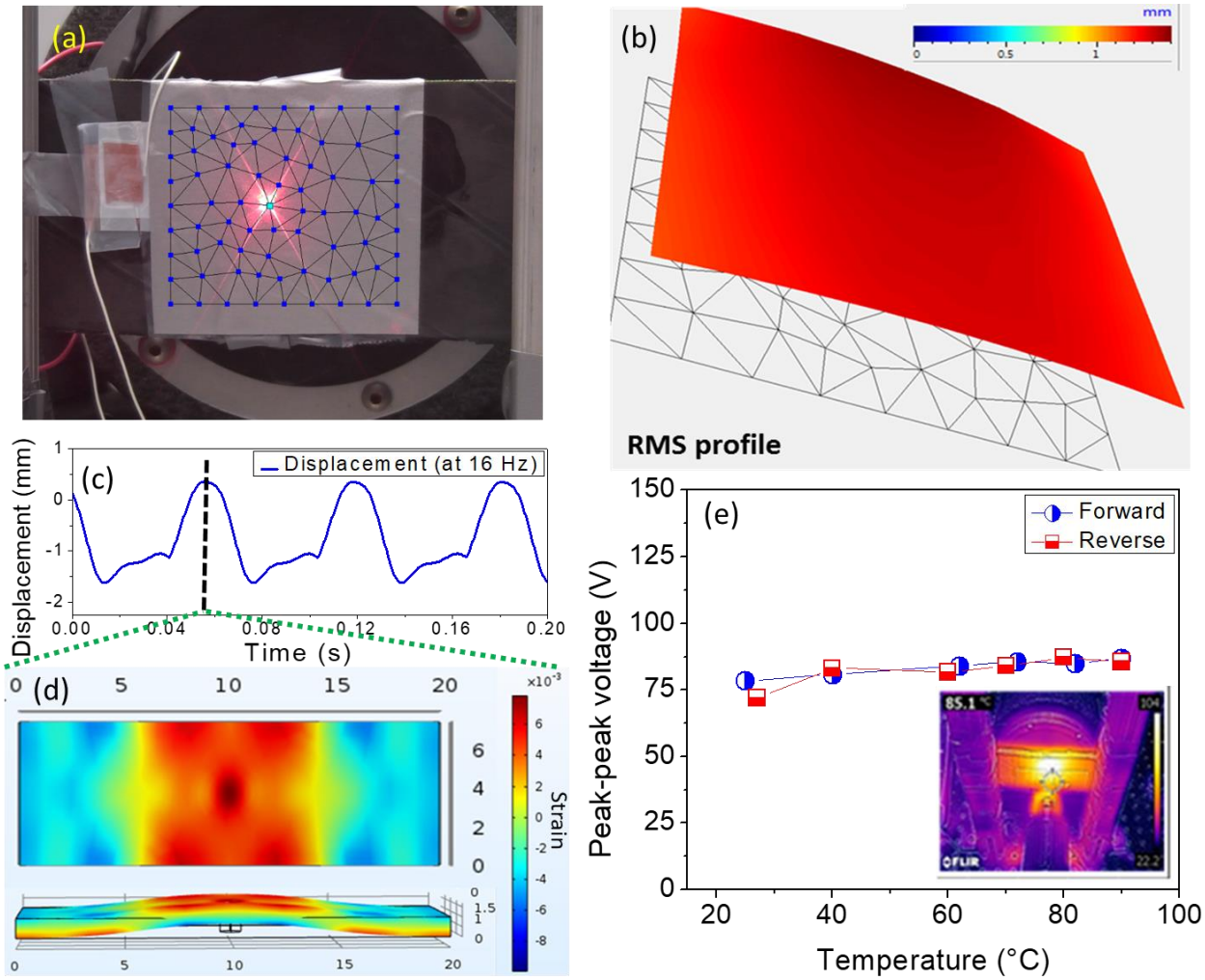

Figure 4: (a) Photograph of the laser scanning path for measuring displacement. (b) Surface displacement measured using laser vibrometer. (c) Displacement at the center point of tire section. (d) Simulated maximum strain contour for the displacement input shown in Figure 4(c). (e) Performance of organic piezoelectric patch at different temperatures. Inset image shows an infrared camera photograph indicating temperature distribution.

This profile shows almost a flat dynamic response (each point has the same displacement) across the scanned area of the tire-section, which illustrate that the tire-section was systematically excited with no relative motion among various points on the surface at a given frequency. These results were used to emulate the dynamics of a tire in

a real moving vehicle, when a particular section of a tire gets a repetitive normal reaction force from the road after a regular interval of time (or at a particular frequency). Figure 4(c) shows the displacement at the center point of the tire section. We have calculated the strain values across the tire section by using the displacement profile (as input) measured at the center of the patch (Figure 4(d)). Corresponding to the displacement of 2mm at 16Hz, a 0.8% maximum strain was estimated for one cycle. During vehicle movement for a long period of time and then applying brakes, could sometimes heat-up tires to the temperatures ~ 80°C-90°C [34], which requires sensors to be stable in that temperature regime. Figure 4(e) shows the peak to peak voltage at variable temperatures. The piezoelectric sensor used in this work was found to exhibit stable voltage output over a temperature range of 25-90°C. From the results under a given thermal cycle, one can infer that the sensor was stable up to 90°C and did not exhibit hysteresis losses due to thermal cycling. It is worthwhile to mention, we tested the piezoelectric patch under controlled mechanical excitation at 16 Hz for 3 days, and did not observe any significant change in the patch output, as shown in Figure 3(b).

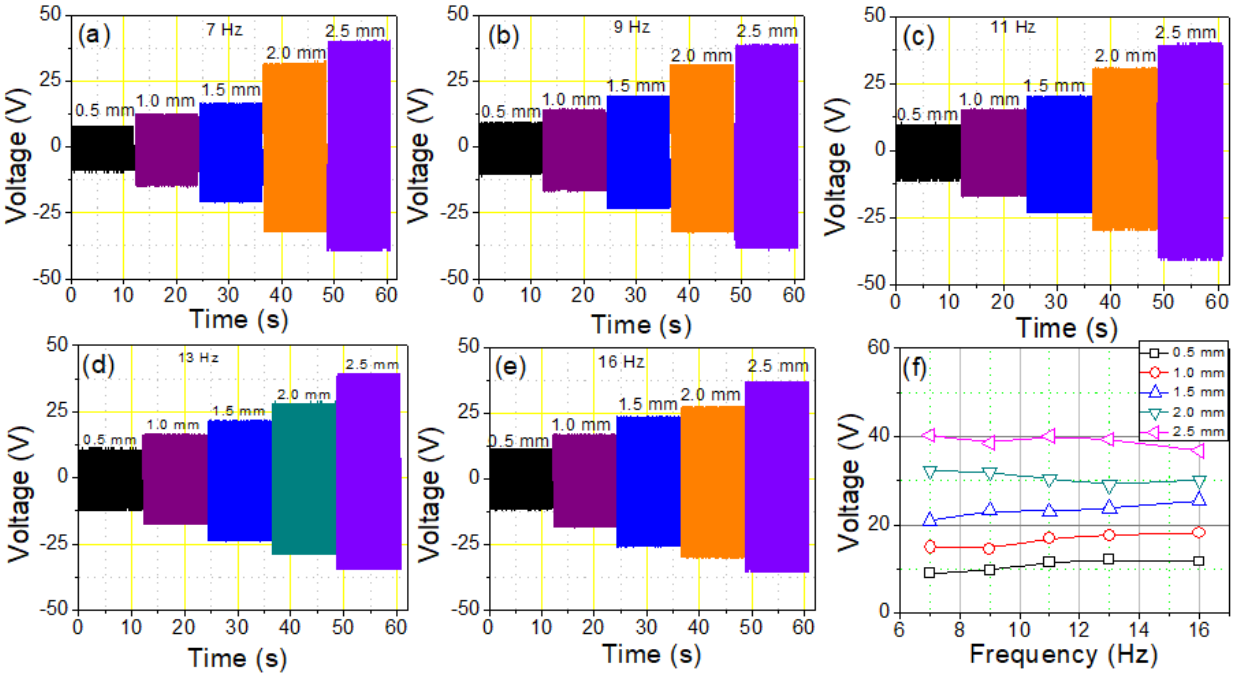

Figure 5: Output voltage at different displacements for (a)7 Hz, (b) 9 Hz, (c) 11Hz, (d) 13 Hz, (e) 16 Hz. (f) Output voltage versus frequency at different displacements. The displacements were measured at the center point of tire section.

Electrical characterization in Lab Environment

We measured the voltage output from the piezoelectric patch under different displacements at various frequencies (7-16 Hz). The frequency range was derived from the vehicle's speed (30-70 mph) considering average tire dimensions (overall diameter-24.98"). One can clearly observe in Figure 5(a)-(e) increase in the open circuit voltage (OCV) output with increasing displacement at the center of the patch. Increased displacement enhances the strain in the tire, which in turn, results in enhanced voltage output. Figure 5(f) shows the summary of voltage output as a function of frequency at different displacements. The output voltage was found to increase monotonously with increasing frequency for displacements up to 1.5 mm. However, for displacements > 1.5 mm, the output voltage was found to decrease with increasing frequency. The voltage-frequency response indicated that the resonance frequency of our experimental system doesn't fall within the given frequency range. This provided us an opportunity to conduct the systematic study on the tire (which should represent the real case as well), in a laboratory environment. Power generation for two different cases was quantified: (i) fixed tire displacement (2 mm) with varying frequencies, and (ii) fixed shaker power input at varying frequencies.

In order to measure maximum instantaneous power generated from the piezoelectric patch, at 2.0 mm displacement, a range of the load resistances was utilized, as shown in Figure 6(a). The maximum power was obtained to be 150 μW at a frequency of 16 Hz across 2 MΩ load resistance. We also measured the power output at various other frequencies using the same experimental setup (at 2 mm displacement), and found that the peak power range varied from 100 μW to 150 μW. On further increasing the input voltage amplitude for the shaker, the maximum power was obtained to be 580 μW (Figure 6(b)). Figure 6(c) shows the open circuit voltage generated at different frequencies for a fixed shaker amplitude. With increasing frequency, the output voltage

was found to increase up to 13 Hz before slightly dropping at 16Hz. Fig. 6(d) shows the force input of shaker to the tire setup. The force measurements were carried out using a Futek force sensor having a sensitivity of 48.6 Newton/Volt (Figure 7). It can be observed that there is a significant difference in the force dynamics (at variable frequencies) at different excitation input. This force difference can be easily observed in power output as well. On increasing the shaker input, although tire displacement saturated, force input to the tire was found to increase (as shown in Figure 6(d)) significantly, thereby, increasing the voltage and power output.

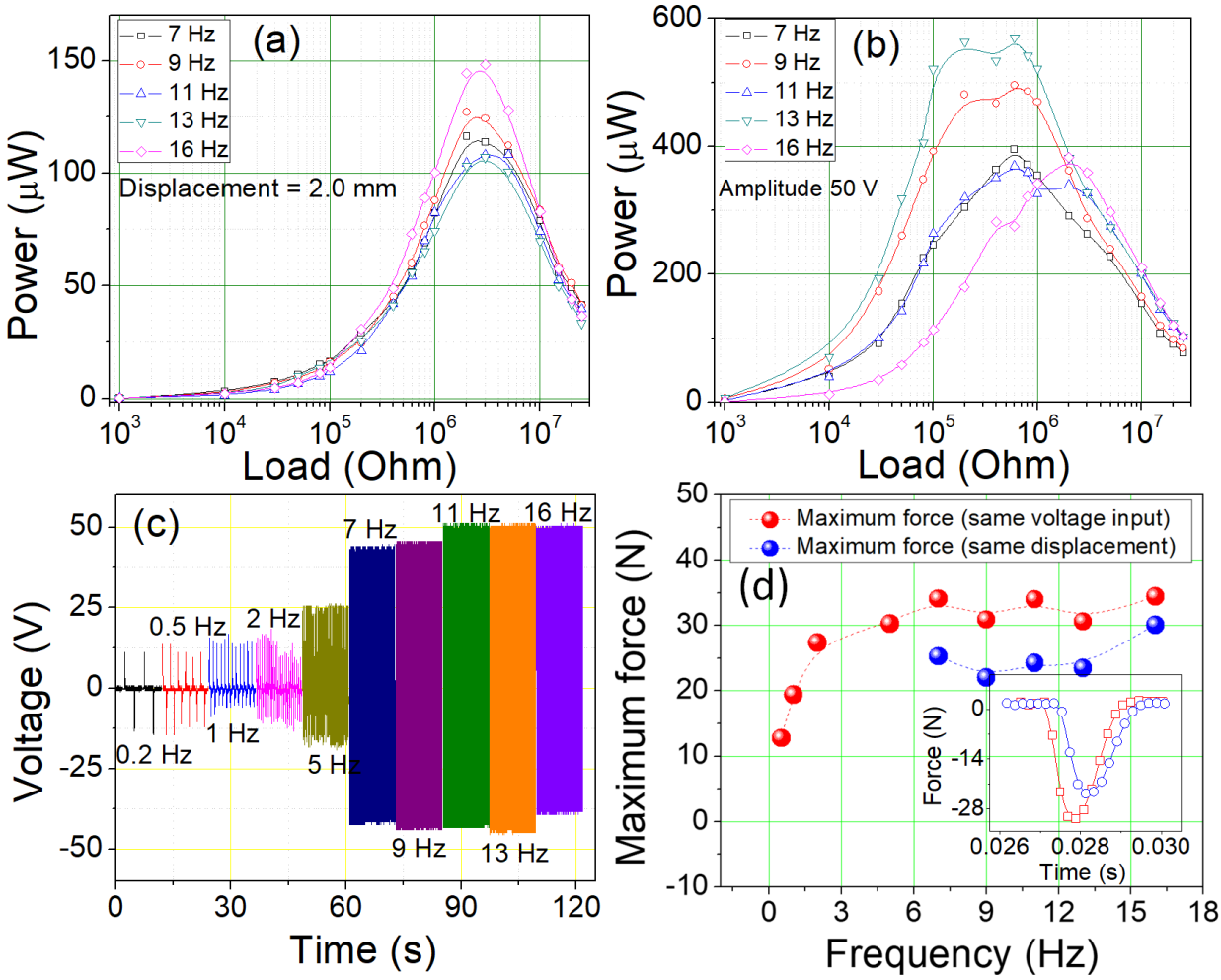

Figure 6: (a) Power output versus resistance at different frequencies at controlled displacements (measured at center point). (b) Power output at the increased level of shaker amplitude (50V input) from the piezoelectric sensor. (c) Voltage output at different frequencies for an increased level of shaker amplitude selected in (b). (d) Force

input to the tire from shaker at different frequencies. Inset image shows the waveform of the force applied by the shaker on the tire section.

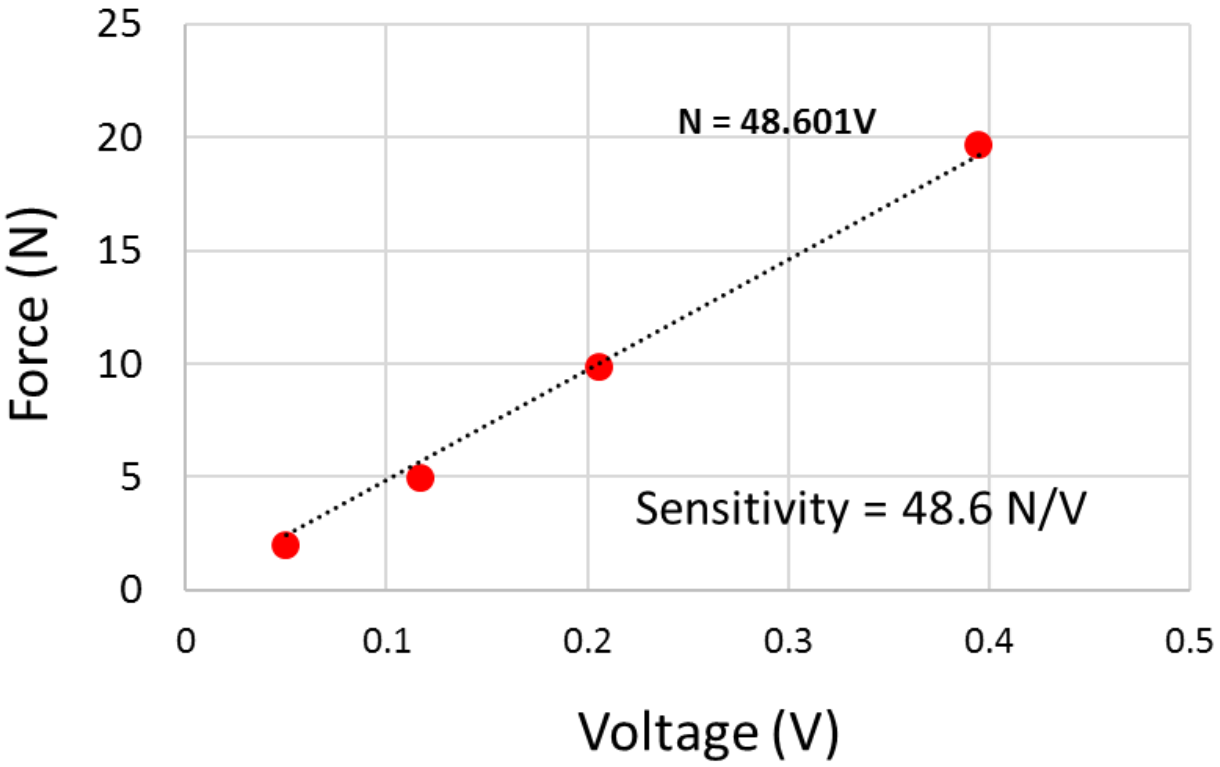

Figure 7: Force versus voltage data for the force sensor. The slope indicates the sensitivity of the force sensor used in the present work.

This harvester-cum-sensor patch can have multiple functions, because, it can sense tire dynamics, and provide power for wireless data transfer. Figure 8(a) shows the setup for the successful demonstration of lighting 78 LEDs directly using the power generated from this piezoelectric patch. To demonstrate real applications of the power generated, we powered a commercial wireless sensor using stored power (in a capacitor) through a rectifier circuit (Figure 9) from the piezoelectric patch, and demonstrated wireless data transfer related to the temperature and humidity, as shown in Figure 8(b). The data transfer was accomplished using a commercial wireless sensor (installed on an electric kettle) and a mobile phone based app. Figure 8(c) illustrates the temperature and

humidity information from the surface of a kettle with respect to time. After switching on the kettle, the surface temperature increased, which, in turn, made the surrounding ambient dry reducing humidity. This demonstration shows the capability of this piezoelectric patch as a sensor to read the real-time information without external bias, and powering the onboard wireless data transfer system to transmit the sensed information. Next, we discuss the power management for this wireless data transfer.

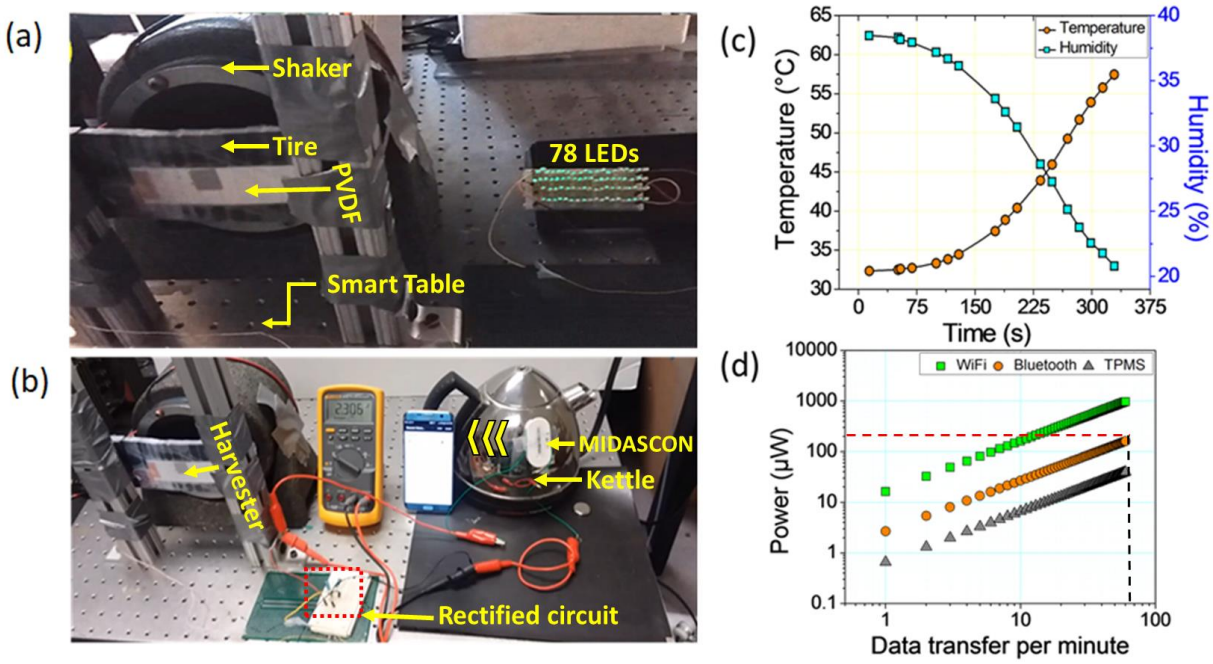

Figure 8: (a) 78 LED were powered using the piezoelectric patch under consideration. (b) Wireless data transfer demonstration using power stored from the piezoelectric patch mounted on the tire section. (c) Temperature and humidity data transferred wirelessly by utilizing stored energy. (d) Power management analysis for various current technologies. The dotted lines show the power (~225 μW) requirement for data transfer (~60 data per minute).

Power management for the wireless data transfer

In a TPMS system, the communication system regularly sends message frames containing tire pressure information. If the tire pressure is below a threshold, the central receiving unit presents an alert on the driver's dashboard. In a TPMS, most of the battery's power is consumed during transmission of the message frames [37]. Hence, to

conserve energy and extend battery life, the frame rate transmitted from the TPMS is traditionally limited to a very low value, e.g., the communication system transmits only one frame per minute [38].

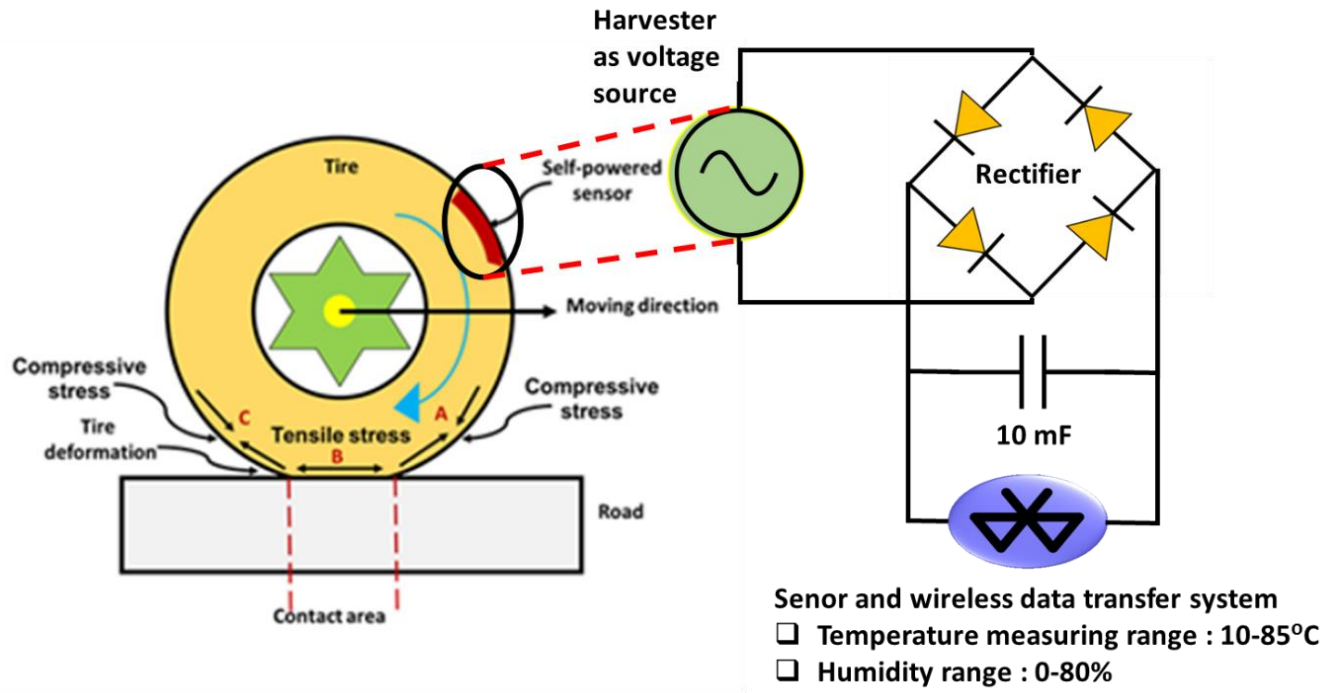

Figure 9: The electric circuit for powering wireless data transfer system.

Note that the transmission of a message frame only lasts for a few milliseconds, and the communication system remains idle for the rest of the time to conserve energy. This reduces drivers' precious reaction time in case of the tire blowout or sudden puncture, which could lead to an accident. Further, the wireless communication system in traditional TPMS cannot support a large amount of data transfer, and hence the data is limited to the minimal information related to tire pressure. The communication of additional information about other important characteristics, such as road friction and tire-road interactions, require more advanced communication systems, such as Bluetooth and Wi-Fi. Figure 8(d) exhibits the power required for the wireless data transfer for the different number of transmitted frames per minute in different state-of-the-art

technologies. These plots show increased power requirement for highly efficient data transfer rate in technologies like Bluetooth and Wi-Fi as compared to TPMS. Therefore, advanced wireless data transfer technologies require more power, increasing the load further on the available energy.

Here, we analyze the frame rate that could be achieved by our self-powered sensor fitted with a state-of-art Bluetooth Low Energy (BLE) communication system [39]. This communication system requires around 4 milliseconds to transmit one message frame which comprises of monitoring information of 512 bits [40]. On average, the communication system draws around 40 mW at 3 V during this transmission. Hence, a total of 160 µJ is required to transmit a frame. Different technologies used in power management: Tire pressure monitoring system (TPMS), Bluetooth , Wi-Fi. A detailed transmission process is shown in Table 2. With an average power generation of around 225 µW in our self-powered sensor, the required energy can be generated and stored in one second. Hence, our self-powered sensor is capable of sending at least one frame per second (60 frames per minute). From the above analysis, we observe two advantages of using our sensor. Firstly, we could utilize Bluetooth technology which supports the transfer of a larger amount of data as compared to the TPMS. Secondly, the achievable frame rate with our sensor could be two orders of magnitude higher than the conventional TPMS. The affordability of sending data with increased frame rate per minute provides increased critical reaction time to the driver to handle the situation in case of a tire blowout or puncture increasing road safety [41].

Table 2: Power transmission process

Transmission process (Phases)	Power (mW)	Time (ms)	Energy (µJ)
Start up	15	1	15
Receive configuration	66	0.512	33.792
Switch interval	45	0.6	27
Transmit	84	0.512	43.008
Post-processing	24	1.4	33.6
Total		4.024	152.4

Tire modeling for field condition

After detailed experimental analysis in a lab environment, a theory has been developed to illustrate the integration of tire dynamics with our piezoelectric patch for the real road conditions to predict the voltage outcomes. In this section, through mathematical modeling, we predicted the displacements of a tire, the voltage output from a patch for different driving conditions such as tire speed.

Theory: Voltage Response from an organic piezoelectric patch on a rotating tire

The voltage response from a PVDF based piezoelectric patch, mounted on a tire, was estimated from the electrical enthalpy density by applying Hamilton's principle [42]. The electrical enthalpy density H, for a piezoelectric patch on a tire, defined by the domain Γ as a function of strain S_{11}, electric field E_3, Young's modulus c_{11}, permittivity ε, and piezoelectric stress coefficient e_{31} is given as:

$$H = \frac{1}{2}\int_{\Gamma}\left(c_{11}S_{11}^2 - 2e_{31}S_{11}E_3 - \varepsilon E_3^2\right)d\Gamma\,, \tag{1}$$

The tire was modeled as a rotating ring with radial and tangential stiffness, as described in references [43-45]. The circumferential strain in the tire, S_{11}, can be written as a function of circumferential deflection, v(θ,t), as [46]

$$S_{11} = \frac{1}{2r^2}\left(v + v''\right)^2 + \frac{z}{r^2}\left(v' + v'''\right), \tag{2}$$

where r is the radius of the tire and z is the distance along the thickness. It may be noted that the inextensible condition ($w = -v'$) was employed in deriving eqn. (2). Following the procedure developed by Meirovitch to estimate the response of gyroscopic systems [47], the radial deflection, w, can be given by

$$w(\theta,t) = \sum_{n=1}^{\infty}\frac{Fn^2\cos\left(n(\theta - \phi_0 + \Omega t)\right)}{\pi b\left(n\Omega\left(m_n n\Omega - g_n\right) - k_n\right)}\,, \tag{3}$$

where the force at an angle ϕ_0, width, stiffness, mass, and damping of nth mode, and wheel rotation rate are denoted by F, b, k_n, m_n and g_n, and Ω respectively [44]. It was assumed that the piezoelectric patch would not affect the dynamics of tire motion. Hence, the voltage developed by the patch was determined by solving the following differential

equation obtained by collecting the terms containing the first variation of voltage from the action integral.

$$\frac{V(t)}{R}\theta_0 + C_p\dot{V}(t) + \frac{b_0 e_{31}(t+t_p)}{2r}\left(v'(\theta_0,t)+\dot{v}''(\theta_0,t)\right)=0\,, \tag{4}$$

where b_0, t, t_p and C_p are width, thickness of tire, piezoelectric patch spanning over an angle of θ_0 and film capacitance respectively.

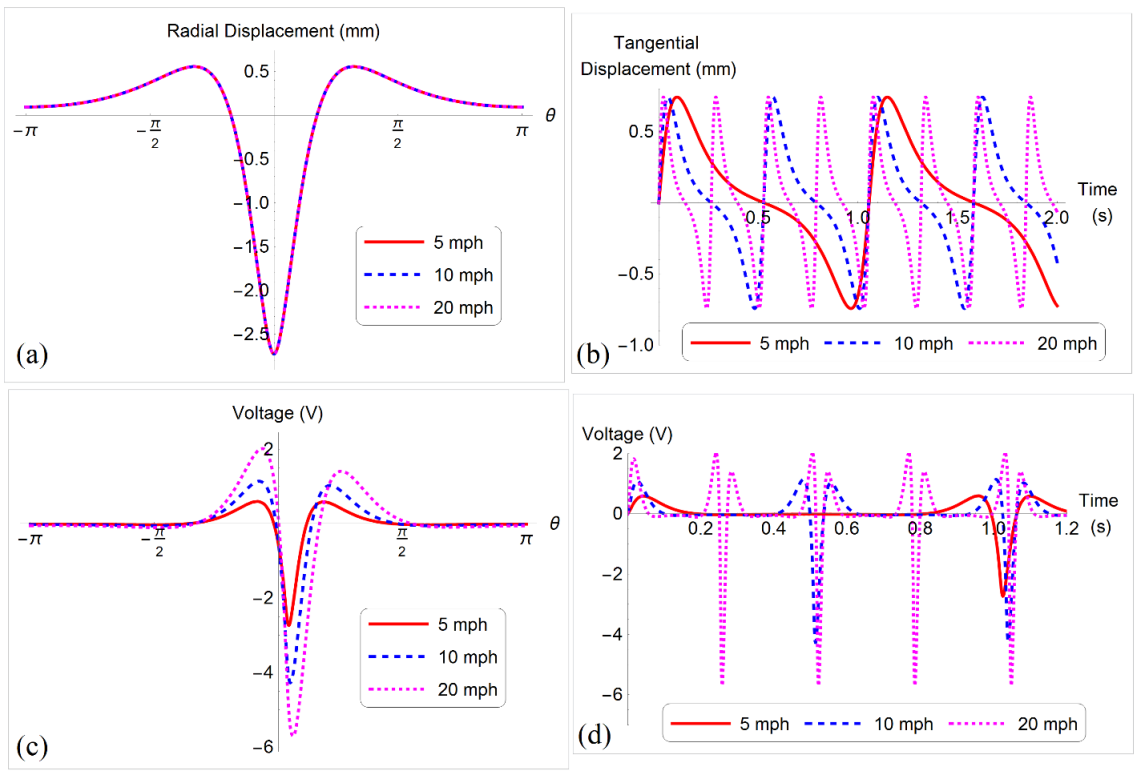

Figure 10: (a) Radial displacement of the tire as a function of angular position at three different speeds of 5 mph, 10 mph, and 20 mph. It can be noticed that the displacement remained same for all the speeds with respect to the angular position. (b) The tangential displacement as a function of angular position for three speeds. It can be observed that the amplitude of the displacement remains the same. However, the rate at which the displacement changes with time, increases with speed. (c) The voltage response as a function of angular position for three speeds. (d) The voltage developed by the piezoelectric patch at different speeds is shown as a function of time. Although the

displacement of the tire was not increasing with speed, the generated voltage and the power was found to increase with speed.

Simulations

The tire model used in the experiments and simulations was P245/65R17 105S. Based on the experimental modal analysis, the equivalent radial and tangential stiffness were estimated to be 1562 kN/m^2 and 2212 k N/m^2 respectively. These numbers were obtained by matching first three tire resonant frequencies corresponding to n = 2, 3 and 4 with experimentally observed frequencies 93, 108 and 132 Hz, respectively. The radial displacement was estimated for a load of 3000 N at three speeds namely, 5 mph, 10 mph and 20 mph. The piezoelectric patch had a width of 80 mm and spanned over an angle of 12 degrees on the tire. The radial displacement and tangential displacement were estimated from eqn. (3), and are plotted in Figure 10(a) and (b) respectively. It can be observed that both radial and tangential displacement amplitudes of the tire do not change with speed. However, the rate of change of the displacement was higher with increasing speed. The voltage developed by the piezoelectric patch was estimated by solving the differential equation given in eqn. (4). The voltage developed by the piezoelectric patch at a load resistance of 100 kOhm for three different speeds is shown in Figure 10(c) as a function of angular position. The voltage developed by the patch in a time domain is shown in Figure 10(d). The RMS voltage at 5 mph, 10 mph, and 20 mph speeds was 0.21 V, 0.62 V, and 1.1 V, respectively. The resulting average power at 5 mph, 10 mph, and 20 mph speeds was 0.4 μW, 3.8 μW and 12 μW, respectively. We performed simulations for different sensor patch length and found that the voltage output increases with the increase in the sensor patch length (Figure 11). By arranging multiple piezoelectric patches along the tire, the generated power can be scaled up.

Real-time field testing of the sensor integrated within a tire

After characterizing the piezoelectric patch and performing the modeling, we mounted the patch on a tire integrated within a mobile test rig, as shown in Figure 12(a). The tire was initially inflated to 28psi. The waveform due to tire deformation was measured using

a piezoelectric sensor mounted inside the tire. The experiments were performed on different terrains such as asphalt and concrete mostly at the speed of 10 mph, and normal loads of 3kN and 4kN. The waveform output is shown in Figure 12(b)-(d). These results illustrate that under the same normal load and varying terrains, the voltage output from the piezoelectric patch remained almost same (Figure 12(b)). This behavior can be explained as stress generated in the tire is proportional to radial acceleration, which remained unchanged for different terrain characteristics (under the same load). This leads to the unchanged voltage output waveform from the sensor.

In another parametric study during the field test, we observed that with increasing normal load on the tire, the voltage output was decreased significantly. This phenomenon could be attributed to the redistribution of the stress at the tire-road contact area, under increased normal load (on the same path) [48]. This redistribution of stress led to a higher stress on the outer periphery (tire shoulder) of the tire-road contact area, reducing stress on the central part (tire crown), where the piezoelectric patch was attached. This resulted in reduced voltage output. In order to observe the effect of the speed, output waveform was measured at 10 and 20 mph. The higher speed was found to result in the higher magnitude of the peaks in the output waveform (Figure 12(e)). This phenomenon can be explained by considering the fact that with increasing velocity, the rate of change of displacement of the tire increases, which further increases the voltage output. This behavior was also modeled in our theoretical calculations. Magnified image of the waveform (Figure 12(f)) clearly shows that our piezoelectric sensor-cum-harvester clearly captured the waveform of tire's compression and tension cycle. We have also performed additional field test under conditions like varying tire pressure, normal load, speed. The corresponding results have been shown in Figure 13.

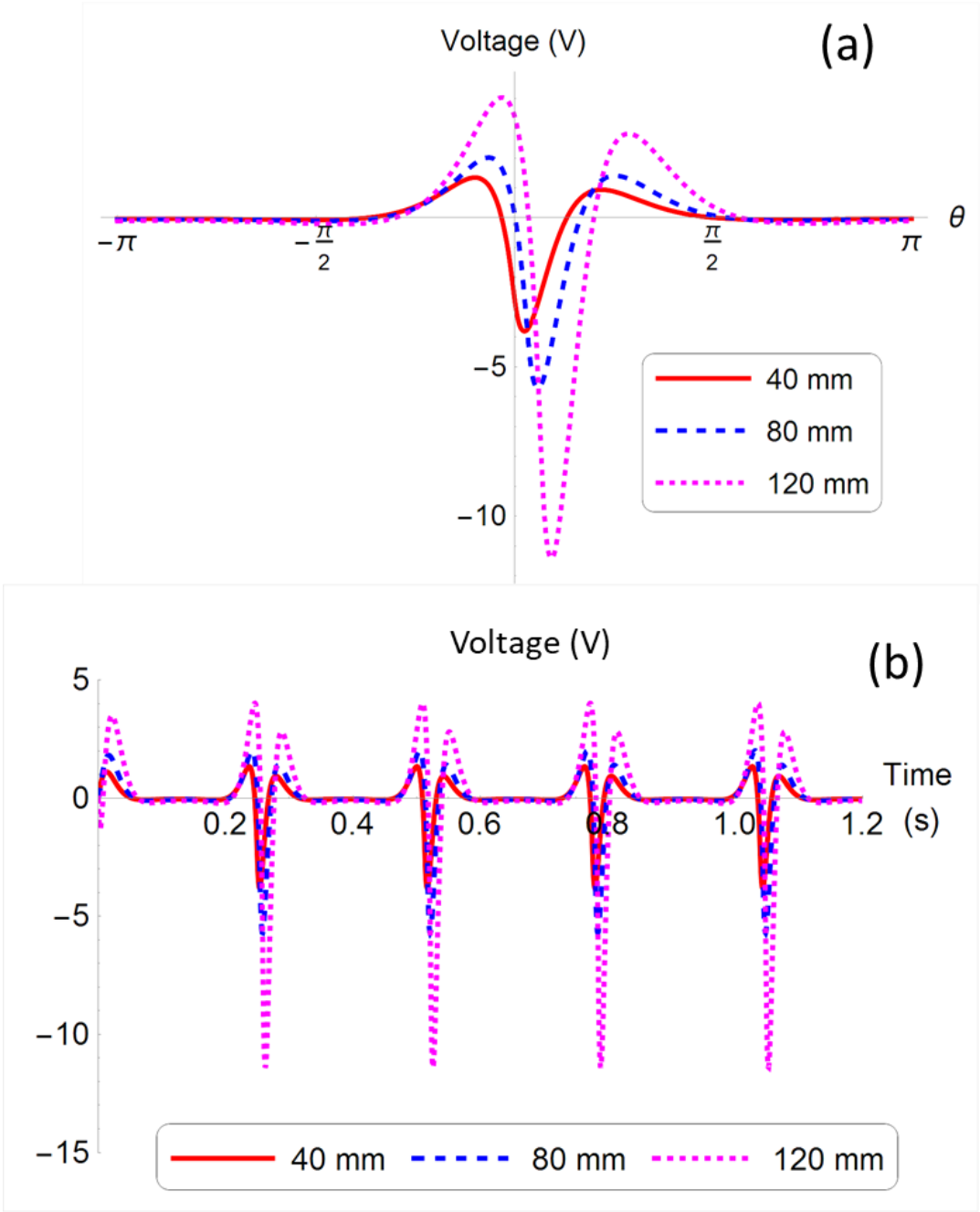

Figure 11: Effect of piezoelectric-patch (integrated with tires under 3000N load and 28 psi tire pressure) length on the voltage output for (a) one rotation, (b) several rotations.

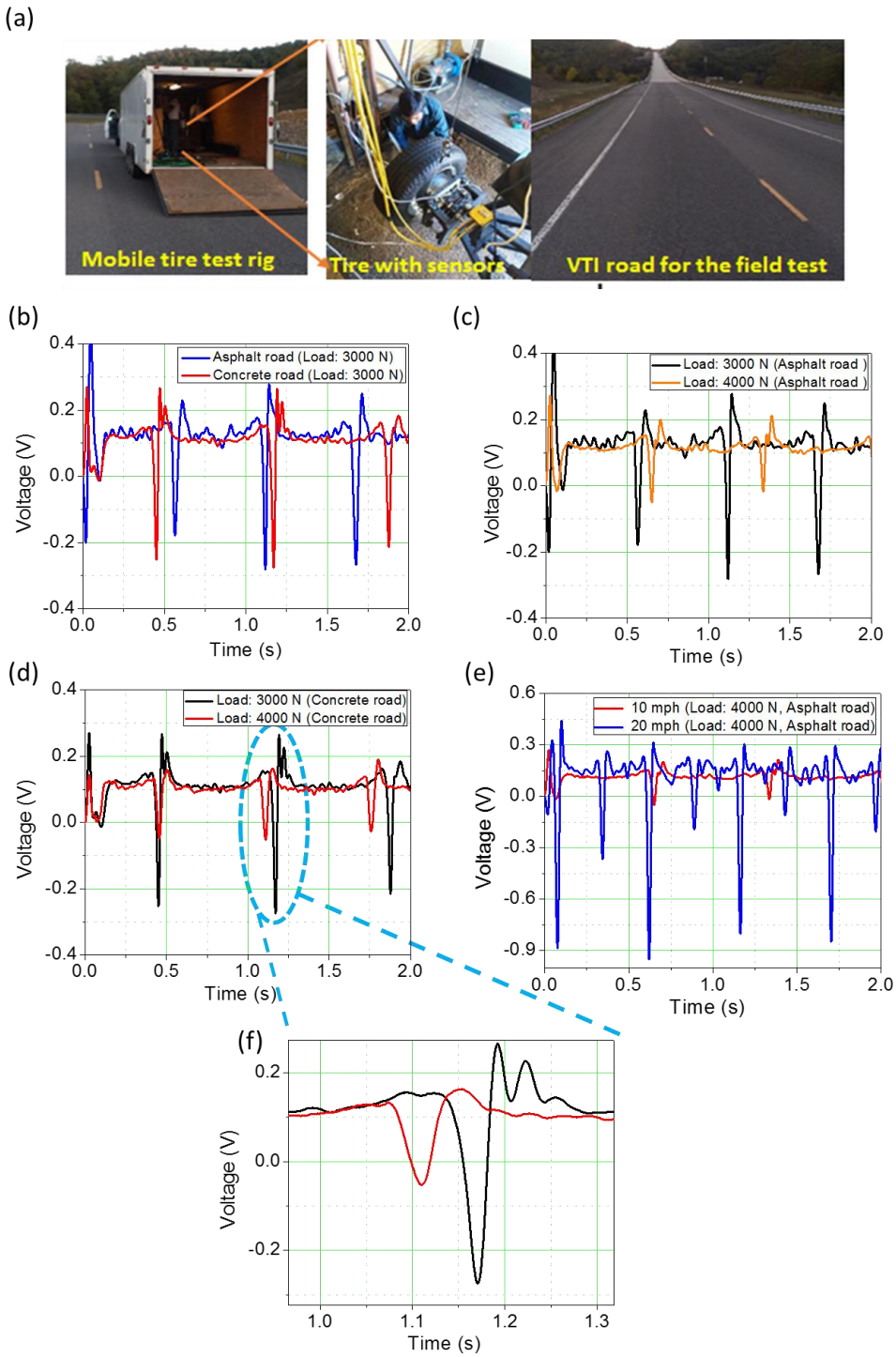

Figure 12: (a) Test setup for the field experiments. (b)-(d) Waveform generated due to tire deformation at the speed of 10 mph on different terrain and loads at 28 psi tire pressure. (e) Comparative waveform change at different speeds of 10 mph and 20 mph. (f) Zoomed image of one cycle of waveform having different wheel load

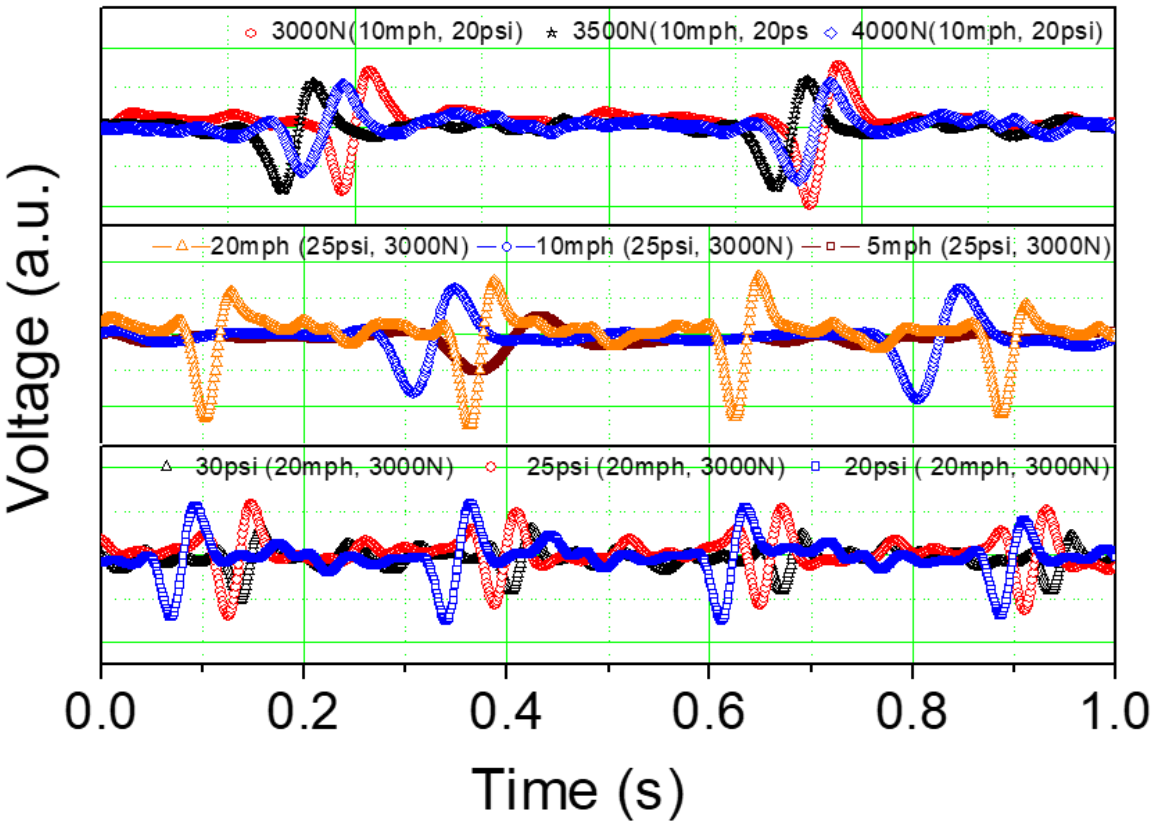

Figure 13**:** Waveform generated under variable tire speed, normal load, and tire pressure.

Additional field tests were performed under varying tire pressure, normal load, and speed, as shown in Figure 13. With increasing load at a constant speed and tire pressure, the output signal from the sensor was found to decrease. On the other hand, at a constant tire pressure and normal load, the amplitude of the output signal was found to increase. On decreasing the tire pressure while keeping other parameters constant (Load and speed), we observed an increase in the sensor output. These results clearly indicate the effect of external variables on the sensor output and their effect on the tire dynamics. The change in the sensor output can be used for monitoring the real conditions like tire pressure, normal load, and vehicle speed. Our experimental results are qualitatively in very good agreement with modeling results. The experimental voltage profile (compression-tension-compression) and trend of increasing voltage with an increase in tire speed (because strain rate of tire-patch increases as explained in modeling section) are consistent with modeling predictions. These results clearly indicate the effect of

external variables on the sensor output and their effect on the tire dynamics, which can be used for sensing terrain characteristics, tire pressure, normal load, and vehicle speed.

Conclusions

In summary, we demonstrated the feasibility of a self-powered tire sensor based on the piezoelectric effect for the autonomous vehicles. We report a detailed experimental analysis of the sensor-cum-harvester and its integration with a tire. Theoretical calculations were performed to model the tire-piezoelectric field testing results. The key features of the present work can be summarized as:

- Detailed experimental analysis of polymer-based piezoelectric patch in the lab environment at different frequencies corresponding to different vehicle speeds. Maximum peak power was evaluated to be ~580μW at 16 Hz.
- Demonstrated the wireless data transfer from the sensor by utilizing the stored energy generated from the piezoelectric patch. The output power was enough to light up 78 LEDs directly. The analysis shows that the power requirement for the wireless data transfer is met using the piezoelectric patch.
- Developed a mathematical model to calculate the radial and tangential displacement of the moving tire, and the generated voltage from the piezoelectric sensor mounted on the tire of the mobile test rig. Our modeling (of real field conditions) results indicated increased voltage output from the sensor (mounted on the tire) with increased vehicle speed.
- Finally, we conducted the field test with the real tire having a piezoelectric sensor, for different parameters, such as different tire speeds, loads and terrains. These field tests indicated no observable change in voltage output (from the sensor) due to change in terrain under the same load. Remarkably, we observed a clear change in the voltage output under varying normal loads and speeds, which were in agreement with our modeling results.

We believe this work is an important milestone in the development of smart tires for the next generation of fully autonomous vehicles.

References

[1] Jo K, Kim J, Kim D, Jang C, Sunwoo M. Development of autonomous car—Part I: Distributed system architecture and development process. IEEE Transactions on Industrial Electronics. 2014;61:7131-40.

[2] Litman T. Autonomous vehicle implementation predictions: Victoria Transport Policy Institute; 2017.

[3] Lee H, Taheri S. Intelligent Tires? A Review of Tire Characterization Literature. IEEE Intelligent Transportation Systems Magazine. 2017;9:114-35.

[4] Matsuzaki R, Todoroki A. Wireless monitoring of automobile tires for intelligent tires. Sensors. 2008;8:8123-38.

[5] Sergio M, Manaresi N, Tartagni M, Canegallo R, Guerrieri R. On a road tire deformation measurement system using a capacitive–resistive sensor. Smart materials and structures. 2006;15:1700.

[6] Eom J, Lee H, Choi B. A study on the tire deformation sensor for intelligent tires. International journal of precision engineering and manufacturing. 2014;15:155-60.

[7] Matsuzaki R, Kamai K, Seki R. Intelligent tires for identifying coefficient of friction of tire/road contact surfaces using three-axis accelerometer. Smart Materials and Structures. 2014;24:025010.

[8] Choi E. Tire-related factors in the pre-crash phase. Report No DOT HS. 2012;811:617.

[9] Consortium A. Intelligent tyre for accident-free traffic. Technical Research Centre of Finland (VTT), Tech Rep. 2003.

[10] Enhancement TR. Accountability, and Documentation (TREAD) Act. Public law. 2000;106:114.

[11] Kubba AE, Jiang K. A comprehensive study on technologies of tyre monitoring systems and possible energy solutions. Sensors. 2014;14:10306-45.

[12] Bowen C, Arafa M. Energy harvesting technologies for tire pressure monitoring systems. Advanced Energy Materials. 2015;5.

[13] Yilmazoglu O, Brandt M, Sigmund J, Genc E, Hartnagel H. Integrated InAs/GaSb 3D magnetic field sensors for “the intelligent tire”. Sensors and Actuators A: Physical. 2001;94:59-63.

[14] Doumiati M, Victorino A, Charara A, Lechner D. Lateral load transfer and normal forces estimation for vehicle safety: experimental test. Vehicle System Dynamics. 2009;47:1511-33.

[15] Braghin F, Brusarosco M, Cheli F, Cigada A, Manzoni S, Mancosu F. Measurement of contact forces and patch features by means of accelerometers fixed inside the tire to improve future car active control. Vehicle System Dynamics. 2006;44:3-13.

[16] Yi J. A piezo-sensor-based “smart tire” system for mobile robots and vehicles. IEEE/ASME transactions on mechatronics. 2008;13:95-103.

[17] Erdogan G, Alexander L, Rajamani R. Estimation of tire-road friction coefficient using a novel wireless piezoelectric tire sensor. IEEE Sensors Journal. 2011;11:267-79.

[18] Hattori Y. Method for detecting strain state of tire, device for detecting strain state, and the tire. Google Patents; 2007.

[19] Becherer T, Fehrle M. Vehicle wheel provided with a pneumatic tire having therein a rubber mixture permeated with magnetizable particles. Google Patents; 1999.

[20] Todoroki A, Miyatani S, Shimamura Y. Wireless strain monitoring using electrical capacitance change of tire: part I—with oscillating circuit. Smart Materials and Structures. 2003;12:403.

[21] Matsuzaki R, Todoroki A. Passive wireless strain monitoring of actual tire using capacitance–resistance change and multiple spectral features. Sensors and Actuators A: Physical. 2006;126:277-86.

[22] Pohl A, Ostermayer G, Reindl L, Seifert F. Monitoring the tire pressure at cars using passive SAW sensors. Ultrasonics Symposium, 1997 Proceedings, 1997 IEEE: IEEE; 1997. p. 471-4.

[23] Dixon B, Kalinin V, Beckley J, Lohr R. A second generation in-car tire pressure monitoring system based on wireless passive SAW sensors. International Frequency Control Symposium and Exposition, 2006 IEEE: IEEE; 2006. p. 374-80.

[24] Ko WH, Wang Q. Touch mode capacitive pressure sensors. Sensors and Actuators A: Physical. 1999;75:242-51.

[25] Pohl A, Steindl R, Reindl L. The" intelligent tire" utilizing passive SAW sensors measurement of tire friction. IEEE transactions on instrumentation and measurement. 1999;48:1041-6.

[26] Lee J, Choi B. Development of a piezoelectric energy harvesting system for implementing wireless sensors on the tires. Energy conversion and management. 2014;78:32-8.

[27] Velupillai S, Guvenc L. Tire Pressure Monitoring [Applications of Control]. IEEE Control Systems. 2007;27:22-5.

[28] Gawron JH, Keoleian GA, De Kleine RD, Wallington TJ, Kim HC. Life Cycle Assessment of Connected and Automated Vehicles: Sensing and Computing Subsystem and Vehicle Level Effects. Environmental science & technology. 2018;52:3249-56.

[29] Singh KB, Bedekar V, Taheri S, Priya S. Piezoelectric vibration energy harvesting system with an adaptive frequency tuning mechanism for intelligent tires. Mechatronics. 2012;22:970-88.

[30] Yang Z, Zhou S, Zu J, Inman D. High-Performance Piezoelectric Energy Harvesters and Their Applications. Joule. 2018.

[31] Schier M, Nasri M, Kraft W, Kevlishvili N, Paulides JJ, Encica L. Combining mechanical, electrical and thermal energy conversion for ecological vehicle energy harvesting concepts. Ecological Vehicles and Renewable Energies (EVER), 2018 Thirteenth International Conference on: IEEE; 2018. p. 1-10.

[32] Tornincasa S, Repetto M, Bonisoli E, Di Monaco F. Energy harvester for vehicle tires: Nonlinear dynamics and experimental outcomes. Journal of Intelligent Material Systems and Structures. 2012;23:3-13.

[33] Hatipoglu G, Urey H. FR4-based electromagnetic energy harvester for wireless tyre sensor nodes. Procedia Chemistry. 2009;1:1211-4.

[34] Van den Ende D, Van de Wiel H, Groen W, Van der Zwaag S. Direct strain energy harvesting in automobile tires using piezoelectric PZT–polymer composites. Smart materials and structures. 2011;21:015011.

[35] Hu Y, Xu C, Zhang Y, Lin L, Snyder RL, Wang ZL. A Nanogenerator for Energy Harvesting from a Rotating Tire and its Application as a Self-Powered Pressure/Speed Sensor. Advanced Materials. 2011;23:4068-71.

[36] Zhang H, Yang Y, Zhong X, Su Y, Zhou Y, Hu C, et al. Single-electrode-based rotating triboelectric nanogenerator for harvesting energy from tires. ACS nano. 2013;8:680-9.

[37] Low-Power Sensing. Freescale Semiconductor, Inc; 2015.

[38] Tire Pressure Monitoring (TPM) System. 2009 Microchip Technology Inc.; 2009.

[39] Gomez C, Oller J, Paradells J. Overview and Evaluation of Bluetooth Low Energy: An Emerging Low-Power Wireless Technology. Sensors. 2012;12:11734.

[40] Siekkinen M, Hiienkari M, Nurminen JK, Nieminen J. How low energy is bluetooth low energy? Comparative measurements with ZigBee/802.15.4. 2012 IEEE Wireless Communications and Networking Conference Workshops (WCNCW)2012. p. 232-7.

[41] Police: Flat tire leads to deadly crash on I-70; thousands of gallons of oil spilled. FOX59 WEB; 2017.

[42] Preumont A. Mechatronics: dynamics of electromechanical and piezoelectric systems: Springer Science & Business Media; 2006.

[43] Sunrong G. A study of in-plane dynamics of tires. Delft University of Technology, The Netherlands PhD Dissertation. 1993.

[44] Wei Y, Nasdala L, Rothert H. Analysis of forced transient response for rotating tires using REF models. Journal of sound and vibration. 2009;320:145-62.

[45] Xiong Y, Tuononen A. The in-plane deformation of a tire carcass: analysis and measurement. Case Studies in Mechanical Systems and Signal Processing. 2015;2:12-8.

[46] Parks VJ, Durelli A. Various forms of the strain-displacement relations applied to experimental strain analysis. Experimental Mechanics. 1964;4:37-47.

[47] Meirovitch L. A modal analysis for the response of linear gyroscopic systems. Journal of Applied Mechanics. 1975;42:446-50.

[48] Tsotras A. On the interaction between modal behaviour and shear force behaviour of a pneumatic tyre: © Achillefs Tsotras; 2010.

Conclusion and Future Work

This dissertation investigates the principles of energy conversion using low-dimensional (geometry) multifunctional materials. Various applications such as energy harvesting, sensing and actuation were demonstrated. A complete material characterization across all three classes of materials investigated within this dissertation was conducted to understand the material properties and invoke them in development of multi-physics models. Suitable system modeling (such as vibration, thermal, structural or acoustic analysis) techniques were developed to understand the active material integration with physical system. Extensive experimental analysis (or field-testing) was conducted to demonstrate the promise of materials considered here. In the following sections, detailed outcomes and future work related to each chapter is discussed.

Chapter 2 and 3

These chapters provide a comprehensive thermo-vibro-acoustic numerical model and experimental studies on MWNT sheet based acoustic transducer, targeting low frequency response (< 180 Hz) in water. An integrated multilayer model was developed to predict the performance of TA transducer under different fluidic environments. All modeling results were validated using results reported in literature and systematic experiments conducted in this dissertation both in air and water. On the basis of our modeling results, two low frequency encapsulated transducers were fabricated and complete vibrational and acoustical characterizations were conducted to identify the operating frequency range. For open system transducer, encapsulation can provide up to 10-12-fold increase in acoustic pressure at resonance.

Future work

- Search for alternative materials (instead of CNT) which are extremely hydrophobic in nature and can survive for longer time in water medium. Different compositions of 3D printed coatings on

nanotube sheets could be investigated the performance and reliability at the same time.

- Study of the close interaction between CNT and Ar to develop the understanding of the interfacial resistance from surrounding medium to the thermal flow.
- Study of the correlation between TA transduction efficiency and CNT-gas atom interaction

Chapter 4:

First systematic study on ocean wave energy harvesting using new twisted- and coiled-MWNT yarn is provided. An electrochemical transduction mechanism is studied that converts mechanical to electrical energy through change in capacitance. These yarns are highly flexible, non-resonant and non-corrosive. They exhibit a long stroke length, and high-power density. The output power is found to increase with frequency in the non-resonant condition. A mechanical frequency amplification mechanism is proposed to obtain the high frequency electrical output on lower frequency input (which is one of the major issues of current state-of-the-art wave energy harvesters).

Future work:

- Although CNT yarns produce very high power per unit weight, the technology still needs to be matured to provide higher output power and higher survivability. In future studies, attempts should be made in material developments to improve the output power at lower frequencies and lower mechanical input.
- Also, the attempts should be made to make the harvesting mechanism scalable (for real ocean wave conditions).

Chapter 5

SMAs can provide the mechanical strain on thermal input. Based on this property, a low grade SMA heat engine was demonstrated that operates below 80°C using ambient as the

heat sink. The electrical power density of the engine was calculated to be 36 W/kg of the active mass (SMA wire). The SMA material's thermodynamic efficiency was found to be 5.0%. The maximum thermal-to-electrical conversion efficiency of the engine was 1.5%, which is 10.5% of the Carnot efficiency. Due to very high-power density, high abundance of low-grade thermal energy, and if used for a long time this harvester could help in reducing the carbon foot print.

Future work

The efficiency and power density of the SMA device could be increased many-fold if the combination of material and mechanical changes are introduced. Some of the key parameters to be addressed in future include:

- Transformation temperatures: SMA material should be chosen to have high cooling and heating rates with a very small hysteresis. Consequently, the frequency of the transformation cycle will be increased which is proportional to the generated power. A proper compositional analysis and material-based modeling should be conducted for such material design.
- Maximum strain: The higher the strain the higher will be the work output per cycle. Thus, materials with high strain should be investigated under different pre-stress conditions.
- Fatigue life: SMAs are known to have issues regarding functional and structural fatigue. Functional fatigue can lead to residual martensite reducing the maximum strain and to a change in the transformation temperatures. Structural fatigue, which is often closely related to the functional fatigue will determine the life time of the SMA material. Thus, fatigue has to be investigated at material-level and for the whole device for very long durations (in years).

Chapter 6

The feasibility of developing and deploying a self-powered tire sensor based on the piezoelectric effect was demonstrated. A detailed experimental analysis of the dual function combining sensing and harvesting in the same structure was conducted.

Theoretical calculations were performed to model the results from testing of tire integrated with piezoelectric patches. The field data is important to guide the understanding between road and tire interactions.

Future work

- Field study: More robust field testing can be performed. The field data can be further used in deep learning to develop the algorithm for predicting road tire interaction features.
- Material study: Detailed investigation could be conducted in future to develop more mechanically robust, flexible and high-power density materials.